THESE de DOCTORAT DE
L'UNIVERSITE CLAUDE BERNARD LYON 1
EN COTUTELLE AVEC L'UNIVERSITE DE LIÈGE

Ecole Doctorale N° 160
L'Électronique, Électrotechnique et Automatique

Discipline : Automatique / Thermodynamique

Soutenue publiquement le 26/11/2025, Par
Ali Salame

Performance optimization of a CO_2 thermally driven heat pump application for domestic heating based on modeling and control

Devant le jury composé de :

Stouffs, Pascal	Professeur, Université De Pau Et Des Pays De L'Adour, France	Président/Rapporteur
Navarro-Peris, Emilio	Professeur, Université Polytechnique de Valence, Espagne	Rapporteur
Tayakout-Fayolle, Melaz	Professeure, Université Claude Bernard Lyon 1, France	Examinatrice
Zemouche, Ali	Professeur, Université De Lorraine, France	Examinateur
Gregoire, Leonard	Professeur, Université De Liège, Belgique	Examinateur
Bako, Laurent	Professeur, École Centrale de Lille, France	Examinateur
Dufour, Pascal	Maître de Conférences, Université Claude Bernard Lyon 1	Directeur de thèse
Lemort, Vincent	Professeur, Université de Liège	Co-directeur de thèse
Nadri, Madiha	Maître de Conférences, Université Claude Bernard Lyon 1	Co-directeur de thèse (Invitée)

“You think you are a small entity,
but within you the entire universe is contained.”

— Ali ibn Abi Talib

Abstract

Natural gas remains the dominant heating fuel in buildings worldwide, accounting for about 40% of total heating energy demand in 2022 according to the International Energy Agency (IEA). Conventional gas boilers still cover most of this demand, despite their contribution to greenhouse gas emissions. A promising alternative is the thermal compressor heat pump (TCHP), a thermally driven heat pump that also uses natural gas but in a fundamentally different way. Instead of converting the fuel directly into heat, as boilers do, the TCHP uses natural gas to drive a thermal compressor (TC), which transfers additional heat from an external source such as ambient air or water. This enables the TCHP to deliver more heat than the fuel energy it consumes, making it a potentially more energy-efficient replacement for conventional gas boilers.

A TCHP is a three-stage cycle that uses CO_2 as a working fluid mainly in its supercritical phase. The main innovation lies in its TC technology, which replaces a conventional electric compressor. However, the presence of multiple interacting components across the three stages, strong nonlinearities, and the sensitivity of the TC to operating conditions make the control of a TCHP particularly challenging. These complexities require advanced strategies that go beyond traditional control approaches. Addressing this challenge, the final aim of this thesis is to develop a new control strategy capable of enhancing the overall performance of the TCHP. To this end, various simulation tools and performance analyses are carried out to support the design and validation of the proposed control solution.

The first part of this thesis is dedicated to the TC, as a key component of a TCHP. To build a detailed understanding of this component, a review of Stirling-type machines is first presented, highlighting the unique features of the TC under study. An experimental campaign is then carried out on a TC integrated into a single-stage heat pump to evaluate its performance. This is complemented with a finite-volume (FV) physical model, which quantifies exergy destruction across the TC's internal components and provides insights about optimal operating conditions. However, due to its high stiffness and slow solving time, this model is not suitable for integration into a dynamic heat pump model. Therefore, several data-driven models are developed from available data to provide fast and reliable predictions. These models are suitable for integration into dynamic heat pump models for control optimization.

The second part of the thesis extends the analysis to the complete TCHP system. This part begins with a review of transcritical CO_2 cycles, discussing their specific characteristics as well as relevant modeling and control techniques. The TCHP cycle and process are then described, and dedicated experimental work is carried out. A dynamic FV model of the full system is proposed and validated against experimental data. Combining real measurements with simulation results, reduced-order recurrent neural network (RNN) models

are identified to provide efficient representations of the system dynamics. Finally, a new model predictive control (MPC) strategy is introduced, relying on the reduced models to enable optimal control of the TCHP system.

In summary, this thesis provides both component-level and system-level modeling tools, validated through experiments, and introduces a novel MPC strategy for a TCHP. These contributions not only support the development of efficient TCHPs as a sustainable alternative to gas boilers but also offer a foundation for future optimization studies.

Keywords: thermal compressor heat pump; transcritical CO_2; thermal compressor; exergy analysis; finite volume method; data-driven modeling; recurrent neural networks; model predictive control

Acknowledgments

Professional acknowledgments

This cotutelle PhD thesis is a collaboration between:

1. Laboratoire d'Automatique, de Génie des Procédés et de Génie Pharmaceutique. (LAGEPP), UMR 5007 CNRS–UCBL1, 43 boulevard du 11 Novembre, 69100 Villeurbanne, France,

2. LABOTHAP, University of Liège, Campus du Sart Tilman, Bât. B49, B-4000 Liège, Belgium,

3. Boostheat company, 41-47 Bd Marcel Sembat, 69200 Vénissieux, France.

The French Ministry of Higher Education and Research is also acknowledged for its financial support of this CIFRE PhD thesis 2022/0549.

Personal acknowledgments

Firstly, I would like to express my sincere gratitude to my supervisors, Pascal Dufour, Vincent Lemort, and Madiha Nadri. Your continuous support, valuable guidance, and insightful advice have been essential throughout this journey. This project would not have been possible without your encouragement and help.

To the members of the examination committee, I sincerely thank you for the time and energy you devoted to reading this manuscript and for your objective evaluation of my work.

I am also grateful to my colleagues Christophe Ancel, Rabah Ibsaine, and Hossein Fallahsohi, who greatly helped me during the first year of my thesis to acquire the knowledge necessary to work on Boostheat's novel technology. I extend my deepest appreciation to my laboratory colleagues Kévin Volet, Thomas Ferrier-Thuillier, and Laurant Dijoux, whose commitment and proficiency played a crucial role in the development of the experimental work that enhanced this thesis. Their contributions have been invaluable, and I am profoundly thankful for their collaboration throughout this project.

I also wish to acknowledge the colleagues I met during my visits to both LAGEPP and Labothap. I will always carry with me the beautiful memories and the inspiring conversations we shared.

My heartfelt thanks go to my friends for their unwavering support, patience, and encouragement throughout this PhD journey. Their belief in me has been a constant source of motivation and inspiration.

Finally, I am deeply grateful to my family for their unconditional love and support. I would especially like to thank my mother, father, sister, and brothers for always standing by me. Your encouragement has been fundamental in helping me reach this milestone.

Nomenclature

List of acronyms

ANN	Artificial Neural Network
BF	Burner Fan
BUF	Buffer
CD	Condenser
CFC	Chlorofluorocarbon
CFD	Computational Fluid Dynamics
COP	Coefficient of Performance
CV	Control Volume
EEV	Electronic Expansion Valve
EV	Evaporator
FHX	Fume Heat Exchanger
FT	Flash Tank
FV	Finite Volume
GC	Gas Cooler
GP	Gaussian Process
GRU	Gated Recurrent Unit
GWP	Global Warming Potential
HCFC	Hydrochlorofluorocarbon
HPV	High-Pressure Valve
IHX	Internal Heat Exchanger
LHV	Lower Heating Value
LMTD	Logarithmic Mean Temperature Difference
LPV	Low-Pressure Valve
LR	Linear Regression
LSTM	Long Short-Term Memory
MAE	Mean Absolute Error
MAPE	Mean Absolute Percentage Error
MB	Moving Boundary
MIMO	Multi Input Multi Output
ML	Machine Learning
MPC	Model Predictive Control
MPG	Monopropylene Glycol
MSE	Mean Squared Error
NN	Neural Network

ODE	Ordinary Differential Equation
ODP	Ozone Depletion Potential
PID	Proportional-Integral-Derivative Controller
PRBS	Pseudo Random Binary Sequence
R^2	Coefficient of Determination
RNN	Recurrent Neural Network
SISO	Single Input Single Output
TC	Thermal Compressor
TCHP	Thermal Compressor Heat Pump
TCHP-HYB	Thermal Compressor Heat Pump Hybrid
TDHP	Thermally Driven Heat Pump
VCC	Vapor Compression Cycle

List of symbols

a	Coefficients	-
A	Wetted area	m^2
A_{cs}	Cross-sectional area	m^2
b	Coefficients	-
c	Coefficients	-
c_p	Isobaric specific heat capacity	$J{\cdot}kg^{-1}{\cdot}K^{-1}$
c_v	Isochoric specific heat capacity	$J{\cdot}kg^{-1}{\cdot}K^{-1}$
C_d	Discharge coefficient	-
d_h	Hydraulic diameter	m
$\dot{E}$	Exergy transfer rate	W or kW
EX	Excess air	-
f	System dynamic function	Multiple
fr	Friction coefficient	-
Fr	Friction force	N
h	Fluid enthalpy	$J{\cdot}kg^{-1}$
$\mathcal{I}$	Set of indices	-
k	Discrete time step	-
K	Thermal conductivity	$W{\cdot}m^{-1}{\cdot}K^{-1}$
L	Minor loss coefficient	-
l	Length	m
LHV	Lower heating value	$MJ.kg^{-1}$
m	Mass	kg
$\dot{m}$	Mass flow rate	$kg.s^{-1}$ (equations) or $g.s^{-1}$ (figures and tables)
N	Number of discretization in space	-
N_s	Number of samples	-
n_c	Control horizon	-
n_p	Prediction horizon	-
Nu	Nusselt number	-

p	Pressure	Pa (equations) or bar (figures and tables)
Pr	Prandtl number	-
q	Vapor quality	-
$\dot{Q}$	Heat transfer rate	W (equations) or kW (figures and tables)
r	Radius	m
$R_{\mathrm{CO_2}}$	Gas constant of CO_2	m
r_p	Pressure ratio	-
r_s	Stoichiometric ratio	-
Re	Reynolds number	-
res	Residual	-
s	Entropy	J·kg^{-1}·K^{-1}
t	Continuous time	s
T	Temperature	K (equations) or °C (figures and tables)
U	Heat transfer coefficient	W·m^{-2}·K^{-1}
u	Input	-
V	Volume	m^3 (equations) or cm^3 (figures and tables)
$\dot{V}$	Volume variation	m^3·s^{-1}
v	Velocity	m·s^{-1}
$\dot{W}$	Power	W
X	Displacement	m
x	State	-
y	Output	-
α	Weighting factor for control objective	-
γ	Regenerator temperature update coefficient	-
Δ	Differential	-
δx	Distance between two nodes on i-axis	m
ϵ	Surface roughness	-
η	Efficiency	-
θ	Crank angle	°
τ	Time constant	s
μ	Viscosity	Pa·s
Φ	Porosity	-
φ	Valve opening	%
ψ	specific flow exergy	J·kg^{-1}
σ	Activation function	-
ω_{m}	Rotational speed	rpm
ρ	Density	kg·m^{-3}
∂x	Distance between two nodes on j-axis	m

bf	burner fan
buf	buffer
cc	cold cavity
comb	combustion
cra	crank
d	displacer
dis	discharge
elec	electricity
ev	evaporator
ex	exergy
f	working fluid
fhx	fume heat exchanger
ft	flash tank
g	gas
gc	gas cooler
h	heater
hc	hot cavity
hpv	high-pressure valve
ihx	internal heat exchanger
i	relative to node i
j	relative to node j
k	cooler
l	liquid
lpv	low-pressure valve
m	motor
max	maximum
mech	mechanical
min	minimum
mpg	monopropylene glycol
opt	optimal
outlet	outlet
pred	prediction
r	regenerator
rec	recovered
ref	reference
ret	return
rnn	recurrent neural network
seq	sequence
sf	secondary fluid
sp	setpoint
str	stroke
suc	suction
sup	supply
sha	shaft
tc	thermal compressor

th	thermal
tot	total
v	vapor
val	valve
w	water
wall	wall

Contents

I Experimental and numerical analysis of a thermal compressor for heat pump cycles **29**

1 Introduction **31**
1.1 Introduction to Stirling machines . . . 31
1.1.1 Stirling engine . . . 31
1.1.2 Stirling thermal compressor . . . 34
1.2 Thermal compressor for heat pumps . . . 34
1.2.1 Components . . . 34
1.2.2 Crank mechanism . . . 36
1.2.3 Thermal compression process . . . 36
1.3 TC experimental work . . . 37
1.3.1 Test bench description . . . 38
1.3.2 Measurements . . . 39
1.3.3 Experimental protocol and conditions . . . 39
1.3.4 TC performance indicators . . . 41
1.3.5 Outliers detection with gaussian process . . . 43
1.3.6 TC performance metric . . . 44
1.4 Conclusion . . . 47

2 Thermal compressor third order model **49**
2.1 Introduction . . . 49
2.1.1 Modeling approaches for Stirling machines . . . 49
2.1.2 Third-order modeling approach . . . 51
2.2 TC third-order model . . . 51
2.2.1 Governing equations . . . 52
2.2.2 Suction and discharge valves . . . 55
2.2.3 Empirical correlations . . . 55
2.3 Numerical model resolution . . . 57
2.3.1 Initial conditions . . . 57
2.3.2 Solving process . . . 57
2.3.3 TC-3RD model-derived performance indicators . . . 58
2.3.4 Python implementation . . . 60
2.4 Model validation with data . . . 60
2.4.1 Transient validation with CFD . . . 60
2.4.2 Steady-state validation . . . 61
2.5 TC-3RD model-based exergy study . . . 62

2.5.1 Methodology . . . 63
2.5.2 Results . . . 65
2.6 Conclusion . . . 66

3 Thermal compressor empirical models 69
3.1 Data extension and re-assessment . . . 69
3.2 Machine learning models . . . 70
3.2.1 Regression models . . . 70
3.2.2 Gaussian process regression . . . 71
3.2.3 Artificial neural network model . . . 72
3.2.4 Common implementation . . . 73
3.3 Models accuracies . . . 73
3.4 Conclusion . . . 75

II Dynamic modeling and control of a three-Stage transcritical CO_2 thermal compressor heat pump 77

4 Introduction 79
4.1 Carbon Dioxide as a refrigerant . . . 79
4.1.1 Historical review . . . 79
4.1.2 Unique properties . . . 80
4.2 Transcritical CO_2 cycle . . . 81
4.2.1 Basic single-stage . . . 81
4.2.2 Architectural modifications . . . 82
4.3 TCHP architecture and experimental setup . . . 83
4.3.1 System architecture and operation . . . 83
4.3.2 Experimental conditions . . . 84
4.3.3 Components . . . 85
4.3.4 Measurements . . . 85
4.3.5 Actuators and system inputs . . . 86
4.3.6 Energy Expressions . . . 87
4.4 Collected experimental data . . . 88
4.4.1 Transient . . . 88
4.4.2 Steady-state . . . 90
4.5 Conclusion . . . 93

5 Dynamic model for the TCHP 95
5.1 Literature review of dynamic models for vapor compression cycles . . . 95
5.1.1 Physics-based: Finite volume and moving boundary methods . . . 96
5.1.2 Dynamic models for transcritical CO_2 cycles . . . 97
5.2 TCHP hybdrid dynamic model . . . 97
5.2.1 Differential equations of the TCHP-HYB model . . . 98
5.2.2 Quasi-static part of the TCHP-HYB model . . . 102
5.3 Numerical resolution . . . 108
5.3.1 Final model summary . . . 108

5.3.2 Final model architecture . . . 110
5.3.3 Solving process . . . 112
5.3.4 Python implementation . . . 112
5.4 Model Validation . . . 113
5.4.1 Steady State . . . 113
5.4.2 Transient Validation . . . 114
5.5 Conclusion . . . 117

6 RNN reduced model and MPC control for a TCHP 121
6.1 Control strategies for vapor compression cycles . . . 121
6.1.1 Degrees of freedom . . . 122
6.1.2 History of control systems . . . 123
6.1.3 MPC and advanced control . . . 123
6.1.4 Reduced models . . . 124
6.1.5 Control of transcritical CO_2 cycles . . . 125
6.2 TCHP control problem formulation . . . 128
6.2.1 Baseline control strategy . . . 128
6.2.2 Experimental case study . . . 130
6.3 MPC-RNN proposed control strategy . . . 131
6.3.1 RNN reduced models . . . 131
6.3.2 MPC design . . . 136
6.3.3 Control strategies validation . . . 138
6.4 Conclusion . . . 139

7 Conclusions and perspectives 143

A Résumé étendu en français de la thèse 147

List of Figures

1 Objectives and steps of Part I and Part II along with their connection. 27

1.1 Stirling engine of beta-type scheme. 32
1.2 Stirling engine cycle: (a) p–V and (b) T–s diagrams. 33
1.3 STC scheme. 35
1.4 TC vertical cross-section showing its components. 35
1.5 Crankshaft mechanism generating the volume variations. When $\theta_{\mathrm{m}} = 0°$, the displacer is at the top of the hot cavity; when $\theta_{\mathrm{m}} = 180°$, it is at the bottom of the cold cavity. 36
1.6 TC behavior: (a) variations of cold-cavity, hot-cavity, and total working volumes during two complete cycles, $\theta_{\mathrm{m}} \in [0°, 720°]$; (b) p–V diagrams of the cold cavity, hot cavity, and total working volumes. 37
1.7 TC processes represented by the variation of internal pressure p as a function of displacer position X_{d}. 38
1.8 TC in a Single-stage heat pump cycle: (a) experimental setup and (b) thermodynamic representation. 40
1.9 TC upper part in the Boostheat test bench, showing the burner fan, methane–air mixture passage, combustion chamber, fume exit pipe, and fume heat exchanger (FHX). 41
1.10 TC lower part in the Boostheat test bench, showing the motor casing containing the electric motor, the water jacket surrounding the cooler, the corresponding water pipes, and the suction and discharge valves. 42
1.11 TC energy conversion processes. 42
1.12 TC collected data outliers detection using GP: (a) Heater heat transfer rate $\dot{Q}_{\mathrm{h}}$, (b) Cooler heat transfer rate $\dot{Q}_{\mathrm{k}}$, (c) mechanical power $\dot{W}_{\mathrm{mech}}$, (d) mass flow rate $\dot{m}_{\mathrm{f}}$, and (e) discharge temperature T_{dis}. 45
1.13 TC exergy efficiency at different operating conditions covered by the experimental campaign. 47

2.1 TC schematic representation of (a) main components and (b) spatially discretized grid. The i-axis contains thermodynamic properties of the CO_2 (p, h, ρ, etc.), while the j-axis denotes interfaces carrying velocity and mass flow rate information ($v_j, \dot{m}_j$). δx is the length of one solid CV, while dx is the distance between two dashed lines. 53
2.2 TC-3RD model scheme containing inputs (operating conditions and component parameters), outputs at each CV and interface, suction and discharge mass flow rates, and performance indicators. 57

2.3 TC-3RD model numerical simulation flow chart. 59
2.4 TC-3RD model (dashed) vs CFD (solid) transient predictions during one periodic steady cycle. 61
2.5 TC-3RD model validation—simulated (sim) vs experimental (exp, markers) performance indicators versus pressure ratio r_p at three rotational speeds $\omega_{\mathrm{m}} \in \{150, 200, 240\}$ rpm. 63
2.6 TC-3RD model validation—simulated (sim) vs experimental (exp, markers) performance indicators as a function of pressure ratio r_p at three charged pressures $p_{\mathrm{charged}} \in \{30, 40, 56\}$ bar. 64
2.7 Breakdown of exergy destruction by component at representative operating conditions of the TC. 65
2.8 Exergy efficiency of the TC as a function of pressure ratio under three different operating conditions: (a) heater temperature T_{h}, (b) rotational speed ω_{m}, and (c) charged pressure p_{charged}, ... 66

3.1 Inputs and outputs of TC-ML models. 70
3.2 Structure of a generic neuron in the ANN model. 72
3.3 TC-ML models accuracy comparison on main outputs: (a) heater heat transfer rate, (b) cooler heat transfer rate, (c) mechanical power, (d) mass flow rate, and (e) discharge temperature. 74

4.1 CO_2 (a) p–T and (b) p–h diagrams with different states generated with the CoolProp library. 81
4.2 Transcritical CO_2 (a) basic cycle scheme and corresponding (b) p–h diagram. 82
4.3 TCHP (a) test Bench layout with the corresponding (b) T-s diagram of CO_2 in the cycle (maybe add numbering). 84
4.4 TCHP scheme showing the inputs and the outputs. 87
4.5 TCHP experimental data from varying the low-pressure valve opening. . . . 90
4.6 TCHP experimental data from varying the high-pressure valve opening. . . . 91
4.7 TCHP experimental data from varying Burner fan speed. 92

5.1 Heat exchanger spatial discretization into N CVs. Each CV on the i-axis carries uniform pressure and enthalpy, while the j-axis carries uniform mass flow rate information. 99
5.2 Flash tank schematic with the corresponding flow streams. 101
5.3 Heater 1 temperature T_{h1} identified model validation. MAE is 15.86 K and R^2 is 0.96, indicating a good fit. The bottom plot shows the burner fan speed and motor 1 rotational speed over time, illustrating their influence on T_{h1} dynamics. 102
5.4 Heater 2 temperature T_{h2} identified model validation. MAE is 16.77 K and R^2 is 0.94, indicating a good fit. The bottom plot shows the burner fan speed and motor 2 rotational speed over time, illustrating their influence on T_{h2} dynamics. 103
5.5 GPR model steady-state parity plots showing the predicted outputs of TC1 compared to measured ones. 104

5.6 GPR model steady-state parity plots showing the predicted outputs of TC2 compared to measured ones. . . . 104
5.7 LR model steady-state parity plots showing the predicted outputs of TC3 compared to measured ones. . . . 104
5.8 Expansion valve models steady-state parity plots showing the predicted mass flow rates from fitted Equations (5.27) and (5.28), compared to the measured ones. . . . 106
5.9 Fume heat exchanger schematic. . . . 107
5.10 Fume heat exchanger model steady-state parity plots showing the predicted heat transfer rate from fitted Equation (5.33) compared to the measured ones. 107
5.11 Fume heat exchanger LMTD iterative method. . . . 108
5.12 Refrigerant-side architecture of the TCHP-HYB model. . . . 111
5.13 Water and fume-side architecture of the TCHP-HYB model. . . . 112
5.14 Flow chart of the TCHP-HYB model solution procedure. . . . 113
5.15 TCHP-HYB model steady-state parity plots showing the gas cooler predicted outputs compared to the measured ones. . . . 114
5.16 TCHP-HYB model steady-state parity plots showing the evaporator predicted outputs compared to measured ones. . . . 115
5.17 TCHP-HYB model steady-state parity plots showing the performance outputs of a TCHP. . . . 115
5.18 TCHP-HYB model transient validation with real experimental data varying the low-pressure valve opening. The real data is in solid, while simulated model is dashed. . . . 117
5.19 TCHP-HYB model transient validation with real experimental data varying the high-pressure valve opening. The real data is in solid, while simulated model is dashed. . . . 118
5.20 TCHP-HYB model transient validation with real experimental data varying the burner fan speed. The real data is in solid, while simulated model is dashed. . . . 119

6.1 VCC overview of a hierarchical control scheme (reproduced from Beghi et al. (2017)). . . . 122
6.2 Transcritical CO_2 cycle p–h diagrams: (1–2–3–4) in red and (1–2′–3′–4′) in blue, each at a different high-pressure value. . . . 127
6.3 TCHP SISO PID schemes. . . . 130
6.4 PID-based control strategy: The TCHP-HYB model is controlled using two parallel PID loops. The first loop adjusts the burner fan speed ω_{bf} to track $T_{\mathrm{h1}}^{\mathrm{sp}}$, which is correlated to $T_{\mathrm{w,sup}}^{\mathrm{sp}}$ via g_1. The second loop controls the HPV opening φ_{hpv} to regulate p_{gc}, where the setpoint $p_{\mathrm{gc}}^{\mathrm{sp}}$ is determined through the mapping $g_4(T_{\mathrm{gc,out}})$. . . . 131
6.5 TCHP baseline control strategy: real evaluation showing variation of outputs: supply water temperature $T_{\mathrm{w,sup}}$, heater temperatures T_{h1} and T_{h2}, and high-pressure p_{gc}. . . . 132
6.6 TCHP baseline control strategy real evaluation of system. Variation of inputs: burner fan speed ω_{bf} and high-pressure valve percentage opening φ_{hpv}. 133

6.7 MPC-based control strategy: This model predictive control framework relies on a learned model of the system based on vanilla RNN or LSTM as reduced models. The optimizer computes the optimal control actions $\varphi_{\mathrm{hpv}}^{\mathrm{opt}}$ and $\omega_{\mathrm{bf}}^{\mathrm{opt}}$ over a prediction horizon to track the $T_{\mathrm{w,sup}}^{\mathrm{sp}}$, given the current return water temperature $T_{\mathrm{w,ret}}$ and water mass flow rate $\dot{m}_{\mathrm{w}}$. The optimizer uses predictions from the reduced model, which captures the system dynamics. The optimized inputs are applied to the TCHP-HYB model, and the resulting outputs $T_{\mathrm{w,sup}}$ and T_{h1} are fed back to the MPC block. 134
6.8 Encoder–decoder RNN architecture unrolled over time steps. The encoder processes past inputs $z(1)$ to $z(l_{\mathrm{seq}})$, and the decoder recursively predicts future outputs $\hat{y}(1)$ to $\hat{y}(l_{\mathrm{pred}})$, conditioned on known future inputs. This structure allows the model to capture temporal dependencies and generate multi-step predictions. 135
6.9 Vanilla RNN model validation on unseen data from experiments (blue) and TCHP-HYB model (purple). The model is initialized using 10 previous samples, followed by prediction of the next 500 samples. The transition between initialization and prediction is indicated by the black dashed line. The plot shows the predicted and true values of the supply water temperature $T_{\mathrm{w,sup}}$. The RNN achieves a MSE of 0.84 K^2 and an R^2 score of 0.975, indicating high predictive accuracy over the forecasting horizon. 136
6.10 LSTM model validation on unseen data from experiments (blue) and TCHP-HYB model (purple). The model is initialized using 10 previous samples, followed by prediction of the next 500 samples. The transition between initialization and prediction is indicated by the black dashed line. The plot shows the predicted and true values of the supply water temperature $T_{\mathrm{w,sup}}$. The LSTM achieves a MSE of 0.76 K^2 and an R^2 score of 0.977, indicating high predictive accuracy over the forecasting horizon. 137
6.11 Transient evaluation of PID, MPC-RNN, and MPC-LSTM: resulting supply water temperature $T_{\mathrm{w,sup}}$, first heater temperature T_{h1}, high pressure p_{gc}, and their corresponding setpoints. 140
6.12 Transient evaluation of PID, MPC-RNN, and MPC-LSTM: resulting control inputs of burner fan speed ω_{bf} and high-pressure valve opening φ_{hpv} (percentage). 141
6.13 Average evaluation of PID, MPC-RNN, and MPC-LSTM: (a) thermal COP and (b) supply water temperature error, shown as bar plots. 141

List of Tables

1.1 Sensor specifications used in the TC experiment. 39
1.2 TC input operating-variable ranges during the experimental campaign. . . . 41
1.3 TC performance-indicator ranges, either measured directly or calculated from measurements. 43

2.1 TC component geometrical parameters. 56
2.2 TC components with the assigned number of CVs for simulation. 58

3.1 TC input variables after data extension. 70
3.2 Cross-validation results of TC-ML models across performance-indicator outputs. Metrics shown are mean $\pm$ standard deviation. 75

4.1 TCHP specifications of components and fluids. 85
4.2 TCHP test bench deployed sensor types and accuracies. 85
4.3 TCHP manipulated input variables, operating ranges, and units. 88
4.4 TCHP controlled output variables, typical value ranges, and units. 89
4.5 TCHP inputs kept constant during transient tests. 89
4.6 TCHP steady-state samples: valve openings, burner fan speed, heater temperature, pressures, and outlet temperatures. 91
4.7 TCHP steady-state samples: TC1, TC2, and TC3 mass flow rates, discharge temperatures, and cooler heat transfer rates. 92
4.8 TCHP steady-state samples: fume heat exchanger inlet/outlet fume temperature, inlet/outlet water temperature, fume and water mass flow rates, and recovered heat. 93
4.9 TCHP steady-state samples: return and supply water/glycol temperatures, total recovered heat, thermal COP, and evaporator and gas cooler heat-transfer rates. 93

5.1 TC models prediction accuracy for each output: MAPE for flow and power variables, MAE for temperatures, and R^2 for all outputs. 105
5.2 Summary of component submodels used in the final TCHP-HYB model. . . . 109
5.3 MAPE, MAE (for pressure), and R^2 of model output predictions under steady-sate data conditions. 115
5.4 MAPE, MAE (for pressure), and R^2 of model output predictions under transient step tests for LPV, HPV, and BF. 117

6.1 System variables categorized for control design. 129

6.2 Operating ranges of input and output variables used for training the RNN reduced models. 135
6.3 Average performance evaluation of PID, MPC-RNN, and MPC-LSTM controllers. 140

General Introduction

Context

Since the beginning of civilization, humans have relied on natural resources to improve comfort and living conditions. Over time, this reliance has grown rapidly, driving technological progress at a pace faster than the environment can naturally adapt. One major consequence is global warming, now recognized as a critical global challenge. The inefficient use of fossil fuels for industry, transport, and households has released large amounts of greenhouse gases into the atmosphere.

According to the Intergovernmental Panel on Climate Change (IPCC (2023)), global temperatures have risen by 1.1°C since the 19th century, leading to extreme weather events and the melting of ice caps. Fossil fuels remain the dominant driver of emissions, accounting for about 75% of global greenhouse gases and nearly 80% of primary energy consumption worldwide (BP (2023)). In the European Union (EU), Eurostat (2022) reports that households accounted for 25.8% of the EU's final energy use in 2022, with space and water heating alone representing 78.4%. These demands remain heavily dependent on gas and oil boilers (IEA (2023)).

While the complete transition to renewable energy sources remains a long-term goal, improving the efficiency of existing fossil fuel-based systems serves as a practical intermediate solution. Despite their potential, electric heat pumps are still less adopted than gas boilers due to various limitations, including infrastructure and efficiency concerns under certain conditions (IEA (2022)). In this context, thermally driven heat pumps offer a viable solution by combining the advantages of gas boilers and electric heat pumps. These systems use heat as the driving force for the heat pump cycle, leveraging outdoor environmental conditions to enhance overall efficiency.

The most widely used thermally driven heat pumps are absorption and adsorption systems, which rely on heat input rather than mechanical work to drive the cycle through chemical processes (Kühn (2013)). These are commonly employed in applications such as district heating, industrial waste heat recovery, and solar-assisted systems. Another established configuration involves coupling a gas engine with a conventional vapor compression heat pump, where the engine drives the compressor and its waste heat can be recovered to enhance overall efficiency (Pawela and Jaszczur (2022)). Less common but conceptually valid configurations include replacing the gas engine with a Stirling one.

A more specific configuration developed by Boostheat, namely the thermal compressor heat pump (TCHP), uses a Stirling-type thermal compressor (TC) instead of a Stirling engine and mechanical compressor coupling (Ibsaine et al. (2016)). The TC is powered by heat energy, which originates from fuel combustion. Due to the relatively low pres-

sure ratio achieved by a single TC and the advantageous characteristics of CO_2 in the transcritical regime, the system architecture involves coupling three TCs in series (Ibsaine (2015)). This increased complexity introduces multiple interdependent processes that must operate in harmony to ensure optimal performance, a challenge that necessitates the implementation of advanced control strategies. Another critical motivation for integrating control systems in such cycles is the unique behavior of CO_2, which requires dynamically adjusting the optimal high-pressure values to maximize efficiency under varying operating conditions (Lorentzen (1994)). Without precise control, maintaining or reaching these optimal pressures becomes challenging, resulting in performance losses and potential system instability. Additionally, this technology relying primarily on gas presents an interesting solution for remote areas lacking access to electrical grids, as it can offer higher efficiency and independence from electricity supply constraints.

In conclusion, addressing the challenges posed by global warming requires a comprehensive approach that balances technological advancement with environmental sustainability. The adoption of energy-efficient solutions, such as heat pumps and natural refrigerants, combined with the gradual phase-out of fossil fuels, can significantly mitigate the impacts of climate change while ensuring a sustainable future. Enhancing system efficiency inherently requires the development of advanced and intelligent control strategies, making them an indispensable component of modern energy solutions.

Objectives

Performance optimization of a CO_2 transcritical cycle can be pursued through modifications to component geometries, adjustments to cycle configurations, or the development of advanced control strategies. In this work, however, with fixed components, cycle layout, and working fluid, the primary objective is to optimize the performance of a TCHP application through a novel Model Predictive Control (MPC). To do so, a comprehensive dynamic model that captures system transient responses is required, beginning with component-level representations that are subsequently integrated into a system-level framework.

Particular attention is devoted to the TC, the key component distinguishing a TCHP from conventional electrically driven heat pump cycles. Due to its high influence on overall performance, the first objective is to characterize this component through experimental testing, detailed physical modeling, and data-driven approaches, thereby establishing performance indicators and identifying optimal operating conditions. Building on these component-level insights, the study then extends to the complete TCHP cycle including three serially connected TCs, where the architecture and processes are described, and a hybrid dynamic model is developed and validated against experimental data in both steady-state and transient regimes. Since the full model is too complex for real-time control, reduced-order recurrent neural network (RNN) models are trained to provide efficient dynamic representations. These reduced models form the basis of a new MPC framework, designed to replace conventional single-input PID loops with a multi-input strategy capable of coordinating the strong couplings and nonlinearities inherent to the system. The validated hybrid dynamic model of the TCHP is finally adopted as the benchmark to evaluate and demonstrate the benefits of the proposed MPC strategy for performance optimization.

Thesis Contributions

The contributions of this thesis revolve around TC modeling and experimentation and extend to TCHP modeling, experimentation, and control. The main contributions are as follows:

- Experimental work on a Stirling-type TC with suction and discharge valves, integrated into a single-stage heat pump cycle, to validate the models and analyze performance (Chapter 1).
- Development of a third-order physical model (finite volume (FV)-based) of a Stirling-type TC for heat pump applications, denoted 'TC-3RD'. The model is implemented in an open-source Python framework and can be adapted for Stirling engine applications (Chapter 2).
- Data-driven modeling of the Stirling-type TC using various machine learning models. Several types of models are trained and compared (Chapter 3).
- Experimental work on a three-stage transcritical CO_2 heat pump for heating. The collected data are used to validate the dynamic model at the system level (Chapter 4).
- Derivation of a hybrid dynamic model combining physical (FV-based) and empirical (data-based) approaches for the three-stage transcritical CO_2 TCHP, denoted 'TCHP-HYB'. The model is developed in a modular Python object-oriented framework, and its predictive capability is validated with real experimental data (Chapter 5).
- Use of an RNN as a reduced-order model for prediction within the MPC framework, connecting supply water temperature to internal inputs such as the opening of the expansion valve and burner fan speed. This provides a proof-of-concept for advanced control of a three-stage transcritical CO_2 TCHP (Chapter 6).

Manuscript content

This manuscript is divided into two main parts.

1. **Part I** investigates the Stirling-type TC for heat pump cycles through experimental, modeling, and performance analysis. This part builds upon Chapters 1 to 3. Chapter 1 presents a state-of-the-art review of Stirling-type machines, with a particular focus on the Stirling engine as the most well-known example. The components of a Stirling engine and its thermodynamic cycle are reviewed. Stirling thermal compressors (STCs) are then discussed, distinguishing between one-orificed types often used for pulse tube cooling and the second type with separate suction and discharge valves, to which the targeted TC belongs. The targeted TC is then introduced, distinguishing it from other Stirling-type machines. Experimental work is conducted by integrating the TC into a single-stage heat pump, from which data are collected and filtered using a Gaussian process method. A new exergy-based performance metric is defined to characterize the TC. Chapter 2 develops a detailed physical model of

the TC, denoted 'TC-3RD', where it is spatially discretized into control volumes using the FV method, and mass, momentum, and energy balance equations are applied. The model is validated against real data under steady-state conditions and assessed for transient behavior through comparison with CFD simulations. A detailed exergy analysis is performed to pinpoint the components contributing most significantly to exergy destruction, providing insights for future optimization. The physical model is computationally slow, thus unsuitable for integration into the TCHP system-level model, so Chapter 3 extends the experimental dataset with previously available data to identify data-driven models, including polynomial regression, Gaussian process regression, and artificial neural networks. The most suitable model, providing fast and reliable predictions, is to be integrated in the complete TCHP model to be developed in Part II.

2. **Part II** extends the analysis to a complete TCHP cycle integrating three TCs in series. This part investigates control-based performance optimization of a TCHP through dynamic modeling and advanced control strategies, also reinforced with experimental work, and corresponds to Chapters 4 to 6. Chapter 4 reviews CO_2 as a refrigerant and its application in transcritical cycles, highlighting the motivation for selecting this working fluid and the required cycle architectural adaptations to handle its specific thermodynamic characteristics. The TCHP test bench is installed at Boostheat for experimentation. Its process and cycle components are described, and two categories of experimental data are presented: (a) transient open-loop and (b) steady-state, to be used for model development and validation. Chapter 5 reviews dynamic modeling approaches applied to vapor compression cycles in general and transcritical CO_2 heat pumps in particular. A hybrid dynamic model of the entire TCHP cycle, denoted 'TCHP-HYB', is derived, discretized in space with the FV method, applying mass and energy balances to the heat exchangers, while TCs are represented with machine learning models developed in Part I and expansion valves are represented algebraically. This TCHP-HYB is validated in both steady-state and transient conditions using experimental data and is used later for control validation. Chapter 6 introduces the application of control systems to TCHPs, emphasizing their crucial role in achieving optimal performance and efficiency. A new control system based on MPC is developed. Because the TCHP-HYB is too complex and stiff for MPC optimization, reduced-order models based on RNNs are identified and trained with both experimental and simulated data. The proposed MPC is designed with an objective function targeting heating demand tracking while minimizing consumption. Based on the reduced models, the new control method is validated and its benefits are demonstrated.

This is summarized in a global visual view of the manuscript content in Figure 1. All the modeling tools are developed in a Python framework. The CoolProp Python library is used to compute the thermophysical properties of the working fluids.

List of publications

Journal (under review):

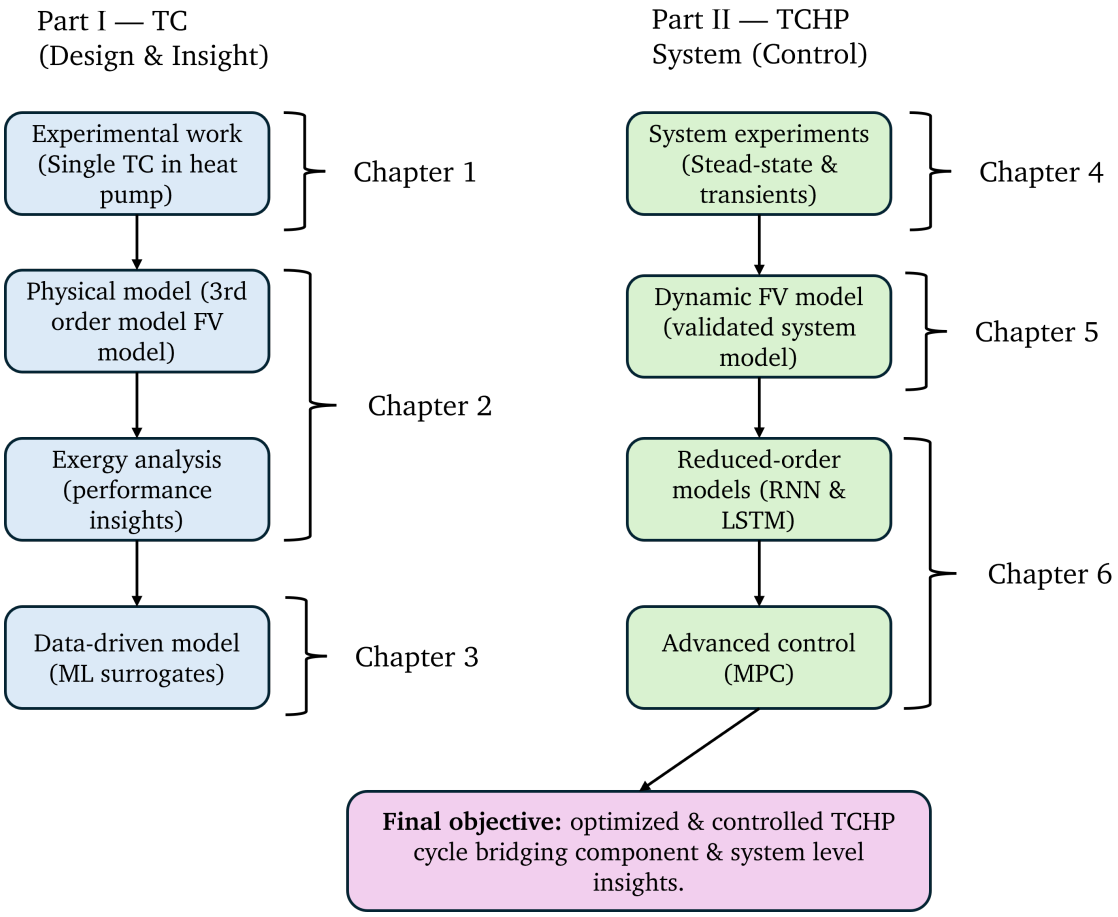

Figure 1: Objectives and steps of Part I and Part II along with their connection.

- Salame, A. A. H., Peralez, J., Nadri, M., Dufour, P., and Lemort, V. (2025). Model Predictive Control-Based Optimization of a Transcritical CO_2 Thermal Compressor Heat Pump Cycle Using an RNN-based Reduced Model.

Conference with review committee and proceedings:

- Salame, A. A. H., Lemort, V., Dufour, P., Nadri, M., and Ibsaine, R. (2024). Dynamic modeling approach of a thermal compressor and validation based on experimental tests. In *Proceedings of ECOS 2024*. National Technical University of Athens.

- Salame, A. A. H., Lemort, V., Dufour, P., Nadri, M., and Ibsaine, R. (2024). An empirical model for a CO_2 thermal compressor based on experimental data. *International Compressor Engineering Conference*. Paper 2868.

- Salame, A. A. H., Lemort, V., Dufour, P., Nadri, M., and Ibsaine, R. (2024). Improving performance of a CO_2 thermally driven heat pump based on a new optimal high-pressure correlation. In *Proceedings of Carnot 2024: Belgian Symposium of Thermodynamics*. University of Liège.

- Salame, A. A. H., Lemort, V., Dufour, P., and Nadri, M. (2024). A dynamic model for a multi-stage CO_2 thermal compressor heat pump application. In *Proceedings of ECOS 2025*. .

- Salame, A. A. H., Lemort, V., Dufour, P., and Nadri, M. (2025). Exergy and performance analysis of a CO_2 single-stage thermal compressor heat pump. In *13th International Conference on Compressors and Their Systems*, London, England.

Part I

Experimental and numerical analysis of a thermal compressor for heat pump cycles

Chapter 1

Introduction

Abstract

The thermal compressor (TC) targeted in this work belongs to the family of Stirling-type machines. Therefore, it is appropriate to start Part I with a state-of-the-art review of such machines. Section 1.1 introduces the Stirling engine as the most famous and widely studied type in the literature. Its components and thermodynamic cycle are described. Subsequently, Stirling thermal compressors (STC) are introduced as a less familiar class, but closer to the targeted TC in this work. Their operating principle is defined and distinguished from that of a Stirling engine. Section 1.2 defines the targeted TC components and the corresponding thermal compression process. Section 1.3.1 describes the test bench used for the experimental work, where the TC is integrated into a single-stage heat pump cycle. To conduct these experiments, Section 1.3.3 defines the test protocol and the ranges of input variables. The resulting data are used to calculate the performance indicators of the TC in Section 1.3.4. In Section 1.3.5, the collected data are filtered using a Gaussian-process model. From the performance indicators, a unified exergy-based performance metric for the TC is defined and plotted against the collected data in Section 1.3.6.

1.1 Introduction to Stirling machines

1.1.1 Stirling engine

A Stirling engine, invented by Robert Stirling in 1816, is an external-combustion engine that operates as a closed, regenerative, piston cycle. It produces mechanical work through cyclic compression and expansion of a working fluid, driven by a temperature difference between a heat source and a heat sink, with net work arising from the phase difference between the compression and expansion volumes. Stirling engines offer several advantages, including high theoretical efficiency, quiet operation, and fuel flexibility, making them suitable for applications such as cryogenic cooling, solar-thermal power, and submarine propulsion.

1.1.1.1 Main components

A Stirling machine is usually composed of five key components:

1. Compression volume (C).

2. Cooler heat exchanger (K): removes heat from the working fluid and transfers it to the heat sink.

3. Regenerator (R).

4. Heater heat exchanger (H): adds heat to the working fluid from the heat source.

5. Expansion volume (E).

The serial connection of these components is illustrated for a beta-type Stirling engine in Figure 1.1. In addition to these components, there are the displacer (D) and the power piston (PP), which are responsible for moving the working fluid and delivering the engine's usable output power, respectively.

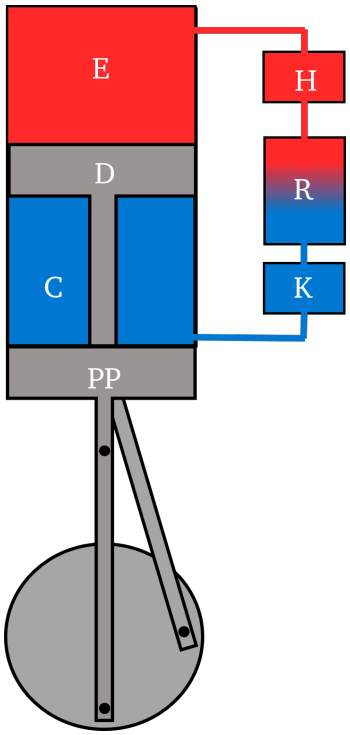

Figure 1.1: Stirling engine of beta-type scheme.

1.1.1.2 Thermodynamic cycle

To understand the operation of a Stirling engine, its theoretical cycle is described. The closed thermodynamic cycle is composed of four elementary processes, shown on the p–V and T–s diagrams in Figure 1.2:

Process 1 (1→2): The working fluid is compressed while mainly occupying the compression volume.

Process 2 (2→3): The working fluid is transferred from the compression volume to the expansion volume while absorbing heat from the regenerator. At nearly constant volume, the heating causes the pressure to rise.

Process 3 (3→4): The hot working fluid is expanded in the expansion volume. Since the pressure is now higher, more work can be extracted than is needed for compression.

Process 4 (4→1): The working fluid goes back from the expansion volume to the compression volume. Its temperature decreases when passing through the regenerator and arrives in the compression volume at a temperature close to that of the cooler. At nearly constant volume, the cooling causes the pressure to decrease. The working fluid returns to its initial state (1).

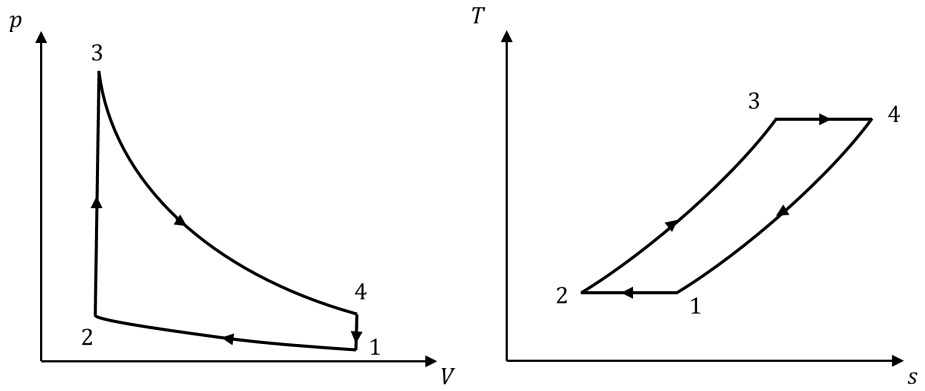

Figure 1.2: Stirling engine cycle: (a) p–V and (b) T–s diagrams.

1.1.1.3 The regenerator

In Stirling machines, the regenerator is essential for efficient thermal cycling. It consists of a porous matrix with a high surface area, typically made from thin wires. Its role is to store and recover heat between the compression and expansion strokes. When the hot working fluid flows through, the regenerator matrix absorbs heat; when flow reverses, it releases it back to the cold working fluid. This alternating process creates a steep axial temperature gradient. The regenerator increases the efficiency of the engine because it reduces the amount of heat needed to produce a given amount of work.

In the case of a perfect regenerator, the heat exchanged with the surroundings is limited to the heat absorbed from the heat source at the heater and the heat rejected at the cooler. Then the theoretical efficiency of a Stirling cycle becomes equivalent to that of the Carnot cycle:

$$\eta_{\text{Carnot}} = 1 - \frac{T_{\text{k}}}{T_{\text{h}}} \tag{1.1}$$

where T_{h} and T_{k} denote the temperatures of the heater (heat source) and cooler (heat sink), respectively. However, the actual Stirling cycle, as implemented in real engines, differs significantly from this theoretical model due to the following inefficiencies:

- Imperfections in the heat exchangers, which reduce the effectiveness of heat transfer.
- Non-ideal regenerator performance, leading to incomplete thermal energy recovery.
- The presence of dead volumes in the heat exchangers and connecting ducts, which are not swept by the pistons and cause spatial variations in thermodynamic properties.

In real Stirling machines, the five basic components can be implemented in different ways, some of which look very different from the schematic in Figure 1.1. There are also differ-

ent mechanisms for moving the displacer and the piston, but the basic working principles remain the same as outlined above.

1.1.2 Stirling thermal compressor

The concept of a Stirling thermal compressor (STC), or thermocompressor, was first disclosed by Bush (1939). Unlike a Stirling engine, a STC is an open system whose operating principle is to use thermal energy to raise pressure. As shown in Figure 1.3, this is achieved by a modified layout in which the power piston of a Stirling engine is typically replaced by an orifice or by separate suction/discharge valves Kornhauser (1996). Consequently, the kinematic linkage that couples the displacer to the power piston is eliminated, and a motor is used solely to drive the displacer. The motor only overcomes displacer mechanical losses, so its electrical power demand is small compared with the input thermal power. This configuration enables transport of the working fluid from the heat source to the heat sink. Like the Stirling engine, the STC is fuel-flexible, can in principle attain high efficiency, and operates quietly due to low mechanical frequency.

In a Stirling engine, the thermodynamic cycle is commonly described in four phases—compression, transfer to the expansion space, expansion, and return to the compression space—and relies on a phase angle between the volume variations of the compression and expansion spaces. By contrast, a STC (Figure 1.3) has a single principal varying volume that generates the pressure waves, so no such phase shift occurs. This volume can be regarded as the combination of the hot and cold cavities (HC and CC), with only a small additional variation introduced by the displacer rod. We use the terms “hot cavity” and “cold cavity” because no true compression/expansion work, as in a Stirling engine, takes place in a STC.

Two STC configurations are distinguished in the literature according to their purpose. Type 1 uses a single flow path and is often applied in pulse-tube refrigeration; it was first proposed and experimentally investigated by Dai et al. (2002) as a replacement for the mechanical compressor driving a pulse-tube refrigerator. Type 2 includes separate suction and discharge valves and is intended to replace mechanical compressors; it was initially proposed by Martini (1969) for powering artificial hearts and later considered for applications such as heat pumps (Ibsaine et al. (2016)).

1.2 Thermal compressor for heat pumps

The targeted thermal compressor is a Stirling thermal compressor (STC) with separate suction and discharge valves, similar to the device studied by Ibsaine et al. (2016) for heat-pump cycles. This chapter complements Ibsaine’s work.

1.2.1 Components

Most components were introduced in Section 1.1; they are restated here with the adaptations specific to the targeted machine. For the remainder of the thesis, the targeted thermal compressor is abbreviated as “TC.” The TC consists mainly of a cylinder with two variable-volume chambers and constant-volume heat exchangers that connect them. Figure 1.4 shows a vertical cross-section of the TC. As illustrated, the cylinder is divided into two spaces—the cold cavity (CC) and the hot cavity (HC)—separated by a displacer (D).

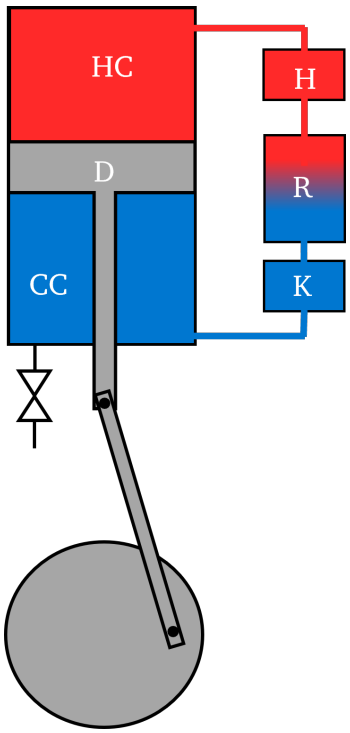

Figure 1.3: STC scheme.

The heat exchangers comprise a cooler (K) composed of 17 pipes, which rejects heat to the surrounding water jacket; a heater (H) of annular shape, which supplies heat; and a regenerator (R) of screen matrix made of a porous matrix. The regenerator absorbs heat when the working fluid flows from the hot to the cold side, and releases it when the flow reverses. The cooler dead volume (KR) of and heater dead volume (HR) are the spaces between the cooler and the regenerator, and between the heater and the regenerator, respectively. Suction (SV) and discharge (DV) valves are connected to the CC to admit and release flow to and from the heat-pump cycle.

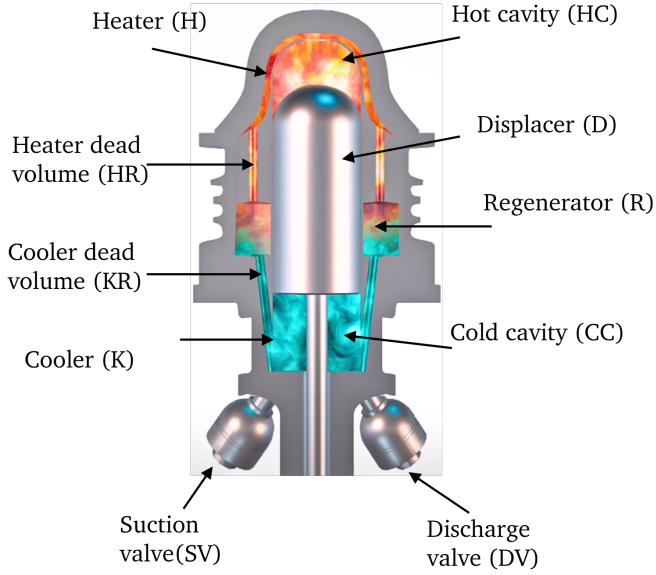

Figure 1.4: TC vertical cross-section showing its components.

1.2.2 Crank mechanism

The variations of the cold- and hot-cavity volumes in the cylinder are determined by the displacement of the displacer. The displacer is connected to a rod, which in turn is linked to a crank mechanism (Figure 1.5). This arrangement produces sinusoidal variations of the cavity volumes:

$$V_{\mathrm{cc}} = \pi\left(r_{\mathrm{d}}^2 - r_{\mathrm{sha}}^2\right)\left(L_{\mathrm{str}} - X_{\mathrm{d}}\right) + V_{\mathrm{cc,min}}, \tag{1.2}$$

$$V_{\mathrm{hc}} = \pi r_{\mathrm{d}}^2 X_{\mathrm{d}} + V_{\mathrm{hc,min}}. \tag{1.3}$$

Here, $V_{\mathrm{cc,min}}$ and $V_{\mathrm{hc,min}}$ denote the minimum cavity volumes; r_{d} is the displacer radius,

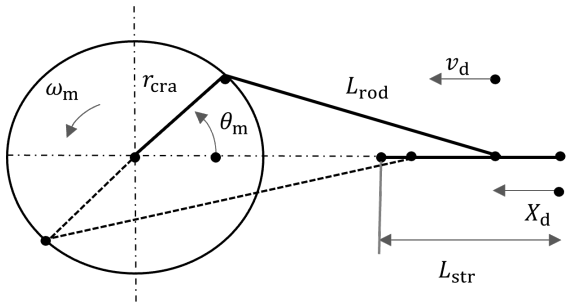

Figure 1.5: Crankshaft mechanism generating the volume variations. When $\theta_{\mathrm{m}} = 0°$, the displacer is at the top of the hot cavity; when $\theta_{\mathrm{m}} = 180°$, it is at the bottom of the cold cavity.

L_{str} the stroke length, and r_{sha} the rod radius. The displacer position X_{d} follows the slider–crank relation:

$$X_{\mathrm{d}} = r_{\mathrm{cra}}\left(1 - \cos\theta_{\mathrm{m}}\right) + L_{\mathrm{rod}}\left[1 - \sqrt{1 - \left(\frac{r_{\mathrm{cra}}}{L_{\mathrm{rod}}}\sin\theta_{\mathrm{m}}\right)^2}\right], \tag{1.4}$$

where θ_{m} is the crank angle, r_{cra} the crank radius, and L_{rod} the rod length. The resulting cavity-volume variations are shown in Figure 1.6a. The cold- and hot-cavity volumes are in phase, so the total working volume changes only slightly (mainly due to the shaft volume). Figure 1.6b presents the p–V diagrams of the cold and hot cavities, along with that of the total working volume. In a Stirling engine, the p–V loop of the working volume encloses a larger area because of the phase difference between the two cavities, and its orientation follows that of the hot cavity (expansion space), highlighting the recovery of useful work (Figure 1.2). In contrast, the TC exhibits a much smaller loop that typically follows the orientation of the cold cavity. This behavior results from the harmonic volume oscillations and from the fact that more work is required to move the fluid upward than is recovered when it flows back downward.

1.2.3 Thermal compression process

Unlike a traditional compressor, a TC generates a pressure wave by heating its working fluid rather than by mechanically compressing it. A convenient way to describe the thermal compression process is to plot the (assumed uniform) internal pressure inside the TC as a function of the displacer position X_{d}. The four processes are shown in Figure 1.7 and are explained below:

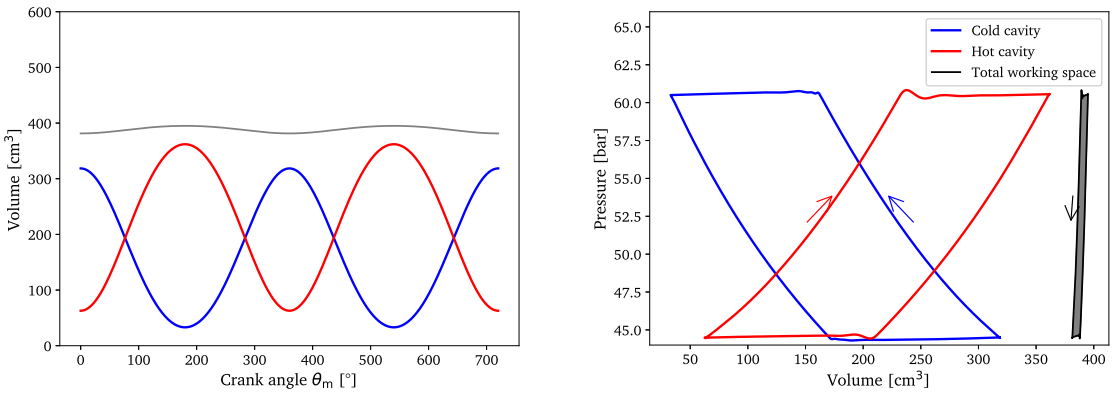

(a) Cavity-volume variations.

(b) p–V diagrams.

Figure 1.6: TC behavior: (a) variations of cold-cavity, hot-cavity, and total working volumes during two complete cycles, $\theta_{\mathrm{m}} \in [0°, 720°]$; (b) p–V diagrams of the cold cavity, hot cavity, and total working volumes.

Process 1 (1→2): Valves closed. As the displacer moves from the upper dead center toward the lower part of the cylinder, the working fluid flows toward the upper hot region. Due to the higher temperature, the pressure increases gradually from p_1 to p_2. The total working volume remains nearly constant, since the shaft volume is small compared with the overall TC volume.

Process 2 (2→3): When the pressure p_2 exceeds the discharge pressure, the discharge valve opens while the displacer continues moving downward.

Process 3 (3→4): Valves closed. As the displacer moves upward from the lower dead center, the working fluid flows toward the lower cold region, and the pressure decreases gradually from p_2 to p_1. The working volume changes only slightly.

Process 4 (4→1): When the pressure p_1 drops below the suction pressure, the suction valve opens while the displacer continues moving upward.

Having defined the TC components, operating principle, and processes, we now proceed to the experimental evaluation by integrating the TC into a single-stage heat pump cycle to analyze its performance.

1.3 TC experimental work

Previously, Ibsaine et al. (2016) investigated the TC as an isolated component under no-load conditions, with the valves kept closed. In that setup, valve dynamics were neglected and no mass flow was considered, meaning the TC was not evaluated in its intended role as the active compression device in a heat pump cycle. In contrast, this section presents an experimental campaign where the TC is integrated into a single-stage CO_2 heat pump cycle, with valve operation, mass flow, and realistic boundary conditions taken into account.

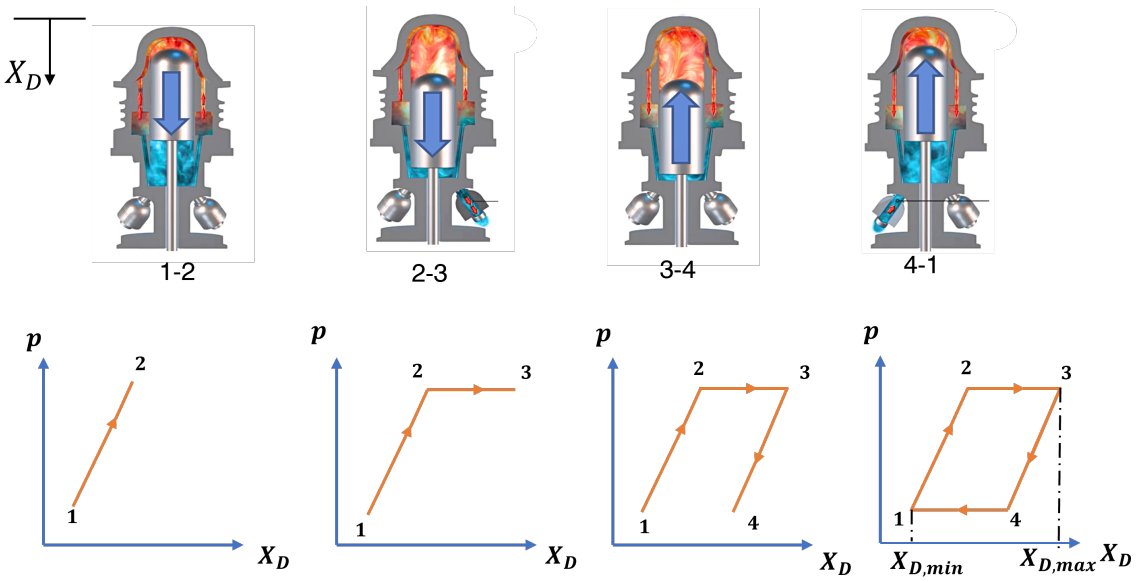

Figure 1.7: TC processes represented by the variation of internal pressure p as a function of displacer position X_{d}.

1.3.1 Test bench description

The experimental work is carried out on the test bench installed at the Boostheat laboratory. This setup includes a thermal compressor (TC), a condenser (CD), an electronic expansion valve (EEV), an evaporator (EV), and a fume heat exchanger (FHX), as shown in Figure 1.8a. From 1 to 2 CO_2 flow (in green) is compressed inside TC, where then it condenses inside CD from 2 to 3. Afterwards, the flow undergoes expansion from 3 to 4 inside the EEV, before finally evaporating inside EV, reaching state 1 again. This is demonstrated by the T–s diagram in Figure 1.8b. For water loop (in red): The water entering the cycle is referred to as return water, while the final outlet stream is called supply water. Water recovers heat in three steps: first in the TC cooler, then in the condenser, and finally in the FHX, where it absorbs heat from the combustion fumes (in gray). This last step ensures that the fumes are sufficiently cooled before being released through a plastic pipe. The top of the TC is surrounded by a well-insulated combustion chamber to minimize heat losses. Ambient air and methane fuel are mixed in a burner fan resulting in an air/methane mixture (in yellow) and directed into the combustion chamber located above the TC. The burner fan regulates the heater temperature under a closed-loop PID controller.

Figure 1.9 shows the upper part of the TC in the Boostheat test bench. This figure includes the burner fan, the methane–air mixture passage, the combustion chamber itself, the fume exit pipe, and the FHX where heat is transferred from the fume. The lower part of the TC is shown in Figure 1.10. Here, the motor casing encloses the electric motor that drives the crank mechanism, the suction and discharge valves where the entry and exit of CO_2. Surrounding the cooler is a water jacket with connected water pipes, where circulating water absorbs the rejected heat and transfers it to circulating water.

The commissioning of the installation involved identifying the sensors, establishing communication between the different control PLCs on the test bench, and developing the data acquisition system in LabVIEW, which mainly collected data from the test bench, ex-

cept for the TC that was controlled using Boostheat's locally designed software, primarily regulating the burner fan and motor rotational speed.

1.3.2 Measurements

The sensors installed on the test bench (Figure 1.8a), their types, and their corresponding ranges and accuracies are listed in Table 1.1. In the water cycle, Pt100 sensors are installed at the inlet and outlet of the TC cooler, the FHX, and the CD. They are chosen for their high accuracy, which is essential for evaluating the heat recovered from these heat exchangers. In the CO_2 cycle, Type T thermocouples are placed at the suction and discharge of the TC to measure the temperatures T_{suc} and T_{dis}, respectively, since they offer a wide operating range and robustness under the high pressures and temperatures of the refrigerant circuit. Type K thermocouple is used to measure the heater temperature, since it can withstand up to 1260 °C. A Huba Control Type 200 vortex sensor is installed on the water side to measure the volumetric flow rate, from which the mass flow rate $\dot{m}_{\mathrm{w}}$ is derived. A Huba Control Type 520 pressure sensor is used to measure the suction and discharge pressures at p_{suc} and p_{dis}, respectively; this type is known for its precision even at high operating pressures. Finally, a Coriolis F-029 sensor is installed between the EEV and the EV to measure the CO2 mass flow rate $\dot{m}_{\mathrm{f}}$ in the cycle.

Sensor	Range	Accuracy
Pt100	-30–300 °C	$\pm(0.15 + 0.002T)$ °C
Type T thermocouple	-200–350 °C	± 0.5 °C or 0.4%
Type K thermocouple	-200–1260 °C	± 1.5 °C or 0.4%
Huba Control Type 520 (pressure)	0–1000 bar	$\pm 0.3\%$
Huba Control Type 200 (vortex flow)	0.5–150 L/min	$\pm 1\%$
Coriolis F-029 (mass flow)	liquid/vapor refrigerant	$\pm 0.2\%$ (liquid), $\pm 0.5\%$ (vapor)

Table 1.1: Sensor specifications used in the TC experiment.

1.3.3 Experimental protocol and conditions

The experiments are conducted by varying main TC inputs: return water temperature $T_{\mathrm{w,ret}}$, heater temperature T_{h}, pressure ratio r_p, rotational speed ω_{m}, suction temperature T_{suc} at different charged pressure p_{charged} values. These vary according to the following protocol:

- $T_{\mathrm{w,ret}}$ is regulated with a chiller so it can be imposed on the cycle.
- T_{h} is regulated by the burner fan speed ω_{bf} (range 2000-9500 rpm), driven with a PID to a defined setpoint.
- r_p (ratio of discharge pressure p_{dis} and suction pressure p_{suc}) is adjusted by varying the percentage valve opening φ_{eev} (range 11-100 %) without targeting a certain value; a minimum opening of 11 % corresponds to the highest pressure ratio and a maximum 100 % opening corresponds to a minimum pressure ratio value.

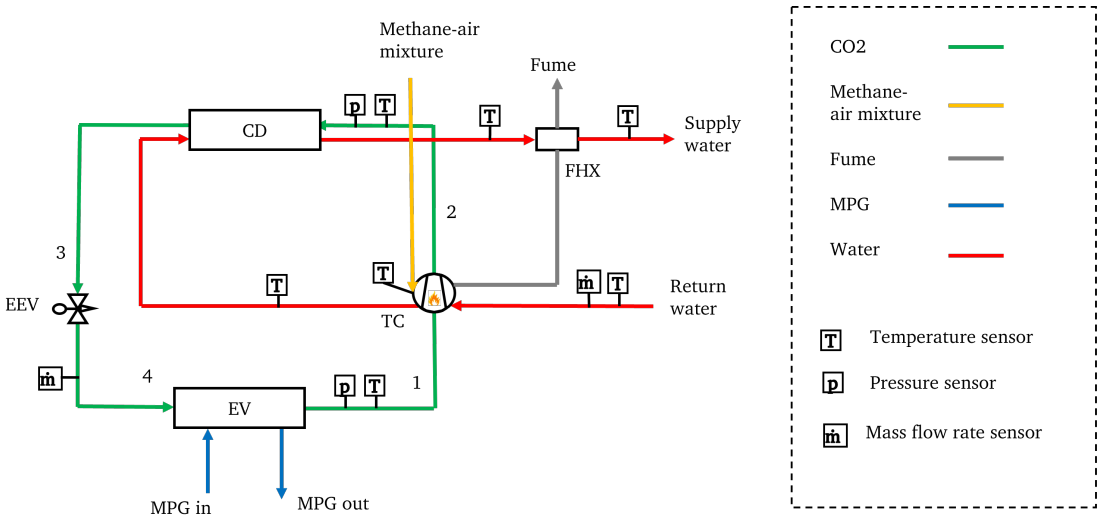

(a) Test bench layout at Boostheat.

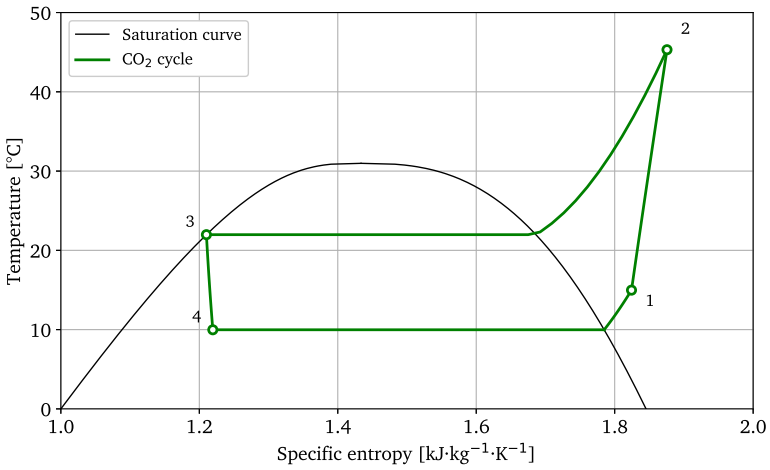

(b) T–s diagram of the same cycle.

Figure 1.8: TC in a Single-stage heat pump cycle: (a) experimental setup and (b) thermodynamic representation.

- p_{charged} is imposed by manually charging (filling) or discharging (emptying) CO_2 into and from the CO_2 cycle.
- ω_{m} (range 100-245 rpm) is imposed using local software.
- T_{suc} is kept as a floating variable.

For the first test, the bench was charged with CO_2 until a pressure of 30 bar was reached. Afterwards, the other parameters were varied. At each rotational speed, the valve opening was adjusted several times before changing the speed again, until the full range of operating conditions was covered. The bench was then charged with additional CO_2, stabilizing at 40, 50, and 56 bar. The same sequence of valve-opening and speed variations was repeated at each pressure level, resulting in a total of 118 samples. The ranges of operating conditions during the experimental campaign are summarized in Table 1.2. The heater temperature was set to either 700 or 800 °C, and its variation was not extensively investigated. This limitation was due to issues with the burner fan's internal regulation:

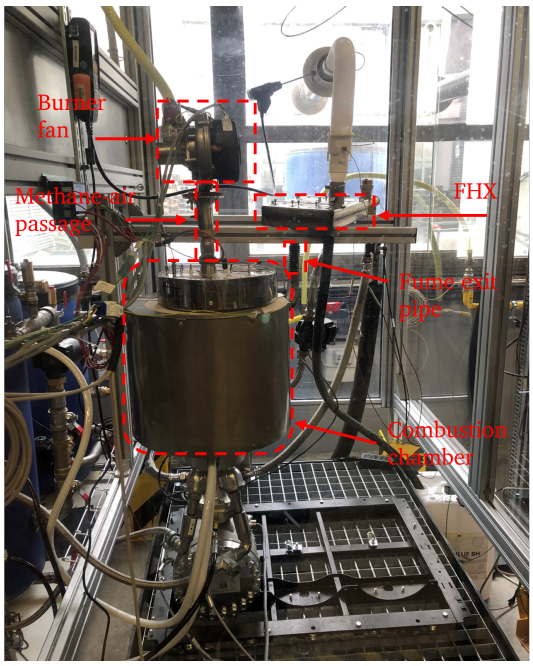

Figure 1.9: TC upper part in the Boostheat test bench, showing the burner fan, methane–air mixture passage, combustion chamber, fume exit pipe, and fume heat exchanger (FHX).

lowering the heater temperature led to flame extinction. In the next section, we define the performance indicators of the TC based on these measurements.

Symbol	Description	Range	Unit
p_{suc}	Suction pressure	22.6–48.7	bar
p_{dis}	Discharge pressure	34.2–64.2	bar
ω_{m}	Rotational speed	100–245	rpm
T_{h}	Heater temperature	700, 800	°C
$T_{\mathrm{w,ret}}$	Return water temperature	17.5–24	°C
T_{suc}	Suction temperature	3–21.6	°C

Table 1.2: TC input operating-variable ranges during the experimental campaign.

1.3.4 TC performance indicators

An important key to understanding a TC is to examine the energy conversion processes illustrated in Figure 1.11. The primary energy supplied to the TC is the heat received at its top part, i.e., the heater, through combustion of a methane–air mixture. This corresponds to the fuel thermal power $\dot{Q}_{\mathrm{fuel}}$. A portion of this heat is absorbed by the heater, denoted by $\dot{Q}_{\mathrm{h}}$, which is regarded as useful heat. Another portion is recovered by the FHX, $\dot{Q}_{\mathrm{fhx}}$, while the remaining part is considered as heat loss, $\dot{Q}_{\mathrm{loss}}$.

In addition, the TC receives a suction enthalpy flow from the heat pump cycle, defined by the suction enthalpy h_{suc} and the mass flow rate $\dot{m}_{\mathrm{f}}$. An electric motor with power input P_{elec} is connected to the displacer to provide the mechanical power $\dot{W}_{\mathrm{mech}}$ required for its movement, although this power is relatively small compared to the fuel thermal

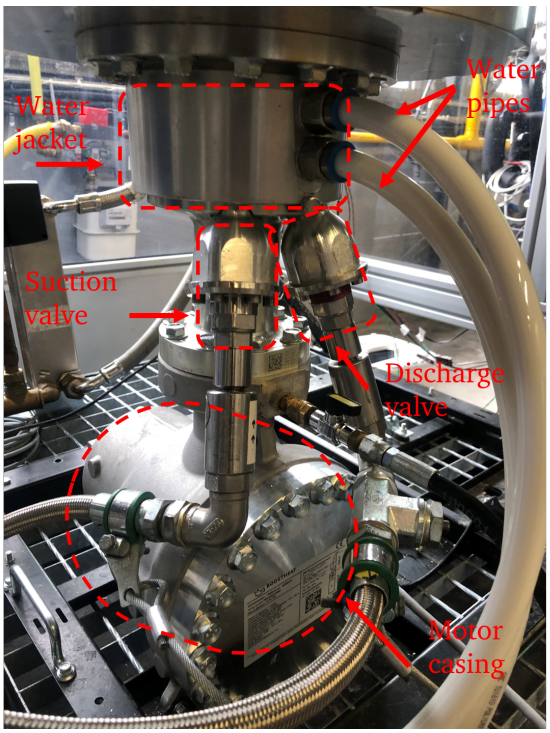

Figure 1.10: TC lower part in the Boostheat test bench, showing the motor casing containing the electric motor, the water jacket surrounding the cooler, the corresponding water pipes, and the suction and discharge valves.

power. Part of the resulting energy is recovered by the cooling water, $\dot{Q}_{\mathrm{k}}$, which circulates around the cooler in a water jacket, while the remainder is delivered to the heat pump cycle as the output enthalpy flow, h_{dis} and $\dot{m}_{\mathrm{f}}$.

The fuel thermal power, expressed in terms of methane combustion, is given by:

$$\dot{Q}_{\mathrm{fuel}} = \dot{m}_{\mathrm{CH_4}} \cdot \mathrm{LHV}_{\mathrm{CH_4}}, \tag{1.5}$$

where $\dot{m}_{\mathrm{CH_4}}$ is the mass flow rate of methane and $\mathrm{LHV}_{\mathrm{CH_4}} = 50$ MJ/kg is its lower heating value.

The heat recovered by the FHX and the TC cooler is calculated from the corresponding

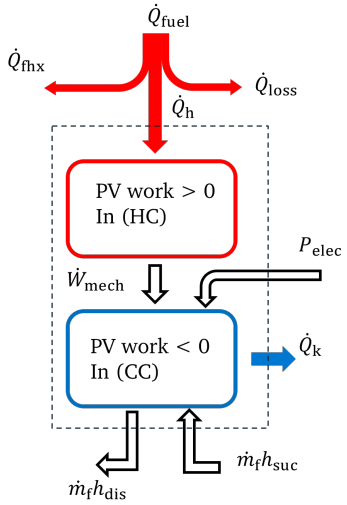

Figure 1.11: TC energy conversion processes.

water mass flow rate, specific heat, and inlet and outlet temperatures:

$$\dot{Q}_{\text{fhx}} = \dot{m}_{\text{w}} c_{p_{\text{w}}} (T_{\text{fhx,w,out}} - T_{\text{fhx,w,in}}), \tag{1.6}$$

$$\dot{Q}_{\text{k}} = \dot{m}_{\text{w}} c_{p_{\text{w}}} (T_{\text{k,w,out}} - T_{\text{k,w,in}}). \tag{1.7}$$

The output (compression) power of the TC is given by:

$$\dot{H}_{\text{comp}} = \dot{m}_{\text{f}} (h_{\text{dis}} - h_{\text{suc}}), \tag{1.8}$$

where h_{suc} and h_{dis} are determined from the corresponding temperature and pressure values at suction and discharge, respectively. The electric power consumed by the motor is measured with a wattmeter. The mechanical power transmitted to the displacer is then obtained as:

$$\dot{W}_{\text{mech}} = P_{\text{elec}} \cdot \eta_{\text{mech}}, \tag{1.9}$$

where $\eta_{\text{mech}} = 0.9$ is the mechanical efficiency of the motor coupled to the TC. Assuming that energy conservation is satisfied for the TC, the useful heater heat $\dot{Q}_{\text{h}}$ can be determined from:

$$\dot{Q}_{\text{h}} = \dot{Q}_{\text{k}} + \dot{H}_{\text{comp}} - \dot{W}_{\text{mech}}. \tag{1.10}$$

After the combustion process, the heat not recovered by the FHX is either absorbed by the TC as useful heat or lost to the ambient. Therefore, the heat loss $\dot{Q}_{\text{loss}}$ is determined from:

$$\dot{Q}_{\text{h}} + \dot{Q}_{\text{loss}} = \dot{Q}_{\text{fuel}} - \dot{Q}_{\text{fhx}}. \tag{1.11}$$

The performance indicators of the TC are summarized in Table 1.3. Samples with negative mechanical power indicate that the thermal input alone was sufficient to drive the entire compression process, so no electric input was required. Since heat losses are not estimated independently, it is not possible to fully validate the experimental data based on energy conservation. Nevertheless, the data can still be assessed using a Gaussian Process (GP) approach.

Symbol	Description	Range	Unit
$\dot{Q}_{\text{h}}$	Heater heat transfer rate	739–3753	W
$\dot{Q}_{\text{k}}$	Cooler heat transfer rate	441–2581	W
$\dot{W}_{\text{mech}}$	Mechanical power	–34.2–368.1	W
$\dot{m}_{\text{f}}$	CO_2 mass flow rate	4.1–44.3	g.s^{-1}
T_{dis}	Discharge temperature	37–67.2	°C

Table 1.3: TC performance-indicator ranges, either measured directly or calculated from measurements.

1.3.5 Outliers detection with gaussian process

Gaussian process (GP) regression builds a smooth multivariate mapping between the outputs and the main input variables, while also providing predictive confidence intervals for each estimate. These intervals quantify uncertainty and highlight abnormal data points. The method is particularly effective for outlier detection and for assessing the sensitivity

and relative importance of the input variables. It also performs well on sparse datasets with noisy measurements, as noted by Quoilin and Schrouff (2016).

In addition to random noise, some measurements may take values that do not reflect the true underlying physical behavior. This can result from sensor malfunction or from unmodeled phenomena that affect the outputs. Such data points are considered outliers and may need to be excluded. GP is well suited for this task: in regions with dense data, outliers lie clearly outside the confidence bounds and are easily identified, while in regions with sparse data the model expresses higher predictive uncertainty. This property is desirable, since it prevents overconfident predictions in poorly sampled areas.

The method is applied to the performance indicators derived from the collected data, and the results are shown in Figure 1.12. Blue points represent the measured data, the black curve corresponds to the GP predictions, the gray area shows the 95% confidence bounds, and red points are outliers lying outside these bounds. Based on this analysis, the heater and cooler heat transfer rates both identify the same two samples as outliers, while three additional samples are flagged from the mass flow rate, resulting in a total of five samples removed before continuing with the filtered dataset in the next section. Further details on the GP model are provided in Section 3.2.2.

1.3.6 TC performance metric

Performance characterization of Stirling-type machines depends strongly on the machine type and its intended application. For instance, a Stirling engine is typically evaluated based on indicated power and thermal efficiency (Cheng and Phung (2021)). In contrast, a Stirling thermal compressor used in pulse-tube cryocoolers is assessed in terms of its thermoacoustic power. Common performance metrics in such cases include the pressure ratio (Pan et al. (2017)) and the peak-to-peak pressure oscillation (Lin et al. (2013)).

The TC investigated in this work, however, is designed to replace a mechanical compressor in heat pump cycles. As such, different evaluation criteria are required. For a traditional mechanical compressor, isentropic and volumetric efficiencies are usually defined. Isentropic efficiency measures how closely the actual compression process approaches a reversible adiabatic (isentropic) transformation, while volumetric efficiency quantifies how effectively the compressor fills its displacement volume with fresh working fluid during the suction stroke, accounting for valve timing, pressure drops, and re-expansion losses.

In contrast, a TC increases the internal pressure by heating the working fluid, rather than by increasing its density through mechanical compression. Moreover, continuous internal circulation of the working fluid between the hot and cold regions is essential to its operation. In other words, the inherently non-isentropic and non-volumetric nature of the TC is a necessary feature of its functioning. As a result, isentropic and volumetric efficiencies are not applicable, and a new performance metric is needed.

Given the importance of energy conversion processes and temperature differences in the system, exergy efficiency presents itself as a suitable metric. It quantifies the useful work potential of the energy supplied, thereby aligning with the thermodynamic principles governing this device. To generalize the analysis, the combustion process supplying heat to the TC during the experiments is excluded from the exergy study. Instead, the heater temperature T_{h} is taken as the effective heat source temperature, regardless of whether

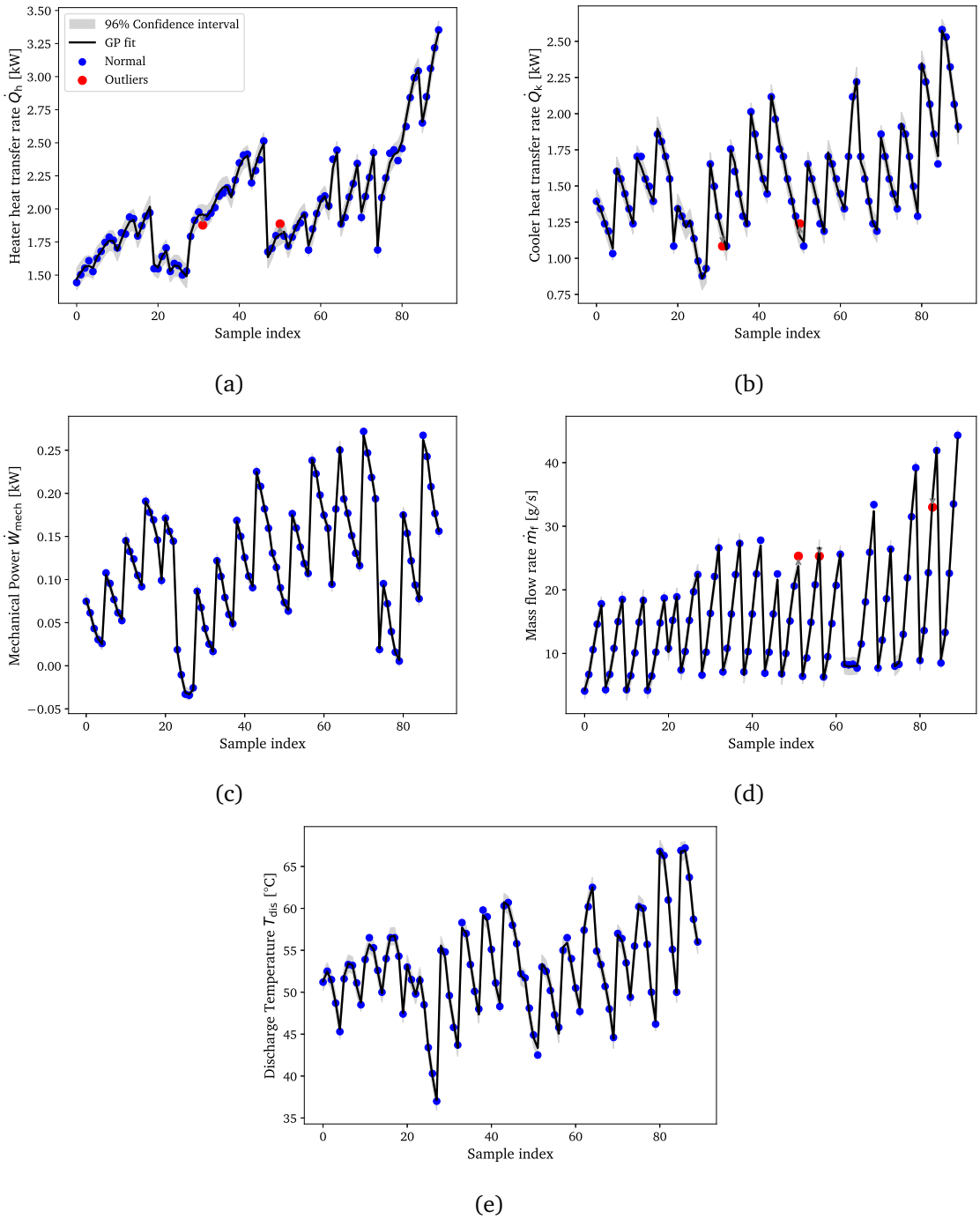

Figure 1.12: TC collected data outliers detection using GP: (a) Heater heat transfer rate $\dot{Q}_{\mathrm{h}}$, (b) Cooler heat transfer rate $\dot{Q}_{\mathrm{k}}$, (c) mechanical power $\dot{W}_{\mathrm{mech}}$, (d) mass flow rate $\dot{m}_{\mathrm{f}}$, and (e) discharge temperature T_{dis}.

the heat originates from combustion, waste heat, or biomass.

1.3.6.1 Exergy definitions

Whenever there is a temperature difference, useful energy can be recovered. The maximum useful energy, or availability, is the amount theoretically obtainable from such a temperature difference. This is represented by the Carnot efficiency, which expresses this

energy potential. Let the specific flow exergy be defined as:

$$\psi = h - T_{\mathrm{ref}} s, \tag{1.12}$$

where T_{ref} is the reference or ambient temperature.

The exergy transfer rate by heat into the TC through the heater is given by:

$$\dot{E}_{\mathrm{h}} = \left(1 - \frac{T_{\mathrm{ref}}}{T_{\mathrm{h}}}\right) \dot{Q}_{\mathrm{h}}. \tag{1.13}$$

Here, the heat source is not explicitly modeled; instead, T_{h} represents the effective temperature of the heater wall in thermal contact with the working fluid.

The exergy transfer rate to the water on the cooler side is:

$$\dot{E}_{\mathrm{k}} = \dot{m}_{\mathrm{w}}(\psi_{\mathrm{k,w,out}} - \psi_{\mathrm{k,w,in}}), \tag{1.14}$$

and the exergy transfer rate to the CO_2 flow undergoing compression is:

$$\dot{E}_{\mathrm{comp}} = \dot{m}_{\mathrm{f}}(\psi_{\mathrm{dis}} - \psi_{\mathrm{suc}}). \tag{1.15}$$

Enthalpy and entropy are calculated from the temperature and pressure at suction and discharge. The exergy transfer rate by work is equivalent to the mechanical power $\dot{W}_{\mathrm{mech}}$.

Assuming steady-state conditions, the exergy balance gives the total exergy destroyed in the TC:

$$\dot{E}_{\mathrm{dest,tc}} = \dot{E}_{\mathrm{h}} + \dot{W}_{\mathrm{mech}} - \dot{E}_{\mathrm{comp}} - \dot{E}_{\mathrm{k}}. \tag{1.16}$$

The exergy efficiency of the TC is then defined as:

$$\eta_{\mathrm{ex,tc}} = \frac{\dot{E}_{\mathrm{comp}} + \dot{E}_{\mathrm{k}}}{\dot{E}_{\mathrm{h}} + \dot{W}_{\mathrm{mech}}} = 1 - \frac{\dot{E}_{\mathrm{dest,tc}}}{\dot{E}_{\mathrm{h}} + \dot{W}_{\mathrm{mech}}}. \tag{1.17}$$

In the next section, the exergy efficiency is plotted against the filtered experimental data.

1.3.6.2 Performance evaluation

Following the experimental protocol, the exergy efficiency was plotted at different charged pressure values while varying rotational speed and pressure ratio at heater temperatures of 700 and 800 °C. Figure 1.13 indicates only a small influence of rotational speed on exergy efficiency, whereas a strong influence is observed from the pressure ratio. The scatter points are mainly concentrated between 1.25 and 1.65. The exergy efficiency decreases as the pressure ratio increases, with a more pronounced drop for $r_p > 1.4$. Efficiency also tends to increase at higher charged pressure values, ranging from 28 to 55 bar. Changing T_{h} from 700 to 800 °C does not appear to significantly affect the exergy efficiency.

Although informative, the data ranges are limited, especially with respect to heater temperature and charged pressure values. To address this gap, we propose the development of a high-fidelity physical model for the following reasons: (i) to gain a deeper understanding of TC thermodynamics, particularly of the internal processes that were not measured; and (ii) to provide a reference model capable of generating data beyond the experimental campaign, such as for different heater temperature values or higher charged pressure levels.

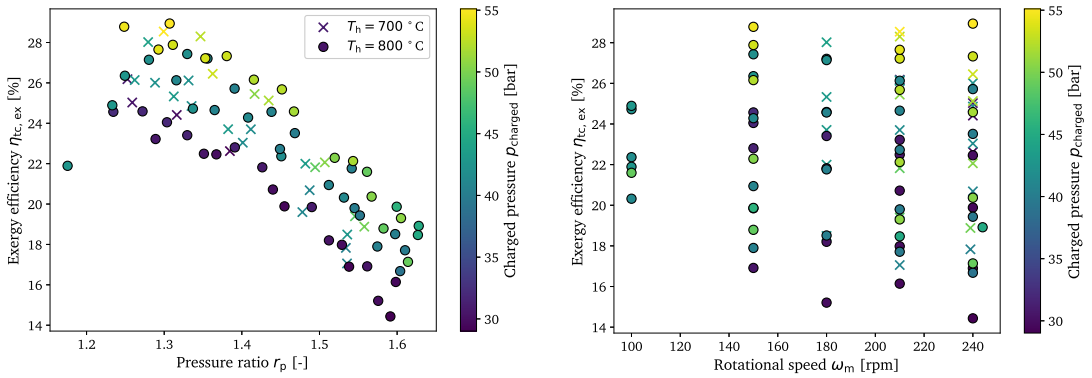

(a) Relative to pressure ratio.

(b) Relative to rotational speed.

Figure 1.13: TC exergy efficiency at different operating conditions covered by the experimental campaign.

1.4 Conclusion

In this chapter:

- Stirling machines were introduced as the broader family to which the targeted thermal compressor belongs. Particular attention was given to the Stirling engine, as the most well-known type, by describing its components and thermodynamic cycle phases. Building on this, the STC was presented as a distinct application that shares a similar design with the Stirling engine. While the Stirling engine converts thermal energy into mechanical work through phase-shifted volumes, the STC uses thermal energy to raise pressure, operating with a single varying volume and equipped with an orifice or valves instead of a power piston.

- The targeted TC investigated in this thesis is a specific type of STC with separate suction and discharge valves, designed by Boostheat as a substitute for a conventional compressor in a heat pump. Its components and thermal compression processes were described in detail.

- The TC was experimentally integrated for the first time into a single-stage heat pump cycle. Key inputs such as pressure ratio, charged pressure, rotational speed, and heater temperature were varied, while outputs including mass flow rate and discharge temperature were measured. From these, additional figures of merit such as cooler and heater heat transfer rates and mechanical power were derived to establish performance indicators. Direct validation was limited by unquantified heat losses, but a Gaussian Process method was successfully applied to filter outliers and provide a consistent dataset for analysis.

- Since the TC departs from conventional compressors and cannot be meaningfully assessed with isentropic or volumetric efficiencies, a new exergy-based performance metric was defined. Using the filtered dataset, exergy efficiency was analyzed under different operating conditions. The results showed a strong influence of charged pressure and pressure ratio, with smaller effects from motor speed, and almost

negligible influence of heater temperature. The limited range of experimental conditions, however, restricts broad generalization, motivating the development of a high-fidelity physical model in the next chapter.

Overall, this chapter introduced the targeted TC and presented the experimental campaign that provided the first dataset of its performance within a heat pump cycle. The results also highlighted the complexity of the TC's thermodynamic behavior, which depends on tightly coupled heat and mass transfer processes that cannot be fully captured by the experiments alone. To advance both understanding and predictive capability, the next chapter develops a high-fidelity physical model of the TC. This model is essential not only to investigate the internal processes that remain inaccessible experimentally, but also to serve as a virtual platform for testing a wider range of operating conditions. In particular, it enables extrapolation beyond the experimental dataset and supports design optimization.

Chapter 2

Thermal compressor third order model

Abstract

This chapter primarily aims to develop a high-fidelity physical model simulation tool for the targeted TC described in the previous chapter. Section 2.1 provides a review of third-order modeling approaches for Stirling machines in general, dominantly used for STCs. Section 2.2 derives a third-order model for the targeted TC. The TC is spatially discretized using the finite volume (FV) method into several control volumes (CVs). For each CV, mass, momentum, and energy balance equations are applied. The mass flow rates through the suction and discharge valves are modeled using quasi-static relations, and empirical correlations for heat transfer and friction coefficients are defined. By connecting all equations, the final model is a set of ordinary differential equations (ODEs), with initial conditions defined in Section 2.3. The numerical solving strategy used to ensure model convergence is also discussed. Afterwards, in Section 2.4, the model is validated in two steps: (1) transiently, through comparison with computational fluid dynamics (CFD) analysis at a single periodic steady cycle, and (2) under steady conditions using previously collected performance indicator data from Section 1.3.4. Finally, the validated model enables a more detailed exergy analysis that captures internal losses and irreversibilities, allowing identification of the components most in need of optimization (Section 2.5).

2.1 Introduction

2.1.1 Modeling approaches for Stirling machines

In order to successfully model a Stirling machine, it is necessary to describe with equations what happens to the working fluid in the different components of the machine during operation. If one chooses a level of detail where the actual working fluid flows are modeled, then one must be able to account for oscillating, compressible flow in heat exchangers, in a porous matrix, and in cylinder volumes. It is also necessary to model the solids or walls of the machine with sufficient detail to determine the surface temperatures, as these play a key role in the heat transfer processes.

Various models have been proposed to describe the thermodynamic behavior of a Stir-

ling engine in the literature. These models are classified into four main levels corresponding to their complexity. Attempts to categorize these modeling techniques were made by Finkelstein (1960), Martini (1983), and Chen and Griffin (1983), until finally settling on the arrangement by Dyson et al. (2004).

Zero-order models, or empirical models, correlate the output power and efficiency to heater and cooler temperatures, piston displacement, engine speed, and mean pressure based on experimental data. One notable example is Beale's correlation, which estimates the engine's power output (West (1981)).

First-order models, or analytical models, are based on the theoretical development of Schmidt (1871). Known as the Schmidt model, it provides a classical analysis of the Stirling engine cycle for three common configurations: alpha, beta, and gamma. This model assumes isothermal compression and expansion, along with perfect regeneration, and describes a sinusoidal volume variation of the working space in reciprocating engines.

Second-order models, or numerical models, discretize the Stirling engine into elements and solve the governing differential equations iteratively for each segment. Most existing models are based on second-order approaches first proposed by Finkelstein (1960). This approach assumes the compression and expansion spaces to be adiabatic instead of isothermal. Urieli and Berchowitz (1984) also derived an adiabatic model based on the second-order approach and further improved its accuracy by including the effects of pressure drop, non-ideal heat transfer, and regeneration in their equations, resulting in what were called the simple model and the quasi-steady model. In a second-order model, the engine is divided into five parts (cooler, heater, regenerator, expansion, and compression spaces). Each part is considered as a CV, and the conservation laws of mass and energy are applied individually.

Third-order models are more complex yet more accurate type of numerical models, where a mono-dimensional flow is assumed, and the system is divided into a network of nodes, each represented by ordinary differential equations (ODEs) derived from the mass, momentum, and energy conservation laws. The resulting ODEs are then solved numerically, providing the instantaneous physical states of the working fluid. Due to the reliability of this method, several simulation tools were created to model a Stirling engine based on this method. For instance, 'Sage' is a famous simulation tool deploying a third-order approach within an object-oriented framework. It is still available as mainstream commercial software (Gedeon (2014)), with a user interface to simulate or optimize Stirling engines.

At an even higher level of fidelity, computational fluid dynamics (CFD) models offer a fourth-order representation, considering two- or three-dimensional flow, making them the closest to real-world behavior among all the modeling approaches (Chen et al. (2015)). However, these models are also the most computationally expensive and time-consuming to run. Typically, CFD models are reserved for situations where accuracy is of utmost importance, though their complexity makes them impractical for control or optimization tasks.

The importance of including fluid inertia in STCs was emphasized by Andersen (2006), who showed that neglecting it leads to errors in predicting phase relationships between pressure and mass flow oscillations. Since the targeted TC is one type of STC, a third-order model is chosen, as it includes fluid inertia while at the same time requiring less computation compared to multi-dimensional CFD, making it more reliable for design and

optimization tasks.

2.1.2 Third-order modeling approach

In his thesis, Andersen (2006) presented a detailed third-order model of a Stirling engine and proposed numerical techniques to accelerate convergence, reducing computational time significantly. More recently, Wang et al. (2016) and Qiu et al. (2021) applied the third-order framework with additional loss mechanisms, showing good agreement with the well-known GPU-3 prototype. As noted by Ahmadi et al. (2017), GPU-3 remains the benchmark experimental data set for Stirling engine validation, having been originally built in 1965 by General Motors and later adopted by NASA. It is a beta-type machine with a rhombic drive and typical working fluids such as hydrogen, helium, or nitrogen. These studies confirm the accuracy and reliability of the third-order framework.

For Type 1 STCs, Dai et al. (2002) first proposed and experimentally tested a prototype intended to drive a pulse tube refrigerator. Subsequent studies improved design and modeling, such as an annular regenerator with a novel piston design Lin et al. (2013), validated third-order models with parametric studies on orifice valve impedance Pan et al. (2017), and investigations of operating conditions and working fluids Wang et al. (2018). Based on similar models, exergy and energy analyses have also been carried out Wang et al. (2019), showing that optimizing external losses could raise exergy efficiency to 60%.

For Type 2 STCs, intended to replace mechanical compressors, an idealized approach was introduced by Kornhauser (1996) and later extended by Edwards and Peterson (2007) to include non-idealities. Simulation results suggested that reducing dead volumes, especially in the cold space, could improve efficiency. Experimental works include the introduction of new displacer controls Thomas and Barth (2022), achieving higher output, and investigations of prototypes for heat pump applications Ibsaine et al. (2016). However, the latter neglected fluid inertia and validated the model only under off-load conditions. In contrast, the present work re-investigates this prototype under full-load operation, integrating the TC into a CO_2 heat pump cycle at the Boostheat laboratory. Unlike earlier simplified approaches, the present model incorporates suction and discharge valve dynamics and non-ideal CO_2 properties, thereby extending realism and applicability. Most existing methods assume ideal gases, which is valid for helium or hydrogen, but becomes challenging when applied to CO_2 due to its strong deviation from ideality.

2.2 TC third-order model

A third-order modeling approach is used to describe the TC working fluid during oscillation, where a one-dimensional flow is assumed and the system is divided into a network of nodes, each represented by ODEs derived from the mass, momentum, and energy conservation laws. These ODEs are solved numerically to provide the instantaneous physical states of the working fluid. Thus, this section presents a novel third-order modeling approach for the TC. Some relevant assumptions are first considered:

- One-dimensional and compressible flow throughout the system.
- The physical field is uniform within each CV.

- Real-gas properties of CO_2 are used.
- Kinetic and potential energy contributions are neglected.
- No flow leakage is assumed between the cold and hot cavities.
- The heat capacities of the walls of the cooler, heater, and cold and hot cavities are much greater than that of the working fluid; therefore, the wall temperatures are taken as constants.

2.2.1 Governing equations

Figure 2.1(a) shows the schematic of the TC with its main components. In particular, the TC is spatially discretized using the finite-volume (FV) method into $N+1$ CVs along an i-axis, where each CV between adjacent solid lines represents uniform pressure p, temperature T, and density ρ. The velocity v and mass flow rate $\dot{m}$ are considered uniform between adjacent dashed lines, corresponding to a j-axis. This results in $N+1$ connected ODEs, where the 0th and the Nth represent the cold- and hot-cavity CVs, respectively. This is shown in Figure 2.1(b).

Positive flow is defined from the cold cavity to the hot cavity. The time derivative of a variable $x(t)$ is written $\left(\frac{\partial x}{\partial t}\right)$ when used in differential form for integration, and $\dot{x}$ when represented algebraically at an instant. Both have the same units but serve different purposes. From a thermodynamics standpoint, $\left(\frac{\partial x}{\partial t}\right)$ indicates the time derivative of a point function (a thermodynamic property), while $\dot{x}$ indicates the time derivative of a path function. Applying the mass balance on each CV, we obtain

$$\frac{\partial m_i}{\partial t} = \dot{m}_{j-1} - \dot{m}_j. \tag{2.1}$$

From the energy balance, the temperature variation is

$$\begin{aligned}\frac{\partial T_i}{\partial t} = \frac{1}{(mc_v)_i}\Big[\dot{Q}_i - T_i\left(\frac{\partial p}{\partial T}\right)_{\rho,i}\left(\dot{V}_i - \frac{1}{\rho_i}\frac{\partial m_i}{\partial t}\right) - h_i\frac{\partial m_i}{\partial t} + \dot{m}_{j-1}h_{j-1} - \dot{m}_j h_j \\ + \left(-KA_{\text{cs}}\frac{\partial T}{\partial x}\right)_{j-1} - \left(-KA_{\text{cs}}\frac{\partial T}{\partial x}\right)_j\Big],\end{aligned} \tag{2.2}$$

where $\left(\frac{\partial p}{\partial T}\right)_\rho$ is the partial derivative of p with respect to T at constant ρ, and $\left(-KA_{\text{cs}}\frac{\partial T}{\partial x}\right)_j$ is the heat conduction term at node j. The derivation of Equation 2.2 can be found in the thesis of Bell (2011). Here, K is the thermal conductivity and A_{cs} is the cross-sectional area. The momentum balance is applied at CV interfaces to derive the velocity variation:

$$\frac{\partial v_j}{\partial t} = \frac{1}{m_j}\left[A_{\text{cs},j}(p_{i-1} - p_i) + (\rho A_{\text{cs}} v|v|)_{i-1} - (\rho A_{\text{cs}} v|v|)_i - Fr_j A_{\text{cs},j} - (\rho A_{\text{cs}} v|v|)_j\right]. \tag{2.3}$$

The wall-temperature variation of the heat-exchanger surfaces directly in contact with CO_2 follows from the energy balance:

$$\frac{\partial T_{\text{wall},i}}{\partial t} = \frac{1}{(mc)_{\text{wall},i}}\left[-\dot{Q}_i + \left(-KA_{\text{cs}}\frac{\partial T}{\partial x}\right)_{\text{wall},j-1} - \left(-KA_{\text{cs}}\frac{\partial T}{\partial x}\right)_{\text{wall},j}\right]. \tag{2.4}$$

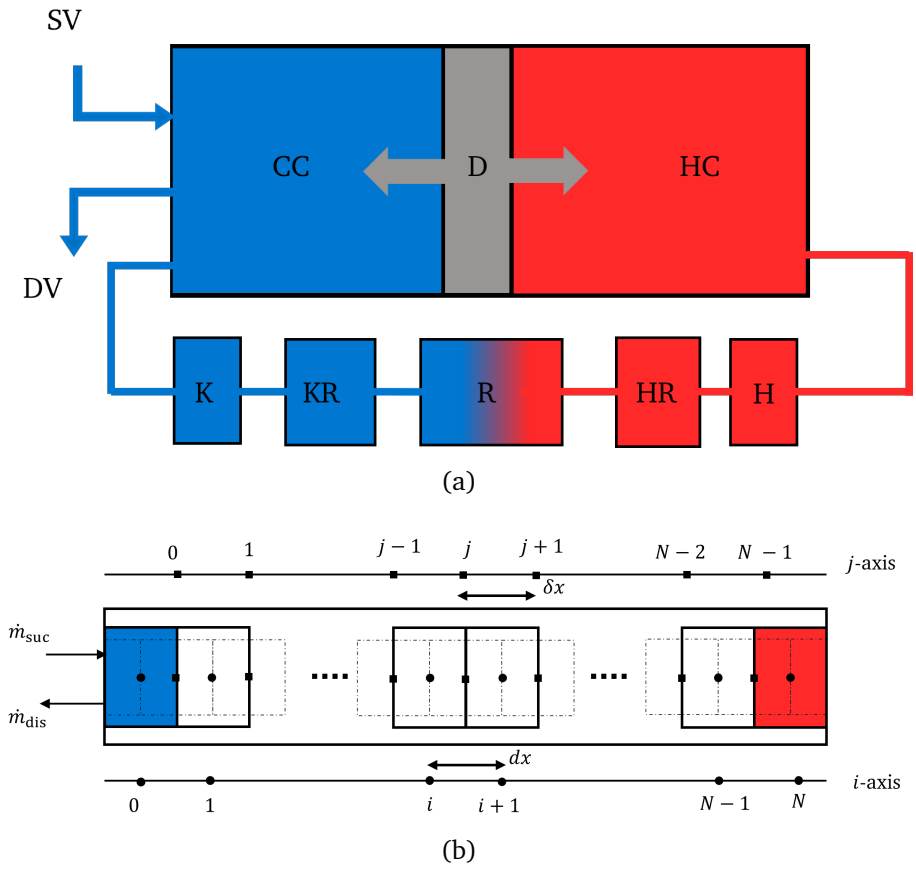

Figure 2.1: TC schematic representation of (a) main components and (b) spatially discretized grid. The i-axis contains thermodynamic properties of the CO_2 (p, h, ρ, etc.), while the j-axis denotes interfaces carrying velocity and mass flow rate information ($v_j, \dot{m}_j$). δx is the length of one solid CV, while dx is the distance between two dashed lines.

The flow direction between CVs is determined by

$$\dot{m}_j = (\rho v A_{\text{cs}})_j, \quad \text{and thus} \quad h_j = \begin{cases} h_i, & \text{if } v_j > 0, \\ h_{i+1}, & \text{otherwise.} \end{cases} \tag{2.5}$$

Additionally, the convective heat-transfer rate between the CO_2 and the surrounding wall is

$$\dot{Q}_i = (AU)_i \big(T_{\text{wall},i} - T_i\big). \tag{2.6}$$

where A denotes the wetted area and U is the heat transfer coefficient to be described in Section 2.2.3. For CO_2 flow inside the cold and hot cavities, several loss mechanisms are included in the energy balance. These comprise working-fluid shuttle heat transfer, displacer finite-speed effects, and displacer friction. Since the gap between the cold cavity and the buffer space (motor casing) is very small, leakage losses are neglected in the cold cavity. Similarly, leakage in the hot cavity is also neglected due to the small gap across the

displacer. The mass and energy equations in the cold cavity ($i = 0, j = 0$) are then

$$\frac{\partial m_i}{\partial t} = \dot{m}_{\text{suc}} - \dot{m}_{\text{dis}} + \dot{m}_j, \tag{2.7}$$

$$\frac{\partial T_i}{\partial t} = \frac{1}{(mc_v)_i}\Big[\dot{Q}_i + \dot{Q}_{\text{sh}} - T_i\left(\frac{\partial p}{\partial T}\right)_{\rho,i}\left(\dot{V}_i - \frac{1}{\rho_i}\frac{\partial m_i}{\partial t}\right) - h_i\frac{\partial m_i}{\partial t} + \dot{m}_{\text{suc}}h_{\text{suc},i} - \dot{m}_{\text{dis}}h_i - \dot{m}_j h_j - \left(-KA_{\text{cs}}\frac{\partial T}{\partial x}\right)_j - \left(\delta p_{i,\text{finite}} + \delta p_{i,\text{fric}}\right)\dot{V}_i\Big], \tag{2.8}$$

where $h_{\text{suc},0}$ is the entering enthalpy through the suction valve assuming isentropic flow. The mass and energy equations in the hot cavity ($i = N, j = N-1$) are

$$\frac{\partial m_i}{\partial t} = \dot{m}_j, \tag{2.9}$$

$$\frac{\partial T_i}{\partial t} = \frac{1}{(mc_v)_i}\Big[\dot{Q}_i - \dot{Q}_{\text{sh}} - T_i\left(\frac{\partial p}{\partial T}\right)_{\rho,i}\left(\dot{V}_i - \frac{1}{\rho_i}\frac{\partial m_i}{\partial t}\right) - h_i\frac{\partial m_i}{\partial t} + \dot{m}_j h_j + \left(-KA_{\text{cs}}\frac{\partial T}{\partial x}\right)_{j-1} - \left(\delta p_{i,\text{finite}} + \delta p_{i,\text{fric}}\right)\dot{V}_i\Big]. \tag{2.10}$$

The literature reports various heat and pressure losses represented with mathematical expressions. For instance:

– Shuttle heat-transfer loss $\dot{Q}_{\text{sh}}$, arising from heat conduction along the displacer wall and enhanced by its oscillatory motion, results in net heat transfer from the hot to the cold cavity Urieli and Berchowitz (1984):

$$\dot{Q}_{\text{sh}} = \frac{\pi K_{\text{d}} X_{\text{d}}^2 r_{\text{d}}(T_N - T_0)}{e_{\text{d}} L_{\text{d}}}, \tag{2.11}$$

where X_{d}, D_{d}, L_{d}, and e_{d} are the displacer position, diameter, length, and the gap width between the displacer and the cylinder, respectively.

– Finite-speed pressure loss δp_{finite}: according to the finite-speed thermodynamic principle, the pressure over the displacer surface differs from the calculated instantaneous pressure in the cold cavity. During compression, the displacer-surface pressure is larger than the instantaneous space pressure; during expansion it is smaller Wang et al. (2016):

$$\delta p_{\text{finite}} = \pm\, p\,|v_d|\sqrt{\frac{\gamma_{\text{CO}_2}}{R_{\text{CO}_2}\,T}} \tag{2.12}$$

Here, $|v_{\text{d}}|$ is the absolute value of the displacer velocity, and γ_{CO_2} and R_{CO_2} are the isentropic exponent and the ideal-gas constant of CO_2, respectively. The positive sign $(+)$ corresponds to the cold cavity, while the negative sign $(-)$ corresponds to the hot cavity.

– Friction pressure loss δp_{fric}: mechanical friction between the displacer and cylinder is another source of pressure loss. Based on experimental data from internal-combustion engines Wang et al. (2016):

$$\delta p_{\text{fric}} = \pm\big(0.97 + 0.045|v_{\text{d}}|\big) \times 10^5. \tag{2.13}$$

2.2.2 Suction and discharge valves

The suction and discharge valves are key components of the investigated TC, distinguishing it from the single-orifice STCs used for pulse-tube coolers. The valves are poppet type, operating in fully open or fully closed states, and the pressure difference required for opening is assumed constant at 0.5 bar. The flow through the valves is assumed isentropic, so the suction and discharge mass flow rates are determined from the Saint-Venant equations for nozzle flow as follows:

$$\dot{m}_{\mathrm{suc}} = C_d A_{\mathrm{cs,sv}} \rho_{\mathrm{suc,\,0}} \sqrt{2\big(h_{\mathrm{suc}} - h_{\mathrm{suc,\,0}}\big)}, \quad \text{if } p_0 < p_{\mathrm{suc}} - 0.5, \tag{2.14}$$

$$\dot{m}_{\mathrm{dis}} = C_d A_{\mathrm{cs,dv}} \rho_{0,\mathrm{dis}} \sqrt{2\big(h_0 - h_{0,\mathrm{dis}}\big)}, \quad \text{if } p_0 > p_{\mathrm{dis}} + 0.5. \tag{2.15}$$

Here, C_d is the discharge coefficient and $A_{\mathrm{cs,sv}}$ and $A_{\mathrm{cs,dv}}$ are the cross-sectional areas of the suction and discharge valves, respectively. The parameters with subscripts "suc, 0" and "0, dis" correspond to properties under the isentropic-flow assumption, i.e., $h_{\mathrm{suc,\,0}} = \mathrm{CP}(s_{\mathrm{suc}}, p_0)$ and $h_{0,\mathrm{dis}} = \mathrm{CP}(s_0, p_{\mathrm{dis}})$, obtained with CoolProp (CP).

2.2.3 Empirical correlations

The friction force Fr in the momentum Equation (2.3) and the heat-transfer coefficient U in the energy Equation (2.2) are expressed using the friction coefficient fr, the minor-loss coefficient L, and the Nusselt number Nu, respectively:

$$Fr = dx \left(\frac{fr}{D_{\mathrm{h}}} + \frac{L}{dx} \right) \frac{\rho v |v|}{2}, \tag{2.16}$$

$$U = \frac{K\,Nu}{D_{\mathrm{h}}}, \tag{2.17}$$

where $L = L_K + \left(1 - A_{\mathrm{cs,1}}/A_{\mathrm{cs,2}}\right)^2$ represents the minor-loss coefficient as a function of bends L_K and cross-sectional area variation (with $A_{\mathrm{cs,1}} < A_{\mathrm{cs,2}}$). D_{h} is the hydraulic diameter. The friction coefficient and Nusselt number are estimated from empirical correlations depending on the flow regime (laminar or turbulent) and the medium type.

2.2.3.1 Heat exchangers and cylinder

In the heat exchangers and inside the cylinder, the friction coefficient of Gedeon (2014) is adopted depending on the flow regime, i.e., laminar ($Re < 2 \times 10^3$) or turbulent ($Re \geq 2 \times 10^3$):

$$f_r = \begin{cases} \dfrac{64}{Re}, & \text{if } Re < 2 \times 10^3, \\ 0.11 \left(\dfrac{\epsilon}{D_{\mathrm{h}}} + \dfrac{68}{Re} \right)^{0.25}, & \text{if } Re \geq 2 \times 10^3, \end{cases} \tag{2.18}$$

where ϵ is the surface roughness. The Reynolds number Re is defined as

$$Re = \frac{\rho v D_{\mathrm{h}}}{\mu}, \tag{2.19}$$

with μ the dynamic viscosity. The Nusselt number correlation according to Boroujerdi et al. (2011) is

$$Nu = \begin{cases} 1.86 \left(\dfrac{Re\,Pr\,D_{\mathrm{h}}}{\delta x} \right)^{0.333} \left(\dfrac{\mu}{\mu_{\mathrm{wall}}} \right)^{0.14}, & \text{if } Re < 2 \times 10^3, \\ 0.023\, Re^{0.8}\, Pr^m, & \text{if } Re \geq 2 \times 10^3, \end{cases} \tag{2.20}$$

where $m = 0.4$ for heated parts (heater and hot-cavity space) and $m = 0.3$ for cooled parts (cooler and cold-cavity space). The Prandtl number is defined as

$$Pr = c_p \frac{\mu}{K}. \tag{2.21}$$

2.2.3.2 Regenerator

For the porous-medium regenerator, the friction coefficient and Nusselt number correlations of Gedeon (2014) are used:

$$f_r = \frac{129}{Re} + 2.91\, Re^{-0.103}, \tag{2.22}$$

$$Nu = \left[1 + 0.99\,(Re\,Pr)^{0.66}\right] \phi^{1.79}, \tag{2.23}$$

with ϕ the porosity of the regenerator. The hydraulic diameter is defined according to Urieli and Berchowitz (1984):

$$D_{\mathrm{h}} = D_{\mathrm{wire}} \frac{\phi}{1-\phi}, \tag{2.24}$$

where D_{wire} is the wire diameter of the mesh screen. The hydraulic diameters of the cooler and heater are the tube diameter and the internal annular diameter, respectively. The geometrical parameters of these components are summarized in Table 2.1. All components are stainless steel except for the cooler, which is aluminum.

Component	**Parameter**	**Value**
Cold cavity	Clearance volume	348.24 cm^3
	Minimum volume	33 cm^3
Hot cavity	Clearance volume	362 cm^3
	Minimum volume	62.8 cm^3
Cooler	Type	Tubes
	Volume	32 cm^3
Cooler dead volume	Type	Tubes
	Volume	21 cm^3
Regenerator	Type	Woven wire mesh
	Porosity	0.5
	Wire diameter	0.06 mm
	Volume	76 cm^3
Heater dead volume	Type	Annular
	Volume	58 cm^3
Heater	Type	Annular
	Volume	10 cm^3
Suction/Discharge valve	Type	Poppet
	Volume	9.8 cm^3

Table 2.1: TC component geometrical parameters.

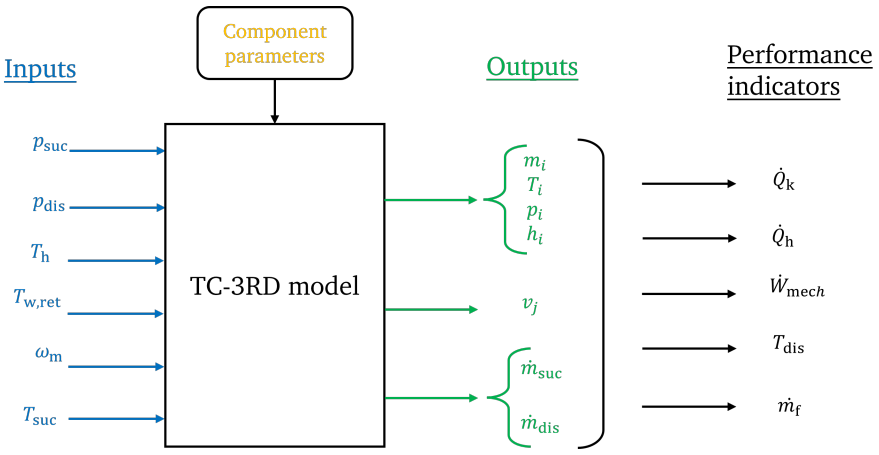

Figure 2.2: TC-3RD model scheme containing inputs (operating conditions and component parameters), outputs at each CV and interface, suction and discharge mass flow rates, and performance indicators.

2.3 Numerical model resolution

The coupling of Equations (2.1)–(2.4) results in a system of connected ODEs, forming the 'TC-3RD model'. Figure 2.2 illustrates the scheme of this model, which includes the operating-condition inputs (suction pressure p_{suc}, discharge pressure p_{dis}, heater temperature T_h, entering water or cooler temperature $T_{w,ret}$, rotational speed ω_m, and suction temperature T_{suc}), as well as component parameters such as geometries from Table 2.1, volume variations from Equations (1.2)–(1.3), and empirical correlations of friction and heat-transfer coefficients (Section 2.2.3). At each CV i, the model predicts the instantaneous thermophysical properties (temperature, pressure, etc.) of CO_2, velocities at interface j, and suction and discharge mass flow rates. From these outputs, the performance indicators are calculated (detailed in Section 2.3.3). To simulate the TC-3RD model, appropriate initial conditions must first be specified, followed by a numerical solving strategy. These two steps are described in the next subsections.

2.3.1 Initial conditions

The state vector of TC-3RD model is initialized as follows: The displacer is considered at the top of the hot cavity ($\theta_m = 0$), so the pressure profile is uniform and equal to the suction pressure. The initial temperature profile of CO_2 and the wall is linearly distributed from a minimum at the cold cavity and cooler CVs, equal to the cooling water temperature $T_{w,ret}$, to a maximum at the heater and hot cavity CVs, equivalent to the measured temperature on the tip of the heater wall T_h. The velocity vector is set to 0.

2.3.2 Solving process

The numerical simulation of the TC-3RD model is illustrated with a flow chart in Figure 2.3. After initialization, the solver proceeds iteratively. At each iteration, the density and temperature at every CV are first evaluated, and then used to compute the remaining thermophysical properties of CO_2 at that CV using CoolProp Bell et al. (2014). Next, the empirical correlations (friction forces, heat transfer rates, and suction/discharge mass

flow rates) are calculated. These quantities are then supplied to the system of ODEs, which is solved using the third-order Runge–Kutta method (RK23) with the 'solve-ivp' function in the Python framework. This method offers a good compromise between computational speed and numerical accuracy, which is particularly important for solving stiff models such as the TC-3RD. The solving is performed directly over one full cycle from $\theta_{\mathrm{m}} = 0 \rightarrow \theta_{\mathrm{m}} = 2\pi$. A periodic steady state is considered to be reached when the following criteria are simultaneously satisfied:

$$\frac{\omega_{\mathrm{m}}}{2\pi} \int_{t}^{t+t_{\mathrm{cyc}}} \sum_{i \in \mathcal{I}_{\mathrm{r}}} |\dot{Q}_i| \, dt < \gamma_1, \tag{2.25}$$

$$\frac{\omega_{\mathrm{m}}}{2\pi} \int_{t}^{t+t_{\mathrm{cyc}}} |\dot{m}_{\mathrm{suc}} - \dot{m}_{\mathrm{dis}}| \, dt < \gamma_2, \tag{2.26}$$

If these conditions are not satisfied, the wall temperatures of the regenerator are updated to accelerate convergence according to the following relation Qiu et al. (2021):

$$T_{\mathrm{wall},i} = T_{\mathrm{wall},i} - \gamma_3 \cdot \dot{Q}_i, \quad i \in \mathcal{I}_{\mathrm{r}} \tag{2.27}$$

where $\gamma_3 = 0.02$ is a convergence coefficient. Following this procedure, the TC-3RD model simulation is executed, and the number of CVs assigned to each component is summarized in Table 2.2.

Component	Number of CVs
Cold cavity	1
Hot cavity	1
Cooler	4
Cooler dead volume	1
Regenerator	14
Heater dead volume	1
Heater	4

Table 2.2: TC components with the assigned number of CVs for simulation.

2.3.3 TC-3RD model-derived performance indicators

The performance indicators are calculated as cycle-averaged quantities from TC-3RD model outputs once TC operation reaches periodic steady state. This state is attained when the integrated state variable no longer changes from one cycle to the next, i.e. $x(t) = x(t+t_{\mathrm{cyc}})$. Using TC-3RD model outputs, the mechanical power required to drive the displacer is obtained as the cycle-averaged work rate in the cold and hot cavities:

$$\dot{W}_{\mathrm{mech}} = \frac{\omega_{\mathrm{m}}}{2\pi} \int_{t}^{t+t_{\mathrm{cyc}}} \left(p_0 \, \dot{V}_0 + p_N \, \dot{V}_N \right) dt. \tag{2.28}$$

The cooler heat transfer rate (heat rejected from the CO_2 in the cooler CVs) is

$$\dot{Q}_{\mathrm{k}} = \frac{\omega_{\mathrm{m}}}{2\pi} \int_{t}^{t+t_{\mathrm{cyc}}} \sum_{i \in \mathcal{I}_{\mathrm{k}}} \dot{Q}_i \, dt, \tag{2.29}$$

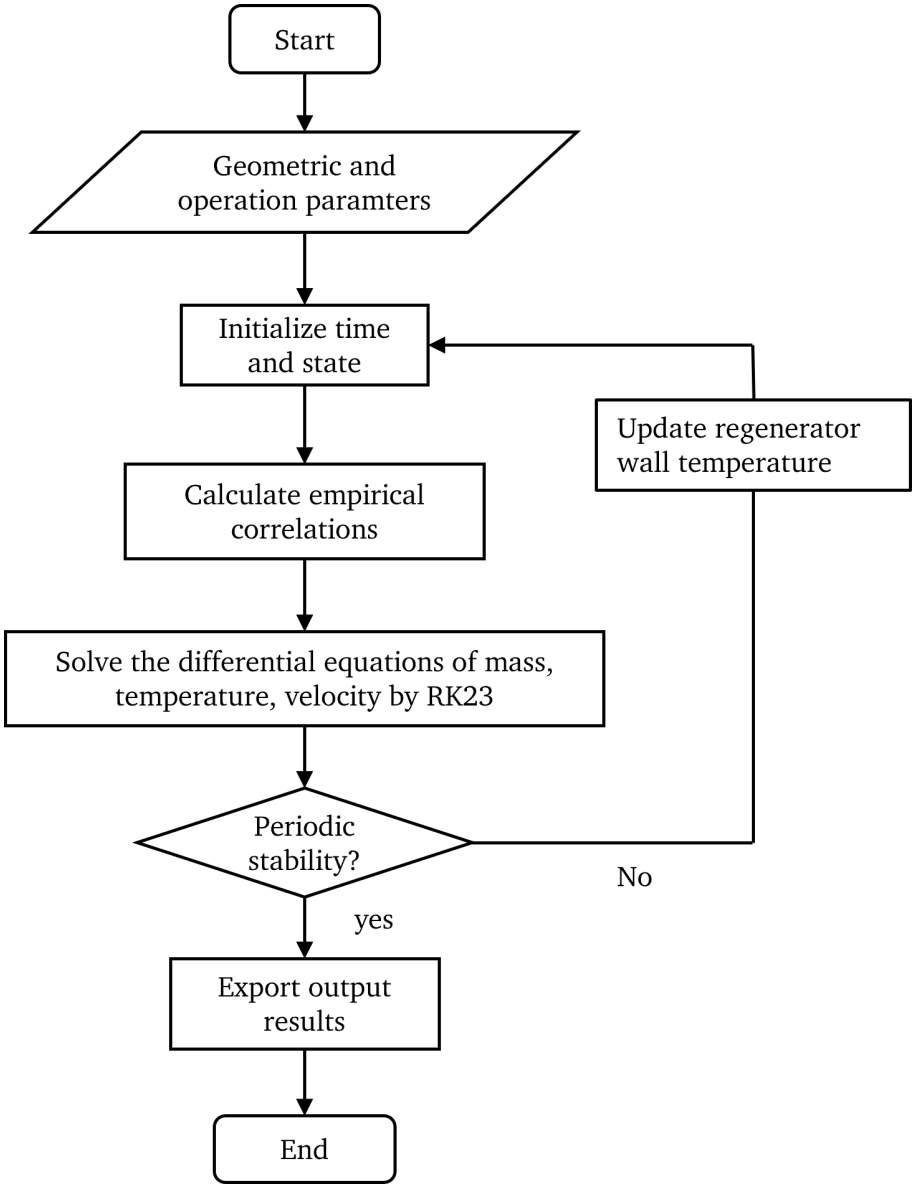

Figure 2.3: TC-3RD model numerical simulation flow chart.

where $\mathcal{I}_\mathrm{k}$ is the set of indices of the cooler CVs. The heater heat transfer rate (heat supplied to the CO_2 in the heater CVs) is

$$\dot{Q}_\mathrm{h} = \frac{\omega_\mathrm{m}}{2\pi} \int_t^{t+t_\mathrm{cyc}} \sum_{i \in \mathcal{I}_\mathrm{h}} \dot{Q}_i \, dt. \tag{2.30}$$

Finally, the compressor power output (net enthalpy flow) is the cycle-average of the discharge minus suction enthalpy streams:

$$\dot{H}_\mathrm{comp} = \frac{\omega_\mathrm{m}}{2\pi} \int_t^{t+t_\mathrm{cyc}} \left(\dot{m}_\mathrm{dis} \, h_\mathrm{dis} - \dot{m}_\mathrm{suc} \, h_\mathrm{suc} \right) dt. \tag{2.31}$$

These indicators are obtained from the numerical solution of the TC-3RD model, which is implemented in Python as described next.

2.3.4 Python implementation

The numerical methods described above are implemented in Python to provide an open-source and flexible simulation framework. While several Stirling engine simulation tools have been developed in the past Andersen (2006), most are proprietary or written in outdated programming languages, which limits their accessibility and reproducibility. The Python implementation developed in this work overcomes these limitations by offering a modern, transparent, and freely available platform Salame (2025a).

The modular structure of the code enables straightforward adaptation to different machine configurations. For instance, by removing the valve models and modifying the volume variations, the same framework can be directly applied to Stirling engines. This open-source implementation thus facilitates both reproducibility of the present results and future extensions of the model by the wider research community.

Having established the numerical framework and its implementation in Python, the next step is to assess the validity of the TC-3RD model. This is done by comparing its predictions with reference data, both from CFD simulations and from experimental measurements.

2.4 Model validation with data

The validation of TC-3RD model is performed in two stages: First stage using a CFD data containing the internal CO_2 thermophysical properties varying in a periodic steady-state cycle. Second stage is on steady-state data containing TC performance indicators collected from experimental work in Chapter 1.

2.4.1 Transient validation with CFD

CFD is used by a hired company to simulate the internal thermophysical properties of CO_2 while the TC is running under the following conditions: $T_\mathrm{h} = 600$ °C, $T_\mathrm{w,ret} = 30$ °C, $\omega_\mathrm{m} = 180$ rpm, $p_\mathrm{suc} = 45$ bar, and $p_\mathrm{dis} = 60$ bar. The TC-3RD model is simulated under similar conditions, and the results are compared to those from CFD. Figure 2.4 shows the variations of (a) masses, (b) temperatures, (c) pressures, and (d) mass flow rates through the suction and discharge valves during one periodically steady cycle. The solid curves

correspond to the CFD predictions, while the dashed curves represent the TC-3RD model. The transient trends of the two models are in good agreement, with notable differences primarily in the temperatures of the hot cavity and heater space. From (d), we can see that both methods start from the same point; however, the TC-3RD model predicts pressure increases and decreases faster during oscillations. This is expected, considering that the TC-3RD model is a simplified version that tends to underestimate internal losses. Given that the TC-3RD model is 336 times faster than CFD, the results are deemed acceptable and provide a satisfactory transient validation.

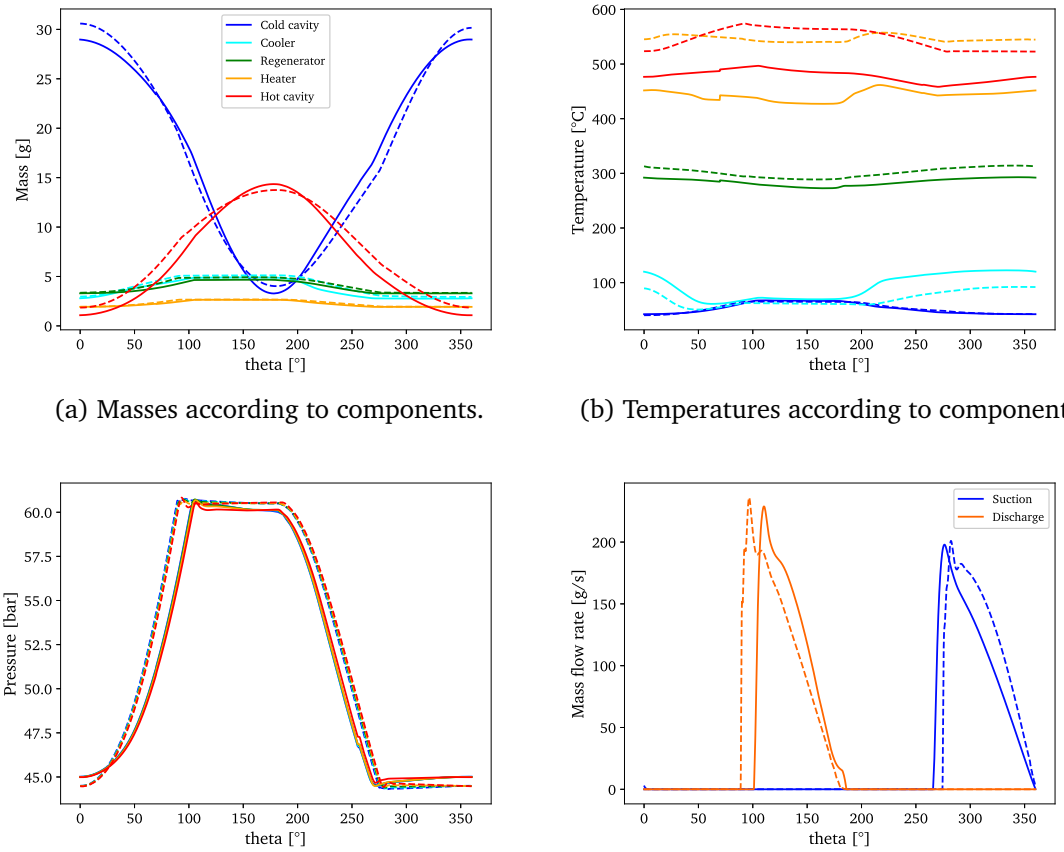

(a) Masses according to components.

(b) Temperatures according to components.

(c) Pressures according to components.

(d) Suction and discharge mass flow rates.

Figure 2.4: TC-3RD model (dashed) vs CFD (solid) transient predictions during one periodic steady cycle.

2.4.2 Steady-state validation

The TC-3RD model is validated at operating points with varying rotational speed $\omega_{\mathrm{m}} \in 150, 200, 240$ rpm, charged pressure $p_{\mathrm{charged}} \in 40, 50, 55$ bar, and pressure ratios $1.23 < r_p < 1.58$. Variations in p_{charged} and r_p translate into changes in suction and discharge pressures, which are direct model inputs. The heater and water return temperatures are fixed at $T_{\mathrm{h}} = 800$ °C and $T_{\mathrm{w,ret}} = 20$ °C, respectively, for all experimental (exp) and simulated (sim) points. Experimental performance indicators are taken from Chapter 1, while simulated values are calculated from Section 2.3.3.

As shown in Figures 2.5 and 2.6, increasing the pressure ratio reduces the heater heat transfer rate due to weaker heat exchange with CO_2, thereby lowering the mass

flow rate and raising the discharge temperature. The rise in mechanical power is linked to flow accumulation inside the TC, which further contributes to the higher discharge temperature.

At $p_{\text{charged}} = 56$ bar, the increase in motor speed from 150 to 240 rpm leads to a higher motor load and thus increases the mechanical power. It also causes a faster flow inside the TC, resulting in greater heat exchange with the internal walls. Consequently, the heater and cooler heat transfer rates increase, as observed in Figure 2.5. The mass flow rate also increases at comparable pressure ratios, and the discharge temperature rises. Mechanical power further increases due to the higher rotational speed. The TC-3RD model captures the general transient trends of these changes; however, it clearly underestimates the mechanical power and cooler heat transfer rate while overestimating the discharge temperature. The relative deviations between measured and predicted performance indicators are 8.6% for the heater heat transfer rate and 25.1% for the cooler heat transfer rate. In contrast, mechanical power is predicted with a relative deviation of 43.7%. The predicted mass flow rate shows a deviation of 11.9%, while the discharge temperature is overestimated by 9.6 K.

At $\omega_{\text{m}} = 150$ rpm, raising the charged pressure from 30 to 56 bar increases the CO_2 density, thereby enhancing the heat exchange rate and resulting in a higher heater heat transfer rate, as shown in Figure 2.6. Increasing the charged pressure from 30 to 50 bar has little influence on the cooler heat transfer rate, while the effect becomes more significant when increasing to 56 bar. The mass flow rate clearly increases, and so does the discharge temperature. The mechanical power, however, shows an unusual trend: while at pressure ratios lower than 1.42 the mechanical power decreases with increasing charged pressure, this trend is reversed once the pressure ratio exceeds 1.42. The derived TC-3RD model is not able to capture this behavior. The relative deviations between measured and predicted performance indicators are 16% for the heater heat transfer rate and 31.7% for the cooler heat transfer rate. Conversely, mechanical power is predicted with a relative deviation of 61.7%. The predicted mass flow rate shows a deviation of 14.4%, while the discharge temperature is again overestimated by 14.8 K.

Overall, it is clear that the TC-3RD model needs improvements, as some physical aspects are not adequately captured. This means it cannot be used for generating data reliably. However, the good physical trends it reproduces can be helpful to investigate the influence of operating conditions on exergy destruction inside internal components and identify which should be targeted in future improvements. This is done in the next section.

2.5 TC-3RD model-based exergy study

In this section, a detailed model-based exergy analysis is carried out on the TC to identify the irreversibilities associated with its internal components.

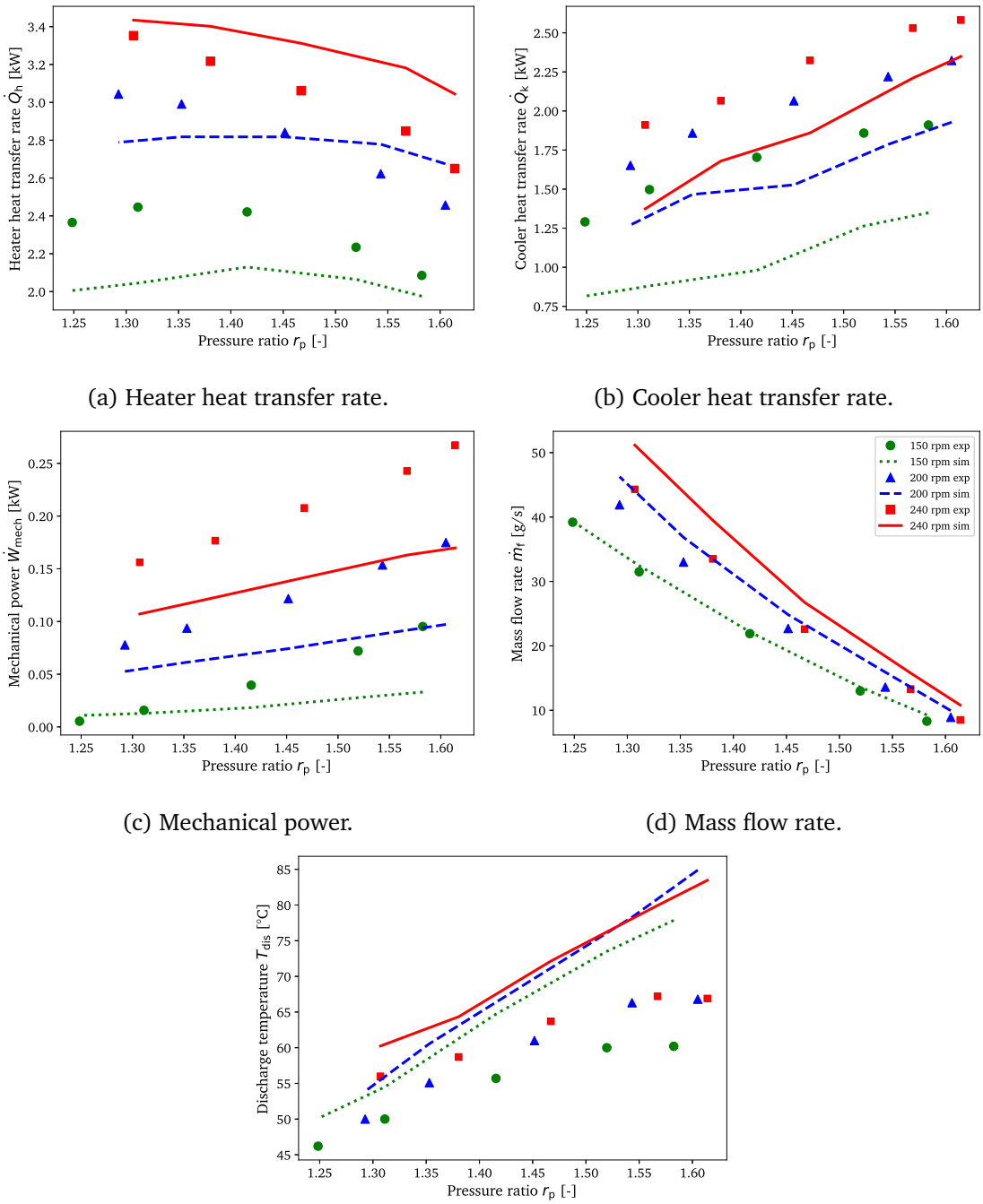

(a) Heater heat transfer rate.

(b) Cooler heat transfer rate.

(c) Mechanical power.

(d) Mass flow rate.

(e) Discharge temperature.

Figure 2.5: TC-3RD model validation—simulated (sim) vs experimental (exp, markers) performance indicators versus pressure ratio r_p at three rotational speeds $\omega_{\mathrm{m}} \in \{150, 200, 240\}$ rpm.

2.5.1 Methodology

The exergy balance for a control volume is expressed as Çengel and Boles (2019):

$$\frac{\partial E_{\mathrm{cv}}}{\partial t} = \sum_{\mathrm{in}} \dot{m}_{\mathrm{in}} \psi_{\mathrm{in}} - \sum_{\mathrm{out}} \dot{m}_{\mathrm{out}} \psi_{\mathrm{out}} + \sum_{i} \left(1 - \frac{T_{\mathrm{ref}}}{T_i}\right) \dot{Q}_i - \dot{W}_{\mathrm{cv}} - \dot{E}_{\mathrm{dest}}. \tag{2.32}$$

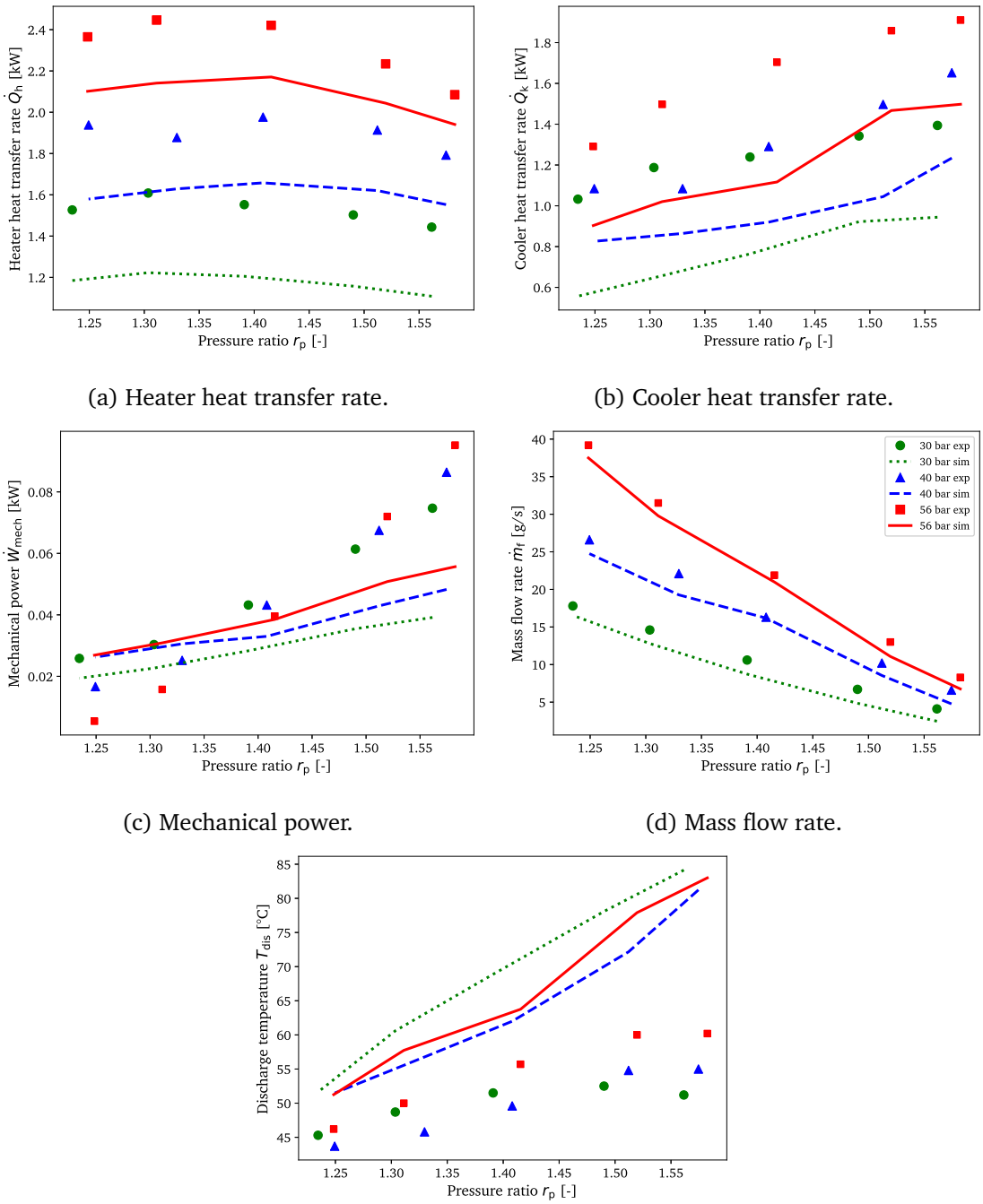

(a) Heater heat transfer rate.

(b) Cooler heat transfer rate.

(c) Mechanical power.

(d) Mass flow rate.

(e) Discharge temperature.

Figure 2.6: TC-3RD model validation—simulated (sim) vs experimental (exp, markers) performance indicators as a function of pressure ratio r_p at three charged pressures $p_{\text{charged}} \in \{30, 40, 56\}$ bar.

At periodic steady state, the transient storage term is zero, leading to:

$$\dot{E}_{\text{dest}} = \sum_{\text{in}} \dot{m}_{\text{in}} \psi_{\text{in}} - \sum_{\text{out}} \dot{m}_{\text{out}} \psi_{\text{out}} + \sum_{i} \left(1 - \frac{T_{\text{ref}}}{T_i}\right) \dot{Q}_i - \dot{W}_{\text{cv}}. \tag{2.33}$$

The term $\dot{E}_{\text{dest}}$ is obtained directly from the TC-3RD model outputs by averaging over one cycle, ensuring that transient storage effects are eliminated. This approach allows irreversibilities to be attributed to each internal component of the thermal compressor.

2.5.2 Results

The mean pressure, rotational speed, and heater temperature were varied at different pressure ratios to quantify the exergy destroyed in each component of the TC. The experimental data analyzed in Section 1.3.6.2 highlighted a strong influence of charged pressure and pressure ratio, with a smaller effect of rotational speed and heater temperature. However, the experimental ranges were limited, especially for charged pressure, rotational speed, and heater temperature. The TC-3RD model was therefore used to extend the ranges and investigate a broader operating map: heater temperature $T_{\mathrm{h}} \in \{500, 650, 800\}$ °C, rotational speed $\omega_{\mathrm{m}} \in \{100, 180, 240\}$ rpm, and charged pressure $p_{\mathrm{charged}} \in \{30, 50, 70\}$ bar.

Figure 2.7 shows the breakdown of exergy destruction among the TC components at fixed operating conditions: $\omega_{\mathrm{m}} = 180$ rpm, $T_{\mathrm{h}} = 650$ °C, $p_{\mathrm{charged}} = 50$ bar, and $r_{\mathrm{p}} = 1.33$. The main outcome is that exergy is primarily destroyed in the regenerator, as expected given the large temperature gradients and pressure drops. The cooler and heater contribute comparably, while the cylinder has the smallest share.

Figure 2.8a shows the effect of heater temperature, indicating that increasing T_{h} slightly improves exergy efficiency.

Figure 2.8b illustrates the influence of rotational speed. The highest exergy efficiency occurs at low ω_{m}, and efficiency decreases significantly as rotational speed increases, indicating limited benefit from operating at high speeds.

Figure 2.8c demonstrates the strong impact of charged pressure. The extended range (30–70 bar) shows that exergy efficiency improves between 30 and 50 bar but deteriorates at 70 bar, suggesting that an optimum lies in between. This result confirms the trend already observed in experimental data.

A key outcome across all cases is the identification of a universal optimum pressure ratio around $r_{\mathrm{p}} = 1.2$–1.4, after which efficiency deteriorates regardless of the varied parameter. This makes r_{p} a robust design and control target.

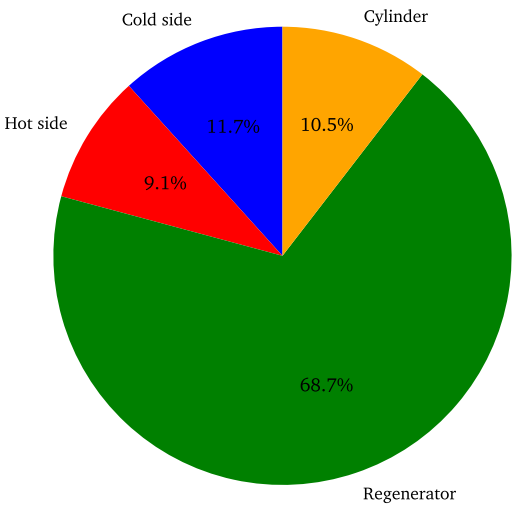

Figure 2.7: Breakdown of exergy destruction by component at representative operating conditions of the TC.

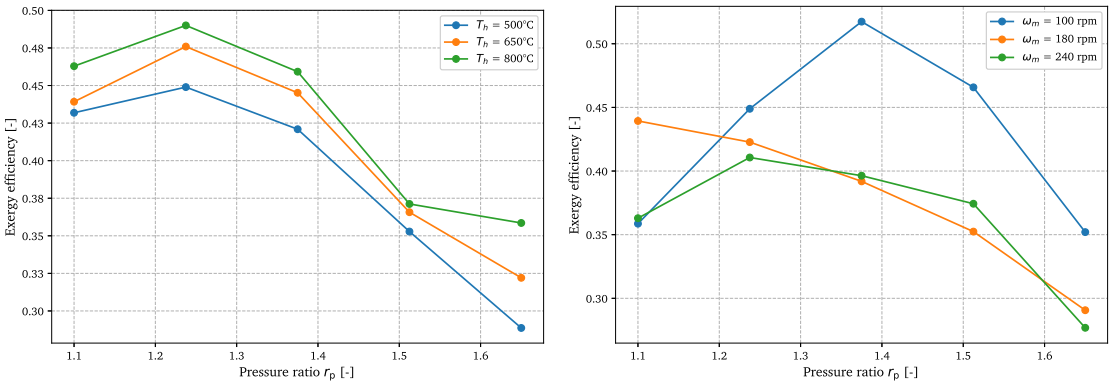

(a) Variation with T_{h}

(b) Variation with ω_{m}

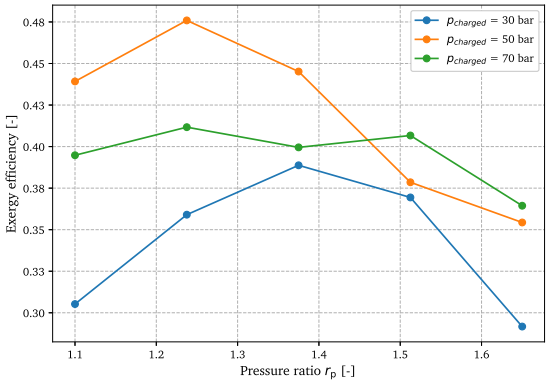

(c) Variation with p_{charged}

Figure 2.8: Exergy efficiency of the TC as a function of pressure ratio under three different operating conditions: (a) heater temperature T_{h}, (b) rotational speed ω_{m}, and (c) charged pressure p_{charged},

2.6 Conclusion

In this chapter:

- A detailed third-order physical model for a two-valve Stirling-type TC was developed, based on mass, energy, and momentum balance equations applied to discretized CVs using the FV method. The suction and discharge valve flow rates were modeled, and empirical correlations for heat transfer and friction coefficients were implemented.

- The resulting model is a system of connected ODEs, referred to as the TC-3RD model. It takes operating conditions and component geometries as inputs and predicts the thermophysical properties of CO_2 across the CVs during oscillation. Performance indicators are obtained as averages over one periodic steady cycle.

- A procedure was defined to accelerate convergence to periodic steady state. Initial conditions and the solving procedure of the TC-3RD model were detailed.

- TC-3RD predictions of internal variations were evaluated against one CFD-simulated operating point at periodic steady state, showing good agreement.

- Steady-state experimental data were used to evaluate performance indicators. The model predicted with the following average relative deviations:
  - 14% for heater heat transfer rate,
  - 28% for cooler heat transfer rate,
  - 67.3% for mechanical power,
  - 13.5% for mass flow rate,
  - 13 K for discharge temperature.
- Although improvement is still possible, the TC-3RD model enabled component-level exergy analysis. Results showed that exergy destruction is dominated by the regenerator (around 70%), followed by the cooler, heater, and cylinder. Future design optimizations should therefore prioritize regenerator performance.
- Extended simulations revealed that an optimal pressure ratio exists around 1.2–1.4, after which efficiency decreases. Increasing charged pressure from 30 to 50 bar improves exergy efficiency, but at 70 bar performance drops sharply, suggesting an optimum in between. Increasing heater temperature slightly improves efficiency, though the effect was less evident in experimental data.

The TC-3RD model is thus a detailed physical representation of the Stirling-type thermal compressor. While its accuracy is limited by empirical correlations and unmodeled physical effects, and in the absence of internal measurements for further validation, the model remains a valuable tool for assessing component-level exergy destruction and the influence of operating conditions.

Chapter 3

Thermal compressor empirical models

Abstract

Although the TC-3RD physical model developed in the previous chapter is important for understanding the physics, its resulting accuracy is not sufficient for reliable data generation. Therefore, in this chapter we use company-recorded data, in addition to the experimental data from Chapter 1, to develop data-driven models. These models are potentially fast and reliable, making them good candidates for integration into a dynamic heat pump cycle model.

In Section 3.1, the collected dataset is extended with data available from earlier tests. The data is then re-assessed and filtered using a Gaussian process regression (GPR) approach. Section 3.2 introduces three types of machine learning (ML) models to predict the performance indicators of a TC based on main inputs that are easily measured. The first type is regression models, including linear (LR) and polynomial (PR). The second is GPR, and the third is an artificial neural network (ANN). These models are trained on the collected data and evaluated using defined performance metrics. Based on these metrics, the three models are compared in Section 3.3.

3.1 Data extension and re-assessment

The collected data lacked variations on heater temperature which is an important input. Extending the data ranges is necessary for a more general performance characterization. For this, we use available data from previous tests performed by colleagues. The tests were carried on same TC technology also in a single stage cycle. The main difference was that the heater was electrically heated, so no gas combustion has taken place and the electric resistance power for heating is assumed to be absorbed by the TC. Therefore, no heat loss is considered and it is omitted. The total collected data from all the experiments combined is equal to 251 samples. Data is re-assessed again for filtering also using GPR model and 20 samples are found to be outliers thus excluded from the dataset. The filtered new dataset is of $N_{\mathrm{s}} = 231$ samples. The new inputs ranges are summarized in Table 3.1.

Symbol	Description	Range	Unit
p_{suc}	Suction pressure	22.6–48.7	bar
p_{dis}	Discharge pressure	34.2–64.2	bar
ω_{m}	Rotational speed	60–260	rpm
T_{h}	Heater temperature	500–800	°C

Table 3.1: TC input variables after data extension.

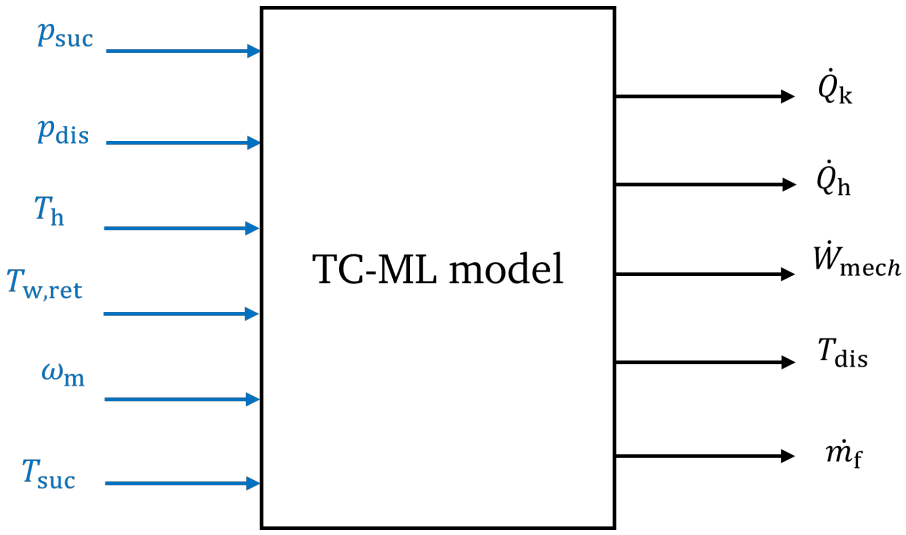

Figure 3.1: Inputs and outputs of TC-ML models.

3.2 Machine learning models

Most Stirling machine modeling efforts have relied on physical equations, with the resulting models used to optimize performance based on geometry or operating conditions. However, the availability of experimental data around targeted TC across various operating conditions makes it attractive to develop ML models for this optimization task. While these models may lack certain physical insights, they offer fast and reliable performance predictions. The TC-ML models derived in this section take the input vector and predict the output vector that are summarized in Figure 3.1.

3.2.1 Regression models

Regression models are fundamental tools in statistics and ML for quantifying the relationship between a dependent variable and one or more independent variables James et al. (2013). The goal of regression analysis is to approximate the expected value of the dependent variable based on the values of the independent variables. For example, Yazar et al. (2017) compared different regression models for predicting compressor and turbine parameters. Among these models, Linear Regression (LR) is the simplest form, assuming a linear relationship between inputs and outputs. Let $\mathbf{u}^{(n)} \in \mathbb{R}^l$ be the input vector of sample n, where $l = 6$ in our case, and let $y^{(n)}$ denote the corresponding output. The LR model predicts

$$y_{\mathrm{LR}}^{(n)} = \alpha_0 + \sum_{j=1}^{l} \alpha_j \, u_j^{(n)}, \tag{3.1}$$

where α_0 is the intercept, α_j are the regression coefficients, and $u_j^{(n)}$ is the j-th input feature of sample n. The optimal coefficients $\boldsymbol{\alpha}$ are determined by solving the ordinary least squares (OLS) minimization problem:

$$\min_{\boldsymbol{\alpha}} \sum_{n=1}^{N_\mathrm{s}} \left(y_\mathrm{LR}^{(n)} - y_\mathrm{meas}^{(n)}\right)^2, \tag{3.2}$$

where N_s is the number of samples. While LR assumes linearity, it can be naturally extended to Polynomial Regression (PR) by augmenting the input vector with higher-order terms of $u^{(n)}$.

The above formulation is implemented in Python using `scikit-learn`. Specifically, `PolynomialFeatures(degree)` is applied to generate polynomial expansions of the input features, which are then fitted using `LinearRegression`. Training and validation sets are obtained by an 80/20 split with `train_test_split`, and model performance is assessed through metrics such as R^2 and mean absolute percentage error (MAPE). This provides a simple yet effective baseline for comparing against more advanced ML models.

3.2.2 Gaussian process regression

The second type of ML model considered in this work is Gaussian process regression (GPR). Following the definitions of Rasmussen (2004), a Gaussian process (GP) is a non-parametric and probabilistic model that does not assume a fixed functional form, but instead defines a distribution over functions through a covariance kernel. In addition to detecting data outliers (Section 1.3.5), Quoilin and Schrouff (2016) applied GPR to an expander and absorption machine dataset, resulting in high accuracy comparable with that of an ANN, but with fewer tuning parameters. We reserve GP for the prior process and use GPR for the regression model throughout.

Given training data $\{(\mathbf{u}^{(n)}, y^{(n)})\}_{n=1}^{N_\mathrm{s}}$, the GPR predictive distribution at a new input $\mathbf{u}_*$ can be expressed as

$$y_\mathrm{GPR}(\mathbf{u}_*) = \sum_{n=1}^{N_\mathrm{s}} \beta_n \, \kappa(\mathbf{u}_*, \mathbf{u}^{(n)}) + \varepsilon, \tag{3.3}$$

where β_n are weights obtained from the inversion of the regularized kernel matrix, $\kappa(\cdot,\cdot)$ is the kernel (covariance) function, and ε is a noise term. The latent function is assumed to follow a GP prior:

$$f(\mathbf{u}) \sim \mathcal{GP}\big(m(\mathbf{u}), \kappa(\mathbf{u}, \mathbf{u}')\big), \tag{3.4}$$

where $m(\mathbf{u})$ is the mean function and $\kappa(\mathbf{u}, \mathbf{u}')$ defines the covariance between two input vectors $\mathbf{u}$ and $\mathbf{u}'$. The choice of kernel is critical, as it encodes prior assumptions about the function, such as smoothness, periodicity, or linearity. In this work, the radial basis function (RBF) kernel is used:

$$\kappa_\mathrm{RBF}(\mathbf{u}, \mathbf{u}') = \mathrm{Var}_f \cdot \exp\left(-\frac{\|\mathbf{u} - \mathbf{u}'\|^2}{2\ell_s^2}\right), \tag{3.5}$$

where ℓ_s is the length-scale hyperparameter controlling smoothness, and Var_f is the signal variance. This formulation allows the GPR model to flexibly capture nonlinearities in the mapping $\mathbf{u} \mapsto y$, while also providing predictive uncertainty estimates.

The GPR formulation above is implemented in Python using `scikit-learn`. For each output dimension, a `GaussianProcessRegressor` is instantiated with an anisotropic RBF kernel. Kernel hyperparameters are optimized by maximizing the log-marginal likelihood.

3.2.3 Artificial neural network model

Artificial Neural Networks (ANNs) are a cornerstone of ML, inspired by the structure and functional aspects of biological neural networks Haykin (2009). Ziviani et al. (2018) demonstrated the application of ANNs for a scroll expander and an injected scroll compressor, achieving higher accuracy than semi-empirical models, since ANNs do not rely on prior assumptions and can be directly trained with experimental data. An ANN consists of interconnected processing units, called neurons, which are arranged into layers (input, hidden, and output) to process data. Each neuron computes a weighted sum of its inputs, adds a bias term, and passes the result through an activation function $\sigma(\cdot)$ to introduce nonlinearity before propagating the signal to subsequent layers.

Let $\mathbf{u}^{(n)} \in \mathbb{R}^l$ denote the input vector of sample n, and w_j the weight associated with its j-th feature. The output of a generic neuron can be expressed as

$$y_{\text{ANN}}^{(n)} = \sigma\left(\sum_{j=1}^{l} w_j u_j^{(n)} + b\right), \tag{3.6}$$

where b is a bias parameter that shifts the activation independently of the inputs. The structure of a generic ANN neuron is illustrated in Figure 3.2.

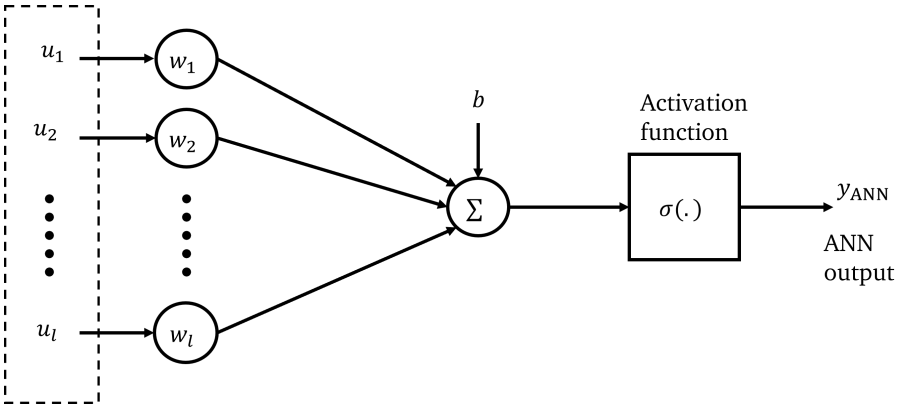

Figure 3.2: Structure of a generic neuron in the ANN model.

In regression tasks, the ANN learns the weights and biases through training, where the objective is to minimize prediction error between model-predicted outputs and measured data. This structured approach enables ANNs to capture complex nonlinear relationships within the data, thereby improving predictive accuracy on unseen samples. Following this, an ANN model is developed for the tested TC. The model for each output variable consists of an input layer, a hidden layer with up to 300 neurons, and a single-neuron output layer. The rectified linear unit (ReLU) activation is used in the hidden layer, while the output neuron is linear to suit regression tasks. The `Adamax` algorithm is chosen for training, and the mean squared error (MSE) serves as the loss function:

$$MSE = \frac{1}{N_{\text{s}}} \sum_{n=1}^{N_{\text{s}}} \left(y_{\text{pred}}^{(n)} - y_{\text{meas}}^{(n)}\right)^2. \tag{3.7}$$

Additional hidden layers or neurons could further increase accuracy, though at the risk of overfitting. The implementation is carried out using Keras functions by Chollet et al. (2015), a high-level neural network API integrated with TensorFlow.

3.2.4 Common implementation

The re-assessed data from Section 3.1 is used to fit the three described models: PR, GPR, and ANN. In total, 80% of the available data is randomly selected for training, while the remaining 20% is kept as test data for validation. Let y_{meas} denote the measured values and y_{pred} the corresponding model predictions. A common indicator of regression model performance is the coefficient of determination (R^2), which quantifies how well the predictions follow the measured data. It is defined as

$$R^2 = 100\% \cdot \frac{\text{Cov}(y_{\text{meas}}, y_{\text{pred}})}{\sqrt{\text{Cov}(y_{\text{meas}}, y_{\text{meas}}) \cdot \text{Cov}(y_{\text{pred}}, y_{\text{pred}})}}, \tag{3.8}$$

where $\text{Cov}(\cdot, \cdot)$ denotes population covariance. A value close to 100% indicates an almost perfect fit, though excessively high values may also suggest overfitting. To complement this, the MAPE is introduced to evaluate prediction accuracy in relative terms:

$$MAPE = 100\% \cdot \frac{1}{N_{\text{s}}} \sum_{n=1}^{N_{\text{s}}} \left| \frac{y_{\text{pred}}^{(n)} - y_{\text{meas}}^{(n)}}{y_{\text{meas}}^{(n)}} \right|, \tag{3.9}$$

where N_{s} is the number of samples. A value of 0% indicates a perfect match between predictions and measurements. MAPE is used for evaluating the accuracy of power and flow rate predictions. For temperature outputs, the mean absolute error (MAE) is additionally to reflect absolute deviations:

$$MAE = \frac{1}{N_{\text{s}}} \sum_{n=1}^{N_{\text{s}}} \left| y_{\text{pred}}^{(n)} - y_{\text{meas}}^{(n)} \right|. \tag{3.10}$$

Finally, to ensure scale uniformity across the input variables, both training and validation datasets are normalized to the range $(0.1, 0.9)$ according to

$$u_{\text{norm}} = 0.8 \cdot \frac{u - u_{\text{min}}}{u_{\text{max}} - u_{\text{min}}} + 0.1, \tag{3.11}$$

where u_{min} and u_{max} denote the minimum and maximum of the input vector u, and u_{norm} is the normalized result.

3.3 Models accuracies

The models accuracies are compared on the test data using parity plots shown in Figure 3.3. The x-axis and y-axis contain the measured and predicted performance indicators respectively. The solid black line corresponds to an ideal line indicating a perfect fit. From observing the plots, we see that GPR model exhibited the highest prediction accuracy, closely followed by the ANN predictions. On the other hand, PR model failed to achieve similar high accuracies specially in predicting $\dot{m}_{\text{f}}$ and $\dot{W}_{\text{mech}}$.

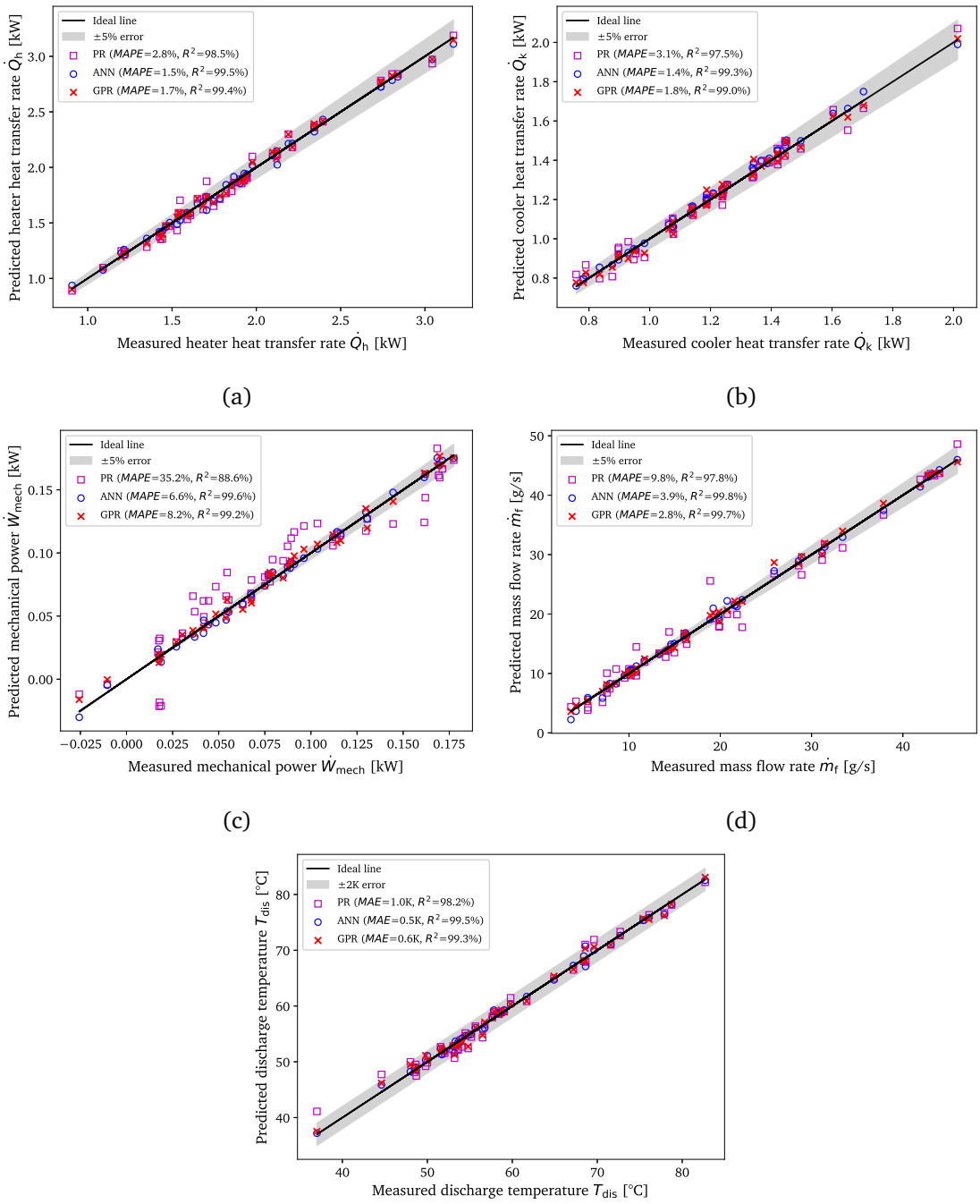

Figure 3.3: TC-ML models accuracy comparison on main outputs: (a) heater heat transfer rate, (b) cooler heat transfer rate, (c) mechanical power, (d) mass flow rate, and (e) discharge temperature.

To ensure the robustness and generalization capability of the trained models, a 5-fold cross-validation strategy is employed. In this approach, the entire dataset is split into five equal parts, and the models were iteratively trained on four parts and validated on the remaining one. This procedure is repeated five times, each time using a different fold as the test set. For each output target, performance metrics such as the R^2, MAPE, and MAE are computed in each fold and then averaged. This allowed a more reliable and statistically sound comparison between models, as it mitigates the risk of overfitting or underfitting to

a single random data split. Cross-validation also enabled a clearer understanding of the variability in model accuracy across different subsets of the data.

The results in Table 3.2 confirm the superior performance of the GPR model across all targets. GPR consistently achieves the highest R^2 scores and the lowest MAPE values, indicating excellent fit, accuracy, and generalization. The ANN model also performs strongly, though slightly behind GPR. In contrast, PR is not suitable for mass flow rate and mechanical power—its deviations are large—although it provides acceptable predictions for the other outputs.

Since the selected ML model will be integrated into a dynamic heat pump model, prediction latency is also important. GPR requires only 3.4 ms per iteration, compared to 660 ms for ANN models, making GPR roughly 200 times faster. This is justified considering that ANNs involve far more hyperparameters. Accordingly, the GPR model is chosen as a reliable predictor of TC performance indicators.

Target	**Model**	R^2 **[%]**	**MAPE [%] or MAE [K]**
$\dot{m}_\mathrm{f}$	PR	97.0 ± 1.4	11.0 ± 2.0
	ANN	98.5 ± 1.0	6.7 ± 2.3
	GPR	99.7 ± 0.1	3.7 ± 0.6
$\dot{Q}_\mathrm{h}$	PR	98.2 ± 0.6	49.8 ± 4.5
	ANN	98.5 ± 0.9	42.8 ± 9.5
	GPR	99.2 ± 0.7	27.6 ± 5.3
$\dot{Q}_\mathrm{k}$	PR	98.0 ± 0.5	36.7 ± 7.0
	ANN	98.9 ± 0.3	27.8 ± 6.3
	GPR	99.1 ± 0.2	23.9 ± 2.5
$\dot{W}_\mathrm{mech}$	PR	91.4 ± 1.6	35.1 ± 5.8
	ANN	97.8 ± 1.5	11.2 ± 1.9
	GPR	99.1 ± 0.2	9.3 ± 3.4
T_dis	PR	97.5 ± 1.0	1.1 ± 0.2
	ANN	97.7 ± 1.9	1.1 ± 0.7
	GPR	99.3 ± 0.3	0.5 ± 0.0

Table 3.2: Cross-validation results of TC-ML models across performance-indicator outputs. Metrics shown are mean $\pm$ standard deviation.

3.4 Conclusion

In this chapter:

- The dataset was extended and re-assessed: 251 samples combined from multiple campaigns, with 20 outliers detected via GPR uncertainty filtering, resulting in $N_\mathrm{s} = 231$ for training and testing.

- Several machine learning models were proposed, including regression models such as LR and PR, ANN, and GPR. The structure of each and the corresponding Python implementation are described. These are trained with 231 real data samples from

previous experimental work, by taking main operating conditions as inputs and predicting performance indicators.

- The models' accuracies were tested on unseen test data, revealing that GPR outperforms other models—slightly compared to ANN, but significantly compared to PR. A k-fold cross-validation is used to ensure that models are reliable and can be generalized over data ranges. Additionally, GPR demonstrated 200 times faster predictions thus more suitable to be integrated in a dynamic heat pump cycle.

In the next chapter, we integrate the selected surrogate into a complete three-stage TC heat pump application and associated control framework.

Part II

Dynamic modeling and control of a three-Stage transcritical CO_2 thermal compressor heat pump

Chapter 4

Introduction

Abstract

Following the derivation of a data-driven model for the TC, the second part of this thesis extends the analysis to the complete thermal compressor heat pump (TCHP) cycle developed by Boostheat. The cycle employs a three-stage TC in series, with CO_2 as the working fluid. To set the stage, the first chapter provides a general review of transcritical CO_2 vapor compression cycles (VCCs) and then introduces the targeted TCHP in this work together with the corresponding experimental campaign.

First, the motivation and challenges of using CO_2 as a refrigerant are presented in Section 4.1. Section 4.2 defines a basic single-stage transcritical CO_2 cycle and summarizes architectural enhancements developed for such cycles. Section 4.3 then presents the Boostheat TCHP as a three-stage system operating with CO_2 in the transcritical regime, describes the test bench and operating procedures, details the system actuators and their influence on the process, and provides energy expressions derived from measurements. Finally, Section 4.3 specifies the two types of data collected—(1) transient and (2) steady-state—to be used later for model development and validation.

4.1 Carbon Dioxide as a refrigerant

4.1.1 Historical review

Until the 1930s, natural refrigerants such as carbon dioxide (CO_2), ammonia (NH_3), and hydrocarbons were commonly used in mechanical refrigeration systems. The introduction of the first synthetic refrigerant, R-12 (a chlorofluorocarbon (CFC)), in 1930 marked a turning point. Synthetic refrigerants such as CFCs and hydrochlorofluorocarbons (HCFCs) gained popularity due to their chemical stability, non-flammability, and ease of handling, gradually replacing natural refrigerants in many applications. The harm done to the ozone layer by such refrigerants did not come to notice until 1970.

In 1987, with the introduction of the Montreal Protocol (1987), there was a significant shift away from CFC and HCFC refrigerants due to their high ozone depletion potential (ODP). While the Montreal Protocol focused on phasing out ozone-depleting substances, many of those substances were also strong greenhouse gases. Their replacements, hydrofluorocarbons (HFCs), were safer for the ozone layer but had high global warming

potential (GWP). This shifted attention to climate change and led to the Kyoto Protocol (1997), which was the first international treaty to set binding emission reduction targets for developed countries. Later, the Paris Agreement (2015) expanded the effort by involving all countries and setting a global target to limit warming to well below 2°C. These agreements encouraged a return to natural refrigerants such as CO_2, valued for their low environmental impact.

The study by Lorentzen (1994) revived the idea of using CO_2 especially in transcritical cycles and motivated much research afterwards to study CO_2 as a refrigerant. The author presented it as a promising fluid and demonstrated that, with optimized operating conditions, a high competing coefficient of performance (COP) could be achieved.

Kim et al. (2004) argued that the natural refrigerant CO_2 is an alternative to synthetic refrigerants because it has a very low GWP, is taken as the reference fluid, and does not contribute to ozone layer depletion (zero ODP). Moreover, it offers certain advantages over other natural refrigerants: it is non-toxic, non-flammable, and non-corrosive, and can operate in a vapor compression cycle (VCC) over a wide temperature range.

4.1.2 Unique properties

Along with its environmentally friendly characteristics, CO_2 exhibits two distinctive thermophysical properties that set it apart from conventional refrigerants. In this thesis, we use transcritical to refer to the cycle configuration and supercritical to refer to the thermodynamic state of CO_2.

Its low critical temperature ($T_{\text{crit}} = 31.1\,°\text{C}$). For instance, in conventional subcritical VCCs, this low critical temperature becomes a challenge: it restricts the heat delivery temperature to below T_{crit}, thereby narrowing the effective operating range. As the system approaches T_{crit}, the enthalpy of vaporization drops significantly, which negatively affects both heating capacity and overall performance (Kim et al. (2004)). However, CO_2's low critical temperature provides the opportunity to operate in a transcritical manner.

Its high critical pressure ($p_{\text{crit}} = 73.7$ bar). Subcritical cycles typically operate at pressures of 60–70 bar, whereas transcritical systems can reach pressures ranging from 80 to 110 bar or more. Although such high pressures pose challenges in terms of compressor capability and component durability, they also present thermodynamic advantages. In particular, CO_2 benefits from high vapor density and a large volumetric heating capacity, which allow for a reduced circulating mass flow to meet the same heating demand. This enables the use of smaller components and more compact system designs, as stated by Cavallini et al. (2005).

To illustrate the transition behavior around the critical point, Figure 4.1a shows the pressure–temperature (p–T) diagram. Three distinct fluid states are relevant in the supercritical region: supercritical fluid (pressure and temperature both above critical values), supercritical liquid (pressure above but temperature below the critical point), and supercritical vapor (temperature above but pressure below the critical point). Figure 4.1b shows the pressure–enthalpy (p–h) diagram. The saturation dome clearly delimits the two-phase region, while the dashed line at the critical pressure separates the subcritical domain—comprising liquid, two-phase, and vapor states—from the supercritical domain.

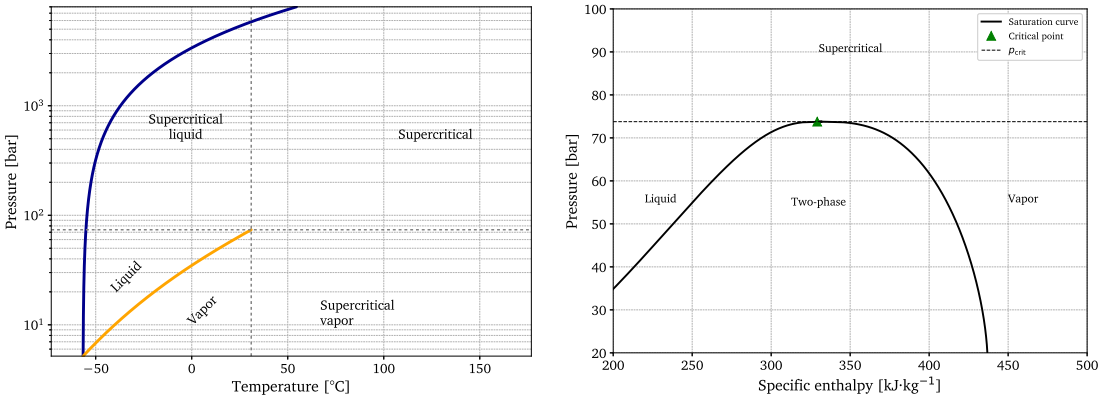

(a) (b)

Figure 4.1: CO_2 (a) p–T and (b) p–h diagrams with different states generated with the CoolProp library.

4.2 Transcritical CO_2 cycle

Several reviews have documented advances in transcritical CO_2 cycles. Starting with Austin and Sumathy (2011), the focus has been on the fundamentals of transcritical operation, component-level improvements, and the impact of different configurations on system performance. More recently, Song et al. (2022) expanded this perspective across applications, highlighting the growing role of CO_2 in building heating, mobility, and commercial refrigeration, as well as the increasing importance of intelligent control strategies in transcritical CO_2 cycles.

4.2.1 Basic single-stage

A VCC transfers heat from a low-temperature reservoir to a high-temperature one, typically using mechanical power. In the conventional (subcritical) case, heat rejection occurs below the critical point: the high-pressure heat exchanger acts as a condenser and the working fluid condenses, benefiting from latent-heat release. By contrast, when heat rejection occurs above the critical point, condensation is not possible; heat is removed by single-phase sensible cooling (gas cooling), and the condenser is then referred to as a gas cooler. This operating mode is termed transcritical.

As shown in Figure 4.2a, a classical transcritical CO_2 VCC consists of four essential components: compressor, gas cooler, expansion valve, and evaporator. The cycle is governed by four key thermodynamic processes (Figure 4.2b). From state 1 to 2 (compression), CO_2 enters the compressor as a superheated vapor at relatively low pressure and is compressed to supercritical conditions, increasing both pressure and temperature; this process is ideally isentropic but is polytropic in practice due to irreversibilities. From state 2 to 3 (gas cooling), heat is rejected to the environment at approximately constant high pressure without a phase change, producing a marked drop in temperature and enthalpy. From state 3 to 4 (expansion), the high-pressure fluid undergoes an isenthalpic expansion through an expansion valve, causing a sharp pressure and temperature drop with partial vaporization. Finally, from state 4 to 1 (evaporation), the refrigerant absorbs heat from a low-temperature source at low pressure, fully evaporates, and increases in

enthalpy to close the cycle.

While this section discusses a basic single-stage transcritical CO_2 cycle, several architectural modifications have been developed to address CO_2's challenging characteristics and enhance performance. Some of these are mentioned next.

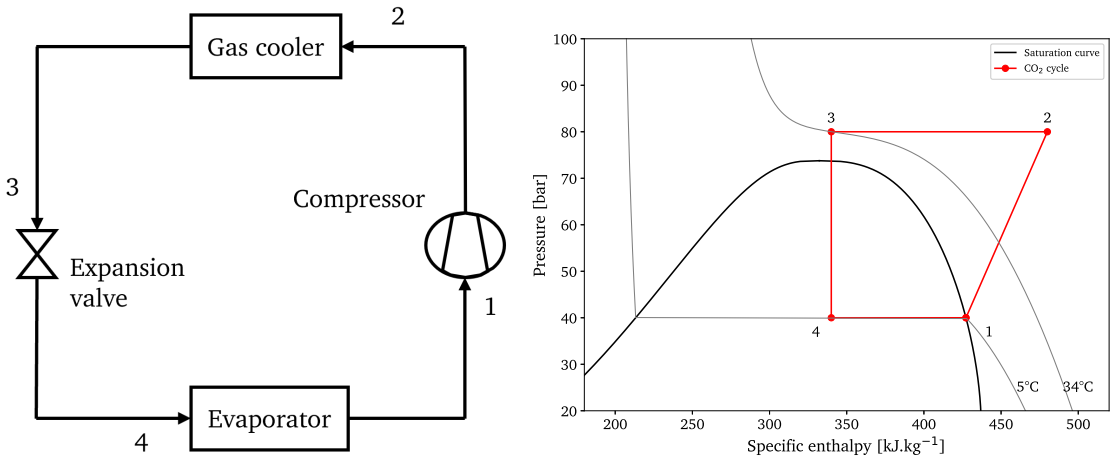

(a) (b)

Figure 4.2: Transcritical CO_2 (a) basic cycle scheme and corresponding (b) p–h diagram.

4.2.2 Architectural modifications

Several modifications to single-stage cycles have been proposed to enhance performance. For instance, the use of two-stage instead of single-stage CO_2 cycles dates back to the 19th century, primarily to mitigate the high discharge temperatures and pressures that place mechanical stress on compressors (Kim et al. (2004)). In such configurations, a flash tank (phase separator) or compressor intercooling is often incorporated to lower the suction temperature of the second-stage compressor. Lorentzen (1994) outlined several advanced CO_2 cycle architectures, including two-stage cycles, cycles with internal cooling, and cycles employing an expander in place of an expansion valve.

In particular, Robinson and Groll (1998) proposed expansion work recovery using an expander to reduce throttling losses caused by large pressure drops, reporting a 25% improvement in COP. Cecchinato et al. (2009) showed that combining intercooling with an internal heat exchanger in a two-stage cycle resulted in COP gains of nearly 30%. Building on the two-stage concept, Agrawal et al. (2007) optimized a transcritical CO_2 cycle and found that flash-gas bypass configurations outperformed those using flash tanks or compressor intercooling. On the other hand, Elbel and Hrnjak (2008) experimentally demonstrated that ejector integration yielded a 7% COP improvement.

Overall, although CO_2 is an environmentally friendly refrigerant needed to reduce global warming and ozone-layer depletion, its challenging characteristics make it a unique fluid that must be handled with tailored architectures. In the following, we turn our attention to the targeted three-stage CO_2 TCHP developed by Boostheat, which integrates and adapts several of these architectural enhancements.

4.3 TCHP architecture and experimental setup

This section introduces the Boostheat thermal compressor heat pump (TCHP)—a three-stage transcritical CO_2 cycle for residential heating—and its experimental setup. We first present the process architecture and operating principle, along with the experimental conditions. The unit under test is a commercial product installed in the Boostheat laboratory; consequently, instrumentation is limited to production-grade sensors. We then specify these sensors and their corresponding measurements, as well as the component characteristics. Finally, the actuators and system inputs, together with their interactions with outputs, are described, and the energy expressions to be used later for model validation and control assessment are defined.

4.3.1 System architecture and operation

As illustrated in Figure 4.3a, the cycle of a TCHP consists of three TCs, three buffers (BUFs), a gas cooler (GC), an evaporator (EV), an internal heat exchanger (IHX), a flash tank (FT), high- and low-pressure expansion valves (HPV and LPV), one way valve (OWV), and a fume heat exchanger (FHX). The process occurs on the CO_2, water, TCs, and glycol sides as follows:

On the CO_2 side (green), the state changes are illustrated in the T–s diagram shown in in Figure 4.3b: At evaporation pressure, CO_2 enters the TC1 and exits at a higher pressure. It is then cooled inside BUF1 by a water flow and mixed with the vapor exiting the FT through a OWV at point MIX before entering the TC2. The CO_2 then exits at a higher intermediate pressure and is cooled again inside BUF2 before entering the TC3. The pressure is then dampened in BUF3 which has no passage for circulating water. In fact, all BUFs after each TC also act dampers for the pressure waves resulting from compression. At its highest pressure level and temperature, CO_2 rejects heat into the water entering the GC. It is then cooled again while passing through one side of the IHX, being cooled by the CO_2 exiting the EV from the other side. After exiting the IHX, the CO_2 refrigerant is expanded in the HPV and enters the FT. There, the gaseous fraction is re-injected to the suction of the TC2 through a OWV, while the remaining liquid expands in the LPV before entering the EV, where it evaporates and becomes superheated. Finally, additional heat is absorbed in the IHX, completing the cycle and returning the fluid to its initial state.

On the water side (red), heat is recovered from several heat exchangers. A smaller portion of the water flow is directed to the BUFs and the TCs, where it is further subdivided between the first two BUFs and then collected before passing through the TC coolers in sequence from the first to the third stage. The larger portion of the return water goes to the gas cooler, after which the two streams mix again before entering the FHX, where the combustion fumes are cooled. The heated water finally leaves as supply water to the user's end.

On the TCs side: The top parts of the first two TCs (i.e., the heaters) are connected to a burner fan, which delivers a methane/air mixture or burning gas (orange) to the top surfaces of their heaters, where it is ignited to heat the surfaces. The resulting fumes (in gray) from both chambers are collected on the top of TC3 and used to heat its heater surface. The fumes are then directed to the FHX, where they are cooled before finally

leaving.

On the glycol side (blue): The EV is heated by a glycol mixture of monopropylene glycol and water (MPG). MPG is selected for its low freezing point, allowing the mixture to withstand low outdoor temperatures without solidifying.

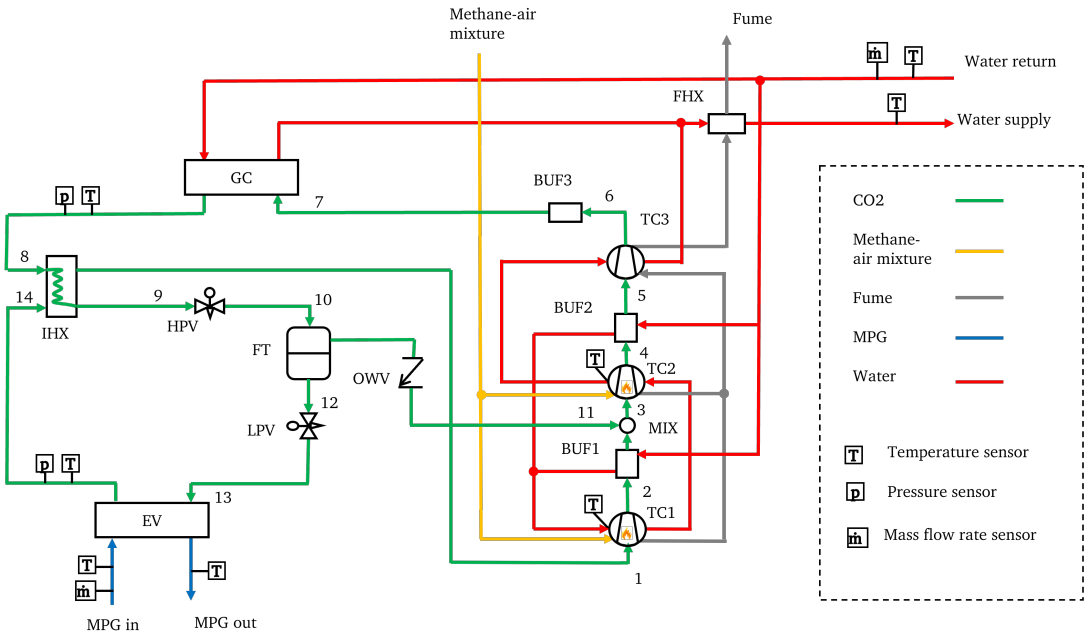

(a)

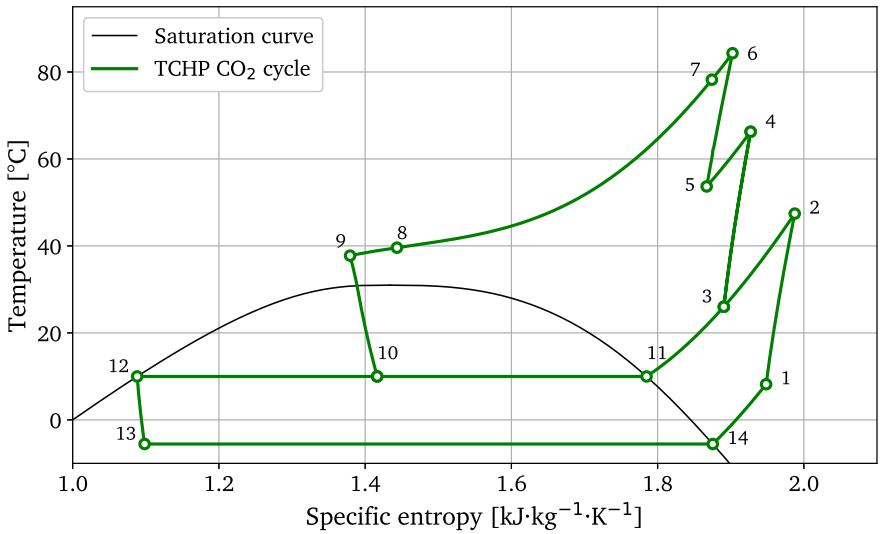

(b)

Figure 4.3: TCHP (a) test Bench layout with the corresponding (b) T-s diagram of CO_2 in the cycle (maybe add numbering).

4.3.2 Experimental conditions

To mimic real environmental or household conditions around the TCHP during testing, two other test benches were designed and installed at the Boostheat laboratory for water and glycol mixture circulation. Glycol mixture interacts with the evaporator, so its temperature is intended to be close to the outdoor temperature, therefore it is cooled using

a chiller to regulate its temperature to a desired testing point. While for the heating the water in the TCHP, the water interacts with a cold-water source to simulate a real house conditions.

4.3.3 Components

TCHP components and fluids (Figure 4.3a) characteristics are summarized in Table 4.1.

Component	Type	Volume [L]	Area [m^2]
Working fluid	CO_2	–	–
Primary heat source fluid	Burning gas	–	–
Secondary heat source fluid	Glycol mixture	–	–
Heat sink fluid	Water	–	–
IHX	Vessel tube	2.5	–
BUF3	Vessel tube	1.8	–
BUF1 & 2	Vessel tube	2.5	–
FT	Vertical tank	2	–
GC	Brazed plates	1.65	1.0422
EV	Brazed plates	1.917	1.235
LPV, HPV	Electronic expansion valves	–	–

Table 4.1: TCHP specifications of components and fluids.

4.3.4 Measurements

The sensor types deployed on the TCHP (Figure 4.3a) and their corresponding accuracies are summarized in Table 4.2. Pt100 sensors are used on the return and supply water lines as well as at the inlet and outlet of the glycol circuit, chosen for their high precision. On the CO_2 cycle, Type T thermocouples are placed at the exits of the gas cooler and evaporator, while Type K thermocouples are used to measure the heater temperatures, as they can withstand high operating temperatures. A Huba Control Type 520 sensor is used to measure the pressures at the evaporator and gas cooler exits. A Huba Control Type 200 vortex sensor is used to measure the volumetric flow in the water and glycol circuits. The following section discusses the cycle actuators and the influence of the inputs on the TCHP outputs or measurements.

Sensor	Accuracy
Pt100 (RTD)	$\pm(0.15 + 0.002T)$ °C
Type T thermocouple	± 1 °C
Type K thermocouple	± 1.5 °C or $\pm 0.4\%$
Huba Control Type 520	$\pm 0.3\%$
Huba Control Type 200	$\pm 1\%$

Table 4.2: TCHP test bench deployed sensor types and accuracies.

4.3.5 Actuators and system inputs

The TCHP system's processes and outputs are influenced by several inputs, which are depicted in Figure 4.4. The coupling between the inputs and the outputs is explained in the following statements:

- The burner fan speed (ω_{bf}) regulates the flow rate of the burning gas (primary heat source), thus influencing the heater temperatures (T_{h1} and T_{h2}), which consequently affect the mass flow rates, discharge temperatures, and heat rejected by the coolers in the TCs (As we saw in Part I). Also, ω_{bf} also has a direct influence on the heat exchanged with the fume heat exchanger, since it affects the fume temperature and flow rate. Therefore, ω_{bf} is considered a crucial input that influences the whole system operation.

- The percentage opening of the high-pressure valve (φ_{hpv}) influences the thermodynamic conditions (the mass flow rate) at the exit of the gas cooler, thus affecting the gas cooler exit temperature (T_8) and the high pressure (p_8).

- The mass flow rate of CO_2 entering the evaporator is directly affected by the percentage opening of the low-pressure valve (φ_{lpv}), which directly affects the superheat (ΔT_{sh}), defined as the difference between the TC1 suction temperature (T_1) and the evaporator outlet temperature (T_{14}).

- The motor speeds of the three TCs ($\omega_{\mathrm{m1}}, \omega_{\mathrm{m2}},$ and ω_{m3}), where the first affects the thermodynamic condition at the outlet of the evaporator and the second two affect the thermodynamic conditions at the inlet of the gas cooler. They also influence the heat recovered by the coolers. However, their influence is less critical than the burner fan speed, considering that TCHP operation mainly relies on gas rather than electricity.

- On the evaporator side, the secondary fluid inputs are the glycol mixture mass flow rate ($\dot{m}_{\mathrm{mpg}}$) and the inlet temperature ($T_{\mathrm{mpg,in}}$). The mass flow rate is typically regulated to maintain a prescribed temperature difference between the inlet and outlet glycol streams, while the inlet temperature is set according to the outdoor conditions emulated in the test bench.

- The water circulation through several TCHP heat exchangers is governed by the water mass flow rate ($\dot{m}_{\mathrm{w}}$) and the return water temperature ($T_{\mathrm{w,ret}}$). The mass flow rate is usually regulated to guarantee a certain temperature difference between the return and supply water, while the return temperature depends on the heating demand imposed on the system.

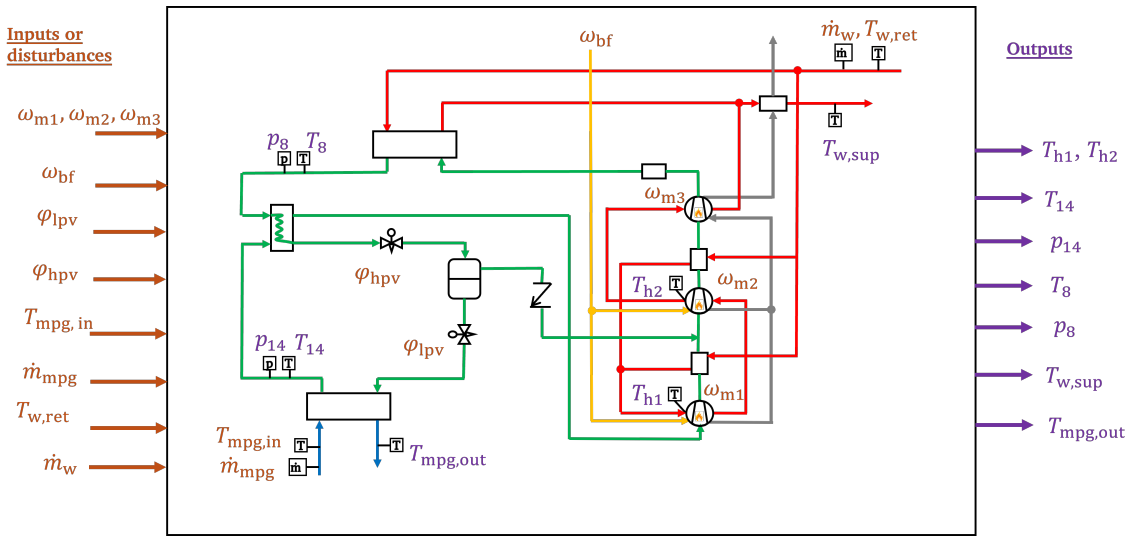

Figure 4.4: TCHP scheme showing the inputs and the outputs.

4.3.6 Energy Expressions

In an electrically driven heat pump, the COP is defined as the ratio between the total heat recovered and the electric power consumed by the cycle. In this work, heat is the primary source of energy. With a small contribution of electricity compared to heat, and for simplicity, a TCHP is evaluated with a thermal COP (COP_{th}), defined as the ratio between the total heat recovered ($\dot{Q}_{\mathrm{rec,tot}}$) and the fuel thermal power consumed ($\dot{Q}_{\mathrm{fuel}}$):

$$COP_{\mathrm{th}} = \frac{\dot{Q}_{\mathrm{rec,tot}}}{\dot{Q}_{\mathrm{fuel}}} \tag{4.1}$$

The circulating water recovers heat from several heat exchangers (Figure 4.3a), so the total heat recovered is calculated as follows:

$$\dot{Q}_{\mathrm{rec,tot}} = \dot{Q}_{\mathrm{gc}} + \dot{Q}_{\mathrm{k1}} + \dot{Q}_{\mathrm{k2}} + \dot{Q}_{\mathrm{k3}} + \dot{Q}_{\mathrm{buf1}} + \dot{Q}_{\mathrm{buf2}} + \dot{Q}_{\mathrm{fhx}} \tag{4.2}$$

which can also be calculated from the temperature difference between the return and supply water:

$$\dot{Q}_{\mathrm{rec,tot}} = \dot{m}_{\mathrm{w}} c_{p_{\mathrm{w}}} (T_{\mathrm{w,sup}} - T_{\mathrm{w,ret}}) \tag{4.3}$$

while the fuel thermal power is given by:

$$\dot{Q}_{\mathrm{fuel}} = \dot{m}_{\mathrm{CH_4}} \cdot \mathrm{LHV}_{\mathrm{CH_4}}, \tag{4.4}$$

where $\dot{m}_{\mathrm{CH_4}}$ is the methane mass flow rate, correlated here as a function of burner fan speed:

$$\dot{m}_{\mathrm{CH_4}} = \left(\omega_{\mathrm{bf}} - 1183\right) 2.49 \times 10^{-8} \tag{4.5}$$

where the methane lower heating value is $\mathrm{LHV}_{\mathrm{CH_4}} = 50\ \mathrm{MJ\,kg^{-1}}$. An excess-air factor of $EX_{\mathrm{air}} = 0.2$ is assumed. The resulting fume mass flow rate (equal to the air–fuel mixture mass flow rate by conservation of mass) is:

$$\dot{m}_{\mathrm{fume}} = \left[1 + (1 + EX_{\mathrm{air}})\, r_s\right] \dot{m}_{\mathrm{CH_4}} \tag{4.6}$$

where $r_s = 17.125$ is the stoichiometric air-to-fuel mass ratio for complete combustion of methane. On the evaporator side, the heat-exchange rate is computed from the temperature difference of the glycol mixture between inlet and outlet:

$$\dot{Q}_{\mathrm{ev}} = \dot{m}_{\mathrm{mpg}}\, c_{p_{\mathrm{mpg}}}\, (T_{\mathrm{mpg,in}} - T_{\mathrm{mpg,out}}) \tag{4.7}$$

These equations quantify TCHP performance and will be used later to validate the model and to evaluate the control strategy. With the system architecture, instrumentation, and performance metrics defined, we now present the experimental datasets used for model development and validation.

4.4 Collected experimental data

This section describes the data collected at Boostheat for model development and validation. The data are divided into two types: (1) transient—open-loop step tests used to capture the system's dynamic behavior. These data were monitored and collected by us, and their procedure and architecture have already been described in Section 4.3.1; and (2) steady-state—15 samples of TCHP outputs at different operating conditions. These data were collected by colleagues at Boostheat on a similar TCHP cycle to the one introduced, but equipped with additional sensors. It was analyzed in Hosseinzade and Sayyaadi (2015).

4.4.1 Transient

The TCHP is excited by step tests on the inputs, with the aim of capturing the transient responses of the corresponding outputs shown in Figure 4.4. For plotting, we focus on the variables most relevant to control development: burner fan speed ω_{bf} (consequently heater temperatures T_{h1} and T_{h2}), low-pressure valve opening φ_{lpv}, and high-pressure valve opening φ_{hpv}. For the displayed outputs, we select those most affected by each varied input (Section 4.3.5), mainly for the sake of clarity and simplicity. Thus, we present here only a sample of the transient tests that are most relevant.

In each test, one input from Table 4.3 is varied, while the corresponding output responses from Table 4.4 are monitored, and the remaining inputs are fixed at the constant values given in Table 4.5.

Variable	Range	Unit
ω_{bf}	2000–9500	rpm
φ_{hpv}	11–100	%
φ_{lpv}	11–100	%
ω_{m1}	60–240	rpm
ω_{m2}	60–240	rpm
ω_{m3}	60–240	rpm

Table 4.3: TCHP manipulated input variables, operating ranges, and units.

The varied low-pressure valve opening φ_{lpv} and corresponding outputs are plotted in Figure 4.5. Closing the valve causes a decrease in mass flow rate entering the evaporator.

Variable	Range	Unit
T_{h1}	300–800	°C
T_{h2}	300–800	°C
$T_{\mathrm{w,sup}}$	24.5–49.6	°C
$T_1 - T_{14}$	0–14	K
p_8	64.4–86.3	bar

Table 4.4: TCHP controlled output variables, typical value ranges, and units.

Parameter	Value	Unit
ω_{bf}	4411	rpm
$T_{\mathrm{w,ret}}$	28	°C
$T_{\mathrm{mpg,in}}$	6	°C
$\dot{m}_{\mathrm{mpg}}$	280	g.s^{-1}
$\dot{m}_{\mathrm{w}}$	230	g.s^{-1}
ω_{m1}	150	rpm
ω_{m2}	150	rpm
ω_{m3}	150	rpm
φ_{hpv}	50	%
φ_{lpv}	50	%

Table 4.5: TCHP inputs kept constant during transient tests.

This decreases the low pressure and consequently increases the superheat, considering that the secondary heat source temperature (glycol mixture inlet temperature) is at a constant value. However, opening the valve reverses this influence.

The varied high-pressure valve opening φ_{hpv} and corresponding outputs are plotted in Figure 4.6. Closing the valve causes a decrease in mass flow rate leaving the gas cooler. With the accumulation of mass inside, the high pressure increases and consequently the gas cooler outlet temperature decreases, considering the return water temperature is constant. However, opening the valve reverses this influence.

The burner fan speed ω_{bf} is a crucial input, considering it is the primary source of heat driving the TCs. The step tests on the burner fan speed cause a very slow variation in the heater temperatures, as shown in Figure 4.7. A decrease step in burner fan speed causes a slow decrease in heater temperatures. This results in an increase of evaporator pressure due to reduction in leaving flow rate and a decrease of gas cooler pressure due to a decrease of entering flow rate. A limitation of the transient dataset is that inputs were varied one at a time, which restricts the excitation of multivariable interactions and limits validation of coupled dynamics. In addition, the tested unit is a commercial product with production-grade instrumentation, so several potentially informative measurements are unavailable. These limitations are addressed by the steady-state dataset described in the next section.

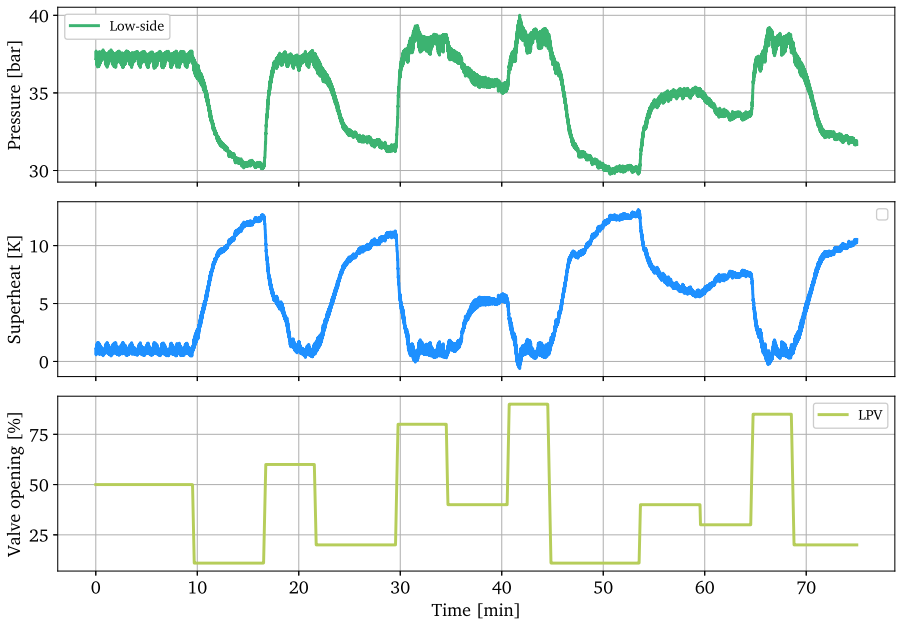

Figure 4.5: TCHP experimental data from varying the low-pressure valve opening.

4.4.2 Steady-state

The performance of a fully automated TCHP was monitored at different outdoor temperatures. Its layout is the same as in Figure 4.3a, but the conducted test employed more sensors than those mentioned in Section 4.3.4. The collected steady-state data were previously analyzed by Fallahsohi (2023) and are used in this work for tuning model correlations and validating steady-state predictions. These tests are particularly important because the TCHP was fully automated, operating under various conditions. Consequently, validation with this steady-state dataset is both valuable and complementary to validation with transient data where each condition was changed one at a time.

To facilitate later reference during model tuning and validation, the steady-state inputs and outputs are reported in the following tables: the TCHP inputs and outputs in Table 4.6, the operating data of TCs in Table 4.7, the data around fume heat exchanger in Table 4.8, and the overall performance indicators in Table 4.9.

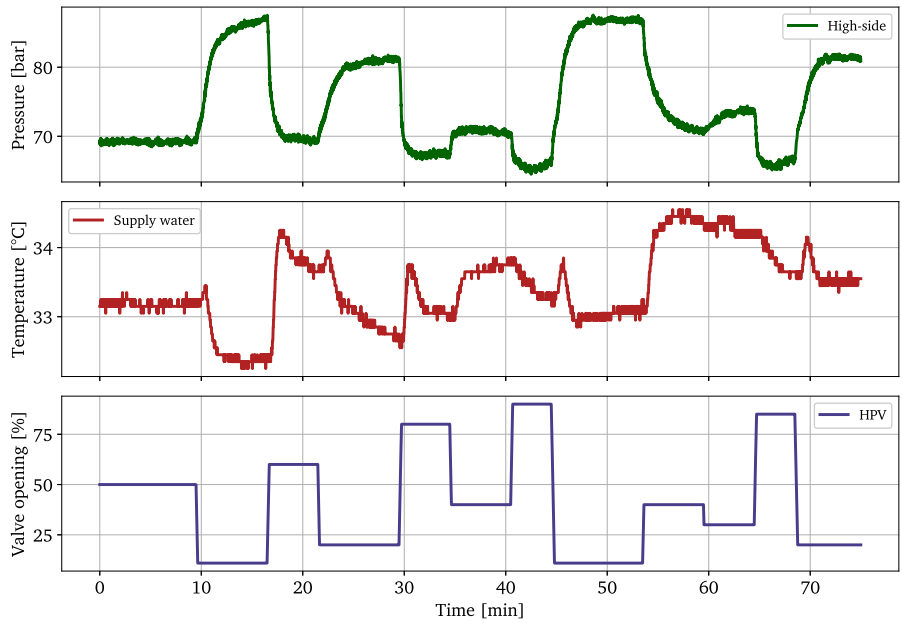

Figure 4.6: TCHP experimental data from varying the high-pressure valve opening.

Sample	φ_{lpv} [%]	φ_{hpv} [%]	ω_{bf} [rpm]	T_{h1}&T_{h2} [°C]	p_{14} [bar]	p_8 [bar]	T_{14} [°C]	T_8 [°C]
1	48	37	3226	521	35	63	6	23
2	54	46	4285	660	31	65	1	25
3	54	51	5084	731	29	66	-1	26
4	56	55	6000	800	27	67	-2	26
5	57	60	6245	800	27	68	-3	28
6	45	44	6000	800	25	69	-6	28
7	37	37	5555	800	23	69	-8	28
8	100	11	3000	533	35	67	9	27
9	93	46	3900	605	35	70	6	29
10	46	53	4900	699	33	76	4	31
11	48	54	6000	783	31	79	2	33
12	54	43	6200	800	30	82	1	33
13	65	11	5800	800	28	84	-3	35
14	29	11	5400	800	26	89	-4	38
15	13	11	5200	800	25	88	-6	40

Table 4.6: TCHP steady-state samples: valve openings, burner fan speed, heater temperature, pressures, and outlet temperatures.

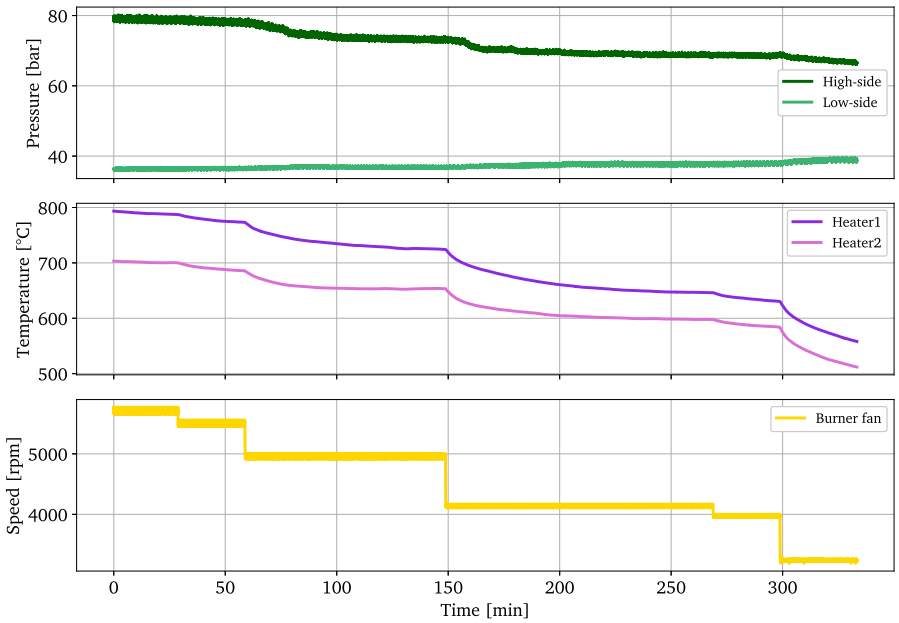

Figure 4.7: TCHP experimental data from varying Burner fan speed.

Sample	$\dot{m}_{tc1}$ [g.s^{-1}]	$T_{tc1,dis}$ [°C]	$\dot{Q}_{k1}$ [kW]	$\dot{m}_{tc2}$ [g.s^{-1}]	$T_{tc2,dis}$ [°C]	$\dot{Q}_{k2}$ [kW]	$\dot{m}_{tc3}$ [g.s^{-1}]	$T_{tc3,dis}$ [°C]	$\dot{Q}_{k3}$ [kW]
1	9	38.6	0.9	12.9	55.8	1	12.9	37.6	0.3
2	11.6	46.8	1	15.8	62.1	1.1	15.8	45.6	0.5
3	12.4	51.9	1.2	16.9	65.1	1.2	16.9	50.7	0.6
4	13.4	56.1	1.3	18.4	66.8	1.3	18.4	54.8	0.8
5	12.3	58.8	1.3	19.7	71	1.6	19.7	57.2	1
6	7.3	58	1.3	14.2	68.8	1.3	14.2	56.2	0.8
7	5	58	1.3	11.1	69.1	1.3	11.1	55.7	0.8
8	3	47.6	0.7	5.7	67.2	1.2	5.7	45.7	0.3
9	5.9	55.2	0.9	12.5	73.7	1.3	12.5	53.5	0.4
10	8.8	62.6	1.3	15.6	74.8	1.2	15.6	60.7	0.6
11	10	69.4	1.5	17	78.4	1.3	17	67	0.8
12	8.4	72.4	1.5	14.3	82.4	1.4	14.3	69.3	0.8
13	5.3	75.2	1.6	8.8	88.6	1.6	8.8	70.8	0.8
14	2.3	74.6	1.6	6.2	86.4	1.5	6.2	69	0.8
15	0.8	73.9	1.7	5.2	84.4	1.3	5.2	67.7	0.8

Table 4.7: TCHP steady-state samples: TC1, TC2, and TC3 mass flow rates, discharge temperatures, and cooler heat transfer rates.

Sample	$T_{\text{fhx,fume,in}}$ [°C]	$T_{\text{fhx,w,in}}$ [°C]	$T_{\text{fhx,w,out}}$ [°C]	$T_{\text{fhx,fume,out}}$ [°C]	$\dot{m}_{\text{fume}}$ [g.s^{-1}]	$\dot{m}_{\text{w}}$ [g.s^{-1}]	$\dot{Q}_{\text{fhx}}$ [kW]
1	129.3	26.5	26.7	31.3	0.9	283.3	0.2
2	204.5	28.1	28.3	36.5	1.4	330	0.3
3	255.8	29	29.2	40.1	1.7	361.7	0.3
4	312.8	29.7	30.2	43.9	2.1	388.3	0.8
5	273.4	30.2	30.6	45.2	2.2	425	0.7
6	304.1	30.2	30.5	44.4	2.1	470	0.7
7	295.6	30.3	30.5	42.9	1.9	513.3	0.6
8	136.6	31.5	31.9	35.5	0.8	130.3	0.2
9	183	34.7	35.3	41.8	1.2	166.7	0.4
10	238.9	38.2	39.3	48.7	1.6	186.7	0.8
11	301.6	40.1	41.6	54.3	2.1	205	1.3
12	309.7	40.8	42.4	55.6	2.2	216.7	1.5
13	301.3	41.7	42.9	55.1	2	233.3	1.2
14	290.6	43.1	44.4	55.3	1.8	250	1.4
15	281.1	44.4	45.6	55.9	1.8	258.3	1.2

Table 4.8: TCHP steady-state samples: fume heat exchanger inlet/outlet fume temperature, inlet/outlet water temperature, fume and water mass flow rates, and recovered heat.

Sample	$T_{\text{w,ret}}$ [°C]	$T_{\text{w,sup}}$ [°C]	$T_{\text{mpg,in}}$ [°C]	$T_{\text{mpg,out}}$ [°C]	$\dot{Q}_{\text{rec,tot}}$ [kW]	COP_{th} [-]	$\dot{Q}_{\text{ev}}$ [kW]	$\dot{Q}_{\text{gc}}$ [kW]
1	22.8	27.1	5.4	2.2	5.1	2.1	1.9	1.7
2	24	28.8	2.4	-2.4	6.6	1.8	2.6	2.3
3	24.7	29.8	0.4	-5.2	7.7	1.6	2.8	2.3
4	25.1	30.6	-0.7	-7	8.9	1.5	3.1	2.3
5	26.5	31.6	-3.6	-6	9.1	1.5	2.8	2.7
6	27	31.5	-7.6	-9.1	8.9	1.5	1.7	1.5
7	27.7	31	-10.7	-11.8	7.1	1.4	1.2	0.9
8	26	31.9	8.1	7.4	3.2	1.5	0.7	0.6
9	28.3	35	5	3.5	4.7	1.4	1.3	1
10	30.5	38.8	2.2	0.7	6.5	1.5	1.9	1.7
11	32.4	41	0.2	-1.8	7.4	1.3	2.1	2.1
12	33.4	41.7	-0.8	-3.1	7.5	1.2	1.8	1.7
13	36.5	42.2	-3.5	-6.1	5.6	1	1.2	0.9
14	38.3	43.6	-7.6	-8.6	5.5	1.1	0.5	0.4
15	40.1	44.6	-9.9	-10.4	4.9	1	0.2	0.2

Table 4.9: TCHP steady-state samples: return and supply water/glycol temperatures, total recovered heat, thermal COP, and evaporator and gas cooler heat-transfer rates.

4.5 Conclusion

In this chapter:

- Synthetic refrigerants have taken over natural ones for the last century. However, environmental harm caused by these has forced serious measures to revive natural refrigerants in general, and CO_2 in particular, mainly for their environmentally friendly characteristics. However, its challenging characteristics, especially the low critical temperature $T_{\text{crit}} = 31.1°\text{C}$ and high critical pressure $p_{\text{crit}} = 73.8$ bar, have made it difficult to valorize its usage with conventional systems.

- A basic single-stage transcritical CO_2 VCC was described, and architectural modifications from the literature were outlined—including multistage cycles, flash tanks, and internal heat exchangers—that aimed to enhance the performance of these cycles.

- The Boostheat three-stage CO_2 TCHP cycle was introduced. The process and test bench were described, along with the main components and available instrumentation. The actuators and system inputs were listed and their influence on key outputs was outlined; the major actuators are the burner-fan speed and the low- and high-pressure valve openings. Energy expressions based on measurements were defined, including the thermal COP and the decomposition of total recovered heat.

- Two complementary datasets were identified: (1) transient data from open-loop step tests where one input is varied at a time, with representative samples shown to illustrate internal TCHP transient responses from key inputs and corresponding outputs; and (2) steady-state data from a fully automated TCHP over different operating conditions, collected by colleagues, which was richer in terms of measurements due to the presence of more equipped sensors.

In overall, this chapter introduced transcritical CO_2 cycles in general and the targeted three-stage TCHP in particular, providing an understanding of its operation and the relation between inputs and outputs. Two complementary datasets—transient step tests and steady-state samples—were curated to capture both dynamic responses and equilibrium conditions. The observed multivariable couplings (e.g., between ω_{bf}, φ_{hpv}, φ_{lpv} and $T_{\mathrm{w,sup}}$, p_8, ΔT_{sh}), together with strict operating constraints on pressures and temperatures, motivate the development of a dynamic, physics-based model capable of reproducing both steady-state and transient behavior. Such a model forms the natural bridge between data collection and controller synthesis. Accordingly, the next chapter develops and validates a dynamic model of the three-stage CO_2 TCHP, calibrated with the steady-state dataset and stress-tested against the transient dataset.

Chapter 5

Dynamic model for the TCHP

Abstract

A simulation model is essential for any optimization task, whether it concerns system design, architecture selection, or the development of control strategies. While a steady-state model is sufficient for the first two tasks, a dynamic model is indispensable for control design. This chapter therefore develops a dynamic model of the targeted Boostheat TCHP introduced in the previous chapter and validates it using the previously collected transient and steady-state experimental data.

Section 5.1 reviews dynamic modeling approaches for vapor compression cycles (VCCs) in general, and on transcritical CO_2 cycles in particular. These approaches are commonly grouped into two families: finite-volume (FV) and moving-boundary (MB). For the TCHP, Section 5.2 presents the component submodels, with some parts described by differential equations and others by algebraic relationships. The differential part adopts the FV method, while the quasi-static part is tuned using the TCHP steady-state data introduced in the previous chapter. In Section 5.3, the components are assembled into the final model architecture and the numerical solution procedure is outlined. Finally, Section 5.4 validates the model using the steady-state and transient datasets introduced in the previous chapter.

5.1 Literature review of dynamic models for vapor compression cycles

The first dynamic models of VCCs date to the 1980s: Chi and Didion (1982) developed a first-order lumped-parameter model for a residential air-to-air heat pump, and MacArthur and Grald (1989) presented a finite-volume (FV) model of a heat pump with mass, momentum, and energy balances; the model's transient responses were validated against experiments. After three decades of VCC dynamic model development, comprehensive reviews by Rasmussen (2012) and Afram and Janabi-Sharifi (2014) summarized FV, moving-boundary (MB), and data-driven approaches for VCCs. In practice, these are typically applied to the heat exchangers, while the compressor and expansion valve are treated with algebraic relations: heat exchangers dominate the slow dynamics, whereas the compressor and valve respond more rapidly and are reasonably approximated by

steady-state maps, eventually resulting in a simpler model version. Much of this literature is ultimately motivated by control design.

5.1.1 Physics-based: Finite volume and moving boundary methods

Physics-based models are often used for real-time representation of a real system. Due to their physical nature, they can be used to investigate ranges that are not achievable with real experiments. The most famous physics-based dynamic models are the FV and MB methods.

In general, FV models are built by directly applying conservation equations to discrete CVs. The result is a high-order dynamic model that is parametrically rich and capable of representing transient behavior in detail, as demonstrated by Eborn (2001). Unlike the MB approach, which uses the mean void fraction to represent the two-phase region, the FV method assumes average fluid properties within each CV, making the prediction of refrigerant charge heavily dependent on the discretization level. Bendapudi et al. (2002) applied the FV method to model a centrifugal liquid chiller, achieving high accuracy in steady-state predictions and good agreement with transient trends. However, simulating this model can be computationally slow due to stiffness arising from the coupling between pressure and mass flow rate. Quoilin (2011) addressed this issue by assuming a uniform pressure across all CVs, allowing the pressure variation to be computed only once; the resulting pressure drops were then estimated using quasi-static correlations. More recently, Husmann and Aschemann (2022) developed a dynamic FV-based model for a VCC, likewise adopting the uniform-pressure approach—referred to as the vanishing-pressure method—and additionally providing a nonlinear state-space formulation.

The MB approach is often used as a simpler alternative to FV modeling for simulating the transient behavior of VCCs. While FV models gain accuracy from fine spatial discretization (Bendapudi et al. (2008)), MB models aim to capture the essential dynamics of phase-change heat exchangers using lumped parameters and by tracking the moving boundaries between fluid regions (liquid, two-phase, vapor). Rasmussen and Alleyne (2006) provided a technical report in which they detailed the derivation of MB models for evaporators and condensers under different phase-change conditions. A constraint of using the MB approach is that the phases of the working fluid at the component exits must be assumed beforehand. This can also be an issue if the phase is changing between single- and two-phase regions or between subcritical and supercritical states. To deal with this, McKinley and Alleyne (2008) proposed a switching algorithm to accommodate different representations of a component according to phase.

An attempt to compare both methods was made by Bendapudi et al. (2008) on centrifugal chillers, concluding that while the FV method resulted in longer computation time compared to MB, it was more robust. In another comparison attempt, Desideri et al. (2016) concluded that MB achieves comparable performance to FV with reduced computation time, without highlighting its lower robustness. Overall, both models obey physical laws and have proven their reliability in predicting real VCC responses. .

5.1.2 Dynamic models for transcritical CO_2 cycles

In the literature, several dynamic models are derived for transcritical CO_2 cycles in particular. For instance, Pfafferott and Schmitz (2004) developed a Modelica-based transient model using mass and energy balances discretized via the FV method, showing good agreement in steady-state and transient regimes. Rasmussen and Alleyne (2004) derived a reduced-order model from a detailed 11th-order nonlinear MB model by isolating fast and slow dynamics, resulting in a simplified 5th-order version suitable for control design. Zheng et al. (2015) created a MB model of a transcritical CO_2 ejector cycle incorporating variable ejector efficiencies, accurately capturing behavior under changing valve and ejector settings. Using Simscape, Ko et al. (2020) developed an FV dynamic model of a transcritical CO_2 heat pump and validated transient mass flow, compressor power, pressures, and COP with good agreement. Diniz et al. (2021) presented a one-dimensional distributed FV model for a solar-assisted CO_2 water-heating heat pump, showing that lower flow rates increase outlet and compressor temperatures. Artuso et al. (2021) developed and validated an FV dynamic model for a reversible CO_2 air-to-water heat pump for heating, cooling, and district water heating. Wolscht et al. (2024) provided a validated Modelica model of a 35 MW transcritical CO_2 heat pump for district heating, using segmented heat exchangers and property tables to match plant transients.

Most of the implementations were based on object-oriented models developed in simulation environments such as Dymola or Modelica, and were generally applied to conventional electric heat pumps with a maximum of two stages. In contrast, the TCHP model developed in this work is built entirely from scratch in Python. The targeted application is a thermally driven system with three stages of compression and a specifically designed thermal compressor.

In this chapter, we develop a dynamic model of the TCHP cycle, a multi-stage CO_2 system with several heat exchangers. A MB formulation depends on the refrigerant regime in the high-pressure heat exchanger (condenser/gas cooler), which must be known or switched a priori. Because the preferred operating range often reaches the supercritical regime, the regime cannot be guaranteed in advance. To avoid hybrid MB models with regime switching (McKinley and Alleyne (2008)), we adopt the FV method. A second motivation is the robustness of the FV approach, which is particularly important for a multi-stage TCHP with tightly coupled component dynamics.

5.2 TCHP hybdrid dynamic model

Each component of a TCHP cycle is first modeled individually and then assembled into a coupled hybrid model consisting of differential equations for the dynamic parts and quasi-static surrogate/algebraic models for the remaining parts. The final model is referred to as the TCHP hybrid (TCHP-HYB) model throughout the remainder of the thesis.

In conventional electrically driven heat pump systems, the expansion valve and compressor are often assumed to operate in steady state, as their dynamics are much faster than those of the heat exchangers (Rasmussen and Alleyne (2006)). Consequently, they are typically represented quasi-statically, while the wall and secondary fluid temperatures in the evaporator and gas cooler (or condenser) are described by differential equations

that dominate the system's transient response. This approach reduces complexity and mitigates numerical stiffness.

In a TCHP, however, this assumption no longer holds: the TCs exhibit the slowest dynamics in the cycle, primarily due to the high thermal inertia of their heaters. This inertia causes gradual variations in the working fluid's mass flow rate, temperature, and pressure. Fully representing the TC dynamics would be computationally expensive, so we instead treat the heater temperature—which evolves slowly—as an input variable (as used in Chapter 3). By selecting heater temperature as the input, the TCs can be modeled using quasi-static models without losing predictive accuracy for the slow dynamics of interest. However, to reach a complete independent TCHP model, the heater-temperature dynamics as a function of burner-fan speed must be modeled separately.

The valves exhibit significantly faster dynamics than the heat exchangers due to their fast response. The fume heat exchanger—being outside the main CO_2 cycle—has a faster response due to the direct influence of burner-fan speed.

As a result, the valves, fume heat exchanger, and TCs are modeled quasi-statically, while the dynamic behavior of the cycle heat exchangers, flash tank, and heater temperatures is captured using differential equations.

5.2.1 Differential equations of the TCHP-HYB model

This section is dedicated for the TCHP-HYB model components that are represented with differential equations.

5.2.1.1 Cycle heat exchangers

As shown in Section 4.3.1, a TCHP cycle incorporates several heat exchangers, including the gas cooler, evaporator, internal heat exchanger, and the first two buffers, all of which are dynamically represented. For modeling the heat exchangers, the following assumptions are made:

- Pressure drops are neglected on both the working-fluid and secondary-fluid sides.
- Heat conduction through the walls is neglected.
- Two-phase regions in the heat exchanger are homogeneous.
- The secondary fluids are assumed to be incompressible.

Each heat exchanger is spatially discretized using the FV method into N CVs with a corresponding i-axis, where each CV between adjacent solid lines represents uniform pressure p and enthalpy h. The mass flow rates $\dot{m}_{\mathrm{f}}$ are considered uniform between adjacent dashed lines, corresponding to the j-axis. For the CO_2 working fluid, the continuity principle yields the following expression for the time derivative of the density in the i-th CV:

$$a_{1i}\frac{\partial p_i}{\partial t} + a_{2i}\frac{\partial h_i}{\partial t} = \dot{m}_{\mathrm{f},j-1} - \dot{m}_{\mathrm{f},j} \tag{5.1}$$

While applying the energy conservation principle yields the following equation:

$$a_{3i}\frac{\partial p_i}{\partial t} + a_{4i}\frac{\partial h_i}{\partial t} = \dot{m}_{\mathrm{f},j-1}\, h_{j-1} - \dot{m}_{\mathrm{f},j}\, h_j - \dot{Q}_{\mathrm{f},i} \tag{5.2}$$

where the coefficients are defined as:

$$a_{1i} = V_i \left(\frac{\partial \rho_i}{\partial p_i}\right)_{h_i} \qquad a_{2i} = V_i \left(\frac{\partial \rho_i}{\partial h_i}\right)_{p_i} \tag{5.3}$$

$$a_{3i} = V_i \left[h_i \left(\frac{\partial \rho_i}{\partial p_i}\right)_{h_i} - 1 \right] \qquad a_{4i} = V_i \left[h_i \left(\frac{\partial \rho_i}{\partial h_i}\right)_{p_i} + \rho_i \right]. \tag{5.4}$$

These equations are adopted from Rossi and Braun (1999). Here, the thermodynamic derivatives $\left(\frac{\partial \rho}{\partial h}\right)_p$ and $\left(\frac{\partial \rho}{\partial p}\right)_h$ denote the partial derivatives of density with respect to enthalpy at constant pressure, and with respect to pressure at constant enthalpy, respectively. As reported by Quoilin (2011), these equations are stiff and thus result in slow solving. The author therefore proposed considering one mass variation per component, so that Equation (5.1) is applied one time per component, and pressure variations are equal across CVs:

$$\frac{\partial p_1}{\partial t} = ... = \frac{\partial p_i}{\partial t} = ... = \frac{\partial p_N}{\partial t} \tag{5.5}$$

The mass flow is thus uniform across all other CVs. In addition, no mass variation is considered in buffer 1 and the internal heat exchanger, so Equation (5.1) is not applied at these two components. For heat exchangers with water or glycol mixture as the secondary fluids, the temperature variation is described by:

$$\left(mc\frac{\partial T}{\partial t}\right)_{\text{sf},i} = \dot{Q}_{\text{sf},i} + \dot{m}_{\text{sf},j} h_{\text{sf},j} - \dot{m}_{\text{sf},j-1} h_{\text{sf},j-1} \tag{5.6}$$

In the internal heat exchanger, Equation (5.2) is applied to both sides as CO_2 flows in both. The temperature variation of the heat exchanger wall is modeled as:

$$\left(mc\frac{\partial T}{\partial t}\right)_{\text{wall},i} = -(\dot{Q}_{\text{f},i} + \dot{Q}_{\text{sf},i}) \tag{5.7}$$

The heat transfer rates for the working fluid (CO_2) and secondary fluid (water or glycol

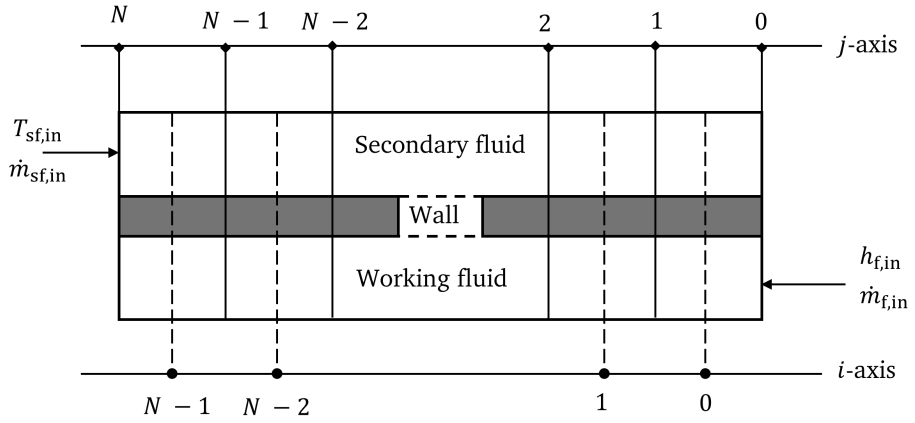

Figure 5.1: Heat exchanger spatial discretization into N CVs. Each CV on the i-axis carries uniform pressure and enthalpy, while the j-axis carries uniform mass flow rate information.

mixture) are expressed as:

$$\dot{Q}_{\text{f},i} = U_{\text{f},i} A_i (T_{\text{wall},i} - T_{\text{f},i}) \tag{5.8}$$

$$\dot{Q}_{\text{sf},i} = U_{\text{sf},i} A_i (T_{\text{wall},i} - T_{\text{sf},i}) \tag{5.9}$$

The determination of the heat transfer coefficient (U_f) is required to model heat exchange between CO_2 and the wall. This coefficient varies with the phase of CO_2 (supercritical, subcritical, or two-phase) and the direction of heat transfer (cooling or heating). Although extensive research has been conducted to define suitable correlations for CO_2, no universally reliable generalization has emerged. The heat transfer coefficient is calculated from Nusselt number (Nu) as follows:

$$U = \frac{K \cdot Nu}{d_h} \tag{5.10}$$

We thus choose from the literature the Nu correlations, based on CO_2 phase, as follows:

- For heat exchangers in the supercritical region where pressure is higher than the critical pressure ($p > 73.8$ bar) and CO_2 is cooled, the correlation proposed by Yoon et al. (2003) is used:

$$\mathrm{Nu} = 0.14\,\mathrm{Re}^{0.66}\,\mathrm{Pr}^{0.6} \tag{5.11}$$

- In the subcritical region where pressure is lower than the critical pressure ($p < 73.8$ bar), in the two-phase regime where vapor quality is between zero and one ($0 < q < 1$): if undergoing evaporation, the heat transfer coefficient is evaluated using the model of Cheng et al. (2006), while when condensing, the correlation by Shah (1979) is used. In both cases, the expressions are complex, so they are not reproduced here.

- In subcritical and single-phase (liquid or vapor) conditions, the standard Dittus–Boelter correlation is applied:

$$\mathrm{Nu} = 0.023\,\mathrm{Re}^{0.8}\,\mathrm{Pr}^{0.4} \tag{5.12}$$

The standard Dittus–Boelter correlation is also used for the secondary-fluid heat transfer coefficient U_sf.

5.2.1.2 Flash tank

For the flash tank, the model provided by Qiao et al. (2015) is adopted, where it is modeled as a lumped CV with one inlet and two outlets (Figure 5.2), and the following simplifications are considered:

- Phases are ideally separated.
- The vapor and liquid in the flash tank are at thermodynamic equilibrium.
- The pressure drop within the flash tank is negligible.
- The flash tank is assumed adiabatic.

The governing equations obtained from applying mass and energy balances on the flash tank CV are:

$$a_{1\mathrm{ft}}\frac{\partial p_\mathrm{ft}}{\partial t} + a_{2\mathrm{ft}}\frac{\partial h_\mathrm{ft}}{\partial t} = \dot{m}_{\mathrm{ft,in}} - \dot{m}_{\mathrm{ft,l,out}} - \dot{m}_{\mathrm{ft,v,out}} \tag{5.13}$$

$$a_{3\mathrm{ft}}\frac{\partial p_\mathrm{ft}}{\partial t} + a_{4\mathrm{ft}}\frac{\partial h_\mathrm{ft}}{\partial t} = (\dot{m}h)_{\mathrm{ft,in}} - (\dot{m}h)_{\mathrm{ft,l,out}} - (\dot{m}h)_{\mathrm{ft,v,out}} \tag{5.14}$$

where the coefficients $a_{1\mathrm{ft}}, a_{2\mathrm{ft}}, a_{3\mathrm{ft}}$, and $a_{4\mathrm{ft}}$ are determined by the formulations in (5.3) and (5.4). The outlet enthalpies of the vapor and liquid streams are dependent on the state of the refrigerant in the flash tank. If CO_2 in the flash tank is in a two-phase state, i.e., the enthalpy of the flash tank h_{ft} lies between the saturated liquid enthalpy $h_{\mathrm{ft,l}}$ and the saturated vapor enthalpy $h_{\mathrm{ft,v}}$ ($h_{\mathrm{ft,l}} < h_{\mathrm{ft}} < h_{\mathrm{ft,v}}$), then the outlet enthalpies of both streams are taken as the mean enthalpy:

$$h_{\mathrm{ft,v,out}} = \frac{h_{\mathrm{ft}}}{2} \tag{5.15}$$

$$h_{\mathrm{ft,l,out}} = \frac{h_{\mathrm{ft}}}{2} \tag{5.16}$$

while if CO_2 in the flash tank is in a single-phase state, i.e., $h_{\mathrm{ft}} \leq h_{\mathrm{ft,l}}$ or $h_{\mathrm{ft}} \geq h_{\mathrm{ft,v}}$, the vapor and liquid are assumed to separate perfectly:

$$h_{\mathrm{ft,v,out}} = h_{\mathrm{ft,v}} \tag{5.17}$$

$$h_{\mathrm{ft,l,out}} = h_{\mathrm{ft,l}} \tag{5.18}$$

The mass flow rates of the streams into and out of the flash tank are discussed later in Section 5.2.2.2.

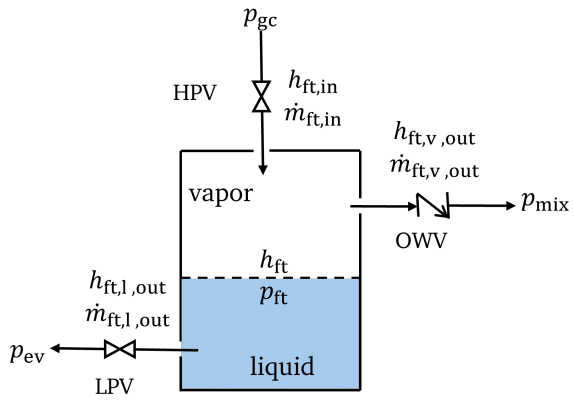

Figure 5.2: Flash tank schematic with the corresponding flow streams.

5.2.1.3 TC heaters

This section models the dynamic variation of the heaters' temperatures. The heaters are externally heated by methane-air mixture combustion and internally cooled by CO_2. Since the detailed study of the combustion chamber lies outside the scope of this work, and because the internal dynamics of the TC operate at a much smaller time scale than the overall TCHP cycle, the TC is treated as a black box. Accordingly, the external and internal heat transfer effects are represented by the burner fan and motor rotational speeds, respectively. System identification is then performed using experimental step tests (from Section 4.4.1) to obtain suitable models. Three different data sets are used: (i) a pseudo-random binary sequence (PRBS) applied to the burner fan speed, (ii) step tests, and (iii) step tests on the motor rotational speeds. The PRBS excitation ensures coverage of the minimum and maximum burner fan speeds. The input ranges for motor rotational speeds are $60 \leq \omega_{\mathrm{m1}}, \omega_{\mathrm{m2}} \leq 240$ rpm and for burner fan speed is $2000 \leq \omega_{\mathrm{bf}} \leq 9500$ rpm. The dynamics of the heater temperatures T_{h1} and T_{h2} are represented by nonlinear system

identification models. The parameters of these models are obtained through minimization of the ordinary least squares error between the measured and predicted T_{h1} and T_{h2}, respectively, leading to the following identified discrete-time models:

$$T_{\mathrm{h1}}(k+1) = 0.45 + T_{\mathrm{h1}}(k) + 2 \times 10^{-4}\,\omega_{\mathrm{bf}}(k) - 7.6 \times 10^{-9}\,\omega_{\mathrm{bf}}^2(k) - 1.1 \times 10^{-3}\,\omega_{\mathrm{m1}}(k) \tag{5.19}$$

$$T_{\mathrm{h2}}(k+1) = 0.51 + T_{\mathrm{h2}}(k) + 1.8 \times 10^{-4}\,\omega_{\mathrm{bf}}(k) - 6.4 \times 10^{-9}\,\omega_{\mathrm{bf}}^2(k) - 1.3 \times 10^{-3}\,\omega_{\mathrm{m2}}(k) \tag{5.20}$$

The fitting of both models is shown in Figures 5.3 and 5.4, which indicate relatively high accuracy, with MAEs of 15.9 K and 16.8 K and R^2 scores of 0.96 and 0.94 for heater temperatures 1 and 2, respectively. Relative to the heater temperature range of 220 to 800 °C (about 580 K difference), the MAE values correspond to relative errors below 3%. These results demonstrate that the identified models reliably predict heater temperature variations and can therefore be confidently used as part of the TCHP-HYB model. The figures also reveal that burner fan speed has a stronger influence on heater temperature compared to rotational speed, and thus a greater impact on system operation.

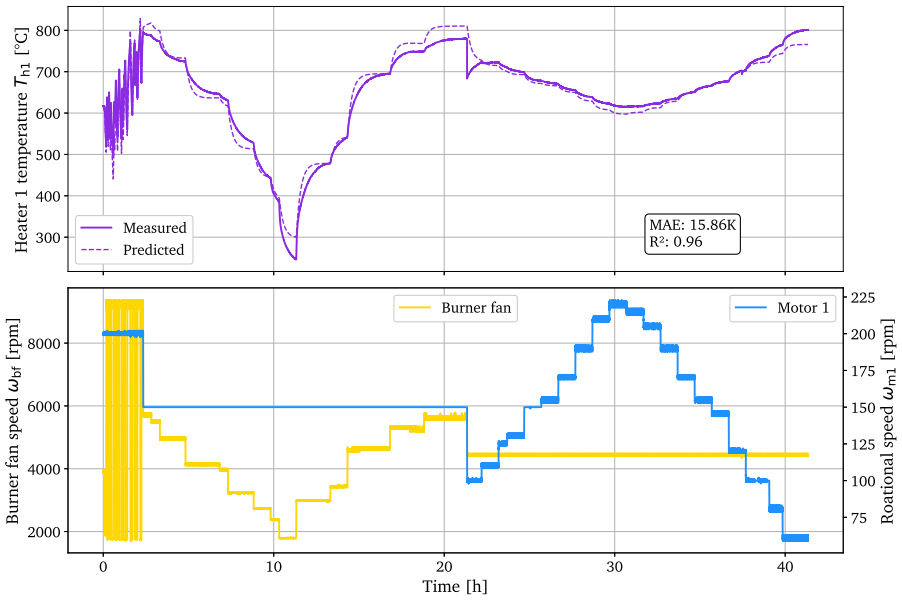

Figure 5.3: Heater 1 temperature T_{h1} identified model validation. MAE is 15.86 K and R^2 is 0.96, indicating a good fit. The bottom plot shows the burner fan speed and motor 1 rotational speed over time, illustrating their influence on T_{h1} dynamics.

5.2.2 Quasi-static part of the TCHP-HYB model

This section is dedicated to the part of the TCHP-HYB model represented quasi-statically. Unlike the differential equations, which are mostly deterministic—except for the heater temperatures described—these models rely greatly on tuning using real data. For this, the TCHP steady-state data from Section 4.4.2 are used.

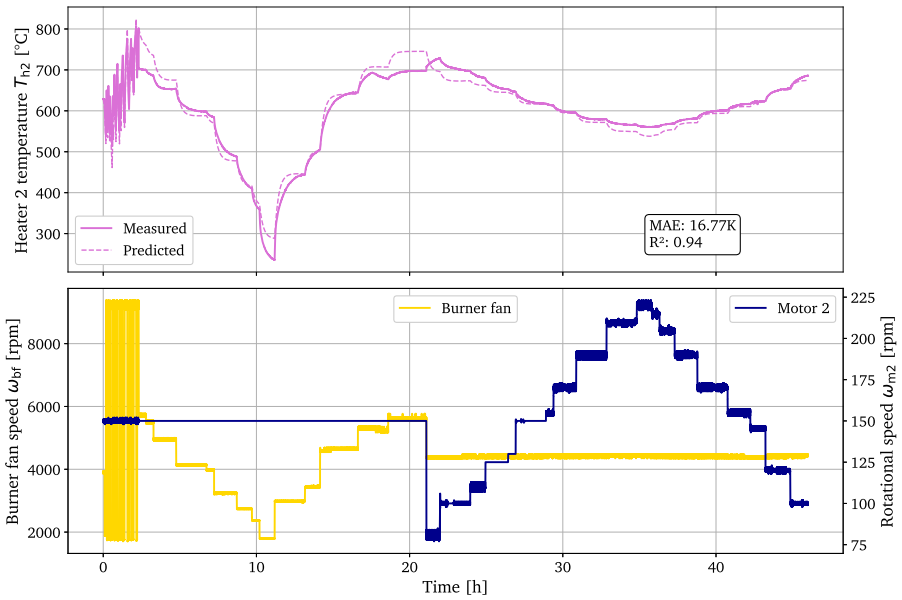

Figure 5.4: Heater 2 temperature T_{h2} identified model validation. MAE is 16.77 K and R^2 is 0.94, indicating a good fit. The bottom plot shows the burner fan speed and motor 2 rotational speed over time, illustrating their influence on T_{h2} dynamics.

5.2.2.1 Thermal compressors

The TCs are crucial components in the TCHP cycle, due to their contribution to the mass flow rates, discharge temperatures, and heat recovered through their coolers. In this section, we employ the Gaussian process regression (GPR) machine learning model type derived in Chapter 3, which has proven to be a suitable candidate—showing higher accuracy than polynomial regression and faster computation than artificial neural networks. Since we have direct heater temperature measurements on the first two TCs, GPR can be used as a prediction model for predicting the outputs: mass flow rates ($\dot{m}_{\mathrm{tc1}}$ and $\dot{m}_{\mathrm{tc2}}$), discharge temperatures ($T_{\mathrm{tc1,dis}}$ and $T_{\mathrm{tc2,dis}}$), and cooler heat transfer rates ($\dot{Q}_{\mathrm{k1}}$ and $\dot{Q}_{\mathrm{k2}}$). Prior to this, the TC data used to train the GPR model is extended with TCHP steady-state data (Table 4.7), then GPR is re-trained and validated afterwards. Since GPR is non-parametric, it cannot be represented with equations here, but the implementation can be found in Salame (2025b).

Since TC3 lacks direct heater measurement, an independent model is derived based on TCHP steady-state data only. Due to the small number of samples, and to avoid overfitting, a simple linear regression (LR) model is chosen. LR models for TC3 define the gas cooler inlet mass flow rate ($\dot{m}_{\mathrm{tc3}}$), so the third buffer between TC3 and the gas cooler is considered part of this model, discharge temperature ($T_{\mathrm{tc3,dis}}$), and heat recovery ($\dot{Q}_{\mathrm{k3}}$)

$$\dot{m}_{\mathrm{tc3}} = 10^{-4}\big(-769\,r_{\mathrm{p3}} + 0.58\,T_{\mathrm{h2}} - 4.3\,T_{\mathrm{tc3,w,in}} + 0.081\,\omega_{\mathrm{m3}} + 2.5\,T_{\mathrm{tc3,suc}}\big) + 0.056 \tag{5.21}$$

$$T_{\mathrm{tc3,dis}} = -58.9\,r_{\mathrm{p3}} + 0.059\,T_{\mathrm{h2}} + 1.2\,T_{\mathrm{tc3,w,in}} - 0.01\,\omega_{\mathrm{m3}} + 0.36\,T_{\mathrm{tc3,suc}} + 298 \tag{5.22}$$

$$\dot{Q}_{\mathrm{k3}} = 203.2\,r_{\mathrm{p3}} + 1.13\,T_{\mathrm{h2}} - 5.6\,T_{\mathrm{tc3,w,in}} + 3.5\,\omega_{\mathrm{m3}} + 6.3\,T_{\mathrm{tc3,suc}} - 990 \tag{5.23}$$

The independent variables are: pressure ratio r_{p3}, second heater temperature T_{h2} to include inertia, inlet water temperature $T_{\mathrm{tc3,w,in}}$ which leaves TC2 cooler, rotational speed

ω_{m3}, and suction temperature $T_{tc3,suc}$. The fitting of the GPR model on TC1 and TC2 outputs is illustrated using parity plots in Figures 5.5 and 5.6, respectively, and for TC3 in Figure 5.7. The accuracies (MAE, MAPE, and R^2) are summarized in Table 5.1. The resulting metrics indicate that the models achieve acceptable accuracy levels. Having accurate TC models is important for predicting mass flow rates, discharge temperatures, and cooler heat transfer rates during simulation as they contribute to the overall prediction accuracy of the TCHP-HYB model.

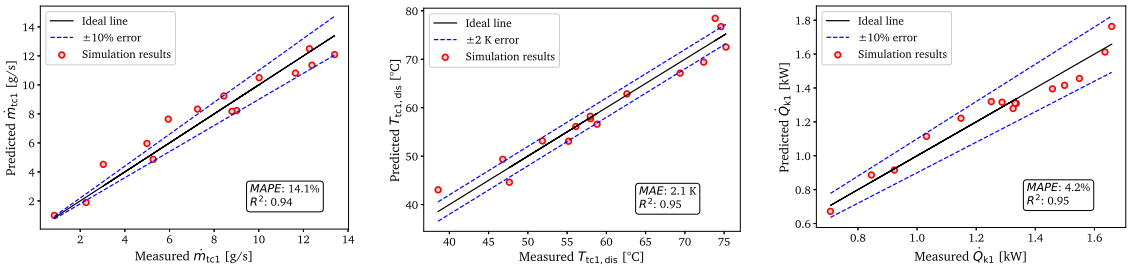

(a) Mass flow rate. (b) Discharge temperature. (c) Cooler heat transfer rate.

Figure 5.5: GPR model steady-state parity plots showing the predicted outputs of TC1 compared to measured ones.

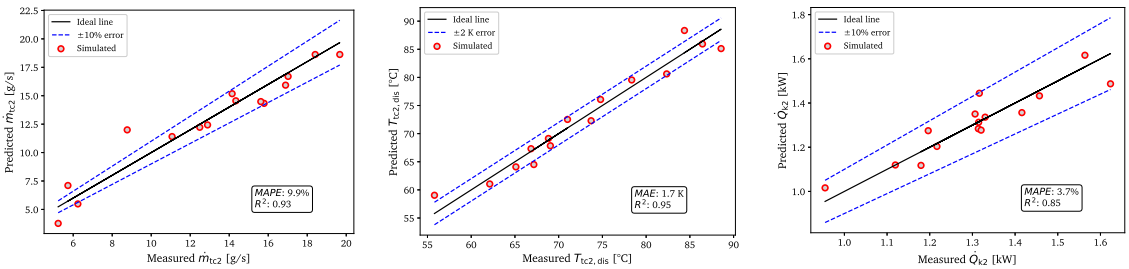

(a) Mass flow rate. (b) Discharge temperature. (c) Cooler heat transfer rate.

Figure 5.6: GPR model steady-state parity plots showing the predicted outputs of TC2 compared to measured ones.

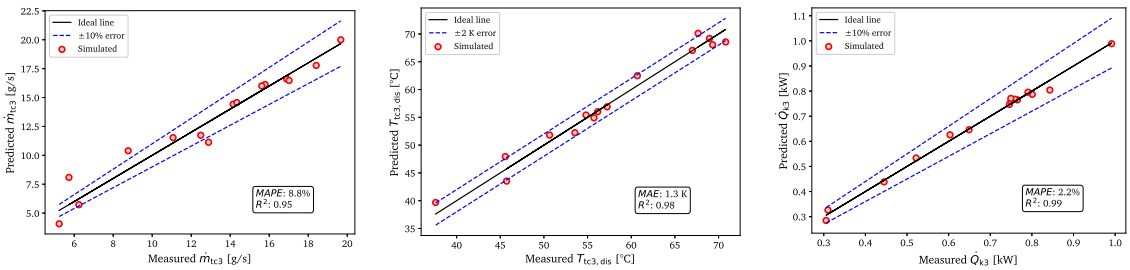

(a) Mass flow rate. (b) Discharge temperature. (c) Cooler heat transfer rate.

Figure 5.7: LR model steady-state parity plots showing the predicted outputs of TC3 compared to measured ones.

Output Variable	MAPE [%] / MAE [K]	R^2
TC1 & TC2: GPR		
$\dot{m}_{\mathrm{tc1}}$	15.2 %	0.9
$T_{\mathrm{tc1,dis}}$	1.9 K	0.96
$\dot{Q}_{\mathrm{k1}}$	4.4 %	0.95
$\dot{m}_{\mathrm{tc2}}$	9.9 %	0.93
$T_{\mathrm{tc2,dis}}$	1.7 K	0.95
$\dot{Q}_{\mathrm{k2}}$	3.7 %	0.85
TC3: LR		
$\dot{m}_{\mathrm{tc3}}$	8.8 %	0.95
$T_{\mathrm{tc3,dis}}$	1.3 K	0.98
$\dot{Q}_{\mathrm{k3}}$	2.2 %	0.99

Table 5.1: TC models prediction accuracy for each output: MAPE for flow and power variables, MAE for temperatures, and R^2 for all outputs.

5.2.2.2 Valves

In a TCHP cycle, there are three flow streams connecting the flash tank with different cycle components (Figure 5.2). The outlet liquid mass flow rate $\dot{m}_{\mathrm{ft,l,out}}$ flows through a low-pressure expansion valve, connecting the flash tank to the inlet of the evaporator. The inlet mass flow rate $\dot{m}_{\mathrm{ft,in}}$ flows through a high-pressure valve. Both these valves are electronic type and their openings can be regulated. On the other hand, the outlet vapor mass flow rate $\dot{m}_{\mathrm{ft,v,out}}$ flows through a one-way valve of fixed opening area to the suction point of the second TC (MIX point). The flow through these valves is considered isenthalpic and is modeled using the following equations:

$$\dot{m}_{\mathrm{lpv}} = (C_d A)_{\mathrm{lpv}} \sqrt{\rho_{\mathrm{ft,l}} \left(p_{\mathrm{ft}} - p_{\mathrm{ev}}\right)} \tag{5.24}$$

$$\dot{m}_{\mathrm{hpv}} = (C_d A)_{\mathrm{hpv}} \sqrt{\rho_{\mathrm{gc}} \left(p_{\mathrm{gc}} - p_{\mathrm{ft}}\right)} \tag{5.25}$$

$$\dot{m}_{\mathrm{owv}} = (C_d A)_{\mathrm{owv}} \sqrt{\rho_{\mathrm{ft,v}} \left(p_{\mathrm{ft}} - p_{\mathrm{mix}}\right)} \tag{5.26}$$

The combined value of the product $(C_d A)$ of the low- and high-pressure valves can be obtained by a regression relation with the percentage valve opening φ Qiao et al. (2015):

$$(C_d A)_{\mathrm{lpv}} = 10^{-9} \left(-100 + 6\,\varphi_{\mathrm{lpv}}\right) \tag{5.27}$$

$$(C_d A)_{\mathrm{hpv}} = 10^{-9} \left(63.8 + 4.76\,\varphi_{\mathrm{hpv}}\right) \tag{5.28}$$

The coefficients are obtained by tuning against TCHP steady-state data (Table 4.7), where the mass flow rate in the low-pressure valve is equal to that in TC1 and in the high-pressure valve equal to that in TC2 and TC3 considering steady-state conditions. The resulting predicted mass flow rates in the low- and high-pressure valves from the fitted correlations are represented in Figure 5.8.

The effective flow area of the one-way valve is assumed constant and set to

$$(C_d A)_{\mathrm{owv}} = 10^{-6} \tag{5.29}$$

Due to missing pressure measurements at the mixing point in the TCHP steady-state data, the correlation could not be calibrated with real data. The chosen value was instead selected arbitrarily based on simulations of the complete TCHP-HYB model. The importance of determining flow rates through the valves lies in well establishing pressure and enthalpy variations inside the flash tank as well as the connected components (evaporator, gas cooler, and mixing point at TC2 suction), and thus affecting the overall predictions of the TCHP-HYB model.

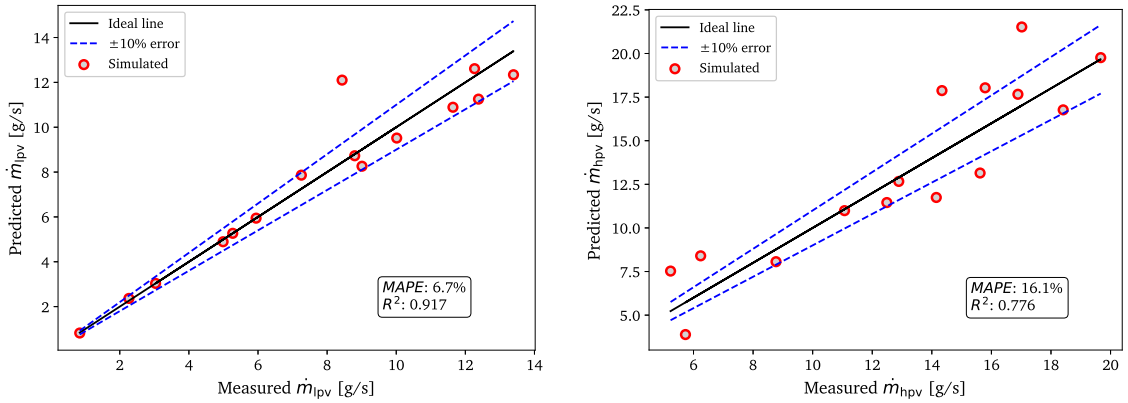

(a) Low pressure valve.

(b) High pressure valve.

Figure 5.8: Expansion valve models steady-state parity plots showing the predicted mass flow rates from fitted Equations (5.27) and (5.28), compared to the measured ones.

5.2.2.3 Fume heat exchanger

In a TCHP cycle, the fume heat exchanger is the last heat exchanger where water recovers heat. Its heat exchange rate is considered faster than cycle heat exchangers from Section 5.2.1.1, as it is directly influenced by the burner fan speed instead of the heater temperatures. For this reason, it is modeled quasi-statically using the logarithmic mean temperature difference (LMTD) method. Figure 5.9 shows the schematic of the fume heat exchanger, where the inlet fume temperature $T_{\text{fhx,fume,in}}$ rejects heat to the inlet water temperature $T_{\text{fhx,w,in}}$, and the streams leave at $T_{\text{fhx,fume,out}}$ and $T_{\text{fhx,w,out}}$, respectively. Along with the mass flow rates $\dot{m}_{\text{w}}$ and $\dot{m}_{\text{fume}}$, the corresponding steady-state data are given in Table 4.8. According to the LMTD method:

$$\dot{Q}_{\text{fhx}} = (AU)_{\text{fhx}}\,\Delta T_{\text{lm}} \tag{5.30}$$

Where:

$$\Delta T_{\text{lm}} = \frac{\Delta T_1 - \Delta T_2}{\ln(\Delta T_1/\Delta T_2)} \tag{5.31}$$

With:

$$\Delta T_1 = T_{\text{fhx,fume,in}} - T_{\text{fhx,w,out}} \qquad \Delta T_2 = T_{\text{fhx,fume,out}} - T_{\text{fhx,w,in}} \tag{5.32}$$

From the inlet and outlet temperatures, mass flow rate on both sides, and the measured heat transfer rate at the fume heat exchanger, $(AU)_{\text{fhx}}$ can be retrieved from data and then tuned as a function of ω_{bf} and $T_{\text{fhx,w,in}}$:

$$(AU)_{\text{fhx}} = 0.000598\,\omega_{\text{bf}} + 0.687\,T_{\text{fhx,w,in}} - 16.34 \tag{5.33}$$

Substituting this fitted correlation in Equation (5.30) gives a MAPE of 15.8% and an R^2 of 0.96 between predicted and measured heat exchange rate (Figure 5.10). For integrating

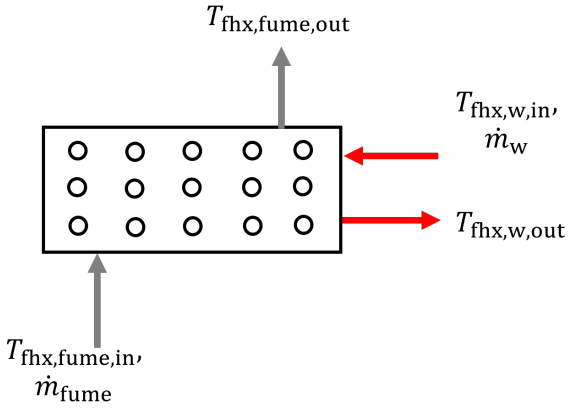

Figure 5.9: Fume heat exchanger schematic.

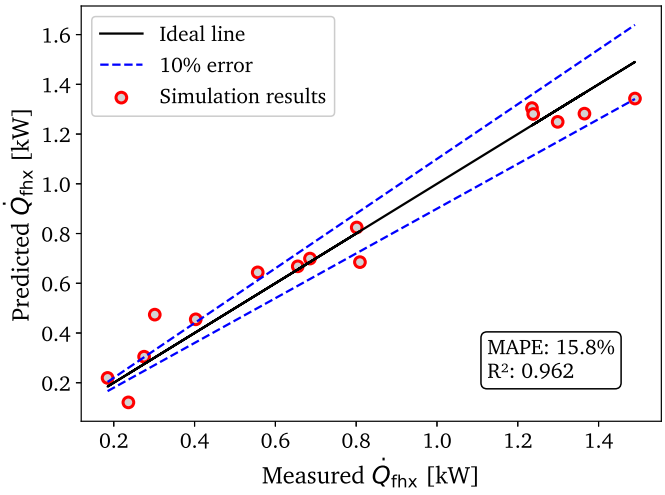

Figure 5.10: Fume heat exchanger model steady-state parity plots showing the predicted heat transfer rate from fitted Equation (5.33) compared to the measured ones.

in the TCHP-HYB model, an LMTD iterative model is proposed (Figure 5.11). At each iteration it finds the appropriate $T_{\text{fhx,w,out}}$, $T_{\text{fhx,fume,out}}$, and $\dot{Q}_{\text{fhx}}$ by taking $T_{\text{fhx,fume,in}}$, $T_{\text{fhx,w,in}}$, $\dot{m}_{\text{w}}$, $\dot{m}_{\text{fume}}$, fume and water specific heats ($c_{p_{\text{fume}}}$ and $c_{p_{\text{w}}}$), and tuned $(AU)_{\text{fhx}}$ as inputs. In short, the method computes these variables while ensuring the energy balance on both water and fume sides is satisfied. The iteration continues until the difference between guessed and computed $\dot{Q}_{\text{fhx}}$ is less than 10^{-6}. Since the inlet fume temperature is not measured, it is correlated from steady-state data as a function of burner fan speed:

$$T_{\text{fhx,fume,in}} = 0.056\,\omega_{\text{bf}} - 36.5 \tag{5.34}$$

While the inlet water temperature is computed from other heat exchangers in the TCHP. After deriving all these component-level models, they are connected to form a final system-level complete TCHP to be validated.

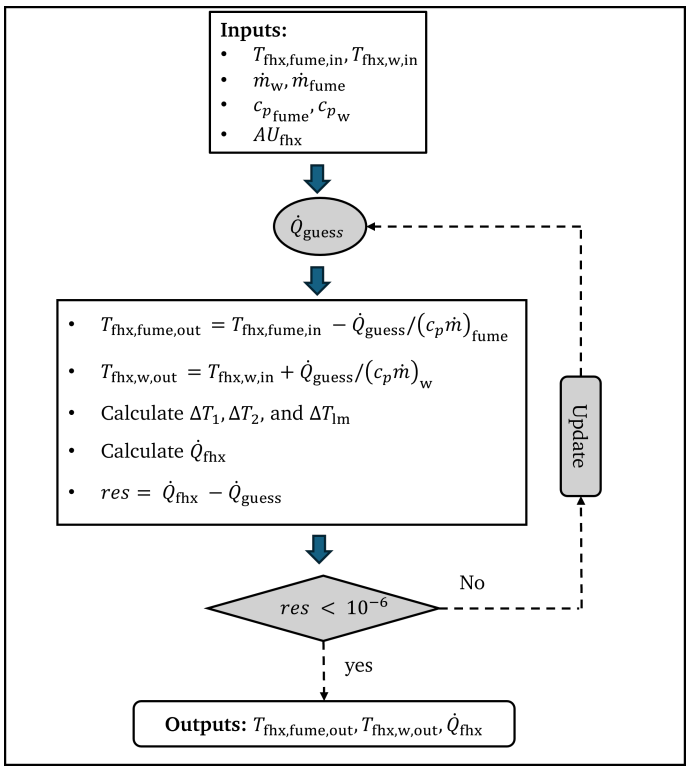

Figure 5.11: Fume heat exchanger LMTD iterative method.

5.3 Numerical resolution

After modeling each component of the TCHP cycle, the submodels are connected to form a complete, independent TCHP-HYB model. This section summarizes the final model, describes its overall architecture and solving process, and presents its Python implementation.

5.3.1 Final model summary

The final TCHP-HYB model consists of two parts. The quasi-static part includes the non-parametric GPR models for TC1 and TC2 (Chapter 3), the linear regression model for TC3 (Equations (5.23)), the valve mass flow rate correlations (Equations (5.24)–(5.26)) for the LPV, HPV, and OWV, together with the iterative LMTD model of the fume heat exchanger (FHX) shown in Figure 5.11.

The differential part includes the mass, energy, and wall and secondary fluid temperature conservation Equations (5.1)–(5.7) for the evaporator (EV), gas cooler (GC), and second buffer (BUF2). The internal heat exchanger (IHX) is modeled with only the energy and wall temperature balances (Equations (5.2), (5.7)), while the first buffer (BUF1) includes the energy, wall and secondary fluid temperature balance Equations (5.2), (5.7), and (5.6), and the TC2 suction point (MIX) includes the mass and energy balances (Equations (5.1), (5.2)). The flash tank (FT) is modeled with its specific balance Equations (5.13) and (5.14). Equation 5.5 is applied to all these components for the purpose of reducing stiffness, as mentioned in Section 5.2.1.1. For simulation, the GC, EV, and IHX are discretized into 10, 12, and 4 CVs, respectively, which offers a trade-off between accuracy and computational efficiency. BUF1, BUF2, MIX, and FT are modeled with a single

CV each, as heat exchange in these volumes is less critical; except for BUF1, their main role is to capture pressure variations at critical points of the cycle. In addition, the heater temperatures T_{h1} and T_{h2} are also modeled with differential equations through a system identification technique. The identified models are represented by Equations 5.19 and 5.20. Taking into account all the assumptions made so far, the component submodel characteristics are summarized in Table 5.2.

Component	Model class	Equations / references	Notes
quasi-static part			
TC1	GPR	Chapter 3	Non-parametric Salame (2025b)
TC2	GPR	Chapter 3	Non-parametric Salame (2025b)
TC3	LR	Equations (5.23)	-
LPV	Valve correlation	Equations (5.24), (5.27)	Electronic expansion valve
HPV	Valve correlation	Equations (5.25), (5.28)	Electronic expansion valve
OWV	Valve correlation	Equation (5.26)	One-way valve, constant $(C_d A)$
FHX	LMTD	Equations (5.30), (5.33)	Iterative model, Fig. 5.11
Differential part			
GC	FV balances	Equations (5.1)–(5.7)	10 CVs
EV	FV balances	Equations (5.1)–(5.7)	12 CVs
IHX	Energy + wall balance	Equations (5.2), (5.7)	4 CVs
BUF1	Lumped CV	Equations (5.2), (5.7), (5.6)	1 CV (no mass balance)
BUF2	FV balances	Equations (5.1)–(5.7)	1 CV (buffer)
MIX	Lumped CV	Equations (5.1), (5.2)	1 CV (TC2 suction)
FT	Lumped CV	Equations (5.13), (5.14)	1 CV, phase separator
T_{h1}	System identification	Equation (5.19)	-
T_{h2}	System identification	Equation (5.20)	-

Table 5.2: Summary of component submodels used in the final TCHP-HYB model.

The resulting TCHP-HYB model's differential equations can also be expressed in a state-space representation, with the resulting state vector given as:

$$\begin{aligned} x = [&p_{\mathrm{gc}}, \bar{h}_{\mathrm{gc}}, \bar{T}_{\mathrm{gc,wall}}, \bar{T}_{\mathrm{gc,w}}, p_{\mathrm{ev}}, \bar{h}_{\mathrm{ev}}, \bar{T}_{\mathrm{ev,wall}}, \bar{T}_{\mathrm{ev,mpg}}, p_{\mathrm{mix}}, h_{\mathrm{mix}}, h_{\mathrm{buf1}}, \\ &T_{\mathrm{buf1,wall}}, T_{\mathrm{buf1,w}}, p_{\mathrm{buf2}}, h_{\mathrm{buf2}}, T_{\mathrm{buf2,wall}}, T_{\mathrm{buf2,w}}, \bar{h}_{\mathrm{ihx1}}, \bar{h}_{\mathrm{ihx2}}, \bar{T}_{\mathrm{ihx,wall}}, p_{\mathrm{ft}}, h_{\mathrm{ft}}] \end{aligned} \tag{5.35}$$

Here, the characters with a bar denote vector quantities, whose dimensions correspond to the number of discretized volumes in the GC, EV, and IHX. The input vector u and output or measured vector y are:

$$u = [\varphi_{\mathrm{hpv}}, \varphi_{\mathrm{lpv}}, \omega_{\mathrm{bf}}, \omega_{\mathrm{m1}}, \omega_{\mathrm{m2}}, \omega_{\mathrm{m3}}, T_{\mathrm{w,ret}}, \dot{m}_{\mathrm{w}}, T_{\mathrm{mpg,in}}, \dot{m}_{\mathrm{mpg}}] \tag{5.36}$$

$$y = [T_{\mathrm{h1}}, T_{\mathrm{h2}}, p_{\mathrm{gc}}, p_{\mathrm{ev}}, T_{\mathrm{gc,out}}, T_{\mathrm{ev,out}}, T_{\mathrm{w,sup}}, T_{\mathrm{mpg,out}}] \tag{5.37}$$

The resulting differential part of the TCHP-HYB model is a set of ordinary differential equations (ODEs):

$$\dot{x} = f(x, u) \tag{5.38}$$

The mapping connecting all the described components is given next.

5.3.2 Final model architecture

The TCHP-HYB final model architecture, showing the interconnection of all refrigerant-side submodels, is illustrated in Figure 5.12. Inputs are shown in blue, outputs in green, and model parameters in yellow. Information flow is determined by the arrows. The figure emphasizes the strong coupling and interdependence between refrigerant-side components, while the water- and fume-side connections are omitted for clarity and presented separately in Figure 5.13. The links according to refrigerant-side components are summarized as follows:

1. TC heaters: Take burner fan speed (ω_{bf}) and motor speeds (ω_{m1} and ω_{m2}) as inputs, and return heater temperatures (T_{h1} and T_{h2}) as intermediary inputs for the TCs.

2. TCs: TC1 suction pressure and temperature correspond to those at the outlet of the IHX (p_{ev} and $T_{\mathrm{ihx2,out}}$), while the discharge pressure is that at the MIX volume (p_{mix}). The external inputs are heater temperature T_{h1} and rotational speed ω_{m1}. The returned outputs are mass flow rate ($\dot{m}_{\mathrm{tc1}}$) and discharge temperature ($T_{\mathrm{tc1,dis}}$).

   TC2 suction pressure and temperature correspond to those at the outlet of the MIX volume (p_{mix} and T_{mix}), while the discharge pressure is that at the BUF2 volume (p_{buf2}). The external inputs are heater temperature T_{h2} and rotational speed ω_{m2}. The returned outputs are mass flow rate ($\dot{m}_{\mathrm{tc2}}$) and discharge temperature ($T_{\mathrm{tc2,dis}}$).

   TC3 suction pressure and temperature correspond to those at the outlet of the BUF2 volume (p_{buf2}), while the discharge pressure is that at the GC (p_{gc}). The external inputs are heater temperature T_{h2} and rotational speed ω_{m3}. The returned outputs are mass flow rate ($\dot{m}_{\mathrm{tc3}}$) and discharge temperature ($T_{\mathrm{tc3,dis}}$).

3. Valves: LPV takes inlet pressure corresponding to the FT and outlet pressure at the EV and returns the liquid mass flow rate leaving FT ($\dot{m}_{\mathrm{lpv}}$). HPV takes inlet pressure corresponding to the GC and outlet pressure at the FT and returns mass flow rate ($\dot{m}_{\mathrm{hpv}}$). OWV takes inlet pressure corresponding to the FT and outlet pressure at the MIX volume and returns the vapor mass flow rate leaving FT ($\dot{m}_{\mathrm{owv}}$).

4. EV: The enthalpy at the EV inlet is equal to the enthalpy of liquid CO_2 in the FT, i.e., $h_{\mathrm{ev,in}} = h_{\mathrm{ft,l}}$. The inlet mass flow rate corresponds to that of the LPV ($\dot{m}_{\mathrm{lpv}}$), while the outlet mass flow rate corresponds to that of TC1 ($\dot{m}_{\mathrm{tc1}}$).

5. GC: The enthalpy at the GC inlet is the discharge enthalpy of TC3, i.e., $h_{\mathrm{gc,in}} = h_{\mathrm{tc3,dis}}$. The inlet mass flow rate corresponds to that of TC3 ($\dot{m}_{\mathrm{tc3}}$), while the outlet mass flow rate corresponds to that of the HPV ($\dot{m}_{\mathrm{hpv}}$).

6. IHX: The enthalpy in the last CV of the EV serves as the inlet to the IHX, i.e., $h_{\mathrm{ihx2,in}} = h_{\mathrm{ev,out}}$. The enthalpy of CO_2 at the outlet of the GC is equal to the inlet enthalpy of the IHX, i.e., $h_{\mathrm{ihx1,in}} = h_{\mathrm{gc,out}}$. No mass accumulation is considered; the mass flow rates on both sides are equal to those at the outlets of the EV and GC, respectively.

7. FT: The enthalpy at the FT inlet is equal to the outlet enthalpy of the IHX on the GC side, i.e., $h_{\mathrm{ft,in}} = h_{\mathrm{ihx1,out}}$. The inlet mass flow rate corresponds to that of the HPV ($\dot{m}_{\mathrm{hpv}}$), while the outlets are for the LPV ($\dot{m}_{\mathrm{lpv}}$) towards the EV, and for the OWV towards the MIX volume ($\dot{m}_{\mathrm{owv}}$).

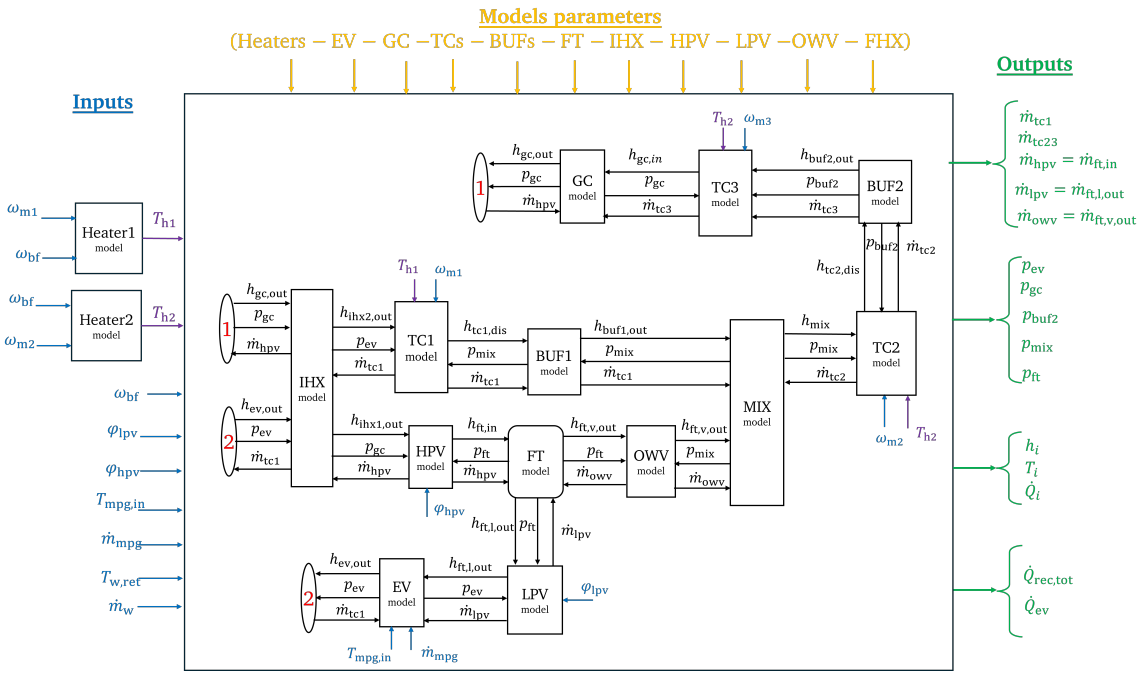

Figure 5.12: Refrigerant-side architecture of the TCHP-HYB model.

8. BUF1: The inlet enthalpy of BUF1 is the outlet enthalpy of TC1, i.e., $h_{\mathrm{buf1,in}} = h_{\mathrm{tc1,dis}}$. No mass variation is considered, so the mass flow rate across the component equals that of TC1 ($\dot{m}_{\mathrm{tc1}}$). Wall balances are included.

9. BUF2: The inlet enthalpy of BUF2 is the outlet enthalpy of TC2, i.e., $h_{\mathrm{buf2,in}} = h_{\mathrm{tc2,dis}}$. The inlet mass flow rate corresponds to that of TC2 ($\dot{m}_{\mathrm{tc2}}$), while the outlet mass flow rate corresponds to that of TC3 ($\dot{m}_{\mathrm{tc3}}$).

10. MIX: The inlet enthalpy of MIX is the mass-weighted combination of the outlet enthalpies of TC1 and the FT vapor stream. The inlet mass flow rates correspond to those of TC1 ($\dot{m}_{\mathrm{tc1}}$) and the OWV ($\dot{m}_{\mathrm{owv}}$), while the outlet mass flow rate corresponds to that of TC2 ($\dot{m}_{\mathrm{tc2}}$).

In addition to the refrigerant backbone, the TCHP-HYB integrates a secondary water and fume circuit demonstrated by architecture in Figure 5.13, whose role is to recover and deliver heat. The circulating water enters the system at the return boundary with temperature $T_{\mathrm{w,ret}}$ and mass flow rate $\dot{m}_{\mathrm{w}}$. A fraction $\dot{m}_{\mathrm{w2}} = 0.7\dot{m}_{\mathrm{w}}$ is directed to the GC, while the remaining flow $\dot{m}_{\mathrm{w1}}$ is split equally between BUF1 ($\dot{m}_{\mathrm{w11}} = 0.5\dot{m}_{\mathrm{w1}}$) and BUF2 ($\dot{m}_{\mathrm{w12}} = 0.5\dot{m}_{\mathrm{w1}}$) before recombining. For illustration, the inlet water temperature to TC1 can be expressed as

$$T_{\mathrm{tc1,w,in}} = \frac{\dot{m}_{\mathrm{w11}}\, T_{\mathrm{buf1,w,out}} + \dot{m}_{\mathrm{w12}}\, T_{\mathrm{buf2,w,out}}}{\dot{m}_{\mathrm{w1}}}. \tag{5.39}$$

The water then recovers heat sequentially from TC1, TC2, and TC3. The outlet water temperature of each TC can be calculated from predicted cooler heat transfer rate as follows:

$$T_{\mathrm{k,w,out}} = T_{\mathrm{k,w,in}} + \frac{\dot{Q}_{\mathrm{k}}}{\dot{m}_{\mathrm{w1}} c_{p,\mathrm{w}}} \tag{5.40}$$

The flow is mixed again with the stream leaving the GC before entering the FHX, and can be retrieved as follows:

$$T_{\mathrm{fhx,w,in}} = \frac{\dot{m}_{\mathrm{w1}}\, T_{\mathrm{tc3,w,out}} + \dot{m}_{\mathrm{w2}}\, T_{\mathrm{gc,w,out}}}{\dot{m}_{\mathrm{w}}}. \tag{5.41}$$

The outlet water temperature retrieved from FHX is the final supply temperature $T_{\mathrm{w,sup}}$. In contrast, the refrigerant-side architecture in Figure 5.12 focuses solely on pressures, enthalpies, and mass flow rates. The thermal compressor outputs in this representation are limited to $\dot{m}_{\mathrm{tc1}}$, $\dot{m}_{\mathrm{tc2}}$, $\dot{m}_{\mathrm{tc3}}$ and $T_{\mathrm{tc1,dis}}$, $T_{\mathrm{tc2,dis}}$, $T_{\mathrm{tc3,dis}}$. The associated heat transfer rates $\dot{Q}_{\mathrm{k1}}$, $\dot{Q}_{\mathrm{k2}}$, $\dot{Q}_{\mathrm{k3}}$ and $\dot{Q}_{\mathrm{fhx}}$ are instead explicitly represented in the water- and fume-side schematic to highlight their role in energy delivery to the secondary loops.

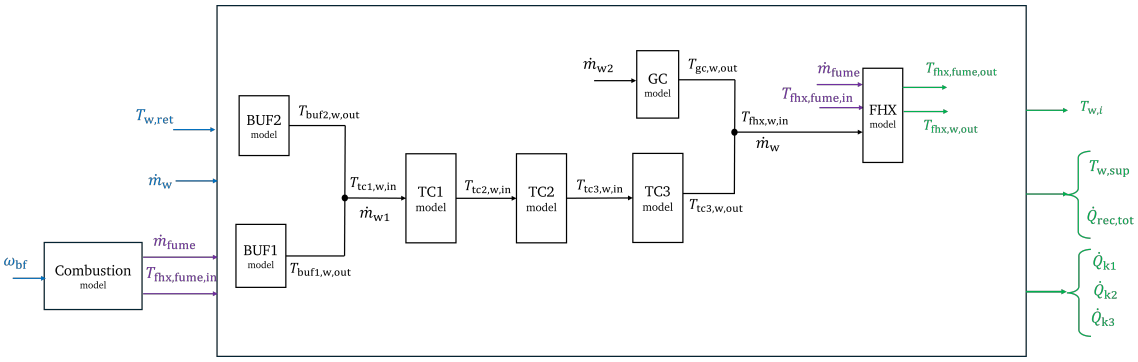

Figure 5.13: Water and fume-side architecture of the TCHP-HYB model.

5.3.3 Solving process

The solution sequence is outlined in Figure 5.14. First, component parameters (coefficients and geometry) are specified and the initial states are set. At each iteration, the quasi-static submodels are evaluated and their outputs provided to the system of differential equations (5.38), which are integrated using the third-order Runge–Kutta method (RK23). The updated state vector, containing pressures and enthalpies, is then used to compute thermo-physical properties (density, temperature, etc.) and the required partial derivatives.

On the refrigerant side, mass and energy balances are inherently satisfied by the formulation. On the water side, however, balances are not automatically enforced; they are imposed explicitly to ensure consistency. In particular, to avoid violating the energy balance of the thermal compressors, the cooler heat transfer rate of TC3 is determined from an overall energy balance across the TCs. Convergence is achieved when $\partial x/\partial t < 0.01$. The final outputs, summarized in Figure 5.12, are then retrieved for validation against both steady-state and transient datasets.

5.3.4 Python implementation

Unlike most implementations in the literature, which rely on object-oriented simulation environments such as Dymola or Modelica, the TCHP-HYB model is developed entirely in Python. The only built-in solver employed is `solve_ivp`. The scripts are organized as an object-oriented library and made available on GitHub for reuse and extension Salame (2025a). With minor modifications, the code can also be adapted for other types of VCCs.

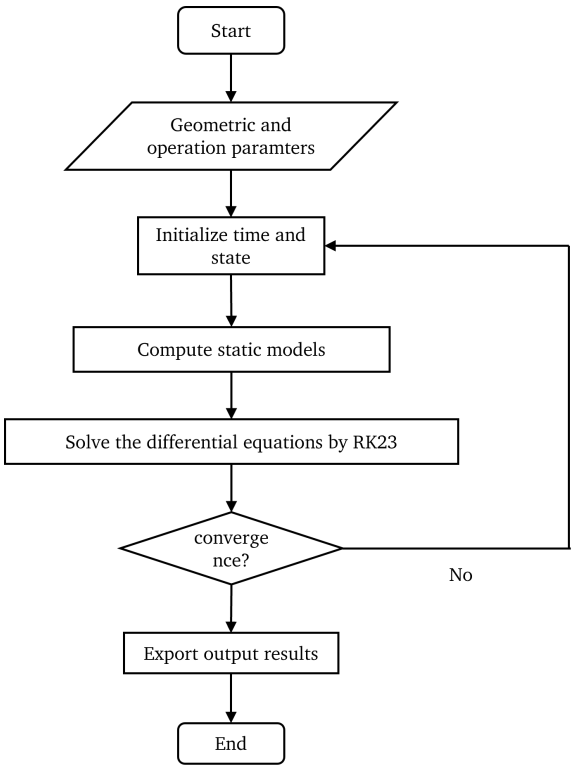

Figure 5.14: Flow chart of the TCHP-HYB model solution procedure.

The accuracy of the derived model depends on several factors: the fidelity of the quasi-static submodels (mass flow rates, discharge temperatures, heat transfer rates), the choice of empirical correlations, and the discretization resolution. The next section presents the validation of the TCHP-HYB model with experimental data.

5.4 Model Validation

The validation of the TCHP-HYB model is conducted on the TCHP steady-state data and the open-loop transient data described in Section 4.3. The steady-state data consist of 15 experimental samples at steady state under various operating conditions, while the transient data contain the step tests on the inputs.

5.4.1 Steady State

The validation is carried out on the measured outputs (from Section 4.3.4), which are: high pressure p_{gc}, low pressure p_{ev}, supply water temperature $T_{\mathrm{w,sup}}$, glycol mixture outlet temperature $T_{\mathrm{mpg,out}}$, the evaporator heat transfer rate $\dot{Q}_{\mathrm{ev}}$, the gas cooler heat transfer rate $\dot{Q}_{\mathrm{gc}}$, the total recovered heat transfer rate $\dot{Q}_{\mathrm{rec,tot}}$, and the thermal COP COP_{th} (calculations in Section 4.3.6). These outputs were selected as performance indicators relevant for later control development. To assess the accuracy of the model's steady-state predictions, parity plots comparing predicted and measured values (Table 4.9) are presented.

Figure 5.15 shows parity plots for high pressure and the gas cooler heat transfer rate. Simulation results for both outputs are in good agreement with the data. High pressure and gas cooler heat transfer rate are predicted with average MAPE values of 1.7% and 17.5%, respectively. This accuracy depends on other predictions such as inlet temperature

(Figure 5.7b), entering mass flow rate (Figure 5.7a), leaving mass flow rate (Figure 5.8b), as well as the empirical heat transfer coefficient correlations in single-phase cooling, subcritical condensation, and supercritical cooling discussed in Section 5.2.1.1. Overall, the prediction accuracy is considered acceptable.

Figure 5.16 shows parity plots for low pressure and the evaporator heat transfer rate. Simulation results for both outputs also align well with the data. Low pressure and evaporator heat transfer rate are predicted with average MAPE values of 3.2% and 19.9%, respectively. This accuracy depends on other predictions such as inlet temperature (Figure 5.5b), entering mass flow rate (Figure 5.8a), leaving mass flow rate (Figure 5.5a), as well as the empirical heat transfer coefficient correlations in subcritical evaporation and single-phase heating (Section 5.2.1.1). Thus, the predictions are judged acceptable.

Figure 5.17 presents parity plots for the total recovered heat transfer rate and the thermal COP. Simulation results for both outputs are in good agreement with the data. These predictions are directly influenced by the accuracy of the gas cooler heat transfer rate (Figure 5.15); the accuracies at the coolers (Figures 5.5c, 5.6c, and 5.7c), the buffers, and the fume heat exchanger (Figure 5.10) are also relevant. This explains why the error on the total recovered heat transfer is smaller than that on the gas cooler.

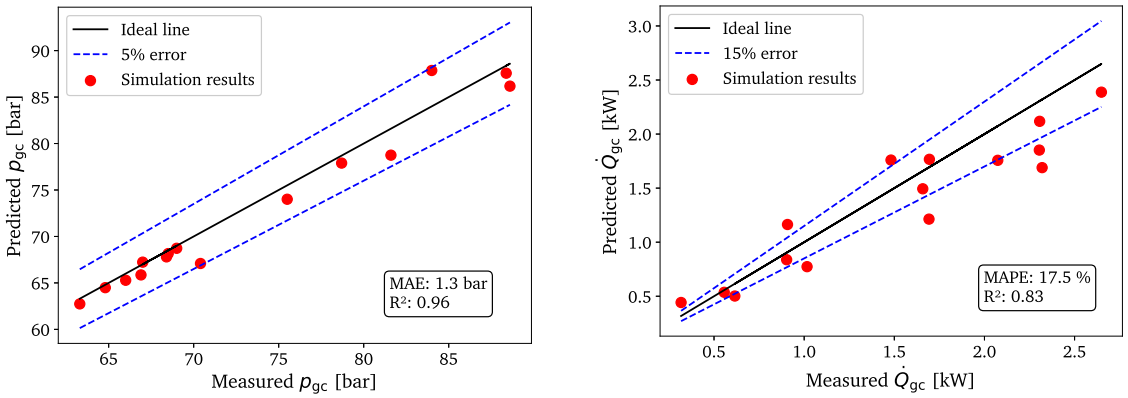

(a) High-pressure.

(b) Gas cooler heat transfer rate.

Figure 5.15: TCHP-HYB model steady-state parity plots showing the gas cooler predicted outputs compared to the measured ones.

The importance of showing R^2 is to evaluate whether the model changes are coherent with the data under different operating conditions, where the inputs are distinct in each case. The resulting MAPE and R^2 for the main model predictions in steady state are summarized in Table 5.3. The model shows strong explanatory power across most variables, with high R^2 values (> 0.8). Overall, the model performs well in fitting and predicting key variables, although there are accuracy limitations in the heat-exchange rates for the evaporator and gas cooler, that are justified by influencing other predicted inputs and the multi-stage error accumulation.

5.4.2 Transient Validation

The transient validation focuses on varying three key inputs: the low-pressure valve opening φ_{lpv}, the high-pressure valve opening φ_{hpv}, and the burner-fan speed ω_{bf}, which in turn governs the heater temperatures. The variation is performed in step-test fashion and

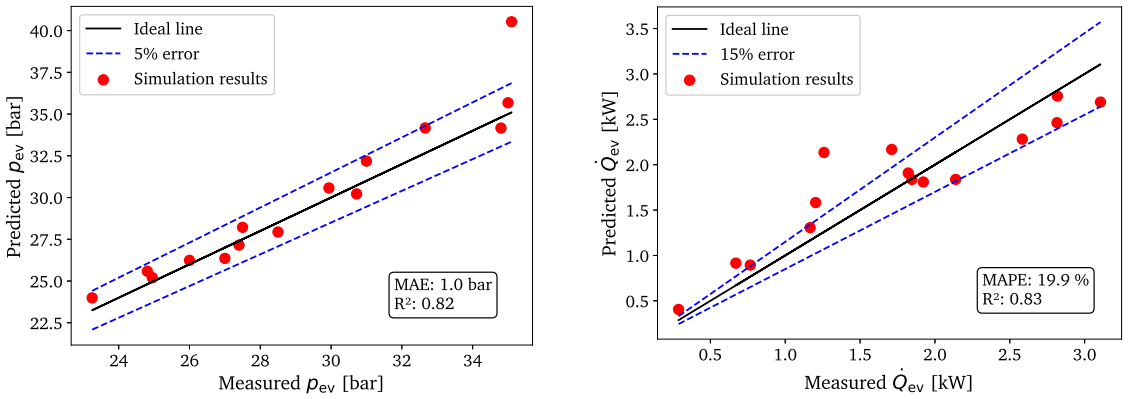

(a) Low-pressure

(b) Evaporator heat transfer rate.

Figure 5.16: TCHP-HYB model steady-state parity plots showing the evaporator predicted outputs compared to measured ones.

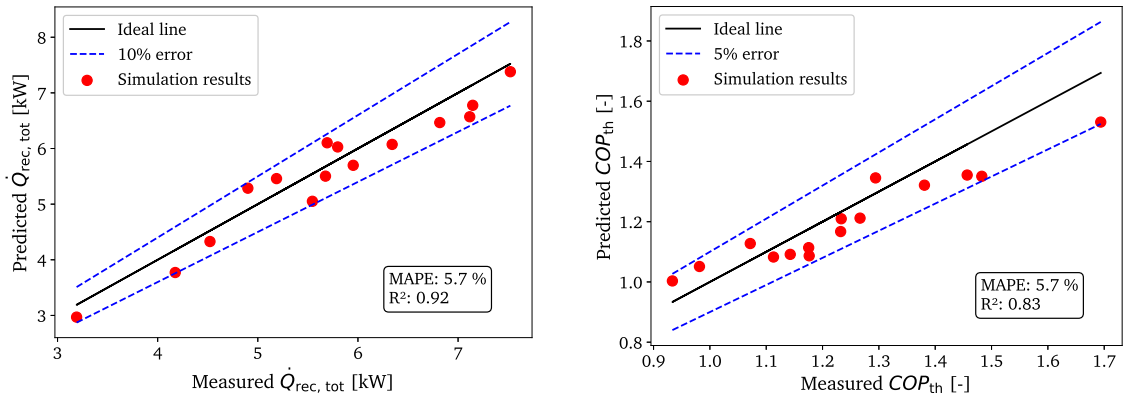

(a) total heat recovery rate.

(b) Thermal COP.

Figure 5.17: TCHP-HYB model steady-state parity plots showing the performance outputs of a TCHP.

Output	**MAPE [%] or MAE [bar]**	R^2
p_{gc}	1.3	0.96
p_{ev}	1	0.82
$\dot{Q}_{\mathrm{ev}}$	19.9 %	0.83
$\dot{Q}_{\mathrm{gc}}$	17.5 %	0.83
$\dot{Q}_{\mathrm{rec,tot}}$	5.7 %	0.92
COP_{th}	5.7 %	0.83

Table 5.3: MAPE, MAE (for pressure), and R^2 of model output predictions under steady-sate data conditions.

was introduced in Section 4.4.1. These tests are used here to validate the model's ability to reproduce transient changes in the outputs validated in Section 5.4.1, except for the gas cooler heat transfer rate, which is not available from the transient test data.

Figure 5.18 illustrates the outputs when the low-pressure valve opening is varied in a step-test manner (LPV test). The greatest influence is seen on the low-pressure level, owing to its strong correlation with mass-flow-rate changes driven by the low-pressure

valve. It also affects the evaporator heat transfer rate. Both transient trends are well captured by the model. A smaller impact is observed on high pressure and on the total recovered heat transfer rate. However, a discrepancy is observed in how these outputs are influenced. Specifically, variations in high pressure are mirrored in the total recovered heat and consequently in the thermal COP. This reflects the strong coupling between high-pressure dynamics and overall heat recovery. In contrast, the influence of changes in the low-pressure valve opening is not fully propagated to the high-pressure side, indicating a limitation in the current model's ability to capture this interaction.

Figure 5.19 presents the output variations when the high-pressure valve opening is changed in a step-test manner (HPV test). The largest influence is observed on the high-pressure level, where the model exhibits transient behavior consistent with the data. The effect on the total heat recovery rate due to changes in high pressure is also evident and well captured. Closing the valve and decreasing the outlet mass flow rate causes the pressure to rise to the supercritical state; however, the total recovered heat and the thermal COP decrease. This is due to a large reduction in mass flow rate to the stage, such that the heat transfer becomes less efficient. Some lag is also observed between the predicted and measured outputs, which is attributed to the single mass or pressure variation being governed by quasi-static mass flow rate equations.

Figure 5.20 shows several step changes applied to burner fan speed over a period of 250 minutes, reflecting the slow dynamics of the heater temperatures (BF test). Variations in burner fan speed (together with heater 1 and heater 2 temperatures) directly affect the mass flow rates, discharge temperatures, and the cooler heat-transfer rates of the TCs, which explains the observed variations in all outputs. The fast response due to sudden change of step test is not shown neither with data nor with model. This can be due to small step changes which are not too relevant on total recovered heat. So we evaluate our model with the PRBS done on burner fans speed

The model successfully captures both the fast response caused by sudden changes in BF and the slower response driven by the gradual evolution of heater temperatures. The resulting MAPE and R^2 metrics for each test are summarized in Table 5.4. Negative R^2 values in the LPV and HPV tests for gas cooler and evaporator pressures, respectively, stem from weak input–output correlations and measurement noise, which limit the model's explanatory power in those cases. In particular, the limited influence of the LPV on the high-pressure side, noted earlier, is reflected here in poor prediction of p_{gc}. In contrast, the BF tests (BF in Table 5.4) show an acceptable fit across all outputs due to the direct influence of BF on heater temperatures and thus on overall system behavior.

From the R^2 results, we conclude that HPV and BF have the strongest impact on system performance and are therefore critical control variables whose regulation can optimize key outputs. The negative R^2 values in the LPV and HPV cases for gas cooler and evaporator outputs may also reflect unmeasured dynamics in intermediate components (i.e., the flash tank and BUF1), for which no instrumentation is available. Nevertheless, the model effectively reproduces the dominant dynamics associated with HPV and BF and is considered suitable for subsequent control and optimization studies.

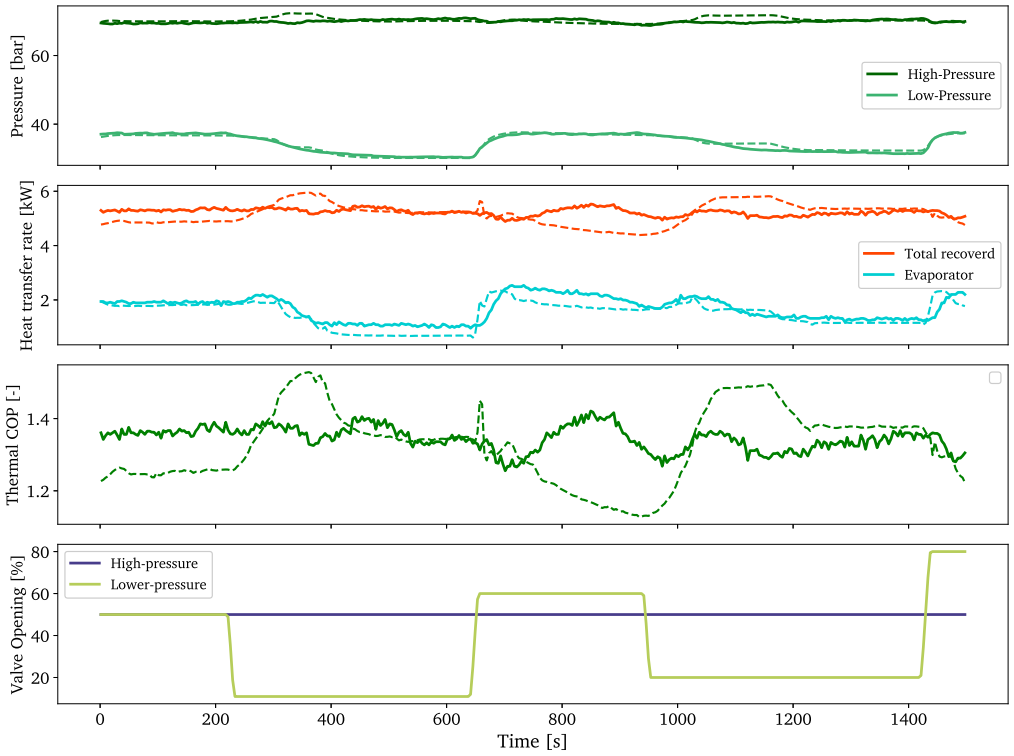

Figure 5.18: TCHP-HYB model transient validation with real experimental data varying the low-pressure valve opening. The real data is in solid, while simulated model is dashed.

Output	MAPE [%] or MAE [bar]			R^2		
	HPV	**LPV**	**BF**	**HPV**	**LPV**	**BF**
p_{ev}	0.97	1.2	0.68	-3.1	0.93	0.65
$\dot{Q}_{\text{ev}}$	14.4	22.2	15.2	0.40	0.72	0.81
p_{gc}	1.5	0.84	1	0.94	-3.3	0.74
$\dot{Q}_{\text{rec,tot}}$	4.7	4.0	3.7	0.61	-3.4	0.96
COP_{th}	4.7	4.0	3.7	0.61	-3.4	0.84

Table 5.4: MAPE, MAE (for pressure), and R^2 of model output predictions under transient step tests for LPV, HPV, and BF.

5.5 Conclusion

In this chapter:

- A literature review of dynamic modeling approaches for VCCs in general, and transcritical CO_2 cycles in particular, was presented. These models enable real-time system representation and are indispensable for control development.
- A dynamic model of the TCHP was developed using the FV method. Each cycle component was modeled individually: slow dynamics (cycle heat exchangers, flash tank, and heater temperature variations) were represented by differential equations derived from mass and energy balances on CVs obtained through spatial discretization, while fast dynamics (thermal compressors, valves, and the fume heat exchanger) were modeled quasi-statically using empirical correlations tuned to steady-state ex-

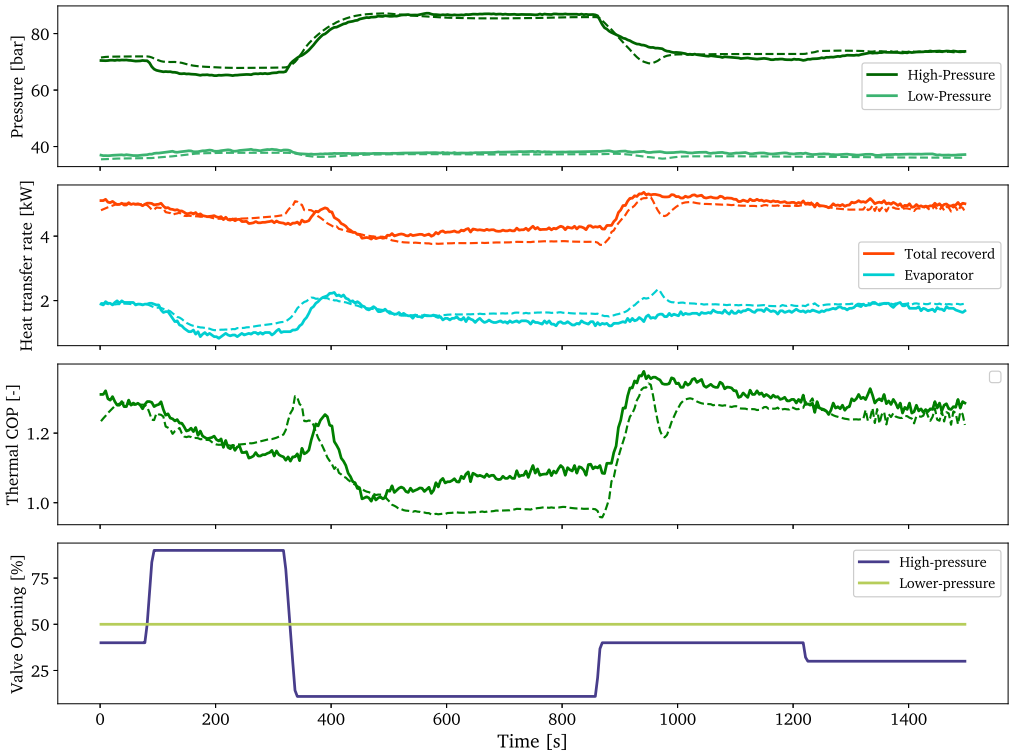

Figure 5.19: TCHP-HYB model transient validation with real experimental data varying the high-pressure valve opening. The real data is in solid, while simulated model is dashed.

perimental data.

- The component submodels were connected into a complete TCHP-HYB model. Their interconnections highlight the coupling and dependencies across the cycle. The solving process of the hybrid model was described in detail.
- The model was validated against both steady-state and transient data. Steady-state validation assessed prediction accuracy across different operating conditions, while transient validation examined the model's dynamic response to single-input variations. These complementary tests confirmed the model's validity, with acceptable MAPE and R^2 values in both steady and transient regimes. The resulting TCHP-HYB model can therefore serve as a reliable reference for future control and optimization studies.

The derived TCHP-HYB model provides a reliable representation of the real system. The steady-state validation confirmed that the model captures the influence of input variations across a wide range of operating conditions, while the transient validation demonstrated its ability to reproduce the main dynamic trends with acceptable accuracy. Together, these results establish the model as a valid reference for analyzing system behavior. Nevertheless, the full TCHP-HYB model remains computationally demanding due to the level of detail in the differential submodels and the iterative nature of the solution process. For real-time applications such as control and optimization, reduced-order models are therefore required. The next chapter addresses this challenge by developing simplified dynamic representations of the system, based on data-driven approaches, and by introducing a new model predictive control (MPC) strategy built upon these reduced models.

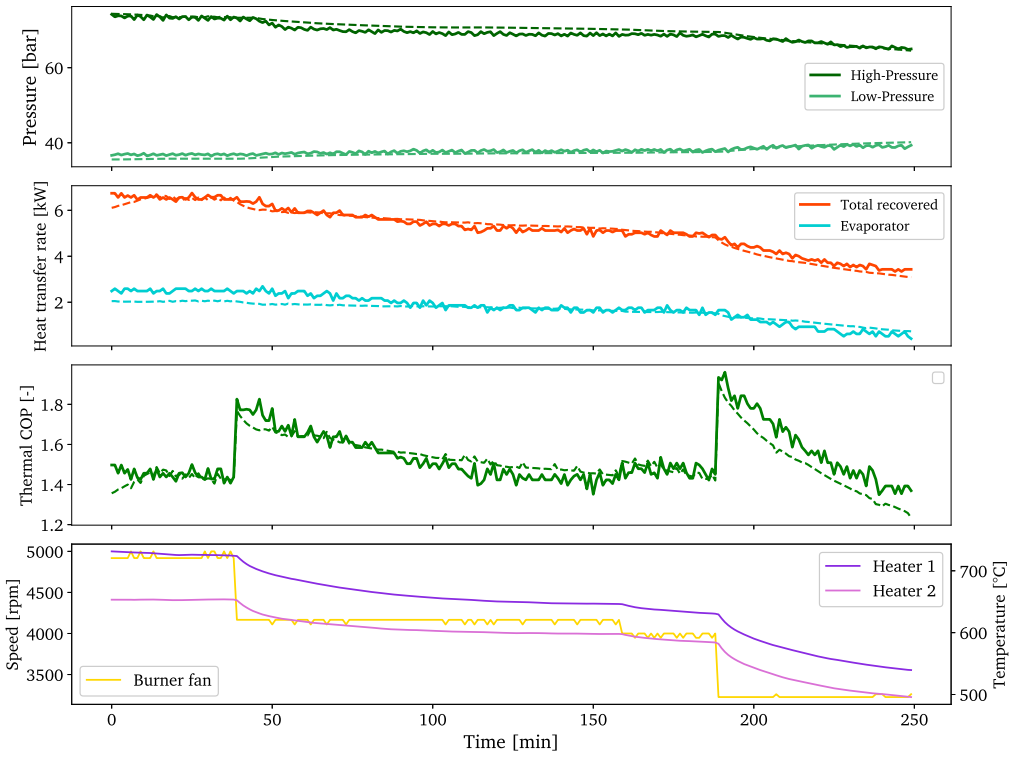

Figure 5.20: TCHP-HYB model transient validation with real experimental data varying the burner fan speed. The real data is in solid, while simulated model is dashed.

Chapter 6

RNN reduced model and MPC control for a TCHP

Abstract

Building on the hybrid TCHP-HYB model developed and validated in the previous chapter, this chapter addresses the design of an advanced control strategy for the TCHP. The objective is to enhance the system's energy efficiency and ensure a more sustainable use of natural gas through improved control. Since the experimental TCHP prototype is no longer available at the time this topic was studied during the PhD thesis, the proposed strategy is implemented and tested on the validated TCHP-HYB model, which serves as the reference system for control development.

Section 6.1 reviews control strategies for VCCs and the reduced models required for their implementation. Since a TCHP operates as a transcritical CO_2 cycle, this section discusses the significant influence of operating high-pressure values on performance, which has led to several attempts to derive optimal correlations. It then reviews control methods specific to such cycles. The review highlights the increasing relevance of advanced strategies in response to growing energy efficiency demands and regulatory constraints. Section 6.2 then formulates the control problem for the targeted TCHP application. The current control strategy is described and evaluated on a real case study to expose its limitations. As a replacement, a new strategy based on model predictive control (MPC) and a recurrent neural network (RNN)-type prediction model is proposed. Section 6.3.1 introduces the two RNN-based reduced models considered: the vanilla RNN and the long short-term memory (LSTM), both trained on real and TCHP-HYB model-generated data and validated on unseen samples. The MPC design, including the objective function, is presented in Section 6.3.2. Finally, Section 6.3.3 compares the MPC strategy with the existing control strategy using the TCHP-HYB model, by varying the water-supply temperature setpoints and evaluating both the temperature error and the thermal COP.

6.1 Control strategies for vapor compression cycles

The primary objective of any control system is to ensure optimal and stable performance under varying operating conditions. In VCCs, this involves meeting heating or cooling demands while maintaining desired temperature levels. However, the intrinsic nonlinear-

ities of the thermodynamic processes, the strong coupling between system variables, and the dependence of performance on boundary conditions (e.g., ambient temperature, load fluctuations) make this task particularly challenging. These challenges become even more critical under increasing energy restrictions, creating a growing need for more flexible and advanced control systems.

VCC control is generally organized into two levels: supervisory control and local control (Figure 6.1). The supervisory layer coordinates multiple local controllers by providing set-points—typically the supply temperature or power output—while considering variables such as outdoor conditions and power consumption (Péan et al. (2019)).

In contrast, local controllers focus on maintaining system stability and accurately tracking the set-points provided by the supervisory layer, often without directly optimizing for energy efficiency. As reviewed by Goyal et al. (2019), local control strategies in VCCs range from basic on/off and proportional–integral-derivative (PID) control to advanced mofrl predictive control(MPC) implementations. The literature highlights the benefits of multivariable control over conventional single-input single-output (SISO) loops, particularly for handling the coupled dynamics of VCCs. This chapter extends primarily on local control approaches for VCCs.

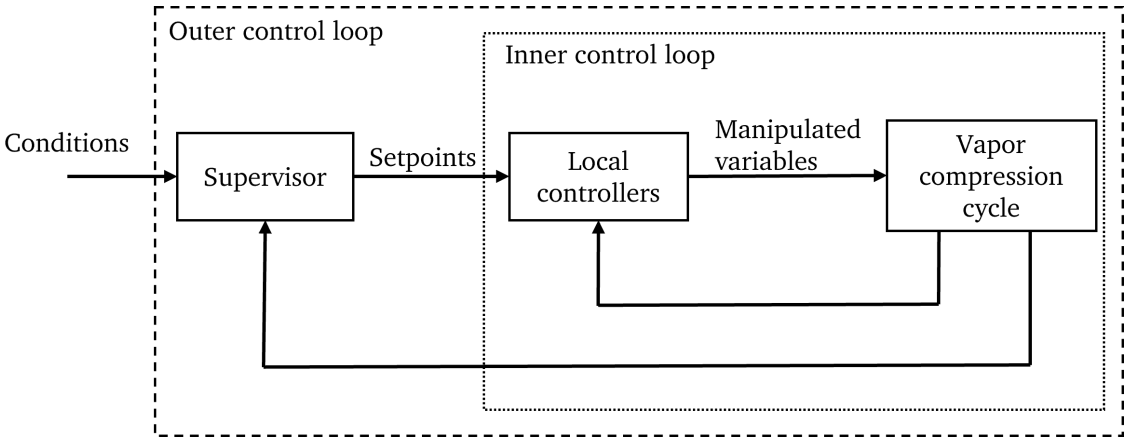

Figure 6.1: VCC overview of a hierarchical control scheme (reproduced from Beghi et al. (2017)).

6.1.1 Degrees of freedom

In a single stage VCC, degrees of freedom are the independent variables that can be manipulated to control system outputs. As detailed by Jensen and Skogestad (2007), the system thermodynamic state can be fully defined by three enthalpy values (at the outlets of the evaporator, condenser, and compressor), one pressure (or temperature), and the refrigerant mass flow rate. This gives five independent variables which, theoretically, could all be used for control. However, in practical applications, only two degrees of freedom are commonly manipulated: the compressor speed and the expansion valve opening. These allow for regulation of key performance metrics while letting other parameters vary based on external conditions.

6.1.2 History of control systems

Initial control strategies in VCCs were primarily based on on/off switching and refrigerant bypass as applied by Zubair and Bahel (1989). The introduction of variable-speed drives, electronic expansion valves, and micro-controllers has enabled more advanced control possibilities Braven et al. (1993). In practice, this meant moving from simple on/off operation to continuous modulation of cycle components, which has since become widely adopted. This shift opened the door to numerous control strategies aimed at optimizing performance under varying operating conditions.

Early implementations of feedback control used variable-speed compressors and controllable expansion valves in single-loop or decoupled PI structures. Based on a VCC model, Vargas and Parise (1995) showed that the closed-loop system achieves significant energy savings compared with on/off operation. Qureshi and Tassou (1996) reviewed several capacity control methods for refrigeration systems, concluding that variable-speed control is the most relevant. Outtagarts et al. (1997) developed and tested two control algorithms to operate the opening and closing of an electric expansion valve in a refrigeration system, validating their performance under both steady-state and transient conditions to ensure stable refrigerant flow and accurate superheat control. Compared to a thermostatic valve, the authors also showed that using an electric expansion valve resulted in faster response and better stability.

Later, Wu et al. (2005) developed a simplified lumped-parameter dynamic model for a multi-evaporator air conditioner and proposed a novel control strategy using suction pressure to modulate compressor speed and room air temperatures to regulate electronic expansion valves, incorporating a self-tuning fuzzy control algorithm that demonstrated effective and stable control performance in simulations. Marcinichen et al. (2008) demonstrated a dual-PI control architecture—one loop for cooling capacity via compressor speed, and another for superheat via valve opening. Both input/output relations were described by linear first-order models with delay, and Ziegler–Nichols was used for tuning the PID parameters. Although effective near the design point, these methods struggled under wide operating conditions, as they could not adequately handle the strong interactions and nonlinearities between cycle variables. This limitation motivated the move toward multivariable and advanced control strategies, which explicitly account for system coupling and operating flexibility.

6.1.3 MPC and advanced control

He et al. (1997) was among the first to question the adequacy of SISO control in a VCC. To this end, the authors developed a MB model for a VCC and studied the effects of control inputs such as compressor speed, condenser fan speed, and expansion valve, showing strong coupling between inputs and outputs, thus suggesting multi-input multi-output (MIMO) controllers as a solution. He et al. (1998) then translated this by introducing a linear–quadratic–Gaussian MIMO controller for a VCC, showing improved response time and robustness compared to traditional SISO systems.

MPC, known for handling multivariable constraints and anticipating disturbances, has been used for VCCs. For a refrigeration system, Leducq et al. (2006) developed an MPC controller for delivering the desired refrigerating capacity while maximizing the COP by

finding the optimal compressor speed and condenser flow rate. The method experimentally increased the COP by 8–20%. Elliott and Rasmussen (2008) employed a MIMO MPC to control the cooling capacity and superheat of each evaporator by adjusting the compressor speed and discharge valve opening, while standard PI controllers regulated system pressures. Wallace et al. (2012) developed a linear MPC with an offset-free mechanism. Controlling both the expansion valve and compressor speed with the MPC resulted in higher efficiency compared to dual SISO PIDs. Focusing on destroyed exergy as a performance criterion, Jain and Alleyne (2015) developed a MIMO MPC controller for a VCC, resulting in reduced destroyed exergy across components and highlighting the importance of MIMO controllers. Prášek et al. (2020) developed and validated a heat pump controller using range MPC control, replacing fixed setpoints with a funnel of time-varying soft constraints to optimize efficiency under feasible operation.

In summary, due to the strong coupling in VCC dynamics, MIMO controllers generally outperform decoupled SISO strategies. Among these, MPC has become the most widely accepted, both in research and industrial applications, thanks to its ability to handle multivariable constraints and anticipate disturbances. A crucial enabler of such controllers is the availability of reduced models, which provide sufficiently accurate dynamics while being computationally efficient for real-time optimization.

6.1.4 Reduced models

Reduced models serve different purposes across control strategies: for PID controllers, they are often used for parameter tuning (Outtagarts et al. (1997)), while for MPC they serve optimization tasks (Wallace et al. (2012)). These models may be mathematically derived from reducing physics-based approaches such as FV and MB formulations (Section 5.1), as in Rodriguez and Rasmussen (2016), or obtained directly from data that can be retrieved from experiments or physical model through system identification or machine learning. Compared to reduced physics-based models, data-driven models are more widely used for control because they are faster to develop and can achieve high accuracy within their training domain. Their main limitation, however, is that validity is often restricted to the conditions under which they were identified or trained. For this reason, model structure and order must be chosen carefully—ideally informed by physical insight—while remaining minimal enough to avoid overfitting. The objective is to capture the essential dynamics with the simplest model that still satisfies control performance requirements.

Another critical step is the design of excitation tests. The input signals must excite the system dynamics sufficiently to reveal nonlinearities, while remaining within safe limits so as not to invalidate the model. These tests form the basis for system identification, where mathematical models of dynamical systems are obtained by observing their input–output behavior. System identification techniques, extensively investigated by Ljung (1999), have been widely applied in VCCs. For example, Lin and Yeh (2007) linearly identified evaporator wall temperature and superheat with compressor speed and valve opening as control inputs. Similarly, Shah et al. (2004) derived a state-space model for automotive air-conditioning systems based on a MB formulation, while Rasmussen and Alleyne (2006) proposed control-oriented modeling approaches and recommended system

identification methods also grounded in MB models.

Machine learning approaches, especially deep networks, have recently been applied to complement and extend classical system identification tools, and their role is expected to grow further Pillonetto et al. (2025). Unlike linear or MB-based identification methods, neural network (NN) models can capture highly nonlinear relationships and complex system dynamics, which makes them particularly relevant for VCC cycles. For example, Nanayakkara et al. (2002) proposed a dynamic NN to control an ammonia evaporator process, and Bechtler et al. (2001) introduced an ANN-based framework for dynamic modeling of vapor-compression liquid chillers.

A common limitation, however, is that standard feedforward NNs are not well-suited for time-series modeling when used in system identification. To overcome this, recurrent neural networks (RNNs) have emerged as more appropriate tools due to their ability to retain memory of past inputs and outputs through hidden states. For instance, Parlos et al. (1994) suggested an RNN structure for modeling transient responses of a heat exchanger, while Ma et al. (2024) developed a GRU-based model to represent VCC components while explicitly enforcing physical conservation laws.

The ability of NNs to capture nonlinear dynamics also makes them highly attractive for integration with MPC, where accurate and adaptable models are essential for real-time optimization Ren et al. (2022). In HVAC applications, most NN–MPC implementations have been explored at the supervisory level, particularly for building energy management systems Afram et al. (2017). At the local control level of vapor-compression cycles, however, only one attempt was found: Turgut and Çoban (2020) proposed an NN–MPC approach for a vapor-compression refrigeration cycle, testing multiple objective functions (COP and exergy efficiency) while tracking a desired cooling load.

6.1.5 Control of transcritical CO_2 cycles

Having outlined control strategies for general VCCs, we now turn to approaches tailored to the unique characteristics of CO_2 systems. Among these, the regulation of high-side pressure has received particular attention due to its dominant influence on cycle performance and its role as a primary control variable in transcritical operation.

6.1.5.1 Optimal high-pressure

In a subcritical heat pump cycle, once the evaporation and condensation temperatures are fixed, system performance is fully determined. In contrast, in a transcritical CO_2 cycle, where the working fluid operates above the critical point, temperature and pressure become independent variables. When the outlet temperature of the gas cooler is specified, the high-side pressure directly impacts the enthalpy of the fluid and therefore the cycle efficiency. Numerous theoretical and experimental studies have shown that the COP of a transcritical CO_2 cycle depends strongly on the high-pressure setting. Consequently, much effort has been devoted to identifying the optimal high-pressure that maximizes COP.

Theoretically, and based on mathematical models, Kauf (1999) proposed a correlation to estimate the optimal pressure based solely on the CO_2 temperature at the gas cooler outlet, valid for temperatures between 35 °C and 50 °C. Liao et al. (2000) extended this by including the evaporator temperature and compressor isentropic efficiency, while Sarkar

et al. (2004) derived expressions to estimate optimal pressure, optimal gas cooler inlet temperature, and corresponding COP, for evaporator temperatures ranging from –10 °C to 10 °C, and gas cooler outlet temperatures between 30 °C and 50 °C. Chen and Gu (2005) derived an optimal high-pressure correlation highlighting the importance of using an IHX.

Enriched with experimental work, Aprea and Maiorino (2009) studied a CO_2 split-system for residential cooling. Based on a simplified predictive model validated by experiments, the authors found an optimal high-pressure correlation and proposed an algorithm to regulate the real high-pressure according to setpoint by control an electronic back-pressure valve. Zhang et al. (2010) developed a new correlation by analyzing a system with dual expansion valves, reducing the deviation from experimental data to less than 1%. Qi et al. (2013) provided a simplified correlation for optimal pressure as a function of the gas cooler outlet temperature, with respective errors of 5% for pressure and 6% for COP, valid for outlet temperatures from 25 °C to 45 °C and ambient temperatures between –15 °C and 30 °C.

The gas cooler exit temperature depends on the secondary fluid inlet temperature; thus, for any given discharge pressure, the cooler exit temperature is fixed by the inlet condition. The existence of an optimal pressure for a fixed cooler exit temperature is supported by the following argument from Sarkar et al. (2004). The COP in heating mode for a transcritical CO_2 cycle (Figure 4.2a) is given by:

$$COP = \frac{\dot{Q}_{gc}}{\dot{W}} = \frac{\dot{m}(h_2 - h_3)}{\dot{m}(h_2 - h_1)} \tag{6.1}$$

If the discharge pressure increases from p_2 to $p_2^{'}$ while maintaining a constant gas cooler outlet temperature (transition from point 3 to 3' in Figure 6.2), the COP becomes:

$$COP = \frac{(h_2 - h_3) + \Delta h_3 + \Delta h_2}{(h_2 - h_1) + \Delta h_2} \tag{6.2}$$

$\Delta h_3 = h_3 - h_3^{'}$ and $\Delta h_2 = h_2^{'} - h_2$. From Figure 6.2, it is observed that $\Delta h_3 > \Delta h_2$, which explains the initial increase in COP. However, beyond a certain pressure, the compression work outweighs the gain in heat transfer, and the COP starts to drop. This critical point defines the optimal cycle pressure. Around the critical pressure, the heat delivered to the hot side increases rapidly, while the compression work rises linearly. The COP follows this trend and reaches a maximum at the optimal pressure.

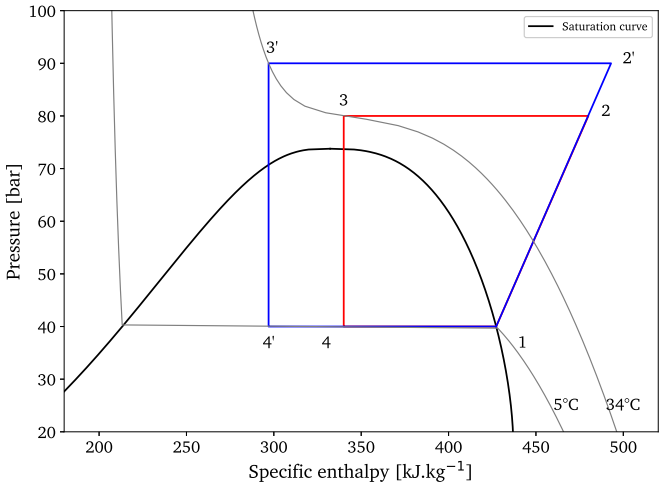

Figure 6.2: Transcritical CO_2 cycle p–h diagrams: (1–2–3–4) in red and (1–2′–3′–4′) in blue, each at a different high-pressure value.

From the various correlations derived in the literature, it is clear that no generalized high-pressure correlation exists for all CO_2 heat pumps; instead, each unit must establish its own relation, either from experimental data or through reliable simulation models, a process that can be time consuming. Once an optimal high-pressure correlation is defined, a control law is required to ensure the system follows it, often implemented by regulating the expansion valve (Aprea and Maiorino (2009)). However, due to their lack of generality and the effort required to derive them, the use of such correlations has been questioned. For instance, Cecchinato et al. (2010) emphasized the need for real-time optimization rather than relying on simplified correlations. Similarly, Minetto (2011) observed that the parameters commonly used in optimal high-pressure correlations are insufficient, and therefore proposed an adaptive control logic after conducting both theoretical and experimental studies on a CO_2 heat pump for domestic hot water.

6.1.5.2 Control methods

This section expands on control methods for transcritical CO_2 cycles reported in the literature. For instance, Zhang and Zhang (2011) proposed a correlation-free online optimal control strategy that dynamically adjusts the high-pressure setpoint to maximize COP. Along similar lines, Cecchinato et al. (2012) employed an online ANN model combined with real-time optimization to determine the high-pressure that maximizes COP, achieving close tracking of the optimal high-pressure and outperforming Liao's correlation, thus reducing energy consumption. Baek et al. (2013) optimized the gas-cooler pressure of a CO_2 heat pump by jointly controlling the expansion valve opening and outdoor fan speed, identifying operating points that maximized COP under varying compressor frequencies and ambient conditions. Salazar and Méndez (2014) compared PID and nonlinear controllers on a lumped transcritical CO_2 model, showing that nonlinear control improved stability in handling the challenging gas cooler dynamics. Peñarrocha et al. (2014) proposed a real-time, model-free optimization strategy that minimizes compressor power using a perturb-and-observe algorithm with auto-tuned controllers, and validated it experimentally. Hu et al. (2015) applied extremum-seeking control on a Modelica-based simulator

to maximize COP in a model-free manner, showing effective adaptation to varying ambient conditions. Rampazzo et al. (2019) applied extremum-seeking control experimentally, showing improved COP tracking and outperforming offline optimal high-pressure correlations. Beghi et al. (2017) applied reinforcement learning for model-free optimization, enhancing energy efficiency and enabling smart grid integration. Qin et al. (2019) analyzed the influence of compressor frequency on system performance and derived a new dimensionless correlation for the optimal discharge pressure using the Buckingham pi theorem. Lastly, Wang et al. (2021) proposed an MPC leveraging a nonlinear data-driven state-space model to maximize COP while meeting water temperature demand.

Control strategies for VCCs have evolved from basic on/off and PID regulation toward more advanced methods such as MPC, reflecting the need for improved efficiency under increasing energy restrictions. For transcritical CO_2 systems, this evolution has led from simple PID control with offline correlations for high-side pressure to online optimization schemes based on MPC or extremum seeking. In parallel, NNs have shown strong potential in capturing complex nonlinear dynamics, yet their application in VCC control remains limited. Since the performance of MPC depends critically on the accuracy of its prediction model, this work proposes the integration of RNNs into an MPC framework. The contribution is to design and evaluate an RNN–MPC control strategy of a TCHP, ensuring accurate supply water temperature tracking while minimizing energy consumption.

6.2 TCHP control problem formulation

As a residential heating application, a TCHP aims to deliver the user's heating demand efficiently. The control objective is therefore to track the supply water temperature setpoint while minimizing gas consumption. To achieve this, a baseline control strategy has been implemented, which is described below together with an experimental case study evaluating its performance.

6.2.1 Baseline control strategy

To operate a fully automated TCHP, the system inputs and outputs are coordinated through a hierarchical control logic designed to ensure stability and proper operation. This hierarchy (Figure 6.1) spans from high-level user commands, such as selecting a desired room temperature, down to low-level actuator decisions like the opening of expansion valves. Within this framework, the manipulated variables, disturbances, controlled outputs, and setpoints are summarized in Table 6.1. Supervisory control is rule-based, defining setpoints through correlations. For instance, the supply water temperature setpoint $T^{\mathrm{sp}}_{\mathrm{w,sup}}$ is derived from a heating-curve correlation based on outdoor conditions and the user's comfort settings. From this, the total recovered heat setpoint $\dot{Q}^{\mathrm{sp}}_{\mathrm{rec,tot}}$ is defined by a PID that minimizes the error between measured and target supply water temperature:

$$\dot{Q}^{\mathrm{sp}}_{\mathrm{rec,tot}} = PID(T_{\mathrm{w,sup}}, T^{\mathrm{sp}}_{\mathrm{w,sup}}). \tag{6.3}$$

This required heat is then mapped to the first heater temperature setpoint using a linear correlation g_1:

$$T^{\mathrm{sp}}_{\mathrm{h1}} = g_1(\dot{Q}^{\mathrm{sp}}_{\mathrm{rec,tot}}), \quad T^{\mathrm{sp}}_{\mathrm{h1}} \in [500, 800]^{\circ}\mathrm{C}. \tag{6.4}$$

Variable	name / Description	Unit
Manipulated variables		
ω_{bf}	Burner fan speed	[rpm]
φ_{hpv}	High-pressure valve opening	[%]
φ_{lpv}	Low-pressure valve opening	[%]
ω_{m1}	Motor 1 speed (TC1)	[rpm]
ω_{m2}	Motor 2 speed (TC2)	[rpm]
ω_{m3}	Motor 3 speed (TC3)	[rpm]
Disturbances		
$T_{\mathrm{w,ret}}$	Water return temperature	[°C]
$T_{\mathrm{mpg,in}}$	MPG inlet temperature	[°C]
$\dot{m}_{\mathrm{w}}$	Water mass flow rate	[g·s^{-1}]
$\dot{m}_{\mathrm{mpg}}$	MPG mass flow rate	[g·s^{-1}]
Controlled outputs		
$T_{\mathrm{w,sup}}$	Water supply temperature	[°C]
T_{h1}	Heater 1 temperature	[°C]
T_{h2}	Heater 2 temperature	[°C]
p_{gc}	Gas cooler pressure	[bar]
ΔT_{sh}	Superheat	[K]
Setpoints		
$T_{\mathrm{w,sup}}^{\mathrm{sp}}$	Water supply temperature setpoint	[°C]
$T_{\mathrm{h1}}^{\mathrm{sp}}$	Heater 1 temperature setpoint	[°C]
$T_{\mathrm{h2}}^{\mathrm{sp}}$	Heater 2 temperature setpoint	[°C]
$p_{\mathrm{gc}}^{\mathrm{sp}}$	Gas cooler pressure setpoint	[bar]
$\Delta T_{\mathrm{sh}}^{\mathrm{sp}}$	Superheat	[K]

Table 6.1: System variables categorized for control design.

The burner fan speed is controlled by a PID to track this heater setpoint (Figure 6.3a):

$$\omega_{\mathrm{bf}} = PID(T_{\mathrm{h1}}, T_{\mathrm{h1}}^{\mathrm{sp}}). \tag{6.5}$$

To prevent heater 2 from exceeding its thermal limit ($T_{\mathrm{h2,max}} = 800°\mathrm{C}$), motor 2 speed is regulated with a PID that tracks the same setpoint as heater 1:

$$\omega_{\mathrm{m2}} = PID(T_{\mathrm{h2}}, T_{\mathrm{h1}}). \tag{6.6}$$

The speeds of TC1 and TC3 are interpolated from the heat demand using empirical mappings g_2 and g_3:

$$\omega_{\mathrm{m1}} = g_2(\dot{Q}_{\mathrm{rec,tot}}^{\mathrm{sp}}), \quad \omega_{\mathrm{m3}} = g_3(\dot{Q}_{\mathrm{rec,tot}}^{\mathrm{sp}}). \tag{6.7}$$

For pressure regulation, a correlation g_4 relates the gas cooler outlet temperature to an optimal pressure setpoint:

$$p_{\mathrm{gc}}^{\mathrm{sp}} = g_4(T_{\mathrm{gc,out}}) = 1.47\, T_{\mathrm{gc,out}} + 31, \tag{6.8}$$

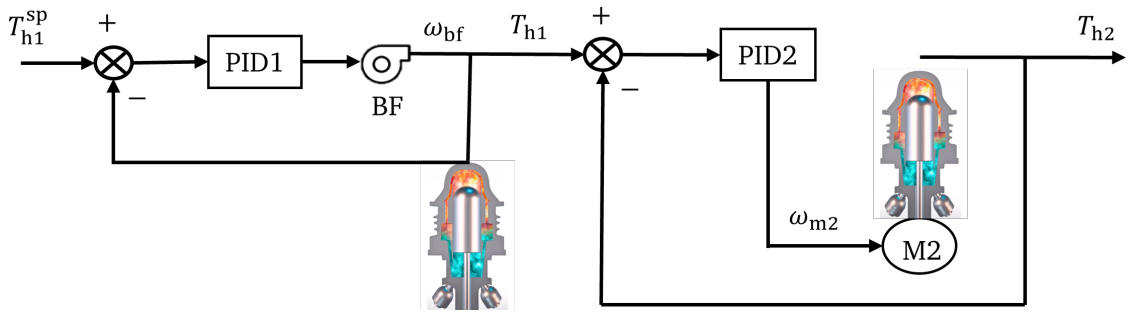

(a) Heater 1 temperature T_{h1} controlled by burner fan ω_{bf} and heater 2 temperature T_{h2} controlled by motor 2 speed ω_{m2} using two separate PIDs.

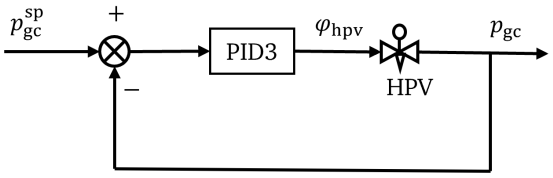

(b) Gas cooler pressure p_{gc} controlled by HPV valve opening φ_{hpv} using PID control.

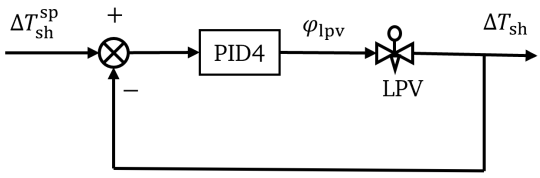

(c) Superheat ΔT_{sh} regulated by LPV valve opening φ_{lpv} using PID control.

Figure 6.3: TCHP SISO PID schemes.

which is followed by the high-pressure valve opening through a PID (Figure 6.3b):

$$\varphi_{\mathrm{hpv}} = PID(p_{\mathrm{gc}}, p_{\mathrm{gc}}^{\mathrm{sp}}). \tag{6.9}$$

Finally, the superheat setpoint ($\Delta T_{\mathrm{sh}}^{\mathrm{sp}} = 5$ K) is enforced by controlling the low-pressure valve opening with a PID (Figure 6.3c):

$$\varphi_{\mathrm{lpv}} = PID(\Delta T_{\mathrm{sh}}, \Delta T_{\mathrm{sh}}^{\mathrm{sp}}). \tag{6.10}$$

A PID controller is expressed as:

$$PID(x, x^{\mathrm{sp}}) = K_{\mathrm{p}}(x^{\mathrm{sp}} - x) + K_{\mathrm{i}} \int (x^{\mathrm{sp}} - x)\, dt + K_{\mathrm{d}} \frac{d(x^{\mathrm{sp}} - x)}{dt}, \tag{6.11}$$

where x^{sp} is the setpoint, x is the measured variable, and K_{p}, K_{i}, and K_{d} are the proportional, integral, and derivative gains. Equations (6.3)-(6.10) constitute the baseline control of the TCHP. While the baseline strategy coordinates all manipulated variables, this thesis focuses on the two most influential ones: burner fan speed ω_{bf} (and thus heater temperatures) and high-pressure valve opening φ_{hpv}. As shown in Chapter 5, these inputs exert the strongest influence on total recovered heat $\dot{Q}_{\mathrm{rec,tot}}$, supply water temperature $T_{\mathrm{w,sup}}$, and thermal COP (COP_{th}). Their importance is illustrated in Figure 6.4 and evaluated in the experimental case study that follows.

6.2.2 Experimental case study

The test is performed on a fully automated TCHP in the Boostheat laboratory using the same test bench as in Figure 4.3a and with the same control strategy described in the previous section. The outputs—supply water temperature, heater temperatures, and high-pressure values—are plotted in Figure 6.5, while the corresponding inputs, high-pressure valve opening and burner fan speed, are plotted in Figure 6.6. When varying the supply

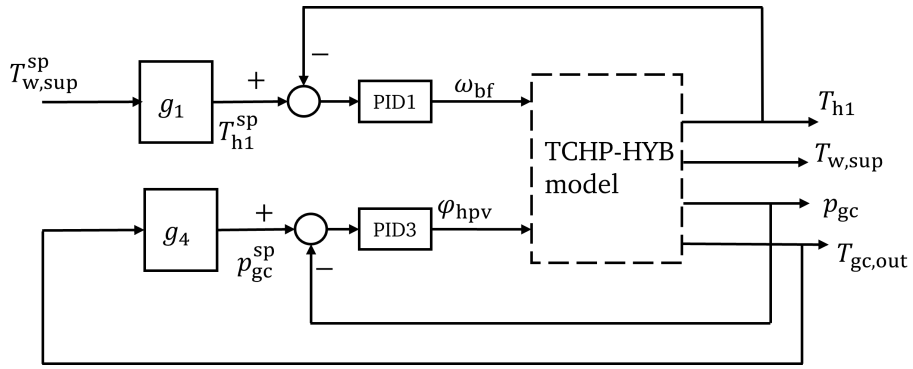

Figure 6.4: PID-based control strategy: The TCHP-HYB model is controlled using two parallel PID loops. The first loop adjusts the burner fan speed ω_{bf} to track $T^{\mathrm{sp}}_{\mathrm{h1}}$, which is correlated to $T^{\mathrm{sp}}_{\mathrm{w,sup}}$ via g_1. The second loop controls the HPV opening φ_{hpv} to regulate p_{gc}, where the setpoint $p^{\mathrm{sp}}_{\mathrm{gc}}$ is determined through the mapping $g_4(T_{\mathrm{gc,out}})$.

water temperature setpoint, the heater temperature setpoint also changes, which activates the PID on burner fan speed to track this setpoint. However, by doing so, the control disregards the faster response of the supply water temperature compared to that of the heater. This results in large overshoots. Another issue arises during the last step change, where tracking the high-pressure setpoint caused a deviation from the supply water temperature setpoint.

This difference in dynamics explains why the overshoot in the supply water temperature $T_{\mathrm{w,sup}}$ is not caused by the heater temperatures or solely by poor PID tuning, but rather by the rapid variation of ω_{bf}. Indeed, the overshoot trend in $T_{\mathrm{w,sup}}$ mirrors that of ω_{bf}. While improved PID tuning could reduce overshoots in the heater temperatures, the core issue lies in the control strategy itself. A more robust approach would link ω_{bf} directly to the supply water temperature $T^{\mathrm{sp}}_{\mathrm{w}}$. A simple PID would not be able to correct this, considering the constraints on heater temperature for not exceeding a maximum $T_{\mathrm{h1,max}} = 800$ °C. For this, an MPC is proposed, due to its ability to handle constraints and to control the two inputs ω_{bf} and φ_{hpv} simultaneously.

6.3 MPC-RNN proposed control strategy

A MIMO control strategy of the MPC type is thus proposed. This control is able to take into account the burner fan speed and the high-pressure valve opening simultaneously, in order to regulate the supply water temperature while minimizing energy consumption and respecting physical constraints. To achieve this, a suitable predictive model and an informative objective function must be defined. The new control strategy focuses mainly on burner fan speed and high-pressure valve opening as control inputs, while the other control logic described in Section 6.2 is kept the same. The MPC-based strategy is designed to replace these two SISO PID loops (Figure 6.4), as illustrated in Figure 6.7.

6.3.1 RNN reduced models

The performance of MPC critically depends on the accuracy of the underlying prediction model. To construct this model, a system identification approach based on NNs is em-

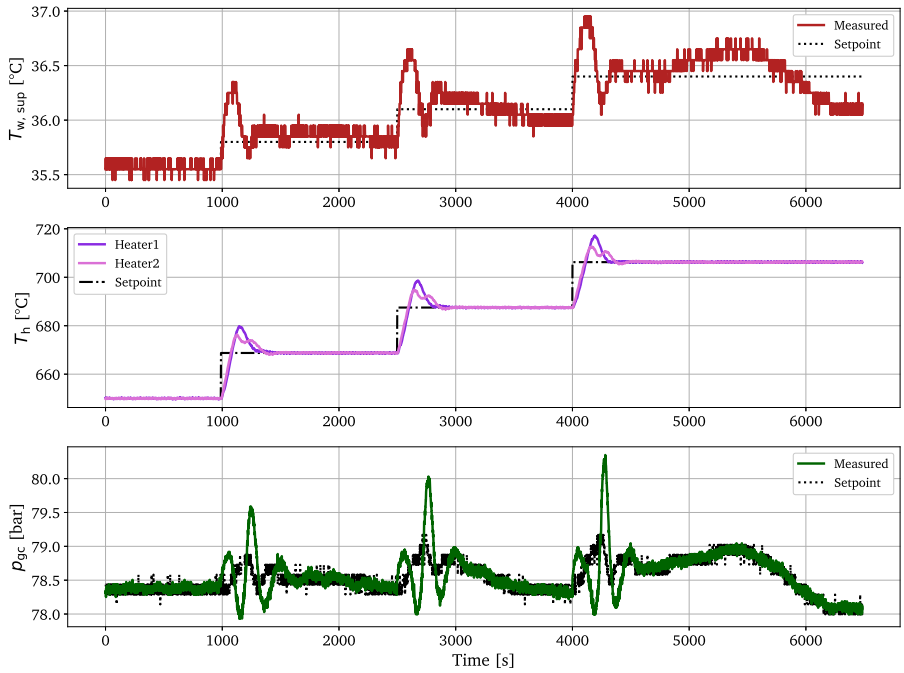

Figure 6.5: TCHP baseline control strategy: real evaluation showing variation of outputs: supply water temperature $T_{\mathrm{w,sup}}$, heater temperatures T_{h1} and T_{h2}, and high-pressure p_{gc}.

ployed due to the nonlinear behavior of TCHP processes. While conventional feedforward NNs offer one-way connections between neurons, RNNs introduce feedback connections that enable information to persist across time steps, making them well-suited for time-series modeling. In short, their ability to capture nonlinear behavior, provide fast computation, and incorporate inherent time-series learning makes RNN-type models an attractive choice as prediction models for MPC Ren et al. (2022).

Here, we implement two RNN-type models for system identification: a vanilla RNN, originally proposed by Elman (1990), and an LSTM, introduced by Hochreiter and Schmidhuber (1997).

6.3.1.1 Vanilla RNN

Since an RNN represents a discrete-time dynamical system, it is particularly well-suited for modeling sequential data where temporal dependencies play a critical role. In contrast to classical state-space models, where the state vector $x(k)$ has a direct physical interpretation, an RNN maintains a latent internal state $h(k)$ that evolves recursively and captures the system memory. This hidden state implicitly encodes temporal correlations through a first-order Markov structure. A vanilla RNN by Elman (1990) used for output prediction is described by the following equations:

$$h(k) = \sigma(W_z z(k) + W_h h(k-1) + b_h), \tag{6.12}$$

$$\hat{y}(k) = W_y h(k) + b_y, \tag{6.13}$$

where $z(k)$ includes past control inputs and outputs, σ is a nonlinear activation function (e.g., hyperbolic tangent $\tanh$), and W_z, W_h, W_y, b_h, and b_y are matrices and vectors learned during training by minimizing the error between predicted outputs $\hat{y}(k)$ and measured outputs $y(k)$.

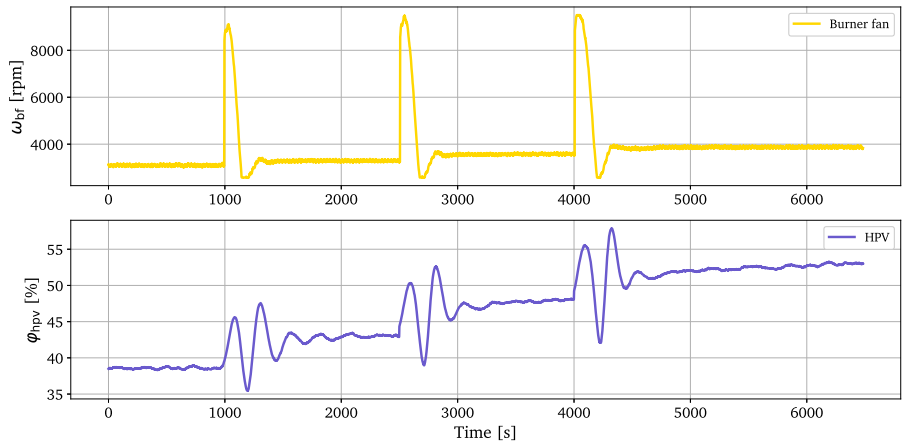

Figure 6.6: TCHP baseline control strategy real evaluation of system. Variation of inputs: burner fan speed ω_{bf} and high-pressure valve percentage opening φ_{hpv}.

6.3.1.2 LSTM

LSTM is a type of RNN proposed by Hochreiter and Schmidhuber (1997) to address the vanishing gradient problem in vanilla RNNs by incorporating internal gating mechanisms. This makes LSTM more suitable for long input sequences and, consequently, for system identification tasks. LSTM networks extend vanilla RNNs by introducing a memory cell $c(k)$ that enables long-term information retention. The hidden state $h(k)$ serves as short-term memory, while a gating mechanism regulates the flow of information. Each LSTM cell includes an input gate $i(k)$, forget gate $\tilde{f}(k)$, candidate cell state $\tilde{c}(k)$, and output gate $o(k)$. The update equations are defined as follows:

$$
\begin{aligned}
i(k) &= \sigma(W_i z(k) + R_i h(k-1) + b_i), \\
\tilde{f}(k) &= \sigma(W_f z(k) + R_f h(k-1) + b_f), \\
\tilde{c}(k) &= \tanh(W_g z(k) + R_g h(k-1) + b_g), \\
o(k) &= \sigma(W_o z(k) + R_o h(k-1) + b_o), \\
c(k) &= \tilde{f}(k) \odot c(k-1) + i(k) \odot \tilde{c}(k), \\
h(k) &= o(k) \odot \tanh(c(k)), \\
\hat{y}(k) &= W_y h(k) + b_y.
\end{aligned}
\tag{6.14}
$$

Here, $\odot$ the Hadamard (element-wise) product. The LSTM weights are grouped as $\{W_i, W_f, W_g, W_o\}$ for the network input $z(k)$ and $\{R_i, R_f, R_g, R_o\}$ for the hidden state $h(k)$. The corresponding bias vectors are $\{b_i, b_f, b_g, b_o\}$. This formulation follows the standard LSTM structure.

6.3.1.3 RNN architecture

Both models are designed to capture the dynamic evolution of the supply water temperature, using input–output data from experiments on the real system and the TCHP-HYB model. To ensure consistency, they adopt an encoder–decoder structure: the encoder processes past outputs and control inputs, while the decoder recursively predicts future outputs over a specified horizon, conditioned on known future control inputs (Figure 6.8).

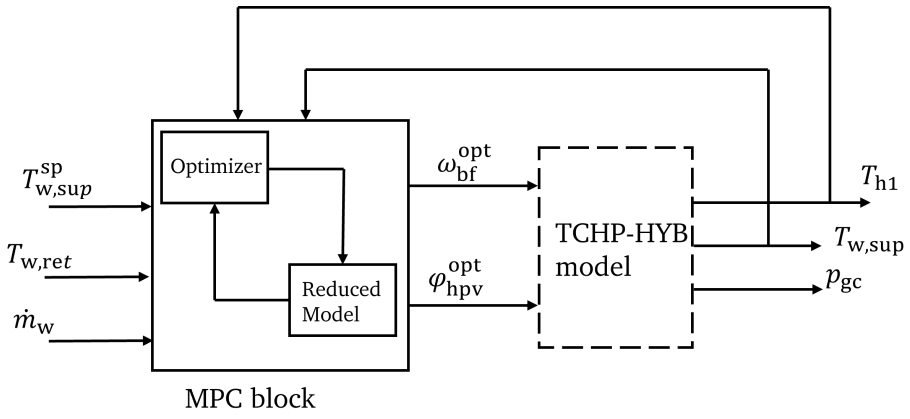

Figure 6.7: MPC-based control strategy: This model predictive control framework relies on a learned model of the system based on vanilla RNN or LSTM as reduced models. The optimizer computes the optimal control actions $\varphi^{\text{opt}}_{\text{hpv}}$ and $\omega^{\text{opt}}_{\text{bf}}$ over a prediction horizon to track the $T^{\text{sp}}_{\text{w,sup}}$, given the current return water temperature $T_{\text{w,ret}}$ and water mass flow rate $\dot{m}_{\text{w}}$. The optimizer uses predictions from the reduced model, which captures the system dynamics. The optimized inputs are applied to the TCHP-HYB model, and the resulting outputs $T_{\text{w,sup}}$ and T_{h1} are fed back to the MPC block.

The input vector for both vanilla RNN and LSTM is $z(k) = [y(k-1),\, u(k),\, d(k)]^\top$, where the measured output is $y = T_{\text{w,sup}}$, the control inputs are $u = [\omega_{\text{bf}},\, \varphi_{\text{hpv}}]^\top$, and the disturbances are $d = [\dot{m}_{\text{w}},\, T_{\text{w,ret}}]^\top$. Training requires y measured under sufficiently exciting variations of u and d.

6.3.1.4 Data processing

To provide sufficient excitation and expand the available dataset (transient sequences from Section 4.4.1), the TCHP-HYB model was further stimulated with step changes of varying amplitudes in u and d, staying within the bounds in Table 6.2. The resulting dataset contains 60,000 samples at one-second resolution, with approximately 30% from experiments and the remainder from simulations. Each subset was split chronologically into training (80%), validation (10%), and test (10%) partitions to preserve temporal continuity. All inputs were standardized (zero mean, unit variance) for numerical stability.

For multi-step prediction, the data was reshaped into overlapping sequences using a sliding window. Each training sequence consists of 10 past time steps ($l_{\text{seq}} = 10$) as encoder input, while the decoder predicts the following 10 steps ($l_{\text{pred}} = 10$).

6.3.1.5 Model training

Both vanilla RNN and LSTM models use a single recurrent layer with 16 hidden units, followed by a fully connected output layer. A dropout rate of 10% is applied after the recurrent layer to mitigate overfitting. Models are trained with the Adam optimizer (learning rate 0.001) and mean squared error (MSE) loss, using mini-batches of size 32. Training lasted up to 200 epochs with early stopping based on validation loss. The best model was selected by validation performance and evaluated on the test set using MSE and R^2.

The vanilla RNN converged in about 21 minutes, reducing MSE validation loss from

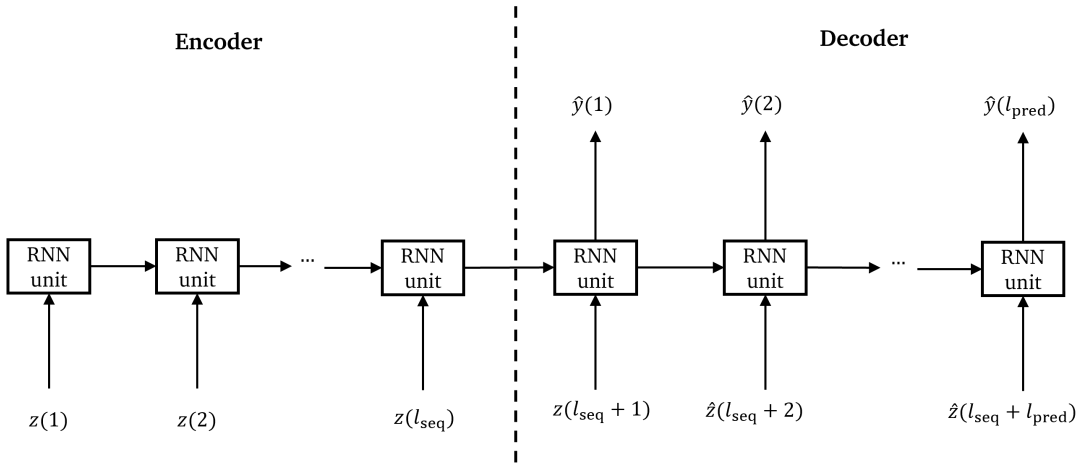

Figure 6.8: Encoder–decoder RNN architecture unrolled over time steps. The encoder processes past inputs $z(1)$ to $z(l_{\text{seq}})$, and the decoder recursively predicts future outputs $\hat{y}(1)$ to $\hat{y}(l_{\text{pred}})$, conditioned on known future inputs. This structure allows the model to capture temporal dependencies and generate multi-step predictions.

5.22 K^2 to 0.0871 K^2. The LSTM required around 40 minutes, with MSE validation loss decreasing from 3.7 K^2 to 0.06 K^2. These results confirm the ability of RNN-type models to capture nonlinear, dynamic behavior effectively.

Parameter	**Description**	**Range**
φ_{hpv}	High-pressure valve opening	11–100 %
ω_{bf}	Burner fan speed	2000–9500 rpm
$T_{\text{w,ret}}$	Return water temperature	20–45 °C
$\dot{m}_{\text{w}}$	Water mass flow rate	130–450 g.s^{-1}
$T_{\text{w,sup}}$	Supply water temperature	25–55 °C

Table 6.2: Operating ranges of input and output variables used for training the RNN reduced models.

6.3.1.6 Models validation

As a prediction model for MPC, both models must be evaluated over multiple future steps.

Figure 6.9 illustrates the model's performance on a test sample of length 5050 from the test dataset. The vanilla RNN is initialized five times using 10 previous samples, and then recursively predicts the next 500 time steps. The supply water temperature $T_{\text{w,sup}}$ is predicted with a MSE of 0.84 K^2 and an R^2 score of 0.975.

Figure 6.10 shows the validation of the LSTM prediction over the next 500 steps, using the same setup as for the vanilla RNN. The supply water temperature $T_{\text{w,sup}}$ is predicted with a MSE of 0.76 K^2 and an R^2 score of 0.977.

Both the vanilla RNN and LSTM models achieve satisfactory prediction accuracy and can be used as forecasting models in a MPC with a prediction horizon of 10 steps, for which the reduced-order models are expected to perform even better than over the 500-step horizon. LSTM performs slightly better, likely due to its enhanced internal structure.

In the following, since model validation performances are quiet similar, both models are used for control performances evaluations.

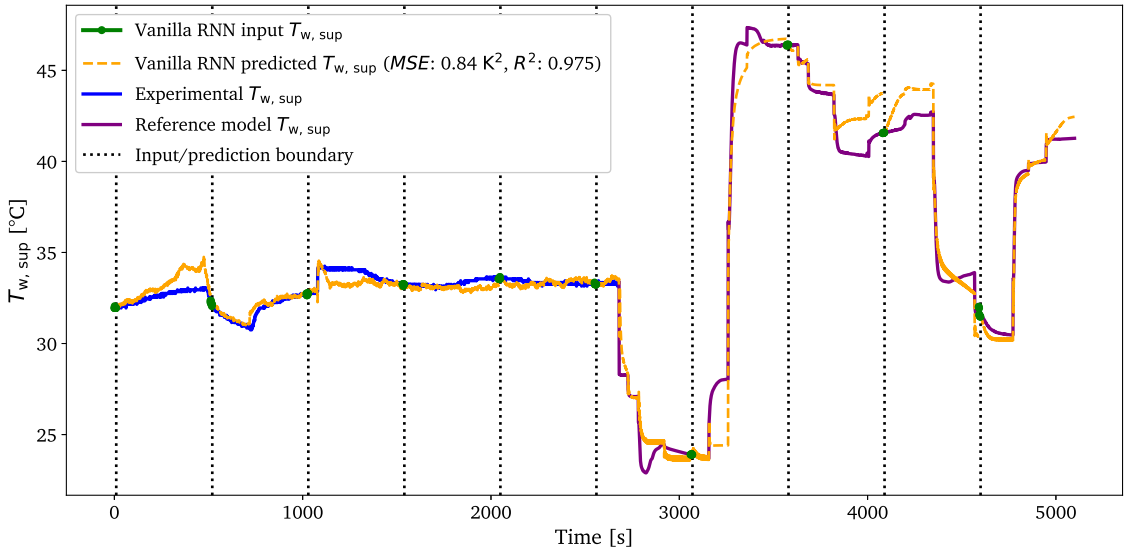

Figure 6.9: Vanilla RNN model validation on unseen data from experiments (blue) and TCHP-HYB model (purple). The model is initialized using 10 previous samples, followed by prediction of the next 500 samples. The transition between initialization and prediction is indicated by the black dashed line. The plot shows the predicted and true values of the supply water temperature $T_{\mathrm{w,sup}}$. The RNN achieves a MSE of 0.84 K^2 and an R^2 score of 0.975, indicating high predictive accuracy over the forecasting horizon.

6.3.2 MPC design

MPC is a model-based control strategy that has gained widespread adoption in industrial applications requiring optimal, constraint-aware control Qin and Badgwell (2003). The performance of MPC depends primarily on four components: (1) an accurate prediction model (here, the previously derived vanilla RNN and LSTM models), (2) the formulation of the cost function, (3) constraint handling, and (4) the choice of optimization algorithm, which are delivered in this section.

6.3.2.1 Objective function

The main control objective is to deliver the desired heating by tracking the supply water temperature setpoint $y^{\mathrm{sp}} = T^{\mathrm{sp}}_{\mathrm{w,sup}}$ with minimal gas consumption. The controller computes the optimal burner fan speed $u_1 = \omega_{\mathrm{bf}}$ and the optimal high-pressure valve opening $u_2 = \varphi_{\mathrm{hpv}}$ by minimizing the following objective function:

$$\begin{aligned}\min_{u_1,u_2} J = \alpha_1 \sum_{j=1}^{n_{\mathrm{p}}} \big(\hat{y}(k+j|k) - y^{\mathrm{sp}}(k+j|k)\big)^2 + \sum_{j=0}^{n_{\mathrm{c}}-1} \alpha_2\, u_1(k+j|k)^2 \\ + \sum_{j=0}^{n_{\mathrm{c}}-1} \big(\alpha_3\, \Delta u_1(k+j|k)^2 + \alpha_4\, \Delta u_2(k+j|k)^2\big) + \alpha_5 \sum_{j=1}^{n_{\mathrm{p}}} L_{\mathrm{constraint}}\big(\hat{T}_{\mathrm{h1}}(k+j|k)\big),\end{aligned} \tag{6.15}$$

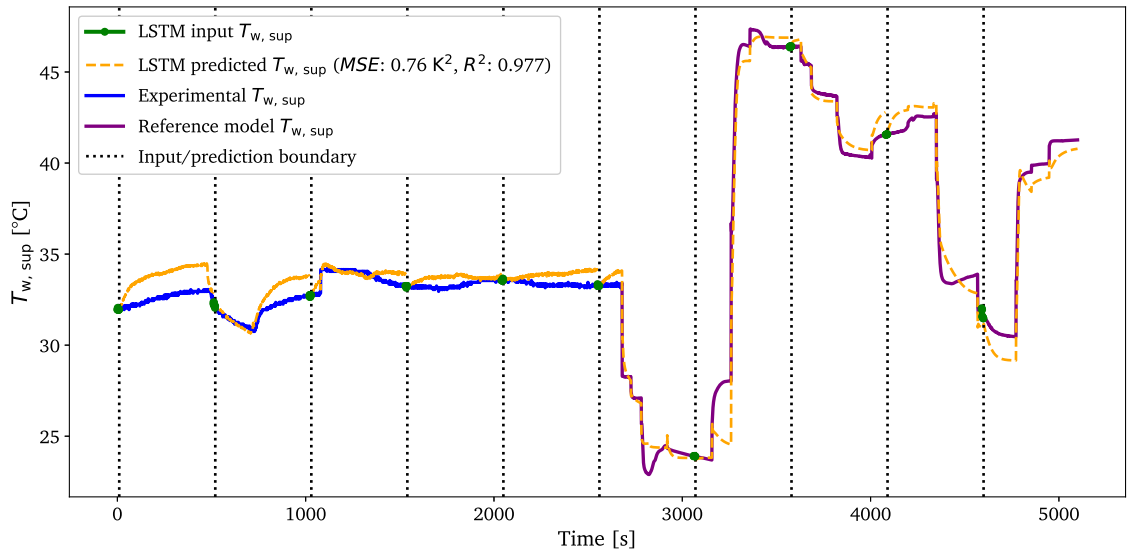

Figure 6.10: LSTM model validation on unseen data from experiments (blue) and TCHP-HYB model (purple). The model is initialized using 10 previous samples, followed by prediction of the next 500 samples. The transition between initialization and prediction is indicated by the black dashed line. The plot shows the predicted and true values of the supply water temperature $T_{\mathrm{w,sup}}$. The LSTM achieves a MSE of 0.76 K^2 and an R^2 score of 0.977, indicating high predictive accuracy over the forecasting horizon.

subject to

$$\hat{y}(k+j|k) = f_{\mathrm{rnn}}\big(y(k-l_{\mathrm{seq}}),\ldots,y(k),\,u(k-l_{\mathrm{seq}}),\ldots,u(k),\,d(k-l_{\mathrm{seq}}),\ldots,d(k)\big),\quad j=1,\ldots,n_{\mathrm{p}}, \tag{6.16}$$

$$\hat{T}_{\mathrm{h1}}(k+j|k) = f_{\mathrm{h1}}\big(\omega_{\mathrm{bf}}(k+j|k),\,\omega_{\mathrm{m1}}(k+j|k)\big),\qquad j=1,\ldots,n_{\mathrm{p}}, \tag{6.17}$$

$$u_{\min} \le u(k+j|k) \le u_{\max},\qquad j=0,\ldots,n_{\mathrm{c}}-1. \tag{6.18}$$

In this formulation, the prediction model f_{rnn} corresponds to either the trained vanilla RNN or LSTM model derived in the previous section, while the heater model f_{h1} is represented by Equation (5.19). The soft constraint term

$$L_{\mathrm{constraint}}(T_{\mathrm{h1}}) = \max\left(0,\ T_{\mathrm{h1}} - T_{\mathrm{h1,max}}\right)$$

is zero when the heater temperature remains within its limit and positive otherwise, thus penalizing unsafe operation. The weight vector $\alpha = [\alpha_1, \alpha_2, \alpha_3, \alpha_4, \alpha_5]$ balances the contribution of each term in the cost:

- $\alpha_1 > 0$ penalizes the tracking error between predicted supply water temperature and its setpoint.
- $\alpha_2 > 0$ discourages excessive burner fan speed ω_{bf}.
- $\alpha_3 > 0$ penalizes variations in burner fan speed $\Delta\omega_{\mathrm{bf}}$.
- $\alpha_4 > 0$ penalizes abrupt changes in high-pressure valve opening $\Delta\varphi_{\mathrm{hpv}}$.

- $\alpha_5 > 0$ penalizes exceeding the maximum heater temperature $T_{\mathrm{h1,max}}$.

Here, n_p and n_c denote the prediction and control horizons, respectively. The notation $k+j|k$ refers to the predicted value at time $k+j$ based on information available at time k. Equation (6.18) enforces hard bounds on the control inputs $u(k+j|k)$, while penalties on $\Delta u(k+j|k)$ ensure smooth actuator behavior.

The MPC controller operates in a receding-horizon fashion: at each time step k, the optimal control sequence $u^{\mathrm{opt}}(k+1) = \{u^{\mathrm{opt}}_{k+1|k}, \ldots, u^{\mathrm{opt}}_{k+n_\mathrm{c}|k}\}$ is computed. Only the first element $u^{\mathrm{opt}}_{k+1|k}$ is applied to the system. At the next time step $k+1$, the state is updated, and the optimization problem is solved again, enabling continuous real-time adaptation.

6.3.2.2 Parameters

The prediction horizon is set to match the capacity of the reduced-order models, i.e., $n_\mathrm{p} = l_\mathrm{pred} = 10$, while the control horizon is fixed at $n_\mathrm{c} = 2$. The weighting factors in the objective function are selected as $\alpha_1 = 0.95$, $\alpha_2 = 0.002$, $\alpha_3 = 0.02$, $\alpha_4 = 0.002$, and $\alpha_5 = 0.001$. MPC operates with a sampling time of 1 s. The objective function is solved with the `Nelder-Mead` algorithm in Python's `minimize` function. In the next section, we validate the defined control strategies on the TCHP-HYB model.

6.3.3 Control strategies validation

This section covers the evaluation of the proposed MPC control strategy (Section 6.3) in comparison to the PID-based one (Section 6.2). The MPC is coupled with both vanilla RNN and LSTM models for comparison. As a result, the three evaluated control strategies are: PID-based, MPC-RNN, and MPC-LSTM.

6.3.3.1 Evaluation conditions

Similarly to Section 6.2.2, the evaluation is done by step changes in the supply water temperature setpoint. However, the evaluation in this section is applied on the TCHP-HYB model, since we had no opportunity for real implementation on the TCHP machine. Supply water temperature setpoint step changes are induced by varying the outdoor temperature between 2 °C and 7 °C over 5000 seconds, with a step change every 1000 seconds. The inlet glycol mixture temperature is assumed equal to the outdoor temperature. The water and glycol mixture flow rates are fixed at 230 g.s^{-1}. φ_lpv is regulated with a PID to maintain a superheat of 5 K, and ω_m2 is regulated with a PID so that T_h2 tracks T_h1. A key point in this simulation is that disturbances are present, and the robustness of the control strategies is also being assessed.

The transient performance of the control strategies is monitored, and a comparison of their rise time, settling time, overshoot, average temperature error, and average thermal COP is conducted.

6.3.3.2 Transient evaluation

The transient responses of the TCHP system under the control strategies are shown in Figures 6.11 and 6.12, corresponding to the outputs (p_gc, $T_\mathrm{w,sup}$, and T_h1) and inputs (φ_hpv and ω_bf), respectively. Both MPC-RNN and MPC-LSTM are able to follow the setpoint,

achieving a smaller error than with PID control. The offset with $T^{\mathrm{sp}}_{\mathrm{w,sup}}$ can be attributed to the independent control of p_{gc}, which also influences $T_{\mathrm{w,sup}}$. The system also exhibits significant overshoot, especially during setpoint increases. This is mainly because ω_{bf} regulates T_{h1} and not $T_{\mathrm{w,sup}}$ directly, meaning that good tracking of $T^{\mathrm{sp}}_{\mathrm{h1}}$ does not necessarily translate to good tracking of $T^{\mathrm{sp}}_{\mathrm{w,sup}}$. This also results in a long settling time of about 200 s. Both issues have already been observed in the real case study (Section 6.2.2) and are reproduced here by simulation. In contrast, the MPC strategy directly connects ω_{bf} to $T_{\mathrm{w,sup}}$ using a reduced model (RNN or LSTM) and uses both φ_{hpv} and ω_{bf} as direct inputs. Thus, it avoids both issues resulting from the baseline control strategy.

6.3.3.3 Average evaluation

The average thermal COP and temperature error of the three strategies during simulation are shown with bar plots in Figure 6.13. The left figure shows the highest thermal COP for MPC-LSTM, closely followed by MPC-RNN, with a significantly lower value for PID. The right figure shows that the smallest average temperature error is achieved by MPC-LSTM, closely followed by MPC-RNN, with a significantly higher error for PID.

Table 6.3 summarizes the performance metrics of the applied control strategies. Compared to the PID strategy ($COP_{\mathrm{th}} = 1.57$), both MPC-RNN and MPC-LSTM show clear improvements, achieving higher average thermal COP values of 1.72 (+9.7%) and 1.82 (+15.8%), respectively. Similarly, the average temperature error decreases from 0.20 °C under PID to 0.092 °C (-50.3%) with MPC-RNN and 0.09 °C (-52.7%) with MPC-LSTM. The average temperature errors from both MPC strategies are relatively close, with a similar behavior on ω_b and T_{h1}, as seen in Figures 6.12 and 6.11. However, the higher thermal COP obtained with MPC-LSTM shows that it is closer to the optimal high pressure compared to MPC-RNN. For the PID strategy, the use of fixed correlations (g_1 and g_4) leads to poor performance because: (1) it is difficult to consider all influencing inputs within the correlation, (2) such correlations are derived under steady-state assumptions, neglecting transient behavior, and (3) system behavior may change over time.

In terms of computation time, using a prediction length equal to the prediction horizon avoided iterations in the optimization process, significantly reducing computation time. Nevertheless, computation time still increased from 0.008 ms (PID) to 20 ms (MPC-RNN) and 24 ms (MPC-LSTM) during each iterative step. This cost could be reduced further by using approximate MPC, for instance, by generating optimal control inputs offline across multiple operating points and learning a control policy via a NN. Another alternative is to linearize the trajectory online, enabling faster optimization using simpler solvers.

Despite their effectiveness, a limitation of both MPC-RNN and MPC-LSTM is the relatively high number of hyperparameters that must be tuned to ensure stability and good performance. Finally, the proposed control strategy is also applicable to more conventional electrically driven heat pumps by replacing the burner fan speed with the electric motor speed as the manipulated variable.

6.4 Conclusion

In this chapter:

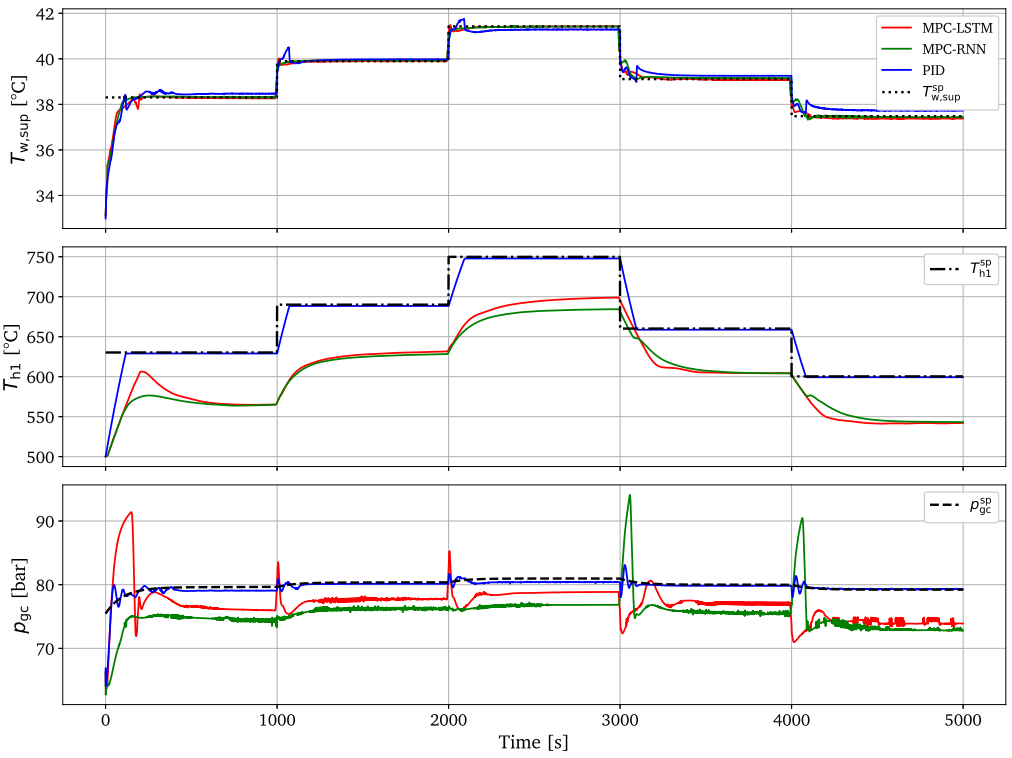

Figure 6.11: Transient evaluation of PID, MPC-RNN, and MPC-LSTM: resulting supply water temperature $T_{\mathrm{w,sup}}$, first heater temperature T_{h1}, high pressure p_{gc}, and their corresponding setpoints.

Controller	Average COP_{th} [-]	Average error [K]	Settling time [s]	Computation time [ms]
MPC-LSTM	1.82	0.09	30	24
MPC-RNN	1.72	0.09	30	20
PID	1.57	0.19	200	0.01

Table 6.3: Average performance evaluation of PID, MPC-RNN, and MPC-LSTM controllers.

- A general review of control strategies for VCCs was provided. The control of these cycles was hierarchically divided into supervisory and local levels. The focus was mainly on local control, ranging from basic on/off and PID to more advanced strategies, particularly MPC. These strategies rely heavily on reduced models, which were also reviewed in the context of VCCs. The literature highlighted the increasing need for advanced control strategies in energy systems, driven by stricter energy regulations and efficiency requirements. In particular, control strategies for transcritical CO_2 cycles were briefly discussed, with emphasis on high-side (gas cooler) pressure control.

- A TCHP, a transcritical CO_2 cycle developed for residential heating, was then considered. The control problem of a TCHP was formulated from the user's demand down to the internal operation of the cycle. The system variables were classified into manipulated, disturbance, and controlled variables. The TCHP control objective of delivering a target supply temperature and the corresponding PID-based control strategy were explicitly described. A real case study was then provided by applying

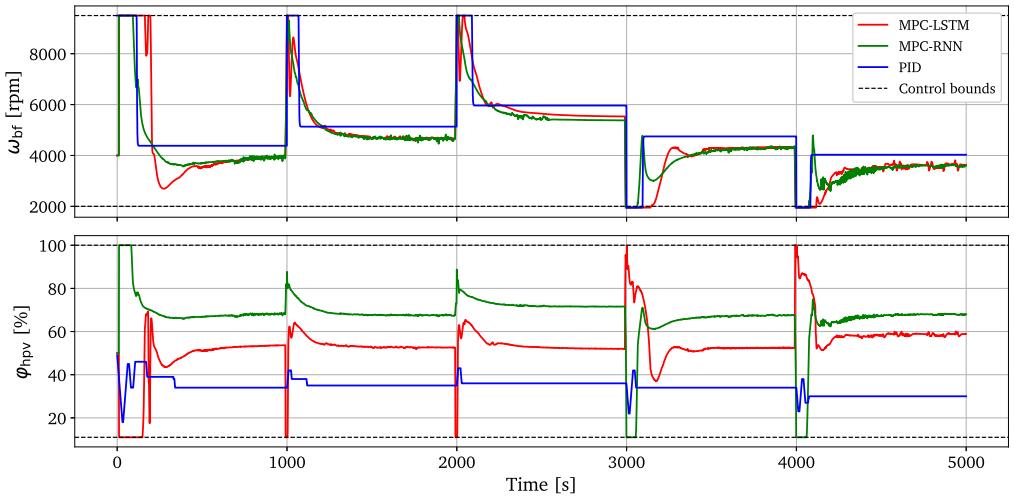

Figure 6.12: Transient evaluation of PID, MPC-RNN, and MPC-LSTM: resulting control inputs of burner fan speed ω_{bf} and high-pressure valve opening φ_{hpv} (percentage).

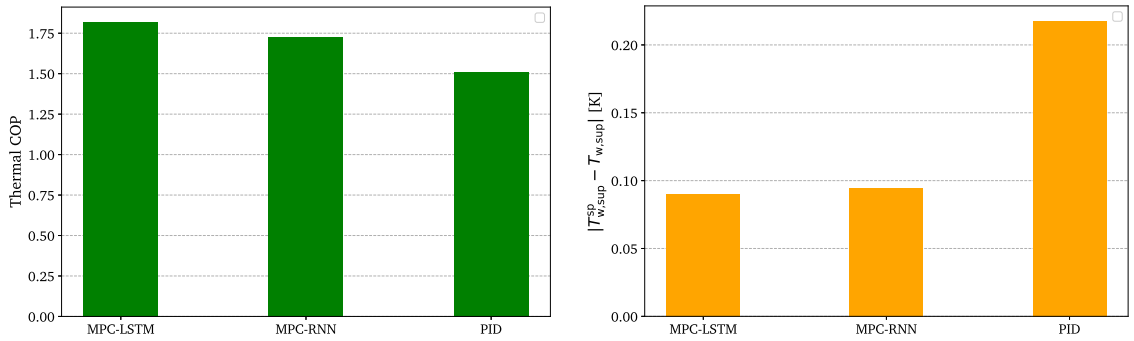

(a) (b)

Figure 6.13: Average evaluation of PID, MPC-RNN, and MPC-LSTM: (a) thermal COP and (b) supply water temperature error, shown as bar plots.

step tests on setpoints to evaluate the baseline control strategy, highlighting its limitations. A new control strategy coupling MPC with a reduced RNN was subsequently proposed.

- Two types of reduced RNN models were developed: a vanilla RNN and an LSTM. The main inputs to be regulated and the outputs to be controlled were identified, and the structure of each model was defined. For training, representative data were required. In addition to the real transient data introduced in Section 4.4.1, further data were obtained by exciting the previously validated TCHP-HYB model. The data were processed, models were trained, and then validated on unseen data.

- A new MPC design was proposed to replace two PIDs. The new MPC strategy was tested on the TCHP-HYB model and compared with the previous PID-based one. The MPC–LSTM coupling increased the COP by 15.8 % and reduced the supply water temperature error by 52.7 %. Although PID produced smoother input trajectories, MPC strategies clearly avoided overshoots, demonstrated robustness to disturbances, and achieved much shorter settling times. Furthermore, the computation time of MPC (20–24 ms) was well below the 1 s sampling time, ensuring feasibility for real-

time implementation.

- The improved performance of MPC–RNN and MPC–LSTM came at the cost of higher computation times compared to PID, underlining the need for approximate MPC schemes to reduce complexity. Future work could also extend the reduced models by including evaporator dynamics to increase degrees of freedom. Overall, this study demonstrates that intelligent control strategies are increasingly necessary in modern heat pump applications, as they can enhance performance while ensuring compliance with operational constraints. The method can be generalized and is not restricted to a TCHP-type machine.

In summary, this chapter presented a novel MPC–RNN control method applied to a TCHP for residential heating. The approach is not restricted to TCHPs and can be generalized to other VCC systems. The RNN effectively captured the nonlinear and complex system dynamics, enabling the MPC to control two key inputs simultaneously and optimize them online. As a result, the supply water temperature setpoint was accurately tracked with reduced energy (gas) consumption. Unfortunately, real validation was not possible as the TCHP machine was no longer available at Boostheat. Future work could focus on accelerating computation, for example by learning MPC optimizations for faster solutions, and on extending the framework to additional inputs such as water mass flow rate, which was not considered here.

Chapter 7

Conclusions and perspectives

This thesis has addressed the problem of performance optimization of a CO_2 thermally driven heat pump (TCHP) intended for residential heating applications. The starting point of this work was the recognition that natural gas remains a dominant heating fuel worldwide, yet conventional gas boilers are inefficient and environmentally harmful. The development of an alternative solution, namely the TCHP, relies on a novel component—the thermal compressor (TC)—which uses natural gas to provide mechanical compression in a fundamentally different way compared to electric compressors. The complexity of this system, driven by strong nonlinearities, multi-component interactions, and the specific thermodynamic characteristics of CO_2, necessitated an integrated research effort that combined experimental studies, physical modeling, data-driven approaches, and the development of advanced control strategies.

In the first part of the manuscript, particular attention was devoted to the TC as the key component distinguishing TCHPs from conventional vapor compression cycles. A detailed review of Stirling-type machines helped situate the TC within its technological family and clarify its similarities and differences with the classical Stirling engine. An extensive experimental campaign was then carried out, integrating the TC into a single-stage heat pump test bench. This setup enabled the collection of valuable measurements, which were first processed to detect and filter outliers, and then used to define relevant performance indicators. From these indicators, an exergy-based performance metric was established to provide a unified criterion for evaluating the TC under different operating conditions. These results already highlighted the potential of the TC concept but also emphasized the sensitivity of its performance to external conditions such as rotational speed, charged pressure, and heater temperature.

To complement the experimental analysis, a third-order finite volume (FV) physical model of the TC was developed, denoted as 'TC-3RD'. This model, spatially discretized into control volumes, allowed the application of mass, momentum, and energy balances to capture the transient thermodynamic behavior of the machine. The model was validated against experimental measurements in both steady-state and transient conditions, the latter being supported by CFD simulations. A detailed exergy analysis was then performed, quantifying irreversibilities across the internal components of the TC and providing deeper insight into optimization opportunities. However, due to its computational cost and stiffness, this physical model was not suitable for integration into a full system simulation or real-time control. Therefore, data-driven approaches were introduced. Based on

the extended experimental database, polynomial regressions, Gaussian process regression (GPR), and artificial neural networks (ANNs) were trained and compared. While polynomial models showed limitations, the neural network (NN) achieved high accuracy at the cost of large computational time. The Gaussian process regression model provided the best compromise, offering accuracy equivalent or superior to the NN while being drastically faster, thus representing the most promising candidate for integration into a dynamic heat pump model.

The second part of the thesis extended the analysis to the complete three-stage TCHP system. The motivation for using CO_2 as a working fluid in transcritical cycles was recalled, underlining its environmental advantages but also its specific challenges in terms of cycle optimization. The experimental setup of the three-stage TCHP developed by Boostheat was presented, and data were collected under both steady-state and transient conditions. Based on this dataset, a comprehensive hybrid dynamic model of the system was derived, denoted as 'TCHP-HYB'. This hybrid model combined FV formulations for heat exchangers with quasi-static models of other components such as valves and TCs (GPR from Part I), resulting in a detailed yet computationally manageable framework. Validation against experimental data confirmed its ability to reproduce both steady-state maps and transient responses. The TCHP-HYB then served as the basis for the development and evaluation of advanced control strategies.

Building on this foundation, the problem of controlling the TCHP was addressed. Traditional PID-based strategies, while simple, proved insufficient to deal with the strong couplings and nonlinearities of the system. To overcome these limitations, a new control approach based on Model Predictive Control (MPC) was proposed. Since the reference model was too complex for direct use in MPC optimization, reduced-order models based on recurrent neural networks (vanilla RNN and LSTM architectures) were identified and trained on both experimental and simulated data. These reduced models captured the essential system dynamics and enabled the design of an MPC strategy capable of handling multiple inputs and outputs simultaneously. The proposed MPC was validated through simulations and experimental data, showing clear advantages over baseline control in terms of transient response, setpoint tracking (-52.7% error), and overall energy efficiency (+15.8% COP). The ability of MPC to anticipate system evolution and to coordinate multiple actuators highlighted its relevance as a candidate for real implementation in future TCHP units.

Overall, the contributions of this thesis are manifold. At the component level, the work has provided both a validated FV physical model and efficient data-driven models of the TC, supported by dedicated experimental campaigns. At the system level, it has delivered a hybrid dynamic model of a three-stage TCHP, also validated with real measurements. On the control side, it has introduced and demonstrated the potential of advanced MPC strategies supported by reduced-order RNN models. All the developed tools have been implemented in Python and made available in an open-source framework, ensuring reproducibility and future extensions by the research community.

In perspective, several directions are worth pursuing. Experimentally, more extensive campaigns covering a wider range of operating conditions would allow improving the robustness of the data-driven models. At the modeling level, further refinement of heat exchanger correlations and valve dynamics could enhance the predictive accuracy of

the system model. On the control side, real-time implementation is limited primarily by computational speed rather than control quality: the MPC performs well on the validated hybrid model, and future work will focus on acceleration and robustness to uncertainties. Coupling the developed control strategies with supervisory energy management systems could also open new perspectives, especially for integrating TCHPs into smart grids or hybrid renewable-based systems. Finally, the adoption of natural refrigerants and thermally driven solutions such as TCHPs contributes to the broader effort of reducing greenhouse gas emissions in the residential heating sector, and the tools developed in this work represent a solid basis for accelerating this transition.

In conclusion, this thesis has demonstrated that combining experimental characterization, physical modeling, data-driven approaches, and advanced control strategies provides an effective methodology for tackling the complexity of novel thermally driven cycles. The developed results not only enhance the understanding and optimization of TCHPs but also pave the way toward their practical deployment as a sustainable alternative to conventional gas boilers.

Appendix A

Résumé étendu en français de la thèse

Le gaz naturel reste le principal combustible de chauffage dans les bâtiments à l'échelle mondiale, représentant environ 40 % de la demande totale d'énergie de chauffage en 2022 selon l'Agence Internationale de l'Énergie (AIE). Les chaudières à gaz conventionnelles couvrent encore la majeure partie de cette demande, malgré leur contribution aux émissions de gaz à effet de serre. Une alternative prometteuse est la pompe à chaleur à compresseur thermique (TCHP), une pompe à chaleur entraînée thermiquement qui utilise également le gaz naturel mais d'une manière fondamentalement différente. Au lieu de convertir directement le combustible en chaleur, comme le font les chaudières, la TCHP utilise le gaz naturel pour actionner un compresseur thermique (TC), qui transfère ensuite de la chaleur supplémentaire à partir d'une source externe telle que l'air ambiant ou l'eau. Cela permet à la TCHP de fournir plus de chaleur que l'énergie du combustible qu'elle consomme, ce qui en fait un remplacement potentiellement plus économe en énergie que les chaudières à gaz conventionnelles.

Une TCHP est un cycle à trois étages qui utilise le CO_2 comme fluide de travail dans sa phase supercritique. L'innovation principale réside dans sa technologie de TC, qui est le composant qui reçoit la chaleur et remplace un compresseur électrique conventionnel. Cependant, la présence de multiples composants interconnectés en raison des différents étages du cycle, les fortes non-linéarités et la sensibilité du TC aux conditions de fonctionnement rendent le contrôle d'une TCHP particulièrement complexe. Ces difficultés exigent des stratégies avancées qui vont au-delà des approches de contrôle traditionnelles. Pour répondre à ce défi, l'objectif final de cette thèse est de développer une nouvelle stratégie de contrôle capable d'améliorer la performance globale de la TCHP. À cette fin, divers outils de simulation et analyses de performance sont mis en œuvre afin de soutenir la conception et la validation de la solution de contrôle proposée.

La première partie de cette thèse (chapitres 1, 2 et 3) est consacrée au TC, en tant que composant clé d'une TCHP. Pour acquérir une compréhension détaillée de ce composant, une revue des machines de type Stirling est d'abord présentée, mettant en évidence les caractéristiques uniques du TC étudié. Une campagne expérimentale est ensuite menée sur un TC intégré dans une pompe à chaleur à un étage afin d'évaluer ses performances. À partir des données collectées, plusieurs modèles empiriques (boîte noire) sont développés afin de fournir des prédictions rapides et fiables. Ces modèles sont destinés à leur

intégration dans un modèle dynamique de pompe à chaleur et à l'appui de la onception de stratégies de commande, sans réalisation d'étude paramétrique d'exergie basée sur l'apprentissage automatique. Pour compléter l'approche boîte noire et permettre une compréhension physique plus approfondie, un modèle physique en volumes finis (VF) est également développé. Ce modèle permet de quantifier les destructions d'exergie au sein des composants internes du TC et constitue une base flexible pour l'optimisation.

La deuxième partie de la thèse (chapitres 4 5 et 6) étend l'analyse au système TCHP complet. Elle commence par une revue des cycles transcritiques au CO_2, discutant de leurs caractéristiques spécifiques ainsi que des techniques de modélisation et de contrôle associées. Le cycle et le procédé de la TCHP sont décrits, et des travaux expérimentaux dédiés sont menés. Un modèle dynamique VF de l'ensemble du système est ensuite proposé et validé par rapport aux données expérimentales. En combinant les mesures réelles avec les résultats de simulation, des modèles réduits de type réseaux de neurones récurrents (RNN) sont identifiés afin de fournir des représentations efficaces de la dynamique du système. Enfin, une nouvelle stratégie de contrôle prédictif par modèle (MPC) est introduite, reposant sur les modèles réduits pour permettre un contrôle optimal du système TCHP.

En résumé, cette thèse fournit à la fois des outils de modélisation au niveau des composants et au niveau du système, validés expérimentalement, et introduit une nouvelle stratégie MPC pour une TCHP. Ces contributions soutiennent non seulement le développement de TCHP efficaces comme alternative durable aux chaudières à gaz, mais offrent également une base pour de futures études d'optimisation.

Mots-clés : pompe à chaleur à compresseur thermique, CO_2 transcritique, compresseur thermique, analyse exergétique, méthode des volumes finis, modélisation empirique, réseaux de neurones récurrents, contrôle prédictif par modèle

Chapitre 1

Ce chapitre présente une analyse expérimentale et numérique d'un TC destiné aux cycles de pompe à chaleur, en s'appuyant sur la famille des machines de type Stirling pour cadrer le fonctionnement et la terminologie. Il commence par rappeler les principes des moteurs de Stirling, machines à combustion externe, fermées et régénératives, où un fluide de travail accomplit des transformations cycliques grâce à un gradient de température entre une source chaude et une source froide. Les éléments constitutifs usuels — volume de compression, refroidisseur, régénérateur, réchauffeur et volume d'expansion — sont décrits conjointement au déplacement assuré par un déplaceur et un piston moteur. Le cycle théorique est présenté sur les diagrammes p–V et T–s comme une suite idéalisée de compression, transfert régénératif à volume quasi constant, expansion et retour, dont le rendement ne peut égaler Carnot qu'en présence d'un régénérateur parfait et d'échangeurs idéaux. Les écarts réels proviennent notamment des irréversibilités d'échange, des performances non idéales du régénérateur et des volumes morts induisant des gradients spatio-temporels des grandeurs thermodynamiques.

Le chapitre distingue ensuite le TC de type Stirling, ou STC, d'un moteur de Stirling. Le STC est un système ouvert qui convertit une fourniture de chaleur en élévation de pression afin d'acheminer un fluide de travail du côté chaud vers le côté froid. En remplaçant le piston moteur par un orifice et par des soupapes d'aspiration et de refoulement, on sup-

prime le couplage cinématique piston–déplaceur et on ne conserve qu'un entraînement électrique du déplaceur pour vaincre les pertes mécaniques, d'où une demande électrique faible au regard de la puissance thermique d'entrée. Contrairement au moteur de Stirling qui s'appuie sur un déphasage volumétrique compression–expansion, le STC engendre les ondes de pression par la seule variation harmonique d'un volume effectif unique, assimilable à la combinaison des cavités chaude et froide. La littérature distingue un STC de type 1, à chemin d'écoulement unique visant la réfrigération par tube à pulsations, et un STC de type 2, muni de soupapes distinctes d'aspiration et de refoulement pour remplacer un compresseur mécanique dans des applications comme les pompes à chaleur.

Le TC étudié est précisément un STC de type 2 à soupapes séparées, conçu pour s'insérer à la place d'un compresseur mécanique dans un cycle de pompe à chaleur à compression de vapeur. Sa géométrie est détaillée à partir d'une coupe verticale: une cavité froide et une cavité chaude séparées par un déplaceur, reliées par des échangeurs à volumes constants comprenant un refroidisseur traversé par une chemise d'eau de refroidissement, un réchauffeur annulaire alimenté thermiquement et un régénérateur en matrice poreuse à fils fins. Des volumes morts existent entre refroidisseur et régénérateur et entre réchauffeur et régénérateur. Les soupapes d'aspiration et de refoulement se connectent à la cavité froide pour admettre et livrer le débit au cycle thermodynamique. La cinématique repose sur un mécanisme bielle-manivelle qui impose au déplaceur un mouvement quasi sinusoïdal; les variations volumétriques des cavités froide et chaude sont en phase, si bien que le volume de travail total ne varie que faiblement et que la boucle p–V totale est étroite et suit l'orientation de la cavité froide, à l'inverse d'un moteur de Stirling où le déphasage crée une aire utile importante et orientée comme l'expansion.

Le processus de compression thermique est rendu intelligible en traçant la pression interne supposée uniforme en fonction de la position du déplaceur. Lorsque les soupapes sont fermées et que le déplaceur descend, le fluide se réchauffe en migrant vers la zone chaude, ce qui élève la pression jusqu'à dépasser la pression de refoulement et ouvrir la soupape de refoulement; symétriquement, lorsque le déplaceur remonte, le fluide retourne vers la zone froide, la pression chute jusqu'à passer en-dessous de la pression d'aspiration et la soupape d'aspiration s'ouvre. Le cycle utile résulte ainsi de deux phases adiabatiques internes à volume total presque constant, séparées par des phases de refoulement et d'admission commandées par les soupapes.

L'évaluation expérimentale intègre pour la première fois le TC dans un cycle de pompe à chaleur CO_2 à un étage comprenant TC, condenseur, détendeur électronique et évaporateur, avec un échangeur de fumées récupérant une partie de la chaleur des gaz de combustion qui chauffent le réchauffeur. Le banc comprend une boucle d'eau qui récupère la chaleur au refroidisseur puis au condenseur et enfin au récupérateur de fumées, et une chambre de combustion isolée dont la température de paroi du réchauffeur est régulée par la vitesse d'un ventilateur-brûleur via une boucle PID. La métrologie associe, côté eau, des Pt100 de haute précision et un débitmètre vortex; côté CO_2, des thermocouples T aux orifices d'aspiration et de refoulement, un thermocouple K au niveau du réchauffeur, des capteurs de pression à haute précision pour p_{suc} et p_{dis} et un débitmètre massique Coriolis en aval du détendeur. L'acquisition synchronise les automates de contrôle du banc et l'interface logicielle de pilotage du TC qui règle vitesse moteur et vitesse du ventilateur-brûleur.

Le protocole de tests explore l'influence des grandeurs d'entrée suivantes: température d'eau de retour $T_{\text{w,ret}}$ imposée par le groupe froid, température de réchauffeur T_{h} asservie par la vitesse du brûleur ω_{bf}, rapport de pression $r_p = p_{\text{dis}}/p_{\text{suc}}$ modulé par l'ouverture de la vanne de détente électronique φ_{eev}, pression moyenne de charge p_{charged} ajustée par ajout ou retrait de CO_2, vitesse de rotation ω_{m} du mécanisme, température d'aspiration T_{suc} laissée flottante. Des campagnes à différentes pressions de charge (environ 30, 40, 50 et 56 bar) balaient des combinaisons de ω_{m} et φ_{eev}, pour un total de 118 échantillons, avec T_{h} fixé à 700 ou 800 °C en raison de limitations de stabilité de flamme. Les intervalles opératoires couvrent typiquement $p_{\text{suc}} \in [22{,}6, 48{,}7]$ bar, $p_{\text{dis}} \in [34{,}2, 64{,}2]$ bar, $\omega_{\text{m}} \in [100, 245]$ rpm, $T_{\text{w,ret}} \in [17{,}5, 24]$ °C et $T_{\text{suc}} \in [3, 21{,}6]$ °C.

Les indicateurs de performance sont définis à partir d'un schéma d'énergie mettant en évidence la puissance thermique de combustible, la chaleur utile absorbée au réchauffeur, la chaleur récupérée au refroidisseur et à l'échangeur de fumées, les pertes thermiques, la puissance mécanique transmise au déplaceur et la puissance de compression déterminée à partir des états d'aspiration et de refoulement. Les bilans permettent d'estimer la chaleur au réchauffeur par conservation d'énergie autour du TC et d'en déduire les pertes thermiques par différence avec l'énergie non récupérée dans les fumées. Les plages observées indiquent des transferts au réchauffeur de l'ordre de 0,7 à 3,8 kW, au refroidisseur de 0,44 à 2,58 kW, des puissances mécaniques parfois négatives ou modestes (–34 à 368 W), des débits massiques CO_2 de 4 à 44 g.s^{-1} et des températures de refoulement de 37 à 67 °C, confirmant que la chaleur d'entrée pilote l'augmentation de pression et le débit utile tandis que l'appoint mécanique reste secondaire.

Afin d'assurer la cohérence du jeu de données et d'écarter les mesures aberrantes induites par le bruit, des défauts de capteurs ou des phénomènes non modélisés, une régression à processus gaussiens est utilisée pour établir des relations lisses multivariées entre indicateurs et variables d'entrée, assorties d'intervalles de confiance prédictifs. Les points sortant des bandes à 95 % sont identifiés comme valeurs atypiques; sept échantillons ont ainsi été retirés, produisant un ensemble filtré mieux adapté à l'analyse et à la modélisation.

Étant donné que le TC ne réalise ni compression isentropique ni remplissage volumétrique au sens d'un compresseur mécanique, les rendements isentropique et volumétrique usuels ne sont pas pertinents. Le chapitre introduit donc une métrique unifiée fondée sur l'exergie, qui mesure le potentiel de travail utile associé aux transferts d'énergie. L'exergie apportée par la chaleur au réchauffeur est calculée à l'aide du facteur de Carnot (fonction de la température de la source chaude et de la température ambiante). L'exergie transmise à l'eau au refroidisseur s'obtient à partir des débits d'eau et des variations de fonctions de flux, et l'exergie de compression du CO_2 se déduit des variations de ces mêmes fonctions entre refoulement et aspiration. À l'état stationnaire, l'exergie détruite dans le TC résulte de la différence entre l'exergie fournie (chaleur au réchauffeur et puissance mécanique) et l'exergie utile produite (compression du fluide et chaleur récupérée au refroidisseur). L'efficacité exergétique est définie comme le rapport entre l'exergie utile (compression plus récupération au refroidisseur) et l'exergie fournie (chaleur au réchauffeur plus puissance mécanique). L'analyse des données filtrées montre que l'influence de la vitesse de rotation sur cette efficacité est faible, tandis que le rapport de pression exerce un effet marqué: l'efficacité tend à décroître lorsque le rapport augmente, plus nettement au-delà

d'environ 1,4. À pression de charge plus élevée, les efficacités observées sont en moyenne supérieures, suggérant l'effet favorable de la densité accrue sur les échanges thermiques et les pertes internes. La variation de la température de la source chaude de 700 à 800 °C n'apparaît pas déterminante dans la plage explorée, probablement du fait de limitations de commande et parce que la source chaude est déjà très supérieure à l'ambiante, ce qui limite l'effet du facteur de Carnot.

En synthèse, ce premier chapitre établit le socle conceptuel et expérimental pour l'étude d'un TC destiné aux cycles CO_2. Il précise le fonctionnement spécifique d'un STC de type 2, son architecture, ses lois de commande et ses grandeurs pertinentes de mesure, formalise les indicateurs énergétiques et propose une métrique d'évaluation par l'exergie mieux adaptée qu'un rendement isentropique ou volumétrique. L'exploitation d'un banc instrumenté intégrant la machine dans un cycle réel a fourni un jeu de données inédit, nettoyé par apprentissage bayésien, qui met en évidence les rôles prépondérants du rapport de pression et de la pression moyenne de charge, face à un effet secondaire de la vitesse et un effet marginal de la température de réchauffeur dans les conditions testées. Les limites intrinsèques des campagnes — étendue réduite des niveaux de température de la source chaude et de pression de charge, accès incomplet aux variables internes et aux pertes — motivent le développement, au chapitre suivant, d'un modèle physique à haute fidélité. Ce modèle permettra d'éclairer les mécanismes internes non mesurés, d'extrapoler au-delà du domaine expérimental et d'ouvrir la voie à l'optimisation de la conception et des conditions opératoires du TC.

Chapitre 2

Ce chapitre est consacré au développement d'un modèle physique détaillé de troisième ordre appliqué au TC étudié dans le cadre de ce travail. Alors que les modèles de données élaborés dans le chapitre précédent se sont révélés utiles pour prédire les performances et identifier les conditions de fonctionnement optimales, ils ne permettent pas de diagnostiquer les déficiences internes du compresseur. L'objectif ici est donc de combler cette lacune en développant un outil de simulation basé sur une modélisation physique de haute fidélité.

La première partie du chapitre s'attarde sur une revue des approches de modélisation existantes pour les machines de type Stirling. Ces approches sont classées selon leur niveau de complexité. Les modèles de premier ordre, analytiques, se basent sur des hypothèses simplifiées comme des compressions et expansions isothermes, et un régénérateur parfait. Les modèles de second ordre introduisent une approche numérique en considérant les espaces de compression et d'expansion comme adiabatiques et en divisant la machine en plusieurs volumes de contrôle. Les modèles de troisième ordre, plus détaillés, reposent sur la discrétisation spatiale et l'application des équations de conservation de la masse, de l'énergie et de la quantité de mouvement sur chaque volume. Ils permettent une meilleure précision tout en restant moins coûteux en calcul que les modèles de dynamique des fluides numériques (CFD). Dans ce travail, ce niveau de détail est jugé le plus adapté car il intègre l'inertie des fluides, élément indispensable à la modélisation des compresseurs thermiques de type Stirling.

Sur cette base, un modèle de troisième ordre spécifique au compresseur étudié est

dérivé. Le compresseur est discrétisé spatialement par la méthode des volumes finis en plusieurs volumes de contrôle, chacun étant caractérisé par une pression, une température et une densité uniformes. Les équations de bilan de masse, d'énergie et de quantité de mouvement sont établies et reliées entre elles afin de constituer un système d'équations différentielles ordinaires. Les pertes réelles, telles que les pertes thermiques par effet de navette et les pertes dues à la vitesse finie et les frottements mécaniques, sont incluses. Les valves d'aspiration et de refoulement, éléments caractéristiques de cette machine par rapport aux machines de type Stirling classiques, sont également modélisées en considérant des relations statiques et un écoulement isentropique. Enfin, des corrélations empiriques issues de la littérature sont utilisées pour évaluer les coefficients de transfert de chaleur et de frottement dans les échangeurs de chaleur, le cylindre et le régénérateur. Les paramètres géométriques de chaque composant sont rassemblés pour définir la base du modèle.

Le couplage de ces équations aboutit à la formation d'un système d'équations différentielles interconnectées appelé modèle TC-3RD. Ce modèle prend en entrée les conditions de fonctionnement (pressions d'aspiration et de refoulement, vitesse de rotation, températures des sources chaude et froide) ainsi que les paramètres géométriques des composants. En sortie, il fournit l'évolution temporelle des propriétés thermophysiques du dioxyde de carbone ainsi que les débits massiques et les flux de chaleur. À partir de ces résultats, les indicateurs de performance du compresseur, tels que la puissance mécanique, les échanges thermiques et la température de refoulement, peuvent être calculés sur un cycle complet. Les conditions initiales sont définies à partir d'une répartition linéaire des températures et d'une pression uniforme, puis le système est résolu numériquement à l'aide de la méthode de Runge–Kutta. Pour accélérer la convergence vers l'état périodique, des techniques issues de la littérature sont employées, notamment l'ajustement progressif des températures du régénérateur.

Une validation du modèle est réalisée en deux étapes. Tout d'abord, les résultats transitoires obtenus avec le TC-3RD sont comparés à une simulation CFD pour un point de fonctionnement donné. Les tendances générales des variations de masse, de température, de pression et des diagrammes pression–volume sont bien reproduites, malgré quelques écarts au niveau des températures de la cavité chaude et de l'espace du réchauffeur. Compte tenu de la rapidité du modèle par rapport au CFD, ces écarts sont jugés acceptables. Ensuite, une validation en régime permanent est menée en comparant les prédictions du modèle avec les données expérimentales collectées précédemment. Les résultats montrent que le modèle capture les tendances globales mais présente des écarts notables, notamment une sous-estimation de la puissance mécanique et des transferts de chaleur dans le refroidisseur, ainsi qu'une surestimation de la température de refoulement. Les écarts relatifs observés varient de 8 à 16 % pour les transferts de chaleur, d'environ 14 % pour les débits massiques et dépassent 40 % pour la puissance mécanique, mettant en évidence la nécessité d'améliorations.

Malgré ces limites, le modèle TC-3RD constitue un outil précieux pour analyser les phénomènes internes et, en particulier, pour réaliser une analyse exergétique détaillée. Cette étude montre que la majorité des destructions d'exergie se produisent dans le régénérateur, suivi par les échangeurs de chaleur, tandis que les cavités chaude et froide contribuent de manière plus marginale. L'analyse paramétrique révèle qu'il existe un rapport de pres-

sion optimal compris entre 1,2 et 1,4, au-delà duquel l'efficacité exergétique se dégrade fortement. L'influence de la pression de charge est également déterminante : une augmentation jusqu'à 50 bar améliore l'efficacité exergétique, mais celle-ci diminue au-delà de 70 bar. L'augmentation de la température de la source chaude a un effet positif mais limité. Ces résultats orientent les perspectives d'optimisation vers la conception du régénérateur et l'adaptation des conditions de fonctionnement.

En conclusion, le modèle physique de troisième ordre développé dans ce chapitre apporte une compréhension approfondie du comportement interne du TC et met en lumière les mécanismes de pertes les plus critiques. Bien qu'il nécessite encore des améliorations pour fournir des prédictions quantitatives précises, il reste un outil adapté pour l'analyse exergétique et l'optimisation des composants. Sa lourdeur computationnelle le rend en revanche inadapté aux besoins de contrôle en temps réel, justifiant le recours à des modèles réduits pour les chapitres suivants.

Chapitre 3

Ce chapitre aborde le développement de modèles empiriques du TC en s'appuyant sur les données expérimentales collectées par l'entreprise et lors des campagnes précédentes. Alors que le modèle physique de troisième ordre présenté au chapitre précédent apporte une compréhension fine des phénomènes internes mais reste limité en précision et en coût de calcul, l'objectif ici est de construire des modèles d'apprentissage statistique capables de fournir des prédictions rapides et fiables des performances du compresseur. Ces modèles constituent des candidats prometteurs pour leur intégration dans un modèle dynamique de pompe à chaleur.

La première étape consiste à enrichir et réévaluer la base de données disponible. Les mesures initiales étaient limitées en termes de variation de température de la source chaude, une variable clé pour caractériser les performances du compresseur. Pour pallier cette lacune, des données issues de tests antérieurs réalisés sur une technologie similaire sont ajoutées. Dans ces essais, la chauffe était assurée électriquement, ce qui permet de considérer l'apport thermique sans pertes par combustion. Au total, 251 échantillons sont rassemblés, puis un filtrage est effectué par une approche de régression gaussienne pour détecter les valeurs aberrantes. Vingt points sont ainsi exclus, ce qui conduit à un jeu de données final de 231 échantillons, couvrant des gammes élargies de pressions d'aspiration et de refoulement, de vitesse de rotation et de températures de chauffe.

Sur cette base, trois familles de modèles d'apprentissage supervisé sont mises en œuvre pour prédire les indicateurs de performance du compresseur à partir de grandeurs d'entrée facilement mesurables. La première famille correspond aux modèles de régression linéaire et polynomiale, qui offrent une base simple mais limitée dès que les relations deviennent fortement non linéaires. La seconde est la régression par processus gaussiens, un modèle probabiliste non paramétrique capable de capturer les relations complexes tout en fournissant une estimation de l'incertitude. Enfin, la troisième famille est représentée par les réseaux de neurones artificiels, qui permettent de modéliser des comportements hautement non linéaires grâce à des architectures comprenant plusieurs couches et de nombreux paramètres ajustables. L'ensemble des modèles est implémenté en Python à l'aide de bibliothèques standards, entraîné sur 80 % des données disponibles et validé sur

les 20 % restants. Les performances sont évaluées au moyen de métriques classiques telles que le coefficient de détermination R^2, l'erreur absolue moyenne (MAE) et l'erreur relative moyenne (MAPE).

Les résultats montrent que les modèles de régression polynomiale atteignent une précision acceptable pour certaines grandeurs thermiques mais échouent sur le débit massique et la puissance mécanique, en raison de la complexité des relations. Les réseaux de neurones offrent une nette amélioration, avec des R^2 élevés et des erreurs faibles, mais leur temps de calcul moyen par itération (environ 660 ms) constitue un frein pour une utilisation en simulation dynamique. À l'inverse, le modèle basé sur les processus gaussiens parvient à une précision équivalente, voire supérieure, tout en réduisant drastiquement le temps d'inférence à environ 3,4 ms, soit près de 200 fois plus rapide. Ce compromis précision–vitesse fait de la GPR le candidat privilégié pour servir de modèle de substitution du TC.

Une validation approfondie est menée par une stratégie de validation croisée en cinq plis, garantissant la robustesse et la généralisation des résultats. Les indicateurs de performance montrent que la GPR domine systématiquement les autres méthodes, avec des écarts réduits et une excellente cohérence entre données prédites et mesurées. L'ANN conserve de bonnes performances mais se montre légèrement moins fiable en généralisation. Quant à la régression polynomiale, elle se révèle inadaptée pour certaines sorties critiques.

En conclusion, ce chapitre démontre que les approches fondées sur l'apprentissage automatique permettent de développer des modèles rapides, fiables et suffisamment précis pour être intégrés dans des modèles dynamiques de cycle complet et utilisés pour la commande. Parmi elles, la régression par processus gaussiens s'impose comme la solution la plus équilibrée, combinant précision et rapidité d'exécution. Cette approche ouvre la voie à l'optimisation des conditions de fonctionnement d'un TC dans une pompe à chaleur à trois étages, présentée dans le chapitre suivant.

Chapitre 4

Ce chapitre introduit la deuxième partie de la thèse, consacrée à la modélisation dynamique et au contrôle d'une TCHP à trois étages. Après avoir développé un modèle empirique du TC, l'analyse s'étend ici au cycle complet de la pompe à chaleur, utilisant le dioxyde de carbone comme fluide frigorigène et intégrant trois compresseurs thermiques en série. L'objectif est d'établir une compréhension globale du cycle, de ses particularités et de ses données expérimentales afin de préparer le développement et la validation d'un modèle dynamique utilisable pour la synthèse de stratégies de commande avancées.

Le chapitre commence par un retour sur l'utilisation du dioxyde de carbone comme réfrigérant. Historiquement remplacé par les fluides synthétiques pour des raisons pratiques, le CO_2 a connu un regain d'intérêt suite aux accords internationaux tels que le Protocole de Montréal et le Protocole de Kyoto, qui ont souligné les effets néfastes des CFC et HCFC sur la couche d'ozone et le climat. Le CO_2 présente l'avantage d'être non toxique, non inflammable et sans impact sur la couche d'ozone, tout en ayant un potentiel de réchauffement global extrêmement faible. Néanmoins, ses propriétés thermophysiques singulières, notamment une température critique très basse (31.1 °C) et une pression critique très élevée (73.7 bar), en font un fluide difficile à valoriser dans des cycles classiques.

Ces caractéristiques justifient le recours à des architectures spécifiques opérant en régime transcritique. Les avantages en termes de densité de vapeur et de capacité volumétrique permettent toutefois de concevoir des systèmes plus compacts et efficaces, à condition de maîtriser les contraintes mécaniques et thermodynamiques.

Le fonctionnement d'un cycle transcritique au CO_2 est ensuite présenté. Contrairement aux cycles subcritiques, où le rejet de chaleur s'effectue par condensation, le CO_2 en régime transcritique rejette sa chaleur par refroidissement sensible dans un refroidisseur de gaz. La description du cycle simple à un étage permet de rappeler les quatre transformations fondamentales : compression, refroidissement, détente et évaporation. La littérature a proposé de nombreuses variantes architecturales pour améliorer le rendement : cycles à deux étages, utilisation de réservoirs séparateurs ou de refroidissement intermédiaire, échangeurs internes et dispositifs de récupération de travail par détendeur ou éjecteur. Ces évolutions visent à réduire les températures de refoulement, améliorer le coefficient de performance et limiter les pertes par étranglement. Plusieurs études expérimentales et numériques démontrent que de telles solutions peuvent améliorer le COP de 7 à 30 %, selon la configuration.

Après cet état de l'art, le chapitre introduit le système cible de cette thèse : la pompe à chaleur Boostheat à TC à trois étages. L'architecture est décrite en détail. Le cycle comprend trois compresseurs thermiques, trois ballons tampons, un refroidisseur de gaz, un évaporateur, un échangeur interne, une bouteille de détente, des vannes de détente haute et basse pression, un échangeur de fumées et divers organes de liaison. Le CO_2 circule au travers de boucle principale, échange de la chaleur avec de l'eau du côté chaud, avec un mélange eau-glycol du côté froid, et reçoit son apport thermique des brûleurs à gaz alimentant les compresseurs. Les ballons tampons ont un double rôle d'échangeurs et d'amortisseurs des pulsations de pression. L'échangeur interne améliore la performance en refroidissant le fluide avant détente et en réchauffant le fluide à la sortie de l'évaporateur. L'ensemble du système illustre une intégration complexe visant à exploiter les atouts du CO_2 tout en maîtrisant ses contraintes.

Les conditions expérimentales sont ensuite décrites. Le banc d'essai a été conçu pour reproduire des conditions réalistes de fonctionnement résidentiel, avec une boucle d'eau pour simuler le réseau de chauffage et une boucle d'eau glycolée pour reproduire les températures extérieures. Les capteurs disponibles incluent des sondes de température Pt100 et thermocouples, des capteurs de pression et de débit, reflétant les limites d'instrumentation d'un produit commercial. Les actionneurs principaux sont identifiés : la vitesse du ventilateur de combustion, les ouvertures des vannes de détente haute et basse pression, et les vitesses des moteurs des compresseurs. Leurs influences respectives sur les températures, pressions et débits circulants sont expliquées, montrant la forte interdépendance entre variables manipulées et variables de sortie. Les expressions énergétiques permettant de calculer le COP thermique et les bilans de chaleur sont également définies à partir des mesures disponibles.

Deux jeux de données expérimentales sont mis en avant. Le premier est constitué d'essais transitoires en boucle ouverte, où un actionneur est excité par échelon et les réponses du système sont enregistrées. Ces données permettent d'analyser les dynamiques propres à chaque entrée, mais sont limitées car elles n'explorent pas les interactions multivariables. Le second jeu est un ensemble de quinze points en régime permanent, collectés

sur une machine similaire mais mieux instrumentée, incluant davantage de mesures internes. Ces données sont particulièrement précieuses pour valider les corrélations de modèles et calibrer les équations énergétiques. L'ensemble fournit une base complémentaire couvrant à la fois le comportement transitoire et les équilibres stationnaires.

En conclusion, ce chapitre montre que le dioxyde de carbone, malgré ses défis techniques, est un candidat incontournable pour les systèmes de chauffage respectueux de l'environnement. Le cycle transcritique et ses variantes architecturales offrent des solutions prometteuses, et l'unité expérimentale développée par Boostheat illustre concrètement ces avancées. L'analyse met en évidence la complexité du système, le rôle crucial de certains actionneurs et l'importance des jeux de données recueillis. Cette étape prépare le terrain pour le développement d'un modèle dynamique du TCHP, capable de reproduire le comportement transitoire et stationnaire de la machine, en vue de la conception et de l'évaluation de stratégies de contrôle avancées.

Chapitre 5

Ce chapitre présente le développement d'un modèle dynamique hybride de la pompe à chaleur à compresseurs thermiques (TCHP) destiné à l'analyse et à la conception de stratégies de contrôle avancées. Une première partie rappelle les approches existantes de modélisation dynamique des cycles à compression de vapeur, principalement basées sur les méthodes à volumes finis et à frontières mobiles. Les premières offrent une précision élevée mais sont coûteuses en calcul, tandis que les secondes sont plus rapides mais nécessitent des hypothèses simplificatrices sur les régimes d'écoulement. Dans le cas du cycle transcritique au CO_2, les transitions fréquentes entre sous-critique et supercritique justifient le choix d'une approche à volumes finis, plus robuste pour représenter les couplages entre composants.

Le modèle hybride est construit en combinant des sous-modèles transitoires et en régime permanent. Les composants décrits de manière différentielle incluent les échangeurs de chaleur (refroidisseur de gaz, évaporateur, échangeur interne, réservoir tampon), la cuve flash, le mélangeur, ainsi que la dynamique thermique des chauffages du TC (éléments chauffants), modélisée par identification système. Les équations de conservation de la masse, de l'énergie et de la température de paroi y sont appliquées. Les composants décrits en régime permanent regroupent les compresseurs thermiques, représentés par des modèles empiriques (régression gaussienne pour TC1 et TC2, régression linéaire pour TC3), les vannes de détente et l'échangeur de fumées décrit par la méthode du LMTD. L'ensemble est interconnecté pour restituer les flux de masse, d'énergie et les échanges thermiques entre le circuit frigorigène et les boucles secondaires eau et fumées. Le système est formulé sous forme d'espace d'état et résolu numériquement par un schéma de Runge–Kutta.

La validation est réalisée en régime permanent et transitoire. En régime permanent, quinze points expérimentaux montrent une bonne cohérence entre prédictions et mesures. Les pressions au gaz refroidisseur et à l'évaporateur sont reproduites avec une erreur absolue moyenne inférieure à deux bars et des coefficients de détermination supérieurs à 0,8, tandis que les puissances thermiques et les COP sont prédits avec une erreur relative inférieure à 6 %. En régime transitoire, des essais en échelon sur l'ouverture des vannes et

sur la vitesse du ventilateur de combustion confirment la capacité du modèle à reproduire les tendances dynamiques principales, en particulier la forte sensibilité à l'ouverture de la vanne haute pression et à la variation du débit de fumées. Certaines limites apparaissent toutefois, comme la faible propagation de l'influence de la vanne basse pression vers la haute pression et la présence de valeurs négatives de R^2 dues au bruit de mesure.

En conclusion, le modèle TCHP-HYB fournit une représentation fidèle du comportement réel de la machine, tant en régime permanent qu'en régime transitoire. Il permet d'analyser l'impact des paramètres d'entrée et de valider la conception du système, mais il reste coûteux en temps de calcul, ce qui limite son utilisation directe pour des applications de commande en temps réel. Ces résultats justifient le recours à des modèles d'ordre réduit, plus adaptés aux stratégies de contrôle prédictif, qui seront développés dans le chapitre suivant.

Chapitre 6

Ce chapitre s'appuie sur le modèle hybride TCHP-HYB développé et validé précédemment afin de concevoir une stratégie de contrôle avancée pour la TCHP. L'objectif est d'améliorer l'efficacité énergétique du système et d'optimiser l'utilisation du gaz naturel grâce à un contrôle plus performant. En l'absence de prototype expérimental disponible, la stratégie proposée est implémentée et testée sur le modèle validé TCHP-HYB, qui sert de référence pour le développement et l'évaluation du contrôle.

La revue de la littérature sur les stratégies de contrôle appliquées aux cycles à compression de vapeur met en évidence les difficultés spécifiques liées à la nature fortement non linéaire de ces systèmes et au couplage prononcé entre les variables. Les premières approches de contrôle, limitées au fonctionnement tout ou rien et aux boucles PID simples, se sont révélées insuffisantes face aux exigences accrues d'efficacité énergétique et de flexibilité. Progressivement, des stratégies plus avancées telles que le contrôle multivariable (MIMO) et, en particulier, le contrôle prédictif par modèle (MPC), ont été introduites afin de mieux gérer les interactions et les contraintes. Ces méthodes nécessitent toutefois des modèles réduits précis et rapides, capables de représenter la dynamique du cycle tout en étant adaptés à une utilisation en temps réel.

Dans le cas des cycles transcritiques au CO_2, l'importance de la pression haute a conduit à de nombreuses tentatives d'optimisation, reposant souvent sur des corrélations dérivées de données expérimentales ou de modèles simplifiés. Toutefois, ces corrélations montrent leurs limites, car elles sont rarement généralisables et nécessitent des recalibrages fréquents. Face à ces contraintes, la recherche récente privilégie les approches de type optimisation en ligne et MPC, parfois couplées à des méthodes d'apprentissage automatique. L'intérêt des réseaux de neurones, en particulier des modèles récurrents (RNN, Recurrent Neural Networks et LSTM, Long Short-Term Memory), est d'offrir une capacité accrue à capturer les dynamiques temporelles complexes et les non-linéarités, rendant possible une intégration efficace dans une boucle MPC.

La problématique de contrôle du TCHP est ainsi formulée en prenant en compte la nécessité de suivre une consigne de température de l'eau de sortie tout en minimisant la consommation de gaz. La stratégie de contrôle de référence, basée sur des boucles PID appliquées au ventilateur de combustion et à la vanne haute pression, a montré ses

limites lors d'essais expérimentaux. Les résultats ont mis en évidence des dépassements de consigne et des temps de stabilisation élevés, liés à l'incapacité de cette stratégie à gérer simultanément les dynamiques rapides de la température de l'eau et les contraintes thermiques imposées aux composants.

Pour dépasser ces limitations, une nouvelle stratégie de type MPC est proposée. Celle-ci repose sur des modèles réduits obtenus par apprentissage supervisé : un RNN simple et un LSTM. Ces modèles sont entraînés à partir de données réelles et simulées (issues du TCHP-HYB), en utilisant une architecture encodeur–décodeur adaptée aux séries temporelles. Ils permettent de prédire l'évolution de la température de l'eau de sortie sur un horizon prédictif d'une dizaine de secondes, à partir des commandes appliquées (vitesse du ventilateur et ouverture de la vanne haute pression) et des conditions de fonctionnement (température de retour de l'eau, débit massique). La qualité des prédictions a été validée par des tests sur échantillons non vus, avec des coefficients de détermination supérieurs à 0,97 et des erreurs quadratiques moyennes faibles.

L'intégration de ces modèles dans un cadre MPC permet d'optimiser simultanément les deux variables de commande, tout en respectant les contraintes physiques, telles que la limite maximale de température des chauffages du TC. L'objectif de la fonction de coût est de minimiser l'écart entre la température de l'eau de sortie et sa consigne, de limiter la consommation de gaz, et de réduire les variations excessives des actionneurs. Les résultats de simulation montrent que le MPC couplé au RNN ou au LSTM améliore considérablement les performances par rapport au contrôle PID : le coefficient de performance thermique est accru d'environ 15 à 20%, l'erreur moyenne sur la température est réduite de moitié, et les dépassements de consigne sont largement diminués. Le temps de stabilisation passe de plusieurs minutes avec le PID à quelques dizaines de secondes avec le MPC. Parmi les deux architectures, le MPC–LSTM s'avère légèrement plus performant que le MPC–RNN, grâce à sa meilleure capacité à capturer les dépendances à long terme.

Ces améliorations se font au prix d'un coût de calcul plus élevé : une vingtaine de millisecondes par pas de calcul pour le MPC–RNN et le MPC–LSTM, contre moins d'une milliseconde pour le PID. Néanmoins, ce coût reste compatible avec une implémentation en temps réel, compte tenu d'un temps d'échantillonnage d'une seconde. Des pistes d'optimisation sont envisageables, notamment par l'utilisation de MPC approché ou de politiques apprises hors ligne.

En conclusion, ce chapitre démontre la pertinence d'associer des modèles réduits basés sur des RNN ou LSTM à une stratégie de contrôle MPC pour améliorer la performance énergétique et la robustesse des cycles transcritiques au CO_2. La méthode proposée permet de dépasser les limites des corrélations empiriques et des PID classiques, en garantissant un suivi précis de la consigne de température de l'eau et en réduisant la consommation de gaz. Bien que la validation ait été limitée au modèle TCHP–HYB, les résultats obtenus confirment le potentiel de généralisation de cette approche à d'autres pompes à chaleur ou cycles à compression de vapeur. Les perspectives de recherche incluent la réduction du coût de calcul, l'extension à de nouvelles variables de commande, ainsi que des validations expérimentales sur systèmes réels.

Conclusion générale

Cette thèse a montré qu'une démarche intégrée, articulant expérimentation, modélisation physique et apprentissage statistique, permet d'aborder efficacement la complexité d'une TCHP au CO_2 et d'en optimiser le contrôle. Au niveau du composant, le TC a été caractérisé sur banc et décrit par deux familles de modèles complémentaires : un modèle physique en volumes finis de troisième ordre, apte à révéler les mécanismes internes et les destructions d'exergie, et des modèles empiriques rapides — en particulier une régression à processus gaussiens — suffisamment précis pour leur intégration dans le modèle dynamique de pompe à chaleur et la synthèse de lois de commande. Au niveau du cycle complet, un modèle dynamique hybride de la pompe à chaleur a été construit et validé, établissant un référentiel cohérent pour la synthèse de lois de commande. Sur cette base, des modèles réduits récurrents ont été identifiés et couplés à un contrôle prédictif par modèle ciblant directement la température d'eau de sortie et la pression haute, ce qui a permis d'améliorer nettement le suivi de consigne, de réduire les dépassements et d'augmenter le coefficient de performance par rapport à une stratégie proportionnelle–intégrale–dérivée fondée sur des corrélations statiques. Si l'absence d'une validation finale sur machine et le coût de calcul supérieur au contrôle classique restent des limites, les résultats démontrent la faisabilité d'une commande avancée en temps réel avec des horizons courts, et ouvrent des perspectives concrètes : élargissement du domaine d'identification, allègement du calcul (contrôle prédictif approché ou politiques apprises hors ligne), prise en compte de degrés de liberté additionnels et intégration dans des stratégies de pilotage multiénergies. Plus largement, les outils développés — modèles, données, méthodologie de contrôle — constituent une base robuste pour accélérer la maturation des TCHP et, au-delà, de cycles transcritiques au CO_2 plus sobres et compatibles avec les objectifs de décarbonation du chauffage résidentiel.

Bibliography

Afram, A. and Janabi-Sharifi, F. (2014). Review of modeling methods for hvac systems. *Applied Thermal Engineering*, 67(1):507–519.

Afram, A., Janabi-Sharifi, F., Fung, A. S., and Raahemifar, K. (2017). Artificial neural network (ann) based model predictive control (mpc) and optimization of hvac systems: A state of the art review and case study of a residential hvac system. *Energy and Buildings*, 141:96–113.

Agrawal, N., Bhattacharyya, S., and Sarkar, J. (2007). Optimization of two-stage transcritical carbon dioxide heat pump cycles. *International Journal of Thermal Sciences*, 46(2):180–187.

Ahmadi, M. H., Ahmadi, M.-A., and Pourfayaz, F. (2017). Thermal models for analysis of performance of stirling engine: A review. *Renewable and Sustainable Energy Reviews*, 68:168–184.

Andersen, S. (2006). *Numerical Simulation of Cyclic Thermodynamic Processes*. PhD thesis. MEK-ET-PHD-2006-01.

Aprea, C. and Maiorino, A. (2009). Heat rejection pressure optimization for a carbon dioxide split system: An experimental study. *Applied Energy*, 86(11):2373–2380.

Artuso, P., Tosato, G., Rossetti, A., Marinetti, S., Hafner, A., Banasiak, K., and Minetto, S. (2021). Dynamic modelling and validation of an air-to-water reversible r744 heat pump for high energy demand buildings. *Energies*, 14(24).

Austin, B. T. and Sumathy, K. (2011). Transcritical carbon dioxide heat pump systems: A review. *Renewable and Sustainable Energy Reviews*, 15(8):4013–4029.

Baek, C., Heo, J., Jung, J., Cho, H., and Kim, Y. (2013). Optimal control of the gas-cooler pressure of a co2 heat pump using eev opening and outdoor fan speed in the cooling mode. *International Journal of Refrigeration*, 36(4):1276–1284.

Bechtler, H., Browne, M., Bansal, P., and Kecman, V. (2001). New approach to dynamic modelling of vapour-compression liquid chillers: artificial neural networks. *Applied Thermal Engineering*, 21(9):941–953.

Beghi, A., Rampazzo, M., and Zorzi, S. (2017). Reinforcement learning control of transcritical carbon dioxide supermarket refrigeration systems. *IFAC-PapersOnLine*, 50(1):13754–13759. 20th IFAC World Congress.

Bell, I. (2011). Theoretical and experimental analysis of liquid flooded compression in scroll compressors.

Bell, I. H., Wronski, J., Quoilin, S., and Lemort, V. (2014). Pure and pseudo-pure fluid thermophysical property evaluation and the open-source thermophysical property library coolprop. *Industrial & Engineering Chemistry Research*, 53(6):2498–2508.

Bendapudi, S., Braun, J. E., and Groll, E. A. (2002). A dynamic model of a vapor compression liquid chiller. In *Proceedings of the International Refrigeration and Air Conditioning Conference at Purdue*, number 568, West Lafayette, IN, USA.

Bendapudi, S., Braun, J. E., and Groll, E. A. (2008). A comparison of moving-boundary and finite-volume formulations for transients in centrifugal chillers. *International Journal of Refrigeration*, 31(8):1437–1452.

Boroujerdi, A., Ashrafizadeh, A., and Mousavi Naeenian, S. (2011). Numerical analysis of stirling type pulse tube cryocoolers. *Cryogenics*, 51(9):521–529.

BP (2023). Statistical review of world energy 2023. Technical report, BP.

Braven, K. D., Penoncello, S., Herold, K., Mei, V., and O'Neal, D. (1993). Improving heat pumps and air conditioning. *Mechanical Engineering; (United States)*, 115:9.

Bush, V. (1939). Apparatus for compressing gases. US Patent 2,157,229.

Cavallini, A., Cecchinato, L., Corradi, M., Fornasieri, E., and Zilio, C. (2005). Two-stage transcritical carbon dioxide cycle optimisation: A theoretical and experimental analysis. *International Journal of Refrigeration*, 28(8):1274–1283. CO2 as Working Fluid - Theory and Applications.

Cecchinato, L., Chiarello, M., Corradi, M., Fornasieri, E., Minetto, S., Stringari, P., and Zilio, C. (2009). Thermodynamic analysis of different two-stage transcritical carbon dioxide cycles. *International Journal of Refrigeration*, 32(5):1058–1067.

Cecchinato, L., Corradi, M., Cosi, G., Minetto, S., and Rampazzo, M. (2012). A real-time algorithm for the determination of r744 systems optimal high pressure. *International Journal of Refrigeration*, 35(4):817–826.

Cecchinato, L., Corradi, M., and Minetto, S. (2010). A critical approach to the determination of optimal heat rejection pressure in transcritical systems. *Applied Thermal Engineering*, 30(13):1812–1823.

Chen, N. C. J. and Griffin, F. P. (1983). Review of Stirling-engine mathematical models.

Chen, W.-L., Yang, Y.-C., and Salazar, J. L. (2015). A cfd parametric study on the performance of a low-temperature-differential -type stirling engine. *Energy Conversion and Management*, 106:635–643.

Chen, Y. and Gu, J. (2005). The optimum high pressure for co2 transcritical refrigeration systems with internal heat exchangers. *International Journal of Refrigeration*, 28(8):1238–1249. CO2 as Working Fluid - Theory and Applications.

Cheng, C.-H. and Phung, D.-T. (2021). Numerical and experimental study of a compact 100-w-class β-type stirling engine. *International Journal of Energy Research*, 45(5):6784–6799.

Cheng, L., Ribatski, G., Wojtan, L., and Thome, J. R. (2006). New flow boiling heat transfer model and flow pattern map for carbon dioxide evaporating inside horizontal tubes. *International Journal of Heat and Mass Transfer*, 49(21):4082–4094.

Chi, J. and Didion, D. (1982). A simulation model of the transient performance of a heat pump. *International Journal of Refrigeration*, 5(3):176–184.

Chollet, F. et al. (2015). Keras. https://github.com/fchollet/keras.

Dai, W., Matsubara, Y., and Kobayashi, H. (2002). Experimental results on v-m type pulse tube refrigerator. *Cryogenics*, 42(6):433–437.

Desideri, A., Dechesne, B., Wronski, J., Van den Broek, M., Gusev, S., Lemort, V., and Quoilin, S. (2016). Comparison of moving boundary and finite-volume heat exchanger models in the modelica language. *Energies*, 9(5).

Diniz, H. A. G., Paulino, T. F., Pabon, J. J. G., Maia, A. A. T., and Oliveira, R. N. (2021). Dynamic model of a transcritical co2 heat pump for residential water heating. *Sustainability*, 13(6).

Dyson, R. W., Wilson, S. D., and Tew, R. C. (2004). Review of computational stirling analysis methods. In *Second International Energy Conversion Engineering Conference*, number NASA/TM-2004-213300, Providence, RI, United States. AIAA Paper 2004-5582, E-14747.

Eborn, J. (2001). *On Model Libraries for Thermo-hydraulic Applications*. Doctoral thesis (compilation), Department of Automatic Control, Lund Institute of Technology (LTH). Department of Automatic Control.

Edwards, M. J. and Peterson, R. B. (2007). Reciprocating thermocompressor performance with non-ideal component characteristics. *Proceedings of the Institution of Mechanical Engineers, Part A: Journal of Power and Energy*, 221(4):459–471.

Elbel, S. and Hrnjak, P. (2008). Experimental validation of a prototype ejector designed to reduce throttling losses encountered in transcritical r744 system operation. *International Journal of Refrigeration*, 31(3):411–422.

Elliott, M. S. and Rasmussen, B. P. (2008). Model-based predictive control of a multi-evaporator vapor compression cooling cycle. In *2008 American Control Conference*, pages 1463–1468.

Elman, J. L. (1990). Finding structure in time. *Cognitive Science*, 14(2):179–211.

Eurostat (2022). Energy use in eu households in 2022 lowest since 2016. Accessed: Jun. 05, 2024.

Fallahsohi, H. (2023). Energy analysis of the heat pump operating with supercritical CO_2 driven by thermal compression. *American Journal of Engineering Research (AJER)*, 12(11):61–74.

Finkelstein, T. (1960). Generalized thermodynamic analysis of stirling engines. SAE Technical Paper 600222, SAE International. Presented at Pre-1964 SAE Technical Papers.

Gedeon, D. (2014). Sage users guide v10 edition. *Athens: Gedeon Associates*, 558.

Goyal, A., Staedter, M. A., and Garimella, S. (2019). A review of control methodologies for vapor compression and absorption heat pumps. *International Journal of Refrigeration*, 97:1–20.

Haykin, S. (2009). *Neural Networks and Learning Machines*. Pearson Practice Hall, 3rd edition edition.

He, X.-D., Liu, S., and Asada, H. H. (1997). Modeling of vapor compression cycles for multivariable feedback control of hvac systems. *Journal of Dynamic Systems, Measurement, and Control*, 119(2):183–191.

He, X.-D., Liu, S., Asada, H. H., and and, H. I. (1998). Multivariable control of vapor compression systems. *HVAC&R Research*, 4(3):205–230.

Hochreiter, S. and Schmidhuber, J. (1997). Long short-term memory. *Neural Comput.*, 9(8):1735–1780.

Hosseinzade, H. and Sayyaadi, H. (2015). Cafs: The combined adiabatic–finite speed thermal model for simulation and optimization of stirling engines. *Energy Conversion and Management*, 91:32–53.

Hu, B., Li, Y., Cao, F., and Xing, Z. (2015). Extremum seeking control of cop optimization for air-source transcritical co2 heat pump water heater system. *Applied Energy*, 147:361–372.

Husmann, R. and Aschemann, H. (2022). Dynamic modeling of a vapor compression cycle. *IFAC-PapersOnLine*, 55(20):523–528. 10th Vienna International Conference on Mathematical Modelling MATHMOD 2022.

Ibsaine, R. (2015). *Étude d'un système tritherme intégrant une compression thermique originale, destiné au marché du chauffage résidentiel*. PhD thesis. Thèse de doctorat dirigée par Stouffs, Pascal Energétique Pau 2015.

Ibsaine, R., Joffroy, J.-M., and Stouffs, P. (2016). Modelling of a new thermal compressor for supercritical co2 heat pump. *Energy*, 117:530–539. The 28th International Conference on Efficiency, Cost, Optimization, Simulation and Environmental Impact of Energy Systems - ECOS 2015.

IEA (2022). The future of heat pumps. Executive Summary. License: CC BY 4.0.

IEA (2023). World energy outlook 2023. Technical report, International Energy Agency.

IPCC (2023). Sixth assessment report: Climate change 2023. Technical report, Intergovernmental Panel on Climate Change.

Jain, N. and Alleyne, A. (2015). Exergy-based optimal control of a vapor compression system. *Energy Conversion and Management*, 92:353–365.

James, G., Witten, D., Hastie, T., and Tibshirani, R. (2013). *An Introduction to Statistical Learning with Applications in R*. Springer, New York.

Jensen, J. B. and Skogestad, S. (2007). Optimal operation of simple refrigeration cycles: Part i: Degrees of freedom and optimality of sub-cooling. *Computers Chemical Engineering*, 31(5):712–721. ESCAPE-15.

Kauf, F. (1999). Determination of the optimum high pressure for transcritical co_2-refrigeration cycles. *International Journal of Thermal Sciences*, 38(4):325–330.

Kim, M.-H., Pettersen, J., and Bullard, C. W. (2004). Fundamental process and system design issues in co_2 vapor compression systems. *Progress in Energy and Combustion Science*, 30(2):119–174.

Ko, J., Takata, N., Thu, K., and Miyazaki, T. (2020). Dynamic modeling and validation of a carbon dioxide heat pump system. *Evergreen*, 7(2):172–194. Publisher Copyright: © 2020, Novel Carbon Resource Sciences. All rights reserved.

Kornhauser, A. (1996). Analysis of an idealized stirling thermocompressor. In *IECEC 96. Proceedings of the 31st Intersociety Energy Conversion Engineering Conference*, volume 2, pages 1331–1336 vol.2.

Kühn, A. (2013). *Thermally driven heat pumps for heating and cooling*. Universitätsverlag der TU Berlin.

Kyoto Protocol (1997). Kyoto protocol to the united nations framework convention on climate change. International treaty. Adopted on 11 December 1997 and entered into force on 16 February 2005.

Leducq, D., Guilpart, J., and Trystram, G. (2006). Non-linear predictive control of a vapour compression cycle. *International Journal of Refrigeration*, 29(5):761–772.

Liao, S., Zhao, T., and Jakobsen, A. (2000). A correlation of optimal heat rejection pressures in transcritical carbon dioxide cycles. *Applied Thermal Engineering*, 20(9):831–841.

Lin, J.-L. and Yeh, T.-J. (2007). Modeling, identification and control of air-conditioning systems. *International Journal of Refrigeration*, 30(2):209–220.

Lin, W.-Y., Wu, X.-H., Yang, J.-L., and Yang, L.-W. (2013). Experimental study and numerical analysis of thermocompressors with annular regenerators. *International Journal of Refrigeration*, 36(4):1376–1387.

Ljung, L. (1999). *System identification (2nd ed.): theory for the user*. Prentice Hall PTR, USA.

Lorentzen, G. (1994). Revival of carbon dioxide as a refrigerant. *International Journal of Refrigeration*, 17(5):292–301.

Ma, J., Dong, Y., Qiao, H., and Laughman, C. R. (2024). A physics-constrained deep learning framework for dynamic modeling of vapor compression systems. *Applied Thermal Engineering*, 254:123734.

MacArthur, J. and Grald, E. (1989). Unsteady compressible two-phase flow model for predicting cyclic heat pump performance and a comparison with experimental data. *International Journal of Refrigeration*, 12(1):29–41.

Marcinichen, J. B., del Holanda, T. N., and Melo, C. (2008). A dual siso controller for a vapor compression refrigeration system. In *International Refrigeration and Air Conditioning Conference*, number Paper 922.

Martini, W. (1969). The thermocompressor and its application to artificial heart power. *Proceedings of the 4th Intersociety Energy Conversion Engineering Conference*, pages 107–114.

Martini, W. R. (1983). Stirling engine design manual, 2nd edition. Technical Report NASA-CR-168088, Martini Engineering.

McKinley, T. L. and Alleyne, A. G. (2008). An advanced nonlinear switched heat exchanger model for vapor compression cycles using the moving-boundary method. *International Journal of Refrigeration*, 31(7):1253–1264.

Minetto, S. (2011). Theoretical and experimental analysis of a co_2 heat pump for domestic hot water. *International Journal of Refrigeration*, 34(3):742–751.

Montreal Protocol (1987). Montreal protocol on substances that deplete the ozone layer. International treaty. Adopted on 16 September 1987 and entered into force on 1 January 1989.

Nanayakkara, V. K., Ikegami, Y., and Uehara, H. (2002). Evolutionary design of dynamic neural networks for evaporator control. *International Journal of Refrigeration*, 25(6):813–826.

Outtagarts, A., Haberschill, P., and Lallemand, M. (1997). The transient response of an evaporator fed through an electronic expansion valve. *International Journal of Energy Research*, 21(9):793–807.

Pan, C., Wang, J., Zhang, T., Wang, J., and Zhou, Y. (2017). Numerical investigation on the thermoacoustics characteristics of thermal compressor for the pulse tube cryocooler. *Applied Thermal Engineering*, 123:234–242.

Paris Agreement (2015). United nations framework convention on climate change. International treaty. Adopted at the 21st Conference of the Parties of the UNFCCC in Paris, France, December 2015.

Parlos, A., Chong, K., and Atiya, A. (1994). Application of the recurrent multilayer perceptron in modeling complex process dynamics. *IEEE Transactions on Neural Networks*, 5(2):255–266.

Pawela, B. and Jaszczur, M. (2022). Review of gas engine heat pumps. *Energies*, 15(13).

Peñarrocha, I., Llopis, R., Tárrega, L., Sánchez, D., and Cabello, R. (2014). A new approach to optimize the energy efficiency of co2 transcritical refrigeration plants. *Applied Thermal Engineering*, 67(1):137–146.

Pfafferott, T. and Schmitz, G. (2004). Modelling and transient simulation of co_2-refrigeration systems with modelica. *International Journal of Refrigeration*, 27(1):42–52.

Pillonetto, G., Aravkin, A., Gedon, D., Ljung, L., Ribeiro, A. H., and Schön, T. B. (2025). Deep networks for system identification: A survey. *Automatica*, 171:111907.

Prášek, J., Trnka, P., Havlena, V., and McGahan, P. (2020). Range control mpc with application to vapor compression cycles. *Control Engineering Practice*, 96:104309.

Péan, T. Q., Salom, J., and Costa-Castelló, R. (2019). Review of control strategies for improving the energy flexibility provided by heat pump systems in buildings. *Journal of Process Control*, 74:35–49. Efficient energy management.

Qi, P.-C., He, Y.-L., Wang, X.-L., and Meng, X.-Z. (2013). Experimental investigation of the optimal heat rejection pressure for a transcritical co_2 heat pump water heater. *Applied Thermal Engineering*, 56(1):120–125.

Qiao, H., Aute, V., and Radermacher, R. (2015). Transient modeling of a flash tank vapor injection heat pump system – part i: Model development. *International Journal of Refrigeration*, 49:169–182.

Qin, S. and Badgwell, T. A. (2003). A survey of industrial model predictive control technology. *Control Engineering Practice*, 11(7):733–764.

Qin, X., Liu, H., Meng, X., Wei, X., Zhao, L., and Yang, L. (2019). A study on the compressor frequency and optimal discharge pressure of the transcritical co2 heat pump system. *International Journal of Refrigeration*, 99:101–113.

Qiu, H., Wang, K., Yu, P., Ni, M., and Xiao, G. (2021). A third-order numerical model and transient characterization of a β-type stirling engine. *Energy*, 222:119973.

Quoilin, S. (04 October 2011). *Sustainable energy conversion through the use of Organic Rankine Cycles for waste heat recovery and solar applications*. PhD thesis, ULiège - Université de Liège.

Quoilin, S. and Schrouff, J. (2016). Assessing steady-state, multivariate experimental data using gaussian processes: The gpexp open-source library. *Energies*, 9(6).

Qureshi, T. and Tassou, S. (1996). Variable-speed capacity control in refrigeration systems. *Applied Thermal Engineering*, 16(2):103–113.

Rampazzo, M., Cervato, A., Corazzol, C., Mattiello, L., Beghi, A., Cecchinato, L., and Virzi, A. (2019). Energy-efficient operation of transcritical and subcritical co2 inverse cycles via extremum seeking control. *Journal of Process Control*, 81:87–97.

Rasmussen, B. P. (2012). Dynamic modeling for vapor compression systems—part i: Literature review. *HVAC&R Research*, 18(5):934–955.

Rasmussen, B. P. and Alleyne, A. G. (2004). Control-oriented modeling of transcritical vapor compression systems. *Journal of Dynamic Systems, Measurement, and Control*, 126(1):54–64.

Rasmussen, B. P. and Alleyne, A. G. (2006). Dynamic modeling and advanced control of air conditioning and refrigeration systems. Technical Report TR-244, Air Conditioning and Refrigeration Center. College of Engineering. University of Illinois at Urbana-Champaign. Air Conditioning and Refrigeration Project 163.

Rasmussen, C. E. (2004). *Gaussian Processes in Machine Learning*, pages 63–71. Springer Berlin Heidelberg, Berlin, Heidelberg.

Ren, Y. M., Alhajeri, M. S., Luo, J., Chen, S., Abdullah, F., Wu, Z., and Christofides, P. D. (2022). A tutorial review of neural network modeling approaches for model predictive control. *Computers Chemical Engineering*, 165:107956.

Robinson, D. M. and Groll, E. A. (1998). Efficiencies of transcritical co2 cycles with and without an expansion turbine: Rendement de cycles transcritiques au co2 avec et sans turbine d'expansion. *International Journal of Refrigeration*, 21(7):577–589.

Rodriguez, E. and Rasmussen, B. P. (2016). A nonlinear reduced-order modeling method for dynamic two-phase flow heat exchanger simulations. *Science and Technology for the Built Environment*, 22(2):164–177.

Rossi, T. and Braun, J. (1999). A real-time transient model for air conditioners. In *Proc. 20th International Congress of Refrigeration, Sydney, Paper*, volume 743.

Salame, A. (2025a). My thesis codes. https://github.com/AliSalami98/My-thesis-codes/tree/main/TC-3RD.

Salame, A. (2025b). My thesis codes. https://github.com/AliSalami98/My-thesis-codes/tree/main/TC-ML.

Salazar, M. and Méndez, F. (2014). Pid control for a single-stage transcritical co2 refrigeration cycle. *Applied Thermal Engineering*, 67(1):429–438.

Sarkar, J., Bhattacharyya, S., and Gopal, M. (2004). Optimization of a transcritical co_2 heat pump cycle for simultaneous cooling and heating applications. *International Journal of Refrigeration*, 27(8):830–838.

Schmidt, G. (1871). Theorie der lehmannschen calorischen maschine. *Zeitschrift des Vereines Deutscher Ingenieure, XV-1*.

Shah, M. (1979). A general correlation for heat transfer during film condensation inside pipes. *International Journal of Heat and Mass Transfer*, 22(4):547–556.

Shah, R., P. Rasmussen, B., and Alleyne, A. G. (2004). Application of a multivariable adaptive control strategy to automotive air conditioning systems. *International Journal of Adaptive Control and Signal Processing*, 18(2):199–221.

Song, Y., Cui, C., Yin, X., and Cao, F. (2022). Advanced development and application of transcritical co2 refrigeration and heat pump technology—a review. *Energy Reports*, 8:7840–7869.

Thomas, S. and Barth, E. J. (2022). Active stirling thermocompressor: Modelling and effects of controlled displacer motion profile on work output. *Applied Energy*, 327:120084.

Turgut, M. S. and Çoban, M. T. (2020). Neural network predictive control of a vapor compression cycle. *Arabian Journal for Science and Engineering*, 45(2):779–796.

Urieli, I. and Berchowitz, D. (1984). *Stirling Cycle Engine Analysis,*. Modern energy studies. Taylor & Francis.

Vargas, J. and Parise, J. (1995). Simulation in transient regime of a heat pump with closed-loop and on-off control. *International Journal of Refrigeration*, 18(4):235–243.

Wallace, M., Das, B., Mhaskar, P., House, J., and Salsbury, T. (2012). Offset-free model predictive control of a vapor compression cycle. *Journal of Process Control*, 22(7):1374–1386.

Wang, J., Pan, C., Luo, K., Chen, L., Wang, J., and Zhou, Y. (2018). Thermal analysis of stirling thermocompressor and its prospect to drive refrigerator by using natural working fluid. *Energy Conversion and Management*, 177:280–291.

Wang, J., Xi, X., Luo, K., Chen, L., Wang, J., and Zhou, Y. (2019). Energy and exergy equilibrium analysis of stirling-type thermal compressor (stc)—the core part in thermal-driven vuilleumier machines. *Energy Conversion and Management*, 199:111961.

Wang, K., Dubey, S., Choo, F. H., and Duan, F. (2016). A transient one-dimensional numerical model for kinetic stirling engine. *Applied Energy*, 183:775–790.

Wang, W., Zhao, Z., Zhou, Q., Qiao, Y., and Cao, F. (2021). Model predictive control for the operation of a transcritical co2 air source heat pump water heater. *Applied Energy*, 300:117339.

West, C. D. (1981). Theoretical basis for the beale number.

Wolscht, L., Knobloch, K., Jacquemoud, E., and Jenny, P. (2024). Dynamic simulation and experimental validation of a 35 mw heat pump based on a transcritical co2 cycle. *Energy*, 294:130897.

Wu, C., Xingxi, Z., and Shiming, D. (2005). Development of control method and dynamic model for multi-evaporator air conditioners (meac). *Energy Conversion and Management*, 46(3):451–465.

Yazar, I., Yavuz, H., and Yavuz, A. (2017). Comparison of various regression models for predicting compressor and turbine performance parameters. *Energy*, 140(Part 2):1398–1406.

Yoon, S. H., Kim, J. H., Hwang, Y. W., Kim, M. S., Min, K., and Kim, Y. (2003). Heat transfer and pressure drop characteristics during the in-tube cooling process of carbon

dioxide in the supercritical region. *International Journal of Refrigeration*, 26(8):857–864.

Zhang, W.-J. and Zhang, C.-L. (2011). A correlation-free on-line optimal control method of heat rejection pressures in co_2 transcritical systems. *International Journal of Refrigeration*, 34(4):844–850.

Zhang, X., Fan, X., Wang, F., and Shen, H. (2010). Theoretical and experimental studies on optimum heat rejection pressure for a co_2 heat pump system. *Applied Thermal Engineering*, 30(16):2537–2544. Selected Papers from the 12th Conference on Process Integration, Modelling and Optimisation for Energy Saving and Pollution Reduction.

Zheng, L., Deng, J., He, Y., and Jiang, P. (2015). Dynamic model of a transcritical co2 ejector expansion refrigeration system. *International Journal of Refrigeration*, 60:247–260.

Ziviani, D., Bahman, A. M., James, N. A., Lumpkin, D., Braun, J. E., and Groll, E. A. (2018). Machine learning applied to positive displacement compressors and expanders performance mapping. In *International Compressor Engineering Conference*, number 2533. Paper 2533.

Zubair, S. and Bahel, V. (1989). Compressor capacity modulation scheme. *HPAC Heating, Piping, Air Conditioning*, 61(1).

Çengel, Y. A. and Boles, M. A. (2019). *Thermodynamics: An Engineering Approach*. McGraw-Hill Education, 9 edition.